Information transmission in normal vision and optogenetically resensitised dystrophic retinas

John Martin Barrett

Thesis submitted in partial fulfilment of the requirements for the degree of Doctor of Philosophy

Newcastle University

Faculty of Medical Sciences

Institute of Neuroscience

February 2016

Abstract

The retina is a sophisticated image processing machine, transforming the visual scene as detected by the photoreceptors into a pattern of action potentials that is sent to the brain by the retinal ganglion cells (RGCs), where it is further processed to help us understand and navigate the world. Understanding this encoding process is important on a number of levels. First, it informs the study of upstream visual processing by elucidating the signals higher visual areas receive as input and how they relate to the outside world. Second, it is important for the development of treatments for retinal blindness, such as retinal prosthetics. In this thesis, I present work using multielectrode array (MEA) recordings of RGC populations from ex-vivo retinal wholemounts to study various aspects of retinal information processing. My results fall into two main themes. In the first part, in collaboration with Dr Geoffrey Portelli and Dr Pierre Kornprobst of INRIA, I use flashed gratings of varying spatial frequency and phase to compare different coding strategies that the retina might use. These results show that information is encoded synergistically by pairs of neurons and that, of the codes tested, a Rank Order Code based on the relative order of firing of the first spikes of a population of neurons following a stimulus provides information about the stimulus faster and more efficiently than other codes. In the later parts, I use optogenetic stimulation of RGCs in congenitally blind retinas to study how visual information is corrupted by the spontaneous hyperactivity that arises as a result of photoreceptor degeneration. I show that by dampening this activity with the gap junction blocker meclofenamic acid, I can improve the signal-to-noise ratio, spatial acuity and contrast sensitivity of prosthetically evoked responses. Taken together, this work provides important insights for the future development of retinal prostheses.

Acknowledgements

First and foremost, I would like to thank my primary supervisor, Dr Evelyne Sernagor, for her teaching, support, and supervision throughout my four years at Newcastle, from the very first lectures of the MRes to the final proof readings of this thesis. Thanks also go to my second supervisor, Dr Patrick Degenaar, for all of his help and guidance throughout my PhD and for providing the microLED array used in chapter 4. Additionally, I want to thank my assessors, Dr Andrew Jackson and Dr Andrew Trevelyan, for all of the advice they have given me.

I must acknowledge Dr Gerrit Hilgen for recording all of the APS multielectrode array data presented in this thesis, for which I am immensely grateful, as well as for all of the help and advice he has given me and useful discussions we have had since he started at Newcastle. Additionally, the work presented in chapter 3 was a collaborative effort between our lab and Dr Geoffrey Portelli and Dr Pierre Kornprobst of INRIA, whom I would also like to thank. They provided the stimuli for those experiments and Dr Portelli conducted the Bayesian decoding analysis.

More generally, I would like to thank everyone else I have worked alongside in Evelyne's lab. Special mention in this regard goes to Dr Cyril Eleftheriou, for being a great friend to me from the start and helping me get started in the lab, and to Yingdi Chen, who has also been a good friend and a source of many entertaining and enlightening discussions. Thanks also to everyone else who has been a friend to me during my PhD. Dr Harbajlit Sohal, for all of the support, advice, and great nights out! My fellow Wellcome Trust students, Ed and Ross. Anderson, Chris, Clare, Felix, Grace, Gemma, Henrik, James, Joe, Josh, Katherine, Matt A, Mikey, Sabine, Vasileios, and everyone who I've shared the Cookson postgrad office with. The postgrad rep team: Emma, Lauren W, Matt C, Nicola, Pav, Stacey, Tom. And anyone else whose name I've run out of room to mention here, you've all made my time at Newcastle wonderful!

Contents

1 Introduction **1**

1.1 The Retina 1

1.1.1 Basic Anatomy 1

1.1.2 Cell Types 3

Photoreceptors 3

Horizontal Cells 6

Bipolar Cells 6

Amacrine Cells 7

Ganglion Cells 7

1.1.3 Information Coding 9

Linear Models 9

Nonlinear Models 9

Biophysical Models 12

How Does the Retina Encode Information? 13

1.2 Retinal Dystrophies 15

1.2.1 Classification of Retinal Dystrophies 15

1.2.2 Animal Models 17

1.2.3 Anatomical Remodelling 21

1.2.4 Physiological Changes 24

1.2.5 Existing and Future Treatments 28

1.3 Retinal Prostheses 31

1.3.1 Electrical Prostheses 31

1.3.2 Optogenetic Prostheses 36

Optogenetics 36

A Brief History of Optogenetic Retinal Prostheses 38

Choice of Target Cell Type 43

Choice of Opsin 45
1.4 Aims of the Thesis 46

2 Materials and Methods 49

2.1 Animals and Breeding 49
2.2 Electrophysiology 54
2.2.1 Dissection 54
2.2.2 MEA Systems 54
2.3 Analysis 56
2.3.1 Spike Extraction and Sorting 56
2.3.2 Information Theory 57
Mutual Information for Discrete Random Variables 57
Mutual Information for Neural Data 59
2.3.3 Bayesian Decoding 60

3 Comparison of Coding Strategies in the Healthy Retina 65

3.1 Introduction 65
3.1.1 How Do Individual RGCs Encode Information? 65
3.1.2 How Do Ensembles of RGCs Encode Information? 66
3.1.3 Aims 69
3.2 Specific Methods 69
3.2.1 Visual Stimulation 70
3.2.2 Data Analysis 72
Responsive Cell Selection 72
Partial Information Decomposition 72
3.3 Results 77
3.3.1 Pairs of RGCs Encode Information Synergistically 77
3.3.2 Spike Count Outperforms Spike Latency and Rank Order Code . . 80
3.3.3 High-Density MEA Recordings 83
3.4 Discussion 90
3.4.1 Rank Order Coding in Large RGC Populations 90

3.4.2 Do RGCs Act as Independent Encoders? . . . 91
3.4.3 Future Work . . . 93
Cell Types . . . 93
Other Stimulus Classes . . . 96
3.4.4 Conclusion . . . 98

4 Pharmacology of Degenerate Spontaneous Activity and Optogenetic Stimulation 99
4.1 Introduction . . . 99
4.2 Specific Methods . . . 101
4.2.1 Drugs . . . 101
4.2.2 Quantification of Oscillations and Spontaneous Activity . . . 101
4.2.3 Optogenetic Stimulation Using MicroLED Arrays . . . 102
4.2.4 Stimuli . . . 103
Detecting Optogenetically Responsive Cells . . . 103
Stimulation Threshold and Signal-to-Noise Ratio . . . 104
Spike Triggered Averaging and Receptive Field Measurement . . . 105
Moving Bars . . . 106
Statistical Analysis . . . 106
4.3 Results . . . 107
4.3.1 Spontaneous Activity . . . 107
4.3.2 ChR2 Responsiveness and Signal-to-Noise Ratio . . . 107
4.3.3 Spatiotemporally Patterned Stimulation . . . 110
4.4 Discussion . . . 116
4.4.1 Blocking spontaneous activity improves SNR regardless of the the mechanism of action . . . 116
4.4.2 Effects on Stimulation Efficiency of ChR2 RGCs . . . 117
4.4.3 Spatiotemporally Patterned Stimulation of Optogenetically Sensitive Retinas . . . 117
4.4.4 Implications for Treatment of Retinal Degenerations . . . 119
4.4.5 Conclusions . . . 120

5 Improving Optogenetic Responses by Dampening Spontaneous Activity 121

5.1 Introduction 121

5.2 Specific Methods 122

5.2.1 Visual and Optogenetic Stimuluation using a DLP Projector and Recording from a Large Scale MEA 123

5.2.2 Experimental Design 124

Detecting Responsive Cells 125

Stimulus Decoding Experiments 125

Simulated Two-Alternative Forced Choice Task 126

5.2.3 Stimuli 126

5.2.4 Psychometric Function Fitting 127

5.2.5 Simulated LogMAR Testing 131

5.2.6 Statistical Analysis 132

5.3 Results 133

5.3.1 Successful Optogenetic Stimulation Using the APS Projector 133

5.3.2 Blockade of Spontaneous Activity Facilitates Decoding of Stimulus Properties 139

5.3.3 Blockade of Spontaneous Activity Improves Spatial Acuity 139

5.3.4 Blockade of Spontaneous Activity Improves Contrast Sensitivity . . 145

5.4 Discussion 148

5.4.1 Interaction Between Optogenetic Responses and Contrast 149

5.4.2 Quality and Stability of `psignifit` Fits 156

5.4.3 Comparison to Healthy Retina Performance 162

5.4.4 Comparison to Electrical Prostheses in Clinical Trials 162

5.4.5 Comparison to Previous Studies on Optogenetic Prostheses 164

5.4.6 Conclusions and Future Work 166

6 General Discussion 169

6.1 Retinal Coding: Implications for Prosthetic Design 169

6.2 Dampening Spontaneous Activity in the Clinic 172

6.2.1 Strategies for Dampening Spontaneous Activity 173

6.2.2 Generalisability 174
6.2.3 Light Intensity and Power Requirements 175

Appendices **177**

Appendix A Development of a Partial Information Decomposition for Spike Trains **177**
Appendix A.1 Introduction 177
Appendix A.2 A Binless PID Estimator 178
Appendix A.3 Evaluation 182
Appendix A.3.1 Generating Simulated Spike Train Data 182
Appendix A.3.2 Direct PID Calculation for Stimulated Poisson Neurons . 184
Appendix A.3.3 Calculating and Evaluating Estimated PID Values 187
Appendix A.4 Results 188
Appendix A.5 Discussion 196

Appendix B Worked PID Examples **201**
Appendix B.1 Different RGC Types Give Rise to Synergy Without Correlations 201
Appendix B.1.1 The Model System and Task 201
Appendix B.1.2 Calculating the Partial Information Decomposition . . . 201
Appendix B.1.3 Computing ΔI 203
Appendix B.2 Direction Selective RGCs with Perpendicular Preferred Directions 203
Appendix B.2.1 The Model System and Task 203
Appendix B.2.2 Computing the Partial Information Decomposition 204

Appendix C Calculating Equivalent Photon Flux for the APS Projector **207**

List of Tables

1.1 Classification of retinal dystrophies 16

1.2 Animal models of photoreceptor dystrophies 18

1.3 Summary of current electrical retinal prosthesis designs 34

1.4 Studies of optogenetic retinal prosthesis 42

2.1 Comparison of MEA systems 55

3.1 Experimental roles for gratings experiments 70

3.2 Joint probability distribution for simple PID example 94

3.3 Joint probability distribution for a neural XOR gate 97

5.1 Stimuli used in APS ChR2 Experiments 128

5.2 Letter decoder performance logistic function parameters and estimated visual acuity 145

5.3 Spatial acuity of optokinetic responses in previous studies of optogenetic retinal prosthesis 165

B.1 Marginal probability distributions of S, A and B. 201

B.2 Joint probability distribution of A and B. 202

B.3 Probability distributions for A and B conditioned on S. 203

B.4 Specific information about S provided by A and B. 203

B.5 Marginal probability distributions of S, A and B 204

B.6 Joint probability distribution of S, A, and B 204

B.7 Probability distributions for A and B conditioned on S. 205

B.8 Specific information about S provided by A and B. 205

C.1 Equivalent photon flux at 450nm for the APS projector 210

List of Figures

1.1 Structure of the mammalian retina by Ramón y Cajal 2

1.2 Phototransduction cascade 5

1.3 Cell types in the mammalian retina 8

1.4 Models of retinal encoding 10

1.5 Different neural coding strategies 14

1.6 Stages of retinal degeneration 22

1.7 Examples of *rd1* spontaneous activity 25

1.8 Origin of spontaneous oscillations in the degenerate retina 29

1.9 Components of major retinal prosthesis designs 48

2.1 Confocal image of a *ChR2rd1* retina showing ChR2 and RBPMS expression 51

2.2 Fluorescence microscope image of a 1 month old *ChR2rd1* retina 51

2.3 Fluorescence microscope image of a 20 month old *ChR2* retina 52

2.4 Fluorescence microscope image of a possible ChR2-expressing amacrine cell 52

2.5 Diagram of MEA systems 55

3.1 Photodiode circuit diagram 71

3.2 Photograph of photodiode attached to monitor 71

3.3 Two variable partial information diagram 73

3.4 Bias correction procedure for mutual information 73

3.5 Rasters of example wild-type responses to flashed gratings 76

3.6 RGC pair information for MCS data 78

3.7 Comparison of synergy measures for MCS data 78

3.8 Spike count PID for MCS data 79

3.9 Spike train PID for MCS data 79

3.10 Code performance versus spatial frequency for MCS data 81

3.11 Code performance versus number of neurons for MCS data 81

3.12 Code performance versus time window for MCS data 82

3.13 PID for P39 retina 84

3.14 PID for P52 retina 85

3.15 Comparison of synergy measures for P39 retina 86

3.16 Comparison of synergy measures for P52 retina 86

3.17 Code performance versus spatial frequency for P39 retina 87

3.18 Code performance versus spatial frequency for P52 retina 87

3.19 Code performance versus number of neurons for P39 retina 88

3.20 Code performance versus number of neurons for P52 retina 88

3.21 Code performance versus time window for P39 retina 89

3.22 Code performance versus time window for P52 retina 89

3.23 Simple retinal circuit giving rise to synergy 95

4.1 Example electrode traces and power spectra from a *ChR2rd1* retina in the presence of varying concentrations of MFA 108

4.2 Spontaneous firing rate and oscillation strength as a function of drug concentration 108

4.3 Number of optogenetically responsive cells as a function of drug concentration 109

4.4 ChR2 response thresholds as a function of drug concentration 109

4.5 Example rasters of a *ChR2rd1* RGC responding to full-field stimulation with and without MFA 111

4.6 Signal-to-noise ratio as a function of drug concentration 111

4.7 Receptive field mapping of *ChR2rd1* RGCs with and without MFA 113

4.8 Rasters of an example *ChR2rd1* RGC responding to moving bars with and without MFA 114

4.9 Difference in Bayesian decoder performance with and without drugs 115

5.1 P95 *ChR2rd1 hetero* mouse retina light responses 134

5.2 P96 *ChR2rd1* mouse retina light responses 136

5.3 Example raster from a P96 *ChR2rd1* mouse RGC 138

5.4 Bayesian classifier performance in decoding the phase of gratings of varying spatial frequency flashed onto *ChR2rd1* retinas 140

5.5 Bayesian classifier performance in decoding the phase of gratings of varying contrast flashed onto *ChR2rd1* retinas 141

5.6 Bayesian decoder performance in distinguishing gratings of varying spatial frequency flashed onto *ChR2rd1* retinas from an isoluminant mask 143

5.7 Bayesian classifier performance in decoding Sloan letters flashed onto *ChR2rd1* retinas 144

5.8 Bayesian decoder performance in distinguishing gratings of varying contrast flashed onto *ChR2rd1* retinas from an isoluminant mask 147

5.9 Response functions for model *ChR2rd1* RGCs 150

5.10 Comparison between observed decoder performance and model mutual information 151

5.11 Spikes fired by each model neuron in response to grating or mask 158

5.12 Information provided by model *ChR2rd1* RGCs as a function of contrast . 159

5.13 Example reponse of a real *ChR2rd1* RGC to gratings of varying contrast . 160

5.14 Example fits to letter decoding performance data with different priors . . . 161

A.1 Actual PID values for 50 pairs of simulated neurons 189

A.2 Redundancy and synergy for 50 pairs of simulated neurons 189

A.3 Average absolute percentage error between estimated and correct information values 191

A.4 Average percentage error between estimated and correct information values 192

A.5 Average absolute percentage error between estimated and correct PID values193

A.6 Average percentage error between estimated and correct PID values 194

A.7 Average absolute percentage error in estimated information for continuous distributions 199

C.1 Spectral flux density for the APS projector 208

C.2 APS Photon flux density versus ChR2 absorption 210

Chapter 1. Introduction

This thesis concerns how retinal ganglion cells (RGCs) encode visual information in the healthy retina, and how information can be faithfully conveyed to RGCs in dystrophic retinas devoid of photoreceptors. More specifically, the first part, discussed in chapter 3, relates to how the retina signals information about the visual scene to the brain, in particular whether and how information is encoded synergistically in the spike trains and firing orders of pairs and populations of RGCs. The second, covered in chapters 4 and 5, addresses the problems associated with the spontaneous hyperactivity that results from retinal degenerations, how this affects the signals that can be transferred to the visual centres of the brain prosthetically, and how to counteract these effects. The final discussion chapter, chapter 6, attempts to relate these two themes and put them into a wider scientific and clinical context. Preceding all of the above, chapter 2 details the experimental procedures and analyses common to the work described in chapters 3 to 5.

In this introductory chapter, I shall give an overview of the scientific background informing and motivating the rest of the thesis. First, I shall briefly describe the structure and function of the retina, leading into a discussion of some of the mathematical, computational and biophysical models that have been proposed to explain how the retina encodes visual information. Following on from this, I shall discuss photoreceptor dystrophies, the anatomical and physiological sequelae thereof, and the various animal models used in the study of these conditions. Finally, I shall discuss various treatments currently in use or under development to restore vision in these conditions, with a special emphasis on retinal prostheses in general and optogenetical retinal prostheses in particular.

1.1 The Retina

1.1.1 *Basic Anatomy*

The retina is a layered neuronal structure at the back of the eye that transduces incoming light into graded electrical signals, which are then processed by the cells of the inner

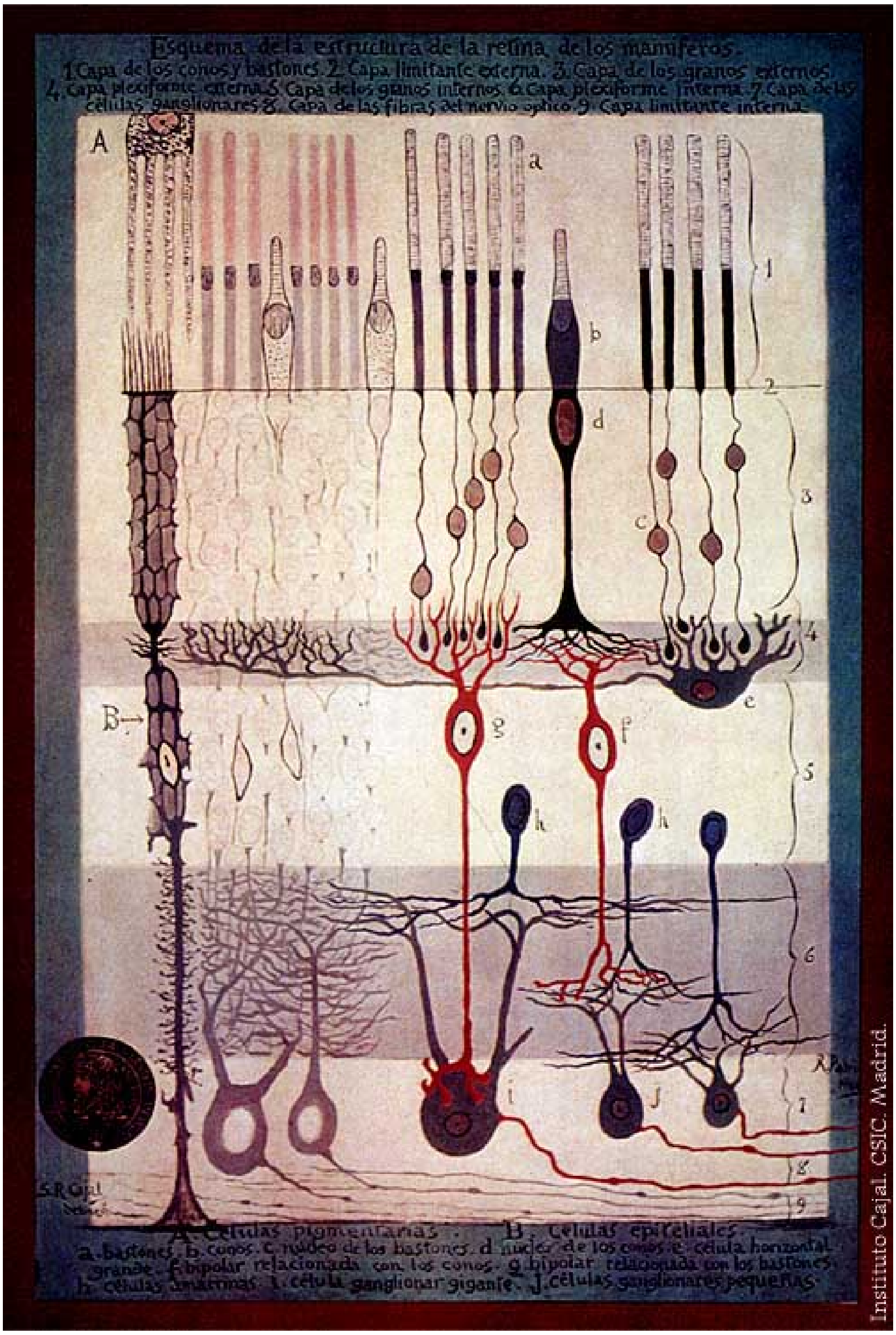

Figure 1.1: Structure of the mammalian retina by Ramón y Cajal (Ramon y Cajal 1900). The text, translated from Spanish, reads as follows: "Outline of the structure of the mammalian retina. 1. Rod and cone layer. 2. External limiting membrane. 3. Outer granular layer. 4. Outer plexiform layer. 5. Inner granular layer. 6. Inner plexiform layer. 7. Ganglion cell layer. 8. Optic nerve fibre layer. 9. Internal limiting membrane. A. Pigmented cells. B. Epithelial cells. a. Rods. b. Cones. c. Rod nucleus. d. Cone Nucleus. e. Large horizontal cell f. Cone-associated bipolar cell. g. Rod-associated bipolar cell. h. Amacrine cells. i. Giant ganglion cell. j. Small ganglion cells." The inner and outer granular layers are also referred to as the inner and outer nuclear layers in modern scientific writing. This drawing is in the public domain, downloaded from: http://commons.wikimedia.org/wiki/File:Cajal_Retina.jpg.

retina, before being encoded as trains of action potentials relaying information about the visual scene to the brain. One of the pioneers of retinal neuroanatomy was Spanish anatomist Santiago Ramón y Cajal who, though careful study of camera lucida drawings of Golgi-stained retinas, was able to discern much of the basic structure of the retina. Figure 1.1 shows a diagram of the retina drawn by Ramon y Cajal (1900). Both the layered structure and the major cell classes are evident. Starting at the outermost part of the retina, photoreceptor outer segments interface with the retinal pigment epithelium in the outer segment layer. Moving proximally past the outer limiting membrane, the photoreceptor cell bodies reside in the outer nuclear layer (ONL) and form synapses with horizontal cells and bipolar cells in the outer plexiform layer (OPL). The cell bodies of the horizontal cells and bipolar cells reside in the inner nuclear layer (INL). In the inner plexiform layer (IPL), the bipolar cells form connections with amacrine cells and RGCs. RGC bodies are located in the ganglion cell layer (GCL), whereas amacrine cell bodies are mostly located at the proximal edge of the INL, although displaced amacrine cell somata can also be found in the GCL, where they may outnumber RGCs (Jeon et al. 1998). Finally, RGCs project their axons radially along the optic nerve fibre layer (NFL) to the optic disk. Here they form the optic nerve, mostly terminating in the lateral geniculate nucleus (LGN) of the thalamus, but also projecting to other areas including the superior colliculus, the suprachiasmatic nucleus, the medial terminal nucleus of the accessory optic tract, and the dorsal raphe nucleus. The inner limiting membrane marks the boundary between the retina and the vitreous humour.

1.1.2 *Cell Types*

Photoreceptors. Photoreceptors transduce incoming light into continuous electrical signals. They are highly specialised sensory cells comprising a ciliary outer segment containing flattened, disc-shaped membranes where phototransduction takes place; an inner segment rich in mitochondria; a soma where the nucleus resides; and a synaptic terminal (Cohen 1961, 1965; Richardson 1969). There are two types of photoreceptors (Bailey and Gouras 1985): rods and cones, named for the morphology of their outer segments (figures 1.1 and 1.3). Rods and cones also differ in their spectral sensitivities, distribution within the retina, connections to other retinal neurons (see below), and range of light intensities over which they operate. Human rhodopsin has an absorption peak at roughly 500nm (Wald 1945), whereas there are three types of cone opsin with peaks at roughly 430, 540 and 575nm (Wald 1964). Each cone expresses only one type of cone opsin and correspondingly there are three subtypes of cone, termed S-, M-, and L-cones (for short-, medium-, and long-wavelength) cones. Other species have cones with different spectral sensitivities: the mouse, for example, has two cone opsins most sensitive to 360nm (ultraviolet) and 510nm photons (Jacobs et al. 1991). Mouse rhodopsin also peaks around 500nm (Imai et al. 2007).

Cone outer segment discs are continuous with the cell membrane (Cohen 1961), but those in rods float freely (Cohen 1965). Outer segment discs contain photopigments: rhodopsin in the rods and cone opsins in the cones (Bailey and Gouras 1985). Incoming photons isomerise a chromophore, 11-cis-retinal, attached to each photopigment molecule into all-trans-retinal, triggering a conformational change. This causes another protein, transducin, to phosphorylate guanosine diphosphate and dissociate from the opsin, whereupon it binds to and activates phosphodiesterase (PDE). PDE hydrolyses cyclic guanosine monophosphate (cGMP), thus closing cGMP-gated Na^+ and Ca^{2+} channels. These channels are open in the dark, allowing Na^+ and Ca^{2+} influx into the cell, resulting in membrane depolarisation (dark current). Their closure hyperpolarises the cell, reducing glutamate release from their terminals in the OPL (Arshavsky et al. 2002; Yau 1994). Figure 1.2 summarises this phototransduction cascade. Changes in ambient light trigger changes in calcium homeostasis, causing an increase in intracellular calcium concentration, which upregulates guanylyl cyclase and downregulates PDE activity, so the cGMP concentration is partially restored, reopening of some of these cationic channels. This process is called light adaptation (Yau 1994).

In the human retina, cones are almost exclusively found in the fovea, which contains no rods. The cone density drops off extremely rapidly with increasing eccentricity and rods, by far more numerous than cones overall, quickly dominate. However, these too become less densely packed towards the periphery, although the drop-off is much gentler (Osterberg 1935). In mice, there is no fovea. UV cones are located primarily in the ventral part of the retina and green cones exclusively in the dorsal half (Szél et al. (1992), but

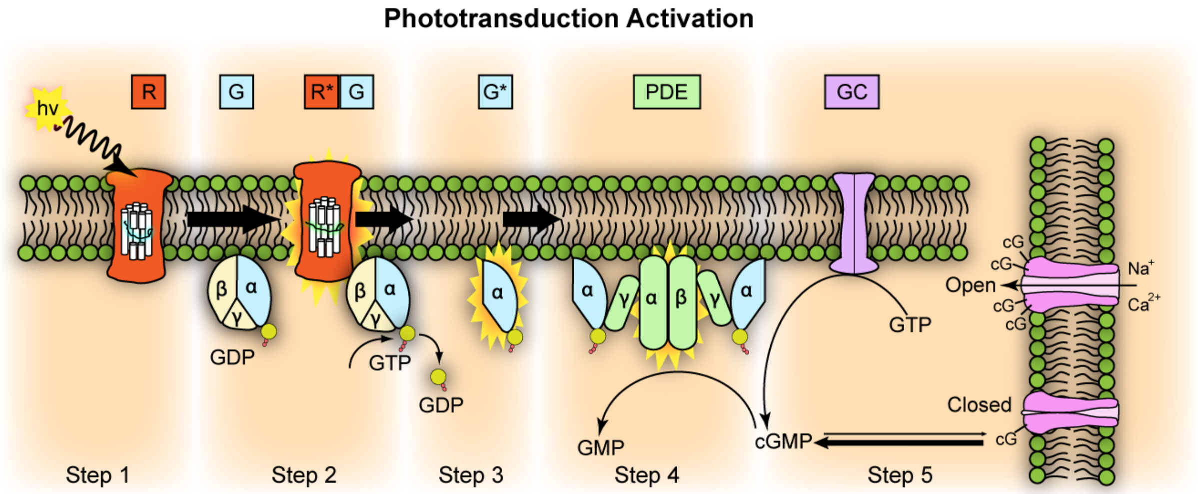

Figure 1.2: Diagram of the rod phototransduction cascade by Jason J. Corneveaux. Downloaded from https://en.wikipedia.org/wiki/File:Phototransduction.png. Licensed under the Creative Commons Attribution 3.0 Unported license. Original caption: Representation of molecular steps in photoactivation (modified from Leskov et al. (2000)). Depicted is an outer membrane disk in a rod. Step 1: Incident photon (hv) is absorbed and activates a rhodopsin by conformational change in the disk membrane to R*. Step 2: Next, R* makes repeated contacts with transducin molecules, catalyzing its activation to G* by the release of bound GDP in exchange for cytoplasmic GTP, which expels its β and γ subunits. Step 3: G* binds inhibitory γ subunits of the phosphodiesterase (PDE) activating its α and β subunits. Step 4: Activated PDE hydrolyzes cGMP. Step 5: Guanylyl cyclase (RGC) synthesizes cGMP, the second messenger in the phototransduction cascade. Reduced levels of cytosolic cGMP cause cyclic nucleotide gated channels to close preventing further influx of Na^+ and Ca^{2+}.

see also Applebury et al. (2000)).

Horizontal Cells. Horizontal cells are the outermost layer of interneurons in the retina. Most mammals have two types: A and B (figure 1.3, second row). Both form dendritic synapses onto cones, but the former has a wider dendritic arbor and no axon, whereas the latter has a long axon that ramifies into telodendria that synapse onto rods (Kolb and Famiglietti 1974). The primate retina has three types: HI-III (Kolb et al. 1994, 1980), with HI and HII being roughly analogous to B and A, while HIII has a very large, asymmetrical dendritic arbour and a very long axon ending in a poorly-structured arborisation. They also differ in their chromatic patterns of cone connections: HI and HIII cells mostly or completely avoid S-cones, respectively, whereas HII dendrites and axons respectively contact these cones preferentially or exclusively (Ahnelt and Kolb 1994b,a). Horizontal cells are also interconnected homotypically via gap junctions (Vaney 1991; Mills and Massey 1994). Horizontal cells are important in mediating the receptive field (RF) organisation of bipolar cells, wherein a narrow centre is accompanied by an antagonistic surround (Werblin and Dowling 1969). This 'centre-surround' RF organisation is common motif in the retina, found in virtually all non-photoreceptor cell types.

Bipolar Cells. Bipolar cells carry signals originating from the photoreceptors through to the IPL in distinct processing pathways. There are around ten classes of bipolar cell in most mammalian retinas (figure 1.3, third row)—distinguished by their morphology, pattern of connectivity to photoreceptors and the level at which their axons ramify in the IPL (Euler and Wässle 1995; Boycott and Wässle 1991; Kolb et al. 1981)—plus the giant bistratified bipolar cell of the primate retina (Mariani 1983). Of these, only one kind, the rod bipolar cell, contacts rods (Wässle et al. 1991); the rest are cone bipolar cells. One important classification of cone bipolar cells is into ON- and OFF-centre types, depolarising in response to light increments and decrements within their RFs, respectively, and with axons stratifying in two different sublaminae of the IPL (Famiglietti and Kolb 1976). OFF-bipolar cells have sign-preserving, AMPA/kainate-sensitive ionotropic glutamate receptors (Morigiwa and Vardi 1999; Sasaki and Kaneko 1996), whereas ON-bipolar cells express sign-inverting mGluR6 metabotropic glutamate receptors (Nomura et al. 1994; Vardi et al. 2000).

Amacrine Cells. Amacrine cells are the most diverse cell type in the mammalian retina, classifiable into at least 20-30 (Kolb et al. 1981; Macneil et al. 1999) and possibly up to 40 (Vaney 1990) distinct morphological types (figure 1.3, fourth row). In most cases their precise functionality is unknown, but they are nevertheless extremely important in shaping processing in the IPL (Masland 2012). A recent review by Werblin (2011) proposed that amacrine cells can be classified into three broad, functionally distinct classes based on their dendritic arbour size, response latency and connectivity patterns.

One particularly well-studied amacrine cell type is the AII amacrine cell (Famiglietti and Kolb 1975; Kolb 1974). Rod bipolar cells never synapse directly onto RGCs, unlike cone bipolars, but make extensive synapses with AII cells. In turn, AIIs synapse onto cone bipolar cells and occasional RGCs in the OFF sublamina of the IPL (Strettoi et al. 1992) and make gap junctions with cone bipolars in the ON sublamina (Strettoi et al. 1992; Kolb 1979). The AII is an inhibitory, glycinergic amacrine cell (Menger et al. 1998), so during scotopic light stimulation of rods it inhibits cone OFF-bipolars, while cone ON-bipolars are excited via the AII's gap junctions (Cohen and Miller 1999; Muller et al. 1988). Thus the AII hijacks the existing cone circuitry to transmit rod-mediated light information to the RGCs.

Ganglion Cells. RGCs are the output cells of the retina and, apart from a few subtypes of amacrine cells, the only neurons in the retina to fire action potentials. Their role is to perform the final stages of image processing, integrating inputs from bipolar cells and amacrine cells and encoding the visual scene into trains of action potentials that can be understood and further processed by the brain. This process is discussed in detail in the following section (section 1.1.3) and hence I shall not dwell too deeply on the function of RGCs here.

There are 11-22 distinct morphological classes of RGC (figure 1.3, bottom row; Rockhill et al. (2002) and Völgyi et al. (2009)). As with bipolar cells, they can be divided into ON- and OFF- types, as well as ON-OFF types that respond to both increases and decreases

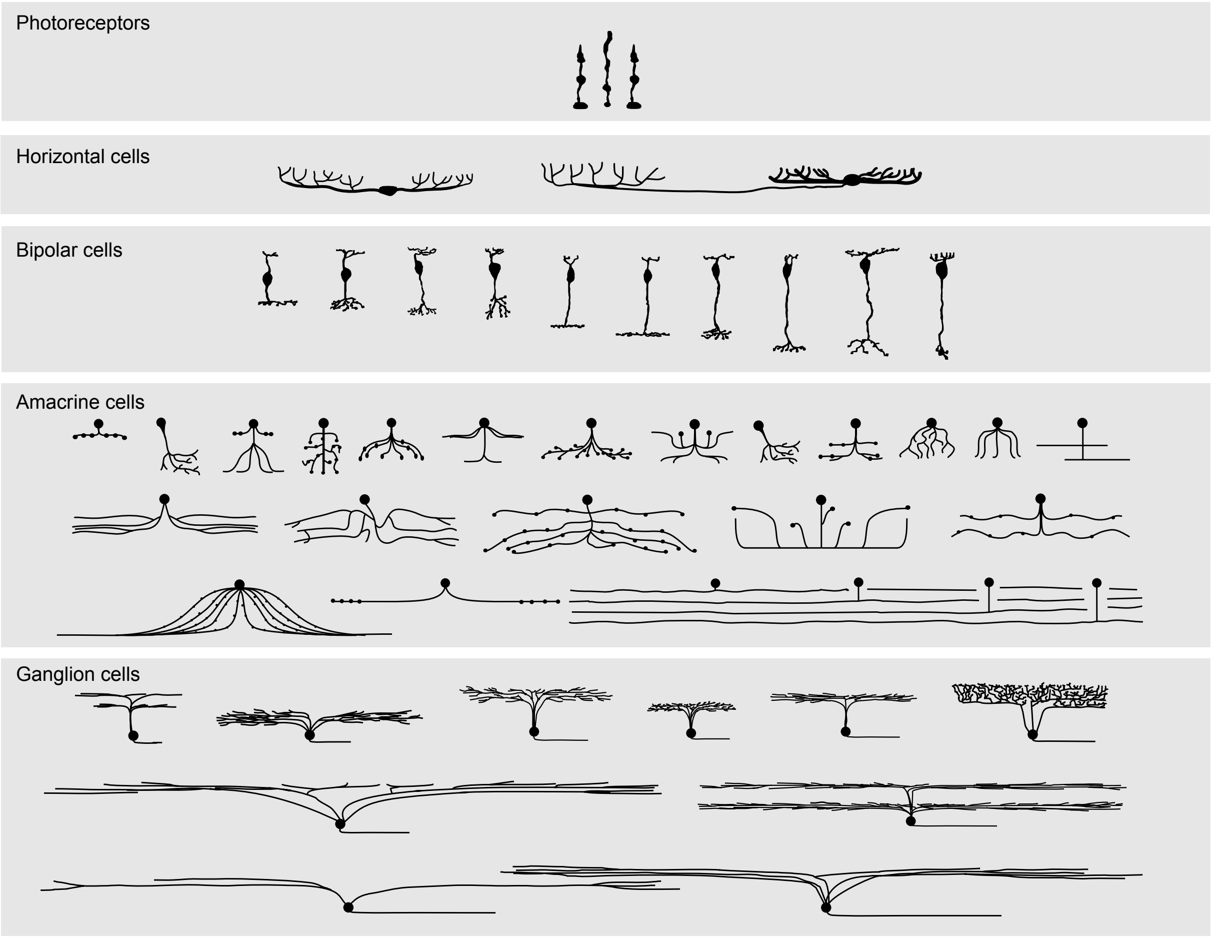

Figure 1.3: Drawings of many subtypes of the major cell types of the mammalian retina, taken from Masland (2001a). Shown are three types of photoreceptor—including a rod (top row, middle) and short- and medium- wavelength sensitive cones (top row, sides)—the two most common types of horizontal cell (bottom row, left: A; right: B), ten types of bipolar cell, and several types of amacrine and ganglion cells.

in light intensity (Hartline 1938), and have a centre-surround RF organisation (Kuffler 1953; Wiesel 1959). They can be highly specific in their preferred stimuli and perform sophisticated feature extraction, including determining the direction of motion of a moving stimulus (Barlow and Hill 1963; Barlow et al. 1964), distinguishing motion towards the observer from lateral motion (Munch et al. 2009) and, in the murine retina, one RGC type has even been proposed to be selective for aerial predators (Zhang et al. 2012).

1.1.3 *Information Coding*

Linear Models. Over the past half-century, there have been numerous attempts to capture quantitatively the way the retina processes incoming visual information. The classic difference-of-Gaussians (DoG) model of Rodieck (1965) describes the RGC RF using two concentric 2D Gaussian functions: one sharp and narrow (the centre) and one broad and shallow (the surround). The response of the cell is then proportional to the convolution of its RF with the pattern of light intensities falling within it. Though simplistic, the DoG model and related models—such as the Laplacian-of-Gaussian (LoG) (Kelly 1975)—remain popular, especially in e.g. retinomorphic hardware applications (Martinez et al. 2009) and cortical models using the retina as an input stage (Gazères et al. 1998; Worgotter and Koch 1991; Zemon and Gordon 2006), where the computational simplicity is advantageous. The DoG model is linear in the sense that it can be expressed as the convolution of the incoming image with a single filter kernel. However, as discussed in the next section, many aspects of retinal processing are fundamentally nonlinear and hence such models can never fully capture retinal response dynamics.

Nonlinear Models. Perhaps the most common nonlinear model is the linear-nonlinear (LN) cascade, in which the incoming image is first convolved with a linear filter and then passed through a static nonlinear function (Paninski et al. 2007). This nonlinearity often performs one or more of rectification (Enroth-Cugell and Freeman 1987), thresholding (Keat et al. 2001) or saturation (Pennartz and Grind 1990) of the signal. There may then be a second linear stage, as in LNL models (Hunter and Korenberg 1986), or some sort of spike generation method, such as in the linear-nonlinear-Poisson (LNP) model (Paninski et al. 2007), in which the result of the LN cascade is used as the rate parameter to a

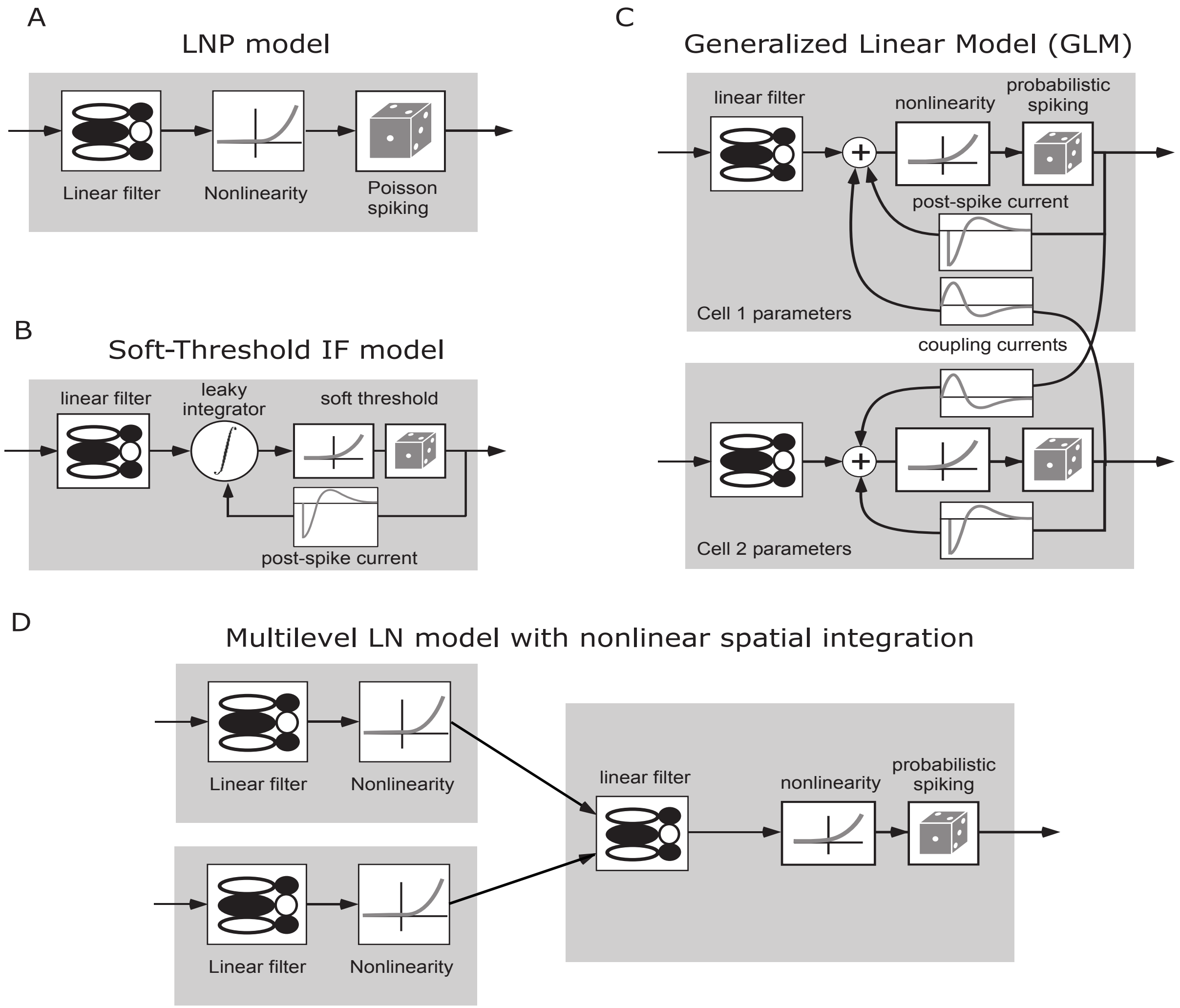

Figure 1.4: Major classes of retinal encoding models; adapted from Paninski et al. (2007). A: a linear-nonlinear-Poisson cascade model. The incoming image is passed through a linear filter followed by a static nonlinearity; the result forms the rate function of an inhomogeneous Poisson process that generates the output spike train. B: a simple biophysical model. The filtered input image provides the input current to a leaky integrate-and-fire model and the membrane voltage, after passing through a thresholding nonlinearity, provides the rate function to the Poisson process. Refractoriness arises due to the post-spike current. Alternatively, the model neuron can fire a spike once the membrane voltage crosses a fixed threshold, after which the voltage resets. This would be a hard threshold integrate-and-fire model. C: an extension of the LNP model incorporating spike history terms and coupling between neurons. Models A-C can be formulated as GLMs. D: example of a model with several layers of linear-nonlinear processing, in this case modelling nonlinear spatial integration by RGCs (Enroth-Cugell and Robson 1966; Schwartz et al. 2012b). The outputs of the first LN layer, representing the bipolar cells, form the inputs to the second LN layer. In the second layer the linear filter represents the weighting of each bipolar cell input to the RGC and the nonlinearity converts the result into the rate function of the Poisson process. Due to the multiple stages on nonlinearity between initial inputs and ultimate outputs, this model is not a GLM.

Poisson process (figure 1.4A).

There are a number of attractive features of LN models and they remain popular in the literature to this day. From a computational complexity perspective, they are not vastly more expensive than linear models: the first stage is itself a linear model and the nonlinearity can be implemented cheaply in the form of a lookup table. LN models fall into the broader category of statistical models known as generalized linear models (GLMs), where an output variable is modelled as a linear combination of inputs and parameters, passed through a single, nonlinear function. As such, there is a well-developed mathematical framework for fitting them to experimental data (Chichilnisky 2001; Paninski et al. 2007). Historically, scientists have made use of first- and second-order Wiener expansions (Benardete and Kaplan 1997a,b; Marmarelis and Naka 1972; Sakai and Naka 1995) for fitting LN models to responses to periodic stimuli such as sinusoidal gratings. These fell from popularity with the application of reverse correlation, or spike-triggered averaging, techniques to the retina (Chichilnisky and Baylor 1999; Chichilnisky 2001; Chichilnisky and Kalmar 2002; Pitkow and Meister 2012), which allow both stages of the LN cascade to be easily recovered from electrophysiological responses to white noise stimuli. LN models have been called the “standard model” of retinal processing (Carandini et al. 2005) and Nirenberg and Pandarinath (2012) recently showed that they may be useful for generating more meaningful spike trains in retinal prosthetic applications. As well as describing the relationship between the input stimulus and the output spike trains, LN models can also incorporate the effects of spike history and network interactions (figure 1.4C; Paninski (2004), Paninski et al. (2007), and Pillow et al. (2008)).

Nevertheless, there are features of retinal processing that cannot be modelled by a single LN cascade. A classic example is the X and Y RGCs of the cat retina (Enroth-Cugell and Robson 1966). When presented with a grating stimulus such that the change in contrast in one half of their RF is equal and opposite to that in the other half, the former respond to neither the onset nor offset of the grating. This is exactly as one would predict from linear spatial integration over the receptive field. However, the Y cells respond vigorously to both the onset and offset of such a grating. Explaining this requires nonlinear spatial summation over the receptive fields, as one might find if a number of bipolar cells integrated the incoming light linearly over their receptive field and the result was nonlinearly transformed by the bipolar cell to RGC synapse, then finally the RGC summed the responses of all its presynaptic bipolar cells (figure 1.4D; Schwartz et al. (2012b)). Various such models involving multiple stages of linear and nonlinear filtering have been proposed to explain specialised computations of the retina, as summarised in a recent review by Gollisch and Meister (2010). The presence of multiple nonlinearities between input and output means these models do not count as GLMs. Furthermore, such models lack the appeal of simple, general mathematical transformation that can capture the RGC response to any arbitrary stimulus (e.g. Nirenberg and Pandarinath (2012)), but given the diversity of RGC types (Masland 2001a; Rockhill et al. 2002), each encoding distinct features of the visual scene (Azeredo da Silveira and Roska 2011), to expect to find such an equation would seem ambitious at best and naïve at worst.

Biophysical Models. The above described models are largely abstract, attempting to explain quantitatively the retinal response but only loosely informed by the underlying biology. Another approach to modelling retinal processing is to directly simulate the physiological processes involved. Certainly, there is a spectrum here. Even the simplest models, such as the DoG (Rodieck 1965), involve an excitatory centre and an inhibitory surround that can be explained in terms of the pattern of excitatory and inhibitory inputs to the cell. Moving progressively less abstract, one has integrate-and-fire (IF) models of RGC spiking, wherein the model RGC integrates some input that is an abstraction of the input image after it has been transduced and processed by retinal layers, then fires when its membrane potential exceeds some threshold (e.g. Paninski et al. (2004), Pillow et al. (2005), Morillas et al. (2007), and Gollisch and Meister (2008)). These models can be extended further to include models of the different layers of retinal processing (e.g. Wohrer and Kornprobst (2009)) or the abstract IF spike generation model can be replaced with differential equations describing the dynamics of cellular membrane potentials as a function of membrane conductances and ionic concentrations over time (e.g. Gaudiano (1994), Hennig and Funke (2001), Momiji et al. (2007), Saglam et al. (2008), and Wohrer and Kornprobst (2009)). Going still further, one has compartmental models that model separately the evolution of the membrane potential in different areas of the cell (e.g. Publio et al. (2009), Schachter et al. (2010), Jarsky et al. (2011), and Choi et al. (2014)), but these are often intended to probe specific aspects of retinal circuitry and lack the generality of the abstract mathematical models described in 1.1.3. They can also become almost arbitrarily complicated, containing hundreds of elements to model a single cell (Borg-Graham 2001; Schachter et al. 2010).

How Does the Retina Encode Information?. There are two broad aspects necessary to understand retinal processing: the first, covered in the sections above, is how the retina integrates visual information over space and time. However, it is also important to understand how this processed visual information is encoded by the RGCs. In other words, what precise feature of the RGC spike trains carries the information about the visual scene? Many of the models discussed above are agnostic to this, although some - for example, LNP models (Paninski et al. 2007) - implicitly assume that information is carried in the instantaneous firing rate of each RGC. This concept of 'rate coding' is a classical assumption in studies of neural coding (Rieke et al. 1999). However, this is not the only way spike trains can carry information. Meister and Berry (1999) argued that there were many problems with this assumption in the context of retina; later Gollisch and Meister (2008) demonstrated experimentally that there was more information in the latencies of individual RGCs (figure 1.5C) than in their firing rates, and yet more information in their relative latencies. However, the form of rate code they used as a control was an extremely crude one: the number of spikes fired in some fixed time window following a stimulus. Jacobs et al. (2009) later showed that crude spike counts (figure 1.5A) carry significantly less information than fine-grained changes in firing rate (figure 1.5B; confusingly, they refer to this code as a 'spike timing' code). However, this code still does not carry enough information to replicate behavioural performance, but a code in which the instantaneous firing rate varies not only with the time since stimulus onset but also with the time since the previous spike is able to match the animal's behaviour. This is consistent with findings that spike train variability is much lower than expected for spikes generated according to a Poisson process, but the statistics of RGC spike trains can be replicated with a model that incorporates refractoriness (Uzzell and Chichilnisky 2004). Jacobs et al. (2009) did not compare either of their rate codes to any latency-based codes, however. Meanwhile,

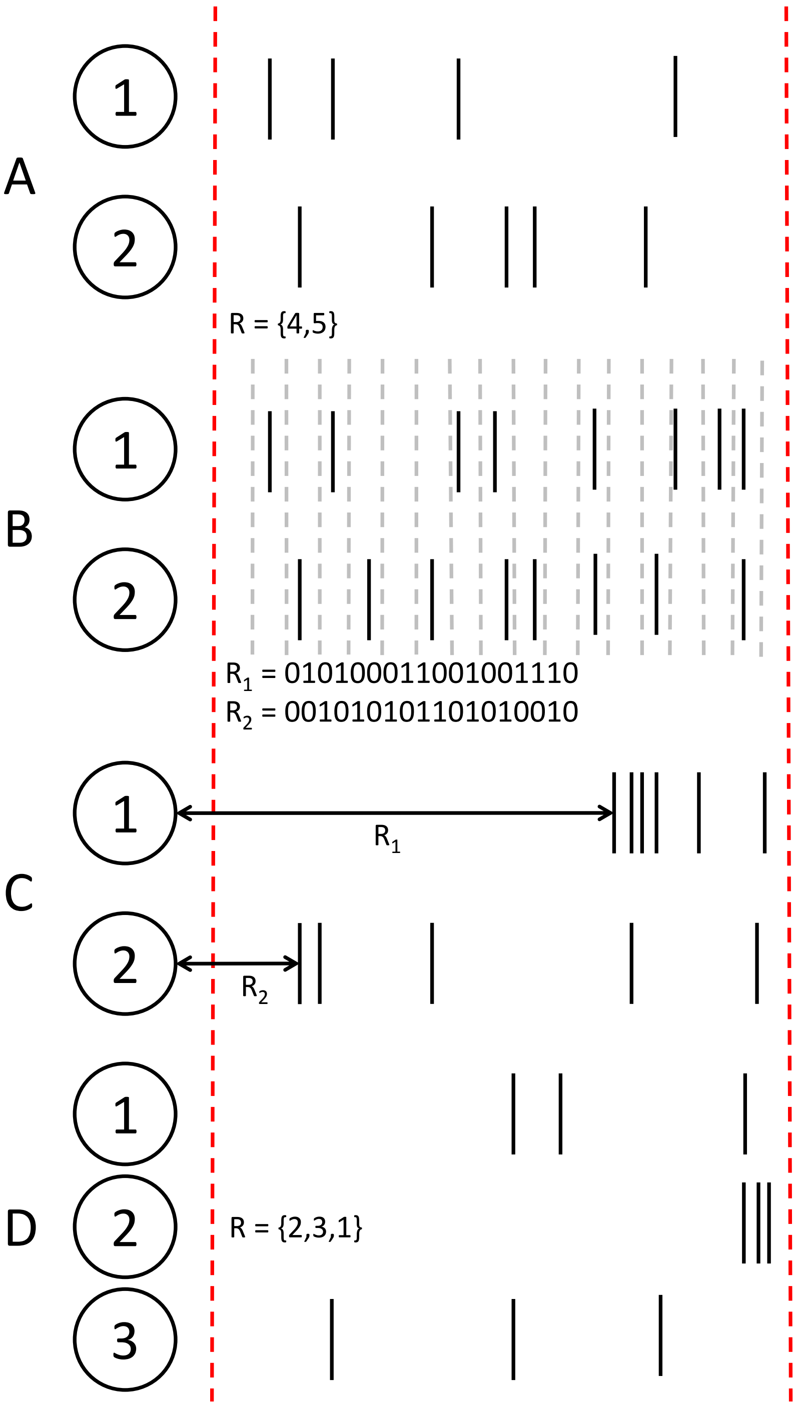

Figure 1.5: Diagrams demonstrating different ways information can be encoded in spike trains. Numbered circles represent different neurons, vertical solid lines represent spikes, and a stimulus is presented between the red dashed lines. A: spike count, the simplest rate code. The relevant feature is the number of spikes fired during some fixed time window, such as presentation of the stimulus. With N neurons, the number of code words is $((M+1)T)^N$, where M is the maximum firing rate of any neuron and T is the length of the time window. B: spike timing, a more fine-grained rate code. Time is divided into small bins of width Δt—represented by the grey dashed lines—ideally such that each neuron can only fire one spike per bin. The number of code words is $2^{\frac{NT}{\Delta t}}$. C: latency coding. Each neuron encodes information in the time it takes to fire its first spike after the stimulus. The number of code words depends on the timing precision of the postsynaptic neuron. D: rank order coding. The relevant feature is the order each neuron fires after the stimulus. There are $N!$ code words.

in an attempt to explain psychophysical experiments in which subjects are able to classify images presented for as briefly as 150ms, Thorpe et al. (2001) proposed a coding strategy, known as rank-order coding, in which the salient feature of the retinal output is the relative firing order of the population of RGCs (figure 1.5D) . Using computational modelling, they demonstrated that this is a much faster and more efficient code that more traditional coding strategies (Van Rullen and Thorpe 2001), but to date the rank-order code has never been tested experimentally in the retina.

Aside from the coding strategy employed, another important question is to what extent RGC encoding can be understood by considering each cell separately or if the full information content of retinal responses can only be recovered by considering the population as a whole. Nirenberg et al. (2001), by comparing the information that can be recovered from the full joint response distributions of RGC pairs versus that available by measuring each neuron's marginal response distribution and treating them as statistically independent, argued that RGCs are largely independent. Later studies contradicted this view, however. For example, Pillow et al. (2008) found that including coupling terms between neurons in a GLM enabled more accurate decoding of stimuli from RGC responses compared to linear decoders or models without these terms. Schwartz et al. (2012a) corroborated the results of Nirenberg et al. (2001) for pairs of neurons, but the amount of information lost by treating neurons as independent increased as the number of neurons grew. Further, they demonstrated that this was true regardless of the coding strategy used.

It is clear, then, that the precise nature of the retinal code is not completely understood. I shall revisit these issues in the introduction to chapter 3. The above all concerns the healthy retina, however. For now I shall turn my attention to what happens in retinal degenerations.

1.2 Retinal Dystrophies

1.2.1 *Classification of Retinal Dystrophies*

Numerous conditions can result in the progressive death of photoreceptors or other cells classes in the retina; these conditions are genetically heterogeneous and in many cases the demarcation between different diseases is blurred (Rivolta 2002). Retinitis pigmentosa is

Condition	Rod Death?	Cone Death?	Spatial Progression	Typical Onset	Global Prevalence
Age-Related Macular Degeneration	Yes	Yes	Central only	Old age	8.69%
Retinitis Pigmentosa	Yes	Later stages	Peripheral to central	Adulthood	0.03%
Stargardt's Disease	Yes	Yes	Central only	Before age 20	0.01%
Cone Dystrophy	No	Yes	Mostly central	Adulthood	0.003%
Leber Congenital Amaurosis	Yes	Yes	Panretinal	Birth	0.001%

Table 1.1: Summary of the main forms of photoreceptor dystrophy, showing the affected cells, spatial extent of each condition, typical onsets, and global prevalence.

characterised by initial progressive loss of rods, leading to night-blindness and a loss of peripheral vision, followed by death of cones as well, leading to eventual blindness (Berson 1993; Hartong et al. 2006). It may occur on its own or as part of polygenic disorders with a constellation of symptoms, such as Bardet-Biedl syndrome (Beales et al. 1999) or Usher syndrome (Petit 2001). Leber congenital amaurosis (LCA) is a particularly severe form of congenital retinal dystrophy featuring death of both rods and cones early in life; in many cases patients are born blind (Perrault et al. 1999). Age-related macular degeneration (AMD) is, as the name suggests, a form of retinal degeneration that occurs with age and results in loss of photoreceptors in the fovea (Green and Enger 1993; Curcio et al. 1996). A characteristic feature of the diseases is the formation of deposits known as ‘drusen’ in the retina and it is divided into two subtypes: ‘dry’ AMD featuring by large areas of retinal atrophy extending to the center of the fovea, and ‘wet’ AMD, characterised by choroidal neovascularisation (Jager et al. 2008). Another form of macular degeneration is Stargardt’s disease (Stargardt 1909; Allikmets et al. 1997), also known as juvenile macular degeneration, which begins in early life and usually involves less severe visual loss than end-stage AMD. Cone dystrophies are disorders in which cones selectively degenerate with relative preservation of rods; it may affect all three cone types (To et al. 1998b) or be selective for some cone types while preserving others (To et al. 1998a).

The above conditions all involve degeneration of the photoreceptors. Additionally, various conditions can cause death of RGCs, including congenital retinal atrophies such as Leber’s hereditary optic neuropathy (Wallace et al. 1988; Man et al. 2002), glaucoma (Quigley et al. 1995), and trauma affecting the optic nerve. Since the RGCs are the only output cells of the retina, in these cases the link between the retina and the brain is severed. Since this thesis is primarily concerned with processing in and restoration of sight to the retina, I shall not discuss these conditions in any great detail. The remainder of this section will focus solely on photoreceptor dystrophies, which are summarised in table 1.1.

1.2.2 *Animal Models*

As expected for such a diverse (Rivolta 2002) and genetically heterogeneous (Daiger et al. 2013) group of disorders, there are multitudinous animal models of retinal degenerations that have been discovered or created over the years (Chang et al. 2002; Marc et al. 2003;

Model	Species	Type	Gene$^{\text{Allele Symbol}}$	Disease Phenotype	Degeneration Onset	Degeneration Time Course	
						Rods	Cones
rd1	Mouse	Natural	$Pde6b^{rd1}$	RP	P8	3 weeks	>18 months
Rd2 (a.k.a. *rds*)	Mouse	Natural	$Prph2^{Rd2}$	AD RP	P7-14	12 months	12 months
rd10	Mouse	Natural	$\mathrm{Pde6b}^{\mathrm{rd10}}$	RP	P16-20	7 weeks	>7 weeks*
Rhodopsin KO	Mouse	Transgenic	$Rho^{-/-}$	RP	PW3-4 (rods)**, PW6 (cones)	4 weeks	7-9 weeks
CGNA3 KO	Mouse	Transgenic	$Cnga3^{-/-}$	Cone dystrophy	Before PM2	N/A	8 months
CGNA3 Rhodospin DKO	Mouse	Transgenic	$Cnga3^{-/-};Rho^{-/-}$	RP	PW4	2 months	2 months
CRX KO	Mouse	Transgenic	$Crx^{-/-}$	LCA	P14-21**	>6 months	>6 months
RCS	Rat	Natural	$Mertk^{rdy}$	RP	PW3	4 weeks	1-2 months
P23H	Rat	Transgenic	Rho^{P23H}	AD RP	P15	variable†	variable†
S334ter	Rat	Transgenic	$Rho^{S334ter}$	AD RP	P11-13	variable†	variable†
LIRD	Rat	Induced	N/A	AMD	Bright light exposure	variable‡	variable‡
P347L	Pig	Transgenic	Rho^{P347L}	RP	Before PW2	6 weeks	>1 year

Table 1.2: Summary of mouse, rat, and pig models of photoreceptor dystrophies discussed in the text. Species, affected genes, modelled disease phenotype, and onset and time course of degeneration (time from onset to complete or almost complete loss of photoreceptors) are shown, as well as whether the degeneration is as a result of natural mutations, transgenics, or deliberately induced retinal injury. AD = autosomal dominant, DKO = double knock-out, KO = knock-out, N/A = not applicable, Pn = n days postnatal, PWn = n weeks postnatal, PMn = n months postnatal. For details of other retinal dystrophy models not listed here, see also Chang et al. (2002), Marc et al. (2003), and Marc et al. (2007). *Chang et al. (2007) report no ONL remains by P60, but Stasheff et al. (2011) report a minority of RGCs respond vigorously beyond this age, suggesting some remaining cone function. **Photoreceptors in these animals never develop outer segments. †Depending on level of transgene expression ‡Depending on light intensity and exposure duration.

Jones and Marc 2005). I shall not attempt to present an exhaustive list of all such models. Rather, I shall focus on some of the more commonly encountered models in research into treatments of retinal degenerations, with a special emphasis on those used in retinal prosthetic research.

One of the more popular RP models in the literature is the naturally-occurring *rd1* mouse (Keeler 1966), in which a mutation in the *Pde6b* gene coding for the β subunit of rod PDE (Pittler and Baehr 1991), an important component of the photoreceptor transduction cascade (see section 1.1.2), causes rapid death of rods followed by secondary degeneration of cones (Carter-Dawson et al. 1978). It was the first mouse model of RP in which abnormal electrophysiological hyperactivity - in the form of local field potential (LFP) oscillations and spontaneous rhythmic bursting of RGCs - was described (figure 1.7, Stasheff (2008); although Drager and Hubel (1978) described rhythmic discharges of retinal origin in the visual cortex and superior colliculus of *rd1* mouse, but wrote these off as an artefact of barbiturate anaesthesia). As a result there has been extensive research into the underlying causes of this hyperactivity (see section 1.2.4). A closely-related mouse model is the *rd10* mouse, in which retinal degeneration arises from a mutation in the same gene, but the onset of degeneration is later—P16-20, when the retina is mostly finished developing—and its progression is somewhat slower than the *rd1* mouse (Chang et al. 2007). It displays similar electrophysiological hyperactivity to *rd1* (Stasheff et al. 2011; Biswas et al. 2014), but light responses persist for much longer (Stasheff et al. 2011).

Two more slow-degenerating RP models include the *Rd2* mouse and the *Cnga3*$^{-/-}$;*Rho*$^{-/-}$ double knock-out mouse. In the *Rd2* mouse, formerly known as the *rds* (for *retinal degeneration slow*) mouse (Nie et al. 1978), photoreceptors degenerate over the course of about a year (Sanyal et al. 1980) as a result of mutations in the gene *Prph2* encoding peripherin, an important component of outer segment discs (Ma et al. 1995). The *Cnga3*$^{-/-}$;*Rho*$^{-/-}$ mouse is a combination of two existing knock-out strains: the *Rho*$^{-/-}$ rhodopsin knock-out mouse (Humphries et al. 1997), which is a popular model for studying pure cone function (Jaissle et al. 2001); and the *Cnga3*$^{-/-}$ mouse, in which the *CNGA3* gene encoding the α3 subunit of the cyclic nucleotide gated (CNG) cation channel is knocked out (Biel et al. 1999). This subunit of the CNG channel is expressed in cones but not rods, so the

Cnga3$^{-/-}$ is useful both for studying pure rod function and as a model of cone dystrophies. Combining these two models results in an RP model in which almost all photoreceptors are lost by about three months postnatal (Claes et al. 2004). One final mouse model I shall mention is the *Crx*$^{-/-}$ cone-rod homeobox knock-out mouse. As a result of the knockout of this gene, photoreceptors in these mice never form functional outer-segments, so these mice are blind from birth and serve as a model for LCA (Furukawa et al. 1999). RGCs in the *Crx*$^{-/-}$ mouse display elevated spontaneous activity similar to that seen in mouse models of RP (Soto et al. 2012; Maccione et al. 2014).

The mouse is popular in retinal research, as in other areas of biology, due to its ease of breeding and genetic manipulability. However, it is not the only animal in which we have models of retinal degeneration. One of the earliest RP models described was the Royal College of Surgeons (RCS) rat (Bourne et al. 1938), in which photoreceptors start degenerating from about three weeks postnatal. This is due to abnormalities in phagocytosis of photoreceptor outer segments by the RPE (Strauss et al. 1998), which was later found to be caused by mutations in the tyrosine kinase receptor gene *Mertk* (D'Cruz 2000; Vollrath et al. 2001). Transgenetic rat lines expressing mutant opsin genes associated with autosomal dominant forms of RP, such as the P23H rat and the S334ter rat (Steinberg et al. 1996; Machida et al. 2000), are also popular in retinal degeneration research. Different lines with the same mutation exhibit different rates of degeneration (Machida et al. 2000; Martinez-Navarrete et al. 2011). Transgenic mouse lines with the same mutations are also available (e.g. Olsson et al. (1992)). Wild-type rats such as Sprague-Dawley and Wistar are also susceptible to light-induced retinal damage (LIRD), which can happen in aged rats exposed to normal ambient lighting (Sullivan et al. 2003) or brief (24-48 hour) exposure to intense visible light (Marc et al. 2008). LIRD in rats serves as a model for advanced AMD (Marc et al. 2008) and can be used in combination with otherwise retinally healthy transgenic lines without necessitating crossbreeding with genetically blind strains (e.g Tomita et al. (2009)).

As well as rats and mice, there are a number of large animal models of retinal dystrophies. These are useful as surgical models and for their more sophisticated repertoire of visually-guided behaviour. For example, the transgenic P347L pig was engineered to express a point mutation in the rhodopsin gene observed in human RP patients, specifically to serve as a surgical model for RP treatments due to the similarity between pig and human eyes (Petters et al. 1997). Additionally, naturally occurring retinal degeneration has also been described in various dog breeds (Aguirre et al. 1978; Wolf et al. 1978; Aguirre et al. 1982a; Aguirre et al. 1982b; Woodford et al. 1982; Acland and Aguirre 1987), Abyssinian cats (Narfstrom 1983; Narfström and Nilsson 1986; Curtis et al. 1987; Narfstrom et al. 1989; Narfström and Nilsson 1989; Leon and Curtis 1990; Leon et al. 1991), and chickens (Ulshafer et al. 1984; Ulshafer and Allen 1985). The animal models discussed here are summarised in table 1.2.

1.2.3 *Anatomical Remodelling*

The major common feature of photoreceptor dystrophies is, as the name suggests, death of photoreceptor cells. Morphological studies of the retinas of human retinal dystrophy patients in the 1990s and early 2000s found that, even in the presence of near total loss of the ONL and OPL, there was remarkable preservation of cell bodies in the INL, and a large fraction of RGCs survived as well (Stone et al. 1992; Santos et al. 1997; Humayun et al. 1999; Medeiros and Curcio 2001; Kim et al. 2002; Kim and Oh 2002). Stone et al. (1992) counted photoreceptors and RGCs at various eccentricities in postmortem retinas from RP patients versus normally-sighted controls: on average, less than half of photoreceptors survived, with the worst degeneration being in the fovea, but RGC counts were around 50-75% of controls' at all eccentricities. Similarly, Santos et al. (1997) showed severe degeneration of photoreceptors and marked but less dramatic loss of RGCs, though no significant change in cell counts in the INL. A later study by the same group examining the extramacular retina (Humayun et al. 1999), unlike the previous two studies, found evidence of loss of cells in the INL as well as the GCL, but an appreciable fraction of cells were still preserved in both layers. In AMD, RGCs are partially or completely preserved, depending on the subtype, despite extensive photoreceptor loss (Medeiros and Curcio 2001; Kim et al. 2002; Kim and Oh 2002). With these findings, it was initially hoped that RP treatments could succeed merely by functional replacement of the missing photoreceptors, whether by prosthetic stimulation of surviving cells (Margalit et al. 2002), transplantation of healthy retinal tissue (Aramant and Seiler 2002) or introduc-

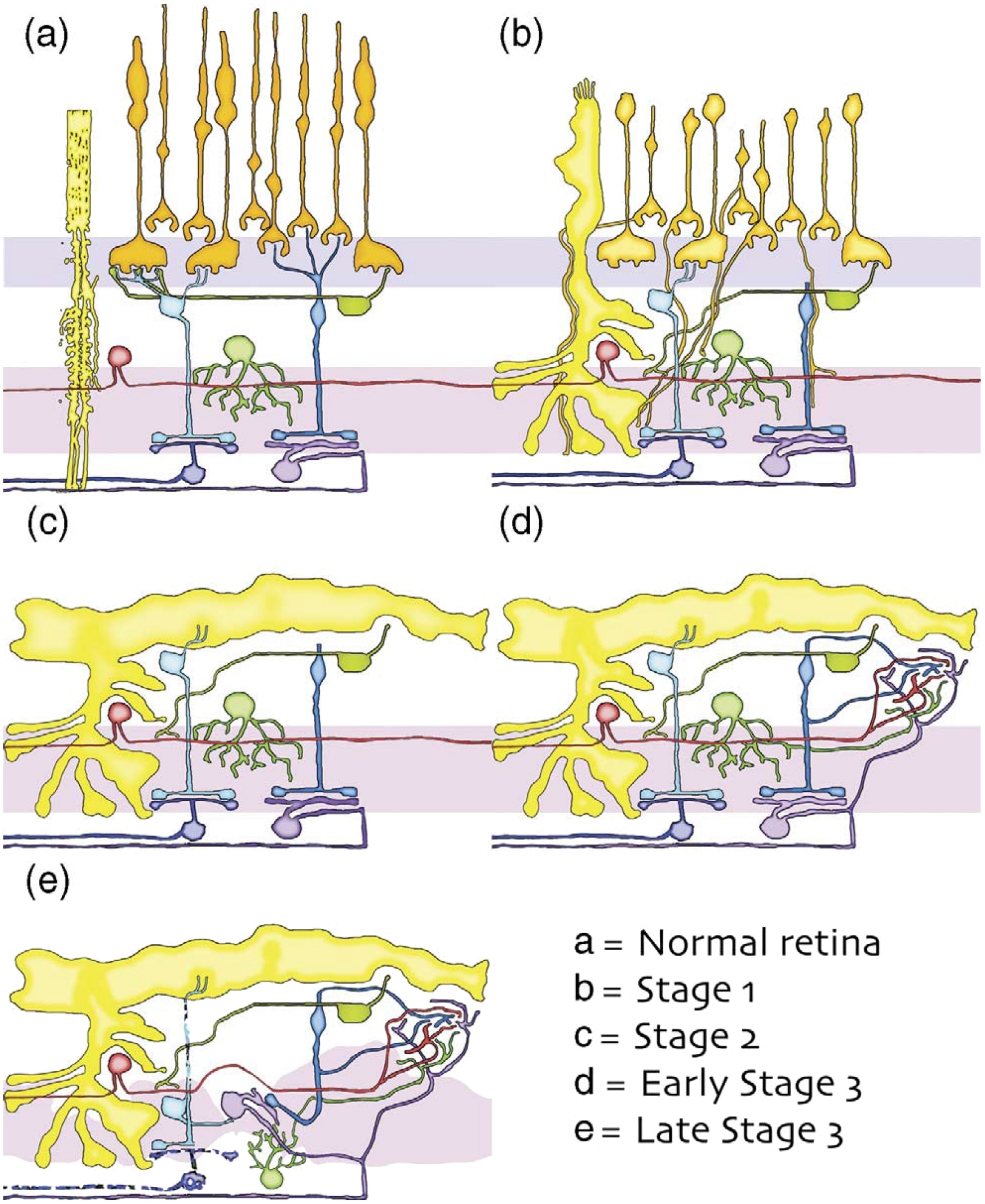

Figure 1.6: Diagrams showing the progression of retinal degeneration, adapted from Jones and Marc (2005). Panel (a) shows a healthy retina, with the photoreceptors in orange, horizontal cells in olive, bipolar cells in blue, amacrine cells in red and green, RGCs in purple, and Müller cells in yellow. The horizontal bands represent the OPL and IPL. In the initial stages of degeneration (b), photoreceptors lose their outer segments; bipolar and horizontal cells lose their dendritic and axonal arbors, respectively, and extend neurites into the inner retina; and Müller cells begin to hypertrophy. Following photoreceptor death, the hypertrophied Müller cells form a glial scar over the outer retina (c). Later, the inner retina begins to remodel, with the formation of neurite fascicles and microneuromas (d) and mislocalisation of cell bodies, and eventually there is also loss of inner retinal neurons (e).

tion of progenitor cells (Young et al. 2000). Unfortunately, subsequent, more detailed studies revealed profound remodelling in the surviving retinal layers (Marc et al. 2003; Jones and Marc 2005; Marc et al. 2007), including Müller cell hypertrophy, glial scarring, abnormal dendritic arborisation and axonal projections, displacement of cell bodies, and microneuromas (bundles of neurites originating from large numbers of distant neurons).

Among the earliest changes observed in the inner retina following photoreceptor degeneration occurs in the cells immediately postsynaptic to rods: the rod bipolar cells and the horizontal cells. Strettoi and Pignatelli (2000) found small (though statistically insignificant) changes in the numbers of both rod bipolar cells and horizontal cells. Rod bipolar cells failed to develop their normal dendritic arbors and exhibited mislocalisation of mGluR6 receptors, while the horizontal cells showed somatic hypertrophy and abnormal axonal arborisation. Later studies by the same group (Strettoi et al. 2002, 2003) corroborated these findings, showing also that cone bipolar cells were affected, but that amacrine cells were relatively unchanged. Alongside the development of abnormal dendritic morphologies, rod bipolar cells lose their sensitivity to glutamate while increasing their responses to GABAergic input (Varela et al. 2003). Peng et al. (2000) also found abnormal rod bipolar cell dendritic morphologies in the P347L pig, as well as abnormal synapses between rod bipolar cells and cones in the P347L pig and the *rd1* mouse. Similar abnormalities in horizontal cell processes have also been observed in the RCS rat (Chu et al. 1993).

Another important initial consequence of retinal degeneration is hypertrophy of the Müller cells, a type of glial cell considered to be the chief support cells of the retina. An important filament protein in Müller cells, glial fibrillary acidic protein (GFAP), is normally localised in the Müller cell end feet (Lewis et al. 1988), which tile the inner limiting membrane. Upregulation of GFAP in Müller cells in response to retinal degeneration is seen across multiple animal models of different species (Eisenfeld et al. 1984; Ekström et al. 1988; Strettoi et al. 2002, 2003). This is accompanied by Müller cell hypertrophy and the formation of a glial seal over the outer retina (Jones et al. 2003).

Other than gliosis and changes in the arborisations of second-order neurons as described above, the full extent of inner retinal remodelling in advanced retinal dystrophies was not appreciated until the advent of computational molecular phenotyping (Marc et al. 1995), which allows large numbers of cells to be automatically located and classified on the basis of their immunocytochemical signatures. Using this technique, Jones et al. (2003) identified a number of changes in the inner retina aside from neuronal death. These included migration of amacrine cell somata to the ONL and GCL (although in the latter case these might not actually have been mislocalisations, see Jeon et al. (1998)) and relocation of bipolar cell bodies to the GCL; fragmentation of the IPL; extensive rewiring in the form of bundles of neurites travelling throughout the IPL and amorphous tangles of neurites and synapses known as microneuromas; glial hypertrophy and scarring as well as Müller cell body migration; and invasion of the retina by blood vessels and RPE cells. Most of these abnormalities were observed in human RP retinas as well as retinas from numerous animal models. Figure 1.6, adapted from Jones and Marc (2005), summarises the various changes that take place as a result of photoreceptor degeneration.

1.2.4 *Physiological Changes*

As well as anatomical remodelling, considerable physiological changes are observed in degenerate retinas. One that I shall focus on is the development of spontaneous rhythmic hyperactivity in the inner retina, which takes the form of slow LFP oscillations and rhythmic bursting of RGCs. Both of these features can be seen in figure 1.7, which shows example traces from one of my own recordings from an *rd1* retina. Bursty firing in areas receiving retinal input was first described by Drager and Hubel (1978), who dismissed it as a result of anaesthesia. It was not until Stasheff (2008) performed multielectrode array (MEA) recordings from *ex-vivo* wholemount *rd1* retinas that direct electrophysiological evidence of sustained hyperactivity originating in the degenerate retina was obtained. Shortly after, Margolis et al. (2008) noted oscillations in the membrane potential of *rd1* RGCs in patch-clamp recordings, as well as the rhythmic nature of their firing patterns, both having a fundamental frequency of around 10Hz. Since then, similar activity has been observed in other models, including the *rd10* mouse (Stasheff et al. 2011; Goo et al. 2011), the CRX mouse (Soto et al. 2012; Maccione et al. 2014) and the P23H rat (Sekirnjak et al. 2009). Due to difficulties in obtaining dystrophic human retinas of sufficient quality for electrophysiological recordings, spontaneous hyperactivity has never been observed

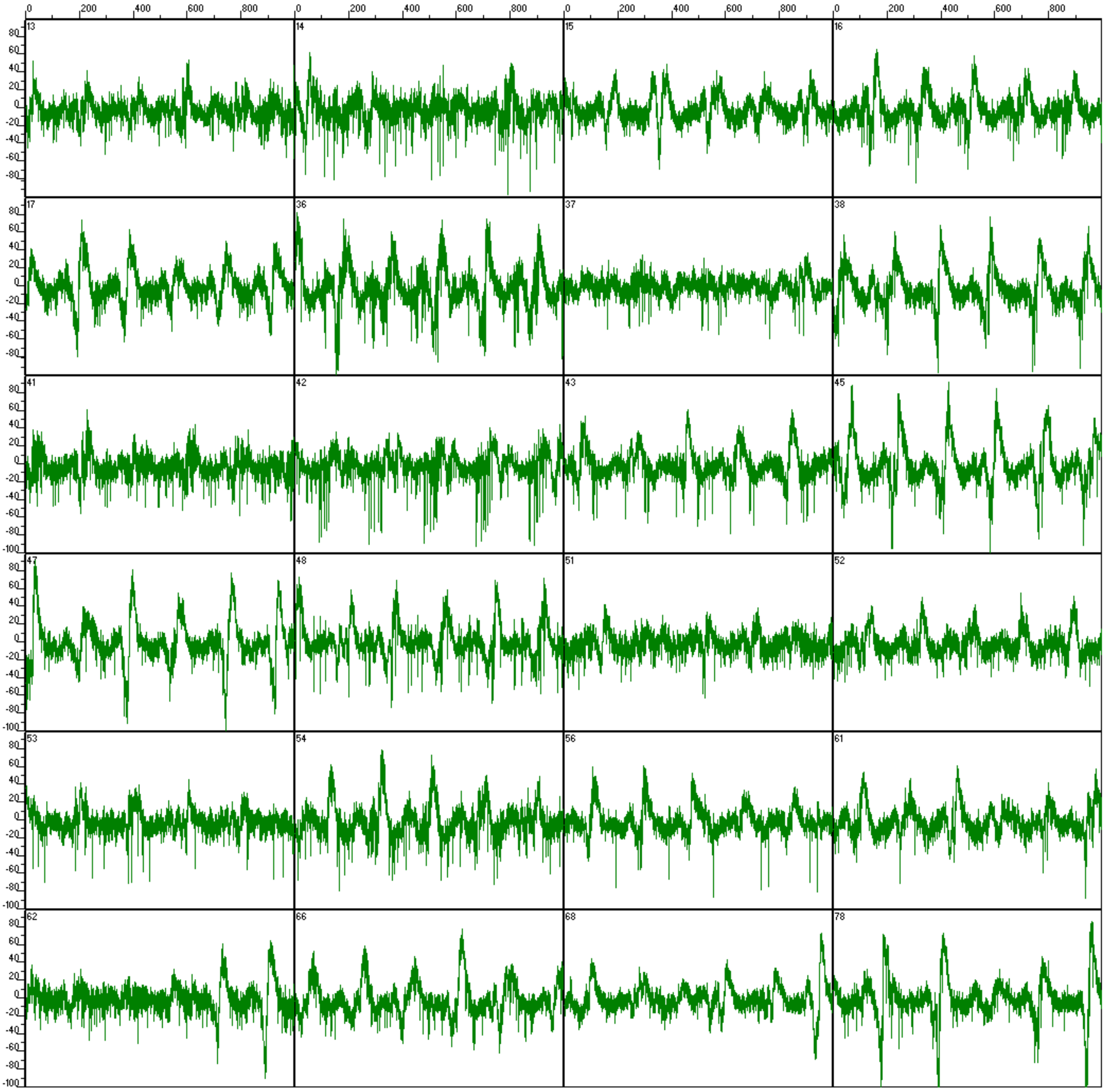

Figure 1.7: MC_Rack screenshot of several channels from a spontaneous activity recording from a P145 *rd1* retina (see chapter 2 for details of recording methods). Note the strong, slow LFP oscillations, particularly prominent on channel 45, accompanied by rhythmic, bursty firing of action potentials, especially noticeable on channel 42. This type of spontaneous hyperactivity is typical of multiple retinal degeneration models. X-axis units: ms, Y-axis units: μV.

in human RP, but it has been postulated that the photopsias sometimes described by early-stage RP patients (Delbeke et al. 2001) could be a consequence of this pathological activity.

What is the source of this hyperactivity? Prior to the work of Stasheff (2008), Marc et al. (2003) put forward a model for how retinal processing might be altered by the various patterns of rewiring observed; among their predictions was spontaneous oscillatory activity. However, in light of more recent research, this is unlikely to be the source of the degenerate hyperactivity. The first to probe the origin of this activity were Menzler and Zeck (2011), who investigated the synchronisation and spatiotemporal propagation of the oscillations underlying RGC bursting. They also found that the oscillations were not blocked by the action potential blocker TTX, nor inhibitory blockers, but ionotropic glutamate receptor antagonists and gap junction blockers abolished the oscillatory activity, implying that it is generated in an inner retinal network and then spread to the RGCs via glutamatergic drive.

Around the same time, Borowska et al. (2011) were also investigating the source of these oscillations. They were the first to note oscillations in ON cone bipolar cells and AII amacrine cells; unlike the RGC oscillations, these were completely insensitive to synaptic blockade. Thus they concluded that the oscillations arise from the electrically coupled ON bipolar cell-AII amacrine cell network, which is consistent with disruption of the oscillations under gap junction blockade. To further test this hypothesis, Trenholm et al. (2012) investigated which ion channels are involved in these oscillations. They found that blocking hyperpolarisation-activated currents strengthened the oscillations while reducing their frequency, whereas blocking voltage-gated sodium channels abolished them. This contradicts the findings of Menzler and Zeck (2011), but possibly this is a result of the different concentrations used (200nM in Menzler and Zeck (2011) vs 500-1000nM in Trenholm et al. (2012)). They were, however, able to replicate the disruption of the oscillations by gap junction blockade. Furthermore, they were the first to note that similar oscillations can be generated in wild-type retinas by blocking glutamatergic input to bipolar cells, suggesting that the oscillations are not a direct result of degeneration, as proposed by Marc et al. (2003), but an intrinsic property of the inner retinal network that is uncovered by photoreceptor death. Combining these results, they proposed a simple computational model of retinal degenerate oscillations involving gap junction coupling between ON bipolar cells and an electrically heterogeneous network of AII amacrine cells that replicates the effects of blocking different ion channels or depolarising the network by introducing photoreceptor input.

Yee et al. (2012) showed that oscillating RGCs in the *rd1* retina receive both inhibitory and excitatory oscillatory input. This is not incompatible with the results of Borowska et al. (2011) and Trenholm et al. (2012), but—surprisingly—they found that inhibitory oscillatory inputs onto *rd1* RGCs were not blocked by gap junction blockade, in stark contrast to previous studies (Menzler and Zeck 2011; Trenholm et al. 2012). Investigating further, they noted two distinct sources of oscillations: a slow, calcium-channel dependent oscillation arising in bipolar cells, as well as fast oscillations in various amacrine cells. They suggested that the amacrine cell oscillations were a result of changes due to degeneration, but this would not explain why similar oscillations are observed in wild-type retinas in which the photoreceptors are pharmacologically isolated. They were also the first to directly test the possibility that spontaneous hyperactivity could reduce the signal-to-noise ratio of synaptic transmission in the *rd1* retina, a finding they later extended to RGC responses to photoreceptor and electrical stimulation of the slower degenerating *rd10* mouse (Toychiev et al. 2013) as well as visual cortical responses to light stimulation in the *rd10* mouse (Ivanova et al. 2015).

The most recent investigation into the origin of these oscillations in the *rd1* retina is that of Choi et al. (2014). Using a compartmental model of the AII amacrine cell, they demonstrated that interactions between fast sodium currents and a slow, M-type potassium current could cause the cell to oscillate when hyperpolarised by removal of photoreceptor input, as occurs in retinal degenerations. However, further hyperpolarisation, either by gap-junction blockade or facilitation of the M-current with flupirtine, abolishes the oscillations again. Further, blocking the M-current causes the typical *rd1* oscillations to be replaced by a slow, calcium-channel dependent oscillation, reminiscent of the slow bipolar cell oscillator proposed by Yee et al. (2012).

Finally, Biswas et al. (2014) investigated the pharmacology of the spontaneous activity in *rd10* RGCs using MEA recordings. Although the fundamental frequency is lower, they share many of the same pharmacological features, including blockade of the oscillations by excitatory blockers (Menzler and Zeck 2011), decrease in frequency and increase in strength with inhibitory blockade (Yee et al. 2012), and abolition of oscillations with MFA (Menzler and Zeck 2011; Trenholm et al. 2012; Choi et al. 2014). This suggests that the oscillations in *rd10* share common origins with those seen in *rd1* retains. Whether this is the case for other retinal degeneration models remains to be seen.

In summary, the past few years have seen extensive pharmacological and computational investigation of the spontaneous hyperactivity typical of disorders related to photoreceptor degeneration. While some discrepancies remain, the most satisfying explanation is that of an intrinstic AII amacrine cell oscillation (Choi et al. 2014), which spreads through the AII-ON bipolar cell network and synaptic connections to the RGCs (Menzler and Zeck 2011; Trenholm et al. 2012; Margolis et al. 2014), potentially interacting with slow bipolar cell oscillations and fast oscillations in other amacrine cell types (Yee et al. 2012). This model is illustrated in figure 1.8. These oscillations represent a considerable source of noise in the degenerate retina and may hamper photoreceptor and electrical stimulation (Trenholm et al. (2012), Toychiev et al. (2013), and Ivanova et al. (2015), but see the discussion of Choi et al. (2014) for a somewhat more optimistic perspective).

1.2.5 *Existing and Future Treatments*

At present, the only clinically-approved vision-restoring treatment for general photoreceptor dystrophies is retinal prosthesis (Margalit et al. 2002; Ho et al. 2015; Stingl et al. 2015), which will be discussed in more detail in section 1.3. However, there are a number of other potential treatments currently being investigated.

In the particular case of wet AMD, several antagonists of vascular endothelial growth factor (VEGF) can slow the progression of visual decline and in some cases reverse it (Chakravarthy et al. 2006; Brown et al. 2009; Heier et al. 2012; Martin et al. 2012; Rofagha et al. 2013). Several such drugs are approved for the treatment of wet AMD and various new compounds targeting this or related pathways are being studied (Santarelli et al. 2015). Dietary supplementation with saffron might also be beneficial in the early

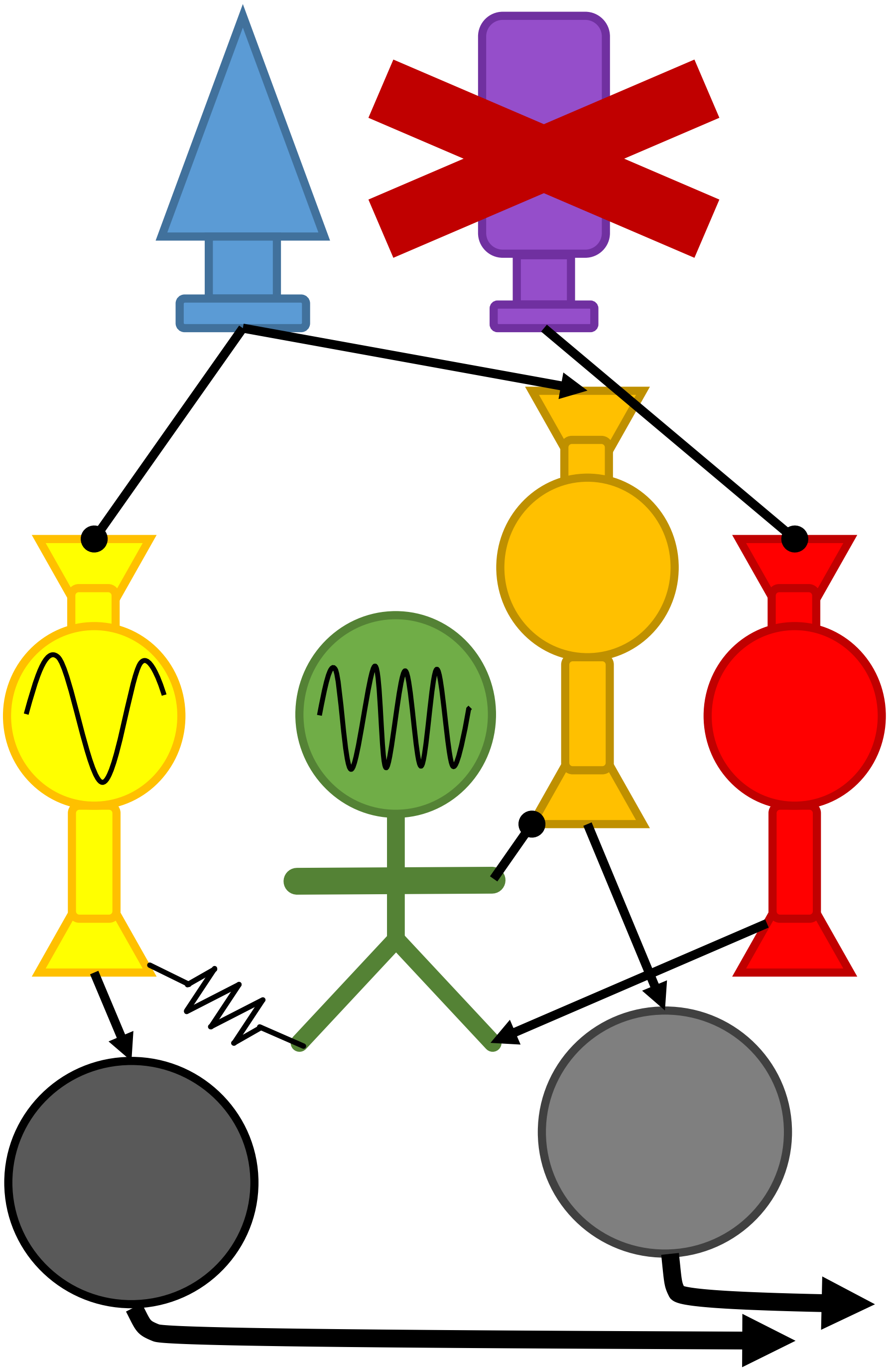

Figure 1.8: Diagram summarising the origin of spontaneous oscillations in the retina. After the rods (purple) degenerate, the AII amacrine cells (green)—originally receiving rod input via rod bipolar cells (red)—are tonically hyperpolarised, revealing intrinsic oscillations. These oscillations spread via gap junctions to the ON cone bipolar cells (yellow), where they are possibly modulated by slow oscillations intrinsic to these cells, and the ON cone bipolars thus provide oscillatory excitation to ON RGCs (dark grey), inducing bursting in these cells. Meanwhile, the AII provides oscillatory inhibition to OFF cone bipolars (orange), which in turn drive OFF RGCs (light grey) to burst in anti-phase with the ON RGCs. Lines ending in arrowheads denote excitatory glutamatergic synapses and lines ending circles denote inhibitory synapses or sign-inverting mGluR6 synapses. The zigzagging line represents a gap junction. Thick arrows represent RGC axons.

stages of AMD (Bisti et al. 2014). For example, Maccarone et al. (2008) showed that saffron pretreatment protects against LIRD and Falsini et al. (2010) showed that saffron supplementation increases the amplitude and decreases the threshold of AMD patients' ERG responses to flickering light.

For photoreceptor dystrophies in which there is a known monogenic mutation, gene therapy to replace the damaged gene might be effective (Cepko 2012; Boye et al. 2013; Sahel and Roska 2013). For example, a recent clinical trial has validated this approach for LCA associated with mutations in the *RPE65* gene (Maguire et al. 2008; Simonelli et al. 2010; Testa et al. 2013), although a trial by another group found only modest benefits (Bainbridge et al. 2015). However, utilising such treatments requires that the damaged gene be identified correctly and further requires developing and testing a new gene therapy for each specific mutation, which is an ambitious undertaking, especially given that most photoreceptor dystrophies are polygenic (Daiger et al. 2013). Moreover, this approach would work only if the gene is corrected before degeneration starts. A related, more general approach is to transfect the retina with a gene coding for neuroprotective factors. For example, Lipinski et al. (2015) showed that viral delivery of a gene for human ciliary neurotrophic factor (CNTF) in a mouse model of RP caused secretion of CNTF from RGCs and Müller cells, leading to improved cone survival and visual function as assessed behaviourally, even if the gene was delivered after the onset of degeneration.

Another approach is to replace the lost photoreceptors by transplantation (Jayakody et al. 2015). Types of donor cells include neonatal rod or cone precursor cells harvested from conspecific donors (e.g. Lakowski et al. (2010) and Pearson et al. (2012)), embryonic stem cells differentiated into photoreceptors of the same developmental stage (e.g. MacLaren et al. (2006), Gonzalez-Cordero et al. (2013), Singh et al. (2013), and Lakowski et al. (2015)), mature photoreceptors (e.g. Gust and Reh (2011)), or induced pluripotent stem cells (e.g. Peng et al. (2014)). Replacement photoreceptors may be transplanted as disocciated cells, as in the preceding examples, or as intact retinal sheets of photoreceptors and/or RPE (Seiler and Aramant 2012). Aside from the considerable molecular biology and tissue engineering challenges of such approaches, photoreceptor replacement strategies—much like subretinal prosthetics (see section 1.3)—rely on the assumption of an intact inner retina in order to restore normal vision, but see sections 1.2.3, 1.2.4 and 1.3 for discussion of whether or not this assumption is justified. An emerging approach, currently being pursued by various groups, is to generate an entire retina, with all retinal cell types and usual laminar organisation, from stem cells *in-vitro* (Eiraku et al. 2011; Nakano et al. 2012; Zhong et al. 2014; Mellough et al. 2014). Such a lab-grown retina could then be used as a wholesale replacement for a diseased retina, obviating any concerns about whether the degenerated inner retina is capable of supporting normal visual processing. However, such retinas then need to be capable of projecting axons to the correct subcortical targets and forming appropriate connections.

1.3 Retinal Prostheses

1.3.1 *Electrical Prostheses*

Ever since it was discovered that appropriately targeted electrical stimulation could elicit the perception of phosphenes in human subjects (Förster 1929; Krause and Schum 1931), it has been postulated that this could be used to artificially restore vision to blind patients (Brindley 1970). The pioneers in this field were Brindley and Lewin (1968), who implanted a grid of electrodes coupled to radio receivers onto the visual cortex of a glaucoma patient and were able to wirelessly elicit phosphenes whose perceived location roughly corresponded to the position of the electrodes on the cortex. Brindley et al. (1972) later replicated this in a second patient, this time with RP, finding that the area of cortex giving simple, punctate phosphenes on stimulation extended into extrastriate cortex. A second group was able to replicate their results using wired electrodes in a number of sighted and hemianoptic patients going in for neurosurgery of the occipital cortex (Dobelle and Mladejovsky 1974) and two blind patients (Dobelle et al. 1974). One of their later patients retained his implant for over 20 years, during which it continued to give useful vision (Dobelle 2000). However, such visual cortical prostheses necessarily involve invasive intracranial surgery; the eye is relatively accessible by comparison, hence the discovery of inner retinal preservation during the 1990s and early 2000s (Santos et al. 1997; Stone et al. 1992; Humayun et al. 1999; Medeiros and Curcio 2001; Kim et al. 2002; Kim and Oh 2002) spurred development of retinal prostheses for the treatment of photoreceptor dystrophies (Margalit et al. 2002).

At present, two companies have electrical prostheses that are clinically approved for the treatment of blindness in the USA or Europe and undergoing long-term clinical trials. These are the Argus II Retinal Prosthesis System (an epiretinal device, in direct contact with the RGC layer) developed by Second Sight (Sylmar, CA, USA; Ho et al. (2015)) and the Alpha IMS (a subretinal device, in contact with the degenerated outer retina) developed by Retina Implant AG (Reutlingen, Germany; Stingl et al. (2015)). Both systems provide improvements in visual function and support a degree of useful vision in daily life for some patients. Other groups are developing electronic retinal prosthetic implants but are still in the preclinical testing or early clinical trial stages. The Bionic Vision Australia research group (Bionic Vision Australia 2015) is currently conducting human tests of a suprachoroidal electrode array implant (Saunders et al. 2014). The IMI Retinal Implant (IMI Intelligent Medical Implants GmbH, Bonn, Germany) incorporates a set of tunable retinal encoders (Hornig et al. 2007) and is currently in clinical trials (Keserü et al. 2012). The EPIRET3 device, developed by the Universities of Aachen and Essen, is a completely wireless intraocular implant that has a good safety profile following implantation (Menzel-Severing et al. 2012) and can elicit visual percepts (Klauke et al. 2011), but thus far no improvement in quality of vision has been reported (Menzel-Severing et al. 2012). An allied group has developed a multielectrode array with hundreds of stimulation sites covering a very wide visual angle, but is still in the *ex-vivo* testing stage (Waschkowski et al. 2014). The Boston Retinal Implant Group has tested their devices with up to 256 electrodes in pigs (Kelly et al. 2011; Kelly et al. 2013), but have yet to conduct human tests. One controversial device was the Artificial Silicon Retina (ASR) developed by Optobionics Corporation (Glen Ellyn, IL, USA), which comprised a standalone array of microphotodiodes (i.e. with no external camera nor any power to the electrodes beyond that provided photovoltaically). It showed improvements in visual function in early clinical trials (Chow et al. 2004), despite the photodiodes not being capable of generating sufficient charge to stimulate the inner retina effectively. Work on the ASR ceased after the company was forced into bankruptcy (Ong and Cruz 2011), although the original founder acquired the name Optobionics and started a new company in 2008 (Chow 2014), later publishing a report showing maintained visual improvement following long-term implantation of the

ASR, but claiming this was due to a neurotrophic effect and not due to direct stimulation of the inner retinal network by the device (Chow et al. 2010). A more promising photovoltaic design is the Stanford Retinal Prosthesis (Mathieson et al. 2012), which comprises a modular array of photodiodes that are driven wirelessly using near-infrared light to provide both power to the electrodes and spatiotemporally patterned stimulation. This obviates the need for transcleral cables for power delivery and, since the light is outside the visible range, does not interfere with normal vision (Lorach et al. 2015). An extremely unique design is that of the Okayama University-type Retinal Prosthesis (OUReP), which uses photoelectric dye-coated polyethylene film in place of discrete electronic or photoelectric pixels (Alamusi et al. 2015), also potentially offering higher resolution vision and a wider field of view than traditional designs (Matsuo et al. 2009). Table 1.3 summarises the devices discussed in this section.

There are a number of design considerations for electronic retinal prosthesis. A major one is the choice of whether to stimulate epiretinally or subretinally (Margalit et al. 2002). The subretinal approach involves stimulating more distal retinal cells, such as bipolar cells and surviving photoreceptors, in order to capitalise on the existing retinal image processing circuitry (but see sections 1.2.3 and 1.2.4 for discussion as to whether is approach is justified). The Alpha IMS (Stingl et al. 2015), the Boston Retina Implant (Kelly et al. 2011), the ASR (Chow et al. 2010), and the Stanford Retinal Prosthesis (Lorach et al. 2015) are all subretinal devices. The subretinal space requires complicated surgery to access; one way of overcoming this is to place the implant suprachoroidally instead, as in the various Bionic Vision Australia devices (Saunders et al. 2014). In this case the stimulation target is still the outer retina, so many of the concerns with subretinal devices also apply to suprachoroidal devices, except now the target tissue is further away and so harder to stimulate. An alternative is the epiretinal approach, in which the device is placed on the inner surface of the retina in order to stimulate the RGCs. Epiretinal devices include the Argus II (Ho et al. 2015), the EPIRET-3 (Menzel-Severing et al. 2012), and the IMI Retinal Implant (Keserü et al. 2012). The epiretinal approach bypasses any dysfunction of the inner retinal circuitry, but to compensate for this the signals should be encoded in a way that higher visual areas can understand (Freeman et al. 2011; Fine

Name	Company	Location	Electrode Type	# Electrodes	Camera	Power	Data	Approval FDA	Approval CE
Alpha IMS	Retina Implant AG	Subretinal	Photovoltaic	1600	No	TC	AL	No	Yes
Argus II	Second Sight	Epiretinal	Conventional	60	Yes	TC	TC	Yes	Yes
Artificial Silicon Retina	Optobionics	Subretinal	Photovoltaic	5000	No	AL	AL	No	No
Bionic Eye	Bionic Vision Australia	Suprachoroidal	Conventional	21-256	Yes	TC	TC	No	No
Boston Retinal Implant	Boston Retinal Implant Group	Subretinal	Conventional	15-256	Yes	TC	TC	No	No
EPI-RET-3	Essen & Aachen Universities	Epiretinal	Conventional	25	Yes	RF	RF	No	No
IMI Retinal Impant	IMI Intelligent Medical Implants	Epiretinal	Conventional	49	Yes	RF	IR	No	No
OUReP	Okayama University	Subretinal	Photoelectric Polymer	N/A	No	AL	AL	No	No
Stanford Retinal Prosthesis	Stanford University	Subretinal	Photovoltaic	142*	Yes	IR	IR	No	No
VLARS	Essen & Aachen Universities	Epiretinal	Conventional	250	Yes**	RF**	RF**	No	No

Table 1.3: Summary of electrical retinal prosthesis designs described in the text and their properties. Listed are the names of each device, the company or institution responsible for their development, implant location, type of electrodes used (conventional, photovoltaic, or other), number of pixels, whether the device incorporates an external camera, how the electrodes are powered, how visual information ('data') is transferred, and whether each device is clinically approved by the US Food and Drug Administration (FDA) or has obtained a CE Mark (CE). AL = ambient light; IR = infrared; N/A = not applicable; RF = radio frequency; TC = transcleral cable. *The Stanford Retinal Prosthesis has a modular design with 142 electrodes per module. **The VLARS has not yet reached *in-vivo* testing, but is based on the same design as the EPI-RET-3

and Boynton 2015). Of the devices currently in human testing, the IMI Retinal Implant is unique in having incorporated retinal encoding models from inception (Hornig et al. 2007), but other groups have successfully evoked patterns of action potentials *in-vitro* that replicate responses to visual stimulation, both with electrical stimulation (Jepson et al. 2014) and optogenetics (Nirenberg and Pandarinath 2012).

Another design choice is whether to use conventional electrodes (Kelly et al. 2011; Menzel-Severing et al. 2012; Ho et al. 2015; Saunders et al. 2014), photovoltaics (Chow et al. 2010; Alamusi et al. 2015; Lorach et al. 2015), or a combination of the two, as in the Alpha IMS (Stingl et al. 2015), wherein implanted photodiodes detect ambient light and the resulting photocurrents are amplified and fed into conventional stimulation electrodes. Using conventional electrodes requires means of delivering both power to the electrodes and specifying the spatiotemporal pattern of current pulses (data transfer), either of which maybe wired or wireless. For example, the Argus II (Ho et al. 2015) uses transcleral cables for both, which may present an infection risk (Chuang et al. 2014); data transfer in the Alpha IMS (Stingl et al. 2015) is wireless but the retinal implant is powered via a transcleral cable from a subdermal implant that receives power wirelessly; and the EPIRET3 (Menzel-Severing et al. 2012) is completely wireless. Related to the choice of photovoltaics or conventional electrodes is whether or not to incorporate an external camera. This is necessary in the case of devices using only conventional electrodes (Kelly et al. 2011; Menzel-Severing et al. 2012; Ho et al. 2015; Saunders et al. 2014), but using photovoltaics either for direct stmiulation (Chow et al. 2004; Alamusi et al. 2015; Lorach et al. 2015) or to drive conventional electrodes (Stingl et al. 2015) means this is not necessary. However, designers of a photovoltaic device might still choose to incorporate an external camera, for example for light amplification or if the implant is most sensitive to wavelengths outside the visible spectrum, as in the Stanford Retinal prosthesis (Mathieson et al. 2012; Lorach et al. 2015), which uses near-infrared light.

One important factor in electronic retinal prosthetic designs is the number, size, and material of electrodes. Current devices have mostly fairly low pixel counts: the prototype Bionic Vision Australia device has just 21 electrodes (Saunders et al. 2014), the EPIRET3 25 (Menzel-Severing et al. 2012), the Argus II 60 (Ho et al. 2015), and the Boston Retinal

Implant up to 256 (Kelly et al. 2013). Of devices in human testing, the Alpha IMS is currently leading the field with 1600 pixels (Stingl et al. 2015), but this is still a very small number compared to the roughly 1 million RGCs in the average human retina. Part of this is the fundamental trade-off between the need to inject sufficient charge per pulse to stimulate cells, but decreasing the size of the electrodes increases the current injection density, which may damage the retina or the electrodes (Cogan 2008). To some extent this may be overcome by novel electrode materials (Shoval et al. 2009; Eleftheriou et al. 2012; Samba et al. 2015), but this still places a limit on the size of the electrodes and ultimately the pixel density that can be acheived. Another issue with electronic prosthesis is that the cell types that are stimulated depends on the physical location of the electrodes and the spatial spread of charge. The latter can be limited by choice of stimulation parameters (Freeman et al. 2011) or implant design (Wong et al. 2009), but beyond the basic cell types (photoreceptors, horizontal cells, bipolar cells, amacrine cells, RGCs), there are numerous distinct subtypes of each cell class with their own distinct roles in retinal processing (Azeredo da Silveira and Roska 2011). At present, classifying retinal cells unambiguously requires detailed analysis of their morphology, hence it is impossible to know which types of cells will be stimulated by each electrode in a given patient's implant. This is of particular concern for epiretinal prostheses that attempt to mimic retinal encoding (Hornig et al. 2007; Jepson et al. 2014), but even for subretinal prosthesis a failure to take into consideration different cell types may prevent proper segregation of the incoming visual scene into ON and OFF pathways, particularly as electrical stimulation has the capacity to excite cells but not inhibit them. One approach that has the potential to overcome these and other limitations of electrical prosthetics is optogenetics, which will be discussed in the following section.

1.3.2 *Optogenetic Prostheses*

Optogenetics. Optogenetics refers to the technique of using ectopically expressed light-sensitive proteins to control neural activity. It had its beginnings in the mid 2000s, when it was discovered that the light-sensitive cation channel channelrhodopsin-2 (ChR2), originally found in the algae *Chlamydomonas reinhardtii* (Nagel et al. 2003), could be transgenically expressed in neurons so that they depolarise when illuminated (Boyden et al.

2005). Similarly, halorhodopsin (HaloR, also known as NpHR for *Natronomas pharaonis* halorhodopsin), a chloride pump (Soliman and Truper 1982) found in the archaebacterium *Natronomas pharaonis*, allows neurons to be hyperpolarised by light (Zhang et al. 2007; Han and Boyden 2007). Since then, optogenetics has exploded in popularity as a neuroscientific technique. Myriads of new optogenetic proteins with different spectral sensitivities, activation and deactivation kinetics, and mechanisms of action have been developed (Zhang et al. 2011; Mei and Zhang 2012) and the technique has been applied towards the study of numerous systems and problems throughout neuroscience (Fenno et al. 2011).

An optogenetic approach to retinal prosthesis avoids many of the problems associated with electrical prostheses (Busskamp et al. 2012; Sahel and Roska 2013; Barrett et al. 2014). The spatial resolution is theoretically limited only by the ability to focus light onto the retina through the optics of the eye; cellular resolution has already been achieved *in-vivo* (Reutsky-Gefen et al. 2013). Both excitatory and inhibitory opsins exist (Zhang et al. 2007; Han and Boyden 2007) and, subject to finding the right promoter, can be targeted to whichever cell type one is interested in activating or silencing (Packer et al. 2013). The eye is transparent, so regardless of whether a particular optogenetic prosthesis uses ambient light or some form of light amplification device (Al-Atabany et al. 2013; Nirenberg and Pandarinath 2012), there is no need to deliver power to an implanted device and 'data transfer' (in the terminology of electrical prosthesis) is intrinsically wireless. Worries about biocompatibility of an implanted device are replaced with the possibility of immune reaction to the foreign protein. For 'subretinal'[1] optogenetic prostheses this is less of a concern as if this happens the eye (which was presumably non-functional before the intervention) can be removed. In the case of epiretinal optogenetic prosthesis, an immune reaction to a protein expressed in RGCs means an immune reaction in the brain and potentially the death of the patient. However, ChR2 has been successfully expressed in the brains of non-human primates without serious adverse events (Gerits et al. 2012) and the company RetroSense Therapeutics has recently received FDA approval to start clinical

---

[1] Although the terminology does not really make sense in the context of optogenetic retinal prosthesis, I will use the terms 'epiretinal' and 'subretinal'—by analogy with electrical prosthesis—respectively to refer to optogenetic approaches targeting RGCs versus those targeting bipolar cells or surviving photoreceptors.

trials of an RGC-targeting optogenetic retinal prosthesis (RetroSense 2015). Alternatively, the problem can be avoided entirely by using human proteins in place of algal or bacterial proteins (Wyk et al. 2015; Cehajic-Kapetanovic et al. 2015).

A Brief History of Optogenetic Retinal Prostheses. It was not long after ChR2 was first expressed in any neuron (Boyden et al. 2005) that it was applied to the retina. Bi et al. (2006) were the first to do so, using an adeno-associated virus (AAV) to transfect *rd1* mice with ChR2 under the control of a hybrid CMV enhancer/chicken β-actin promoter. Expression was primarily in RGCs and they were able to record light evoked RGC spikes and cortical visual evoked potentials (VEPs), but no behavioural data was reported. This was followed shortly after by another group applying the same technique to the RCS rat (Tomita et al. 2007); they were able to recover VEPs but not electroretinograms (ERGs, a measure of photoreceptor function) and, some years later, light-evoked behaviour (Tomita et al. 2010).

Expression in the studies of Bi et al. (2006) and Tomita et al. (2007, 2010) was driven by non-specific promoters, so RGCs in both the ON and OFF pathways are likely to have been traduced. This has the potential to be confusing to higher visual centres, so to overcome this Lagali et al. (2008) electroporated *rd1* mice with a plasmid encoding ChR2 under the control of a promoter based on the gene for mGluR6, which is exclusively expressed in ON bipolar cells (Nomura et al. 1994; Vardi et al. 2000). As well as recording optogenetically-evoked RGC spikes, they were the first to report positive results on behavioural measures of light sensitivity, including light-evoked increases in optomotor activity and optokinetic reponses (OKRs)[2], as a result of optogenetic therapy. Another group to investigate this issue was that of Zhang et al. (2009), who transfected retinas with both ChR2 and HaloR and were able to demonstrate ON and OFF responses evoked with different wavelengths of light. However, they used a non-specific promoter, so many cells co-expressed both opsins, effectively turning them into ON-OFF cells (rather than pure ON or pure OFF cells), regardless of their original identity. A novel solution to this limitation was employed by Greenberg et al. (2011), who used a single promoter but dif-

---

[2] A rodent reflex wherein they automatically track a drifting grating pattern with their head.

ferent cellular targeting motifs to express ChR2 and HaloR in different parts of the same RGC, e.g. ChR2 throughout the cell and HaloR in the soma and proximal dendrites, or vice-versa. In this way, they were able to optogenetically re-engineer the classic centre-surround receptive field of RGCs, wherein they respond with one polarity to light in the centre of their RF but the opposite polarity in the surround (Kuffler 1953). Greenberg et al. (2011) used biolistic gene delivery in their study; Wu et al. (2013) later replicated their approach using viral transfection, a more clinically relevant method of gene delivery, instead. Innovative though the approaches of Zhang et al. (2009), Greenberg et al. (2011), and Wu et al. (2013) are, both groups have only reported RGC responses from *in-vitro* recordings; neither has presented cortical or behavioural evidence of the efficacy of their optogenetic prosthetic designs.

Lin et al. (2008) were the first to recognise the potential limitations of ChR2 for retinal prosthesis due to the high intensity light required, meaning it is unlikely to respond to ambient light in most conditions and may be phototoxic (but see Degenaar et al. (2009)). To overcome this, they expressed the mammalian photopigment melanopsin in non-intrinsically-photosensitive RGCs. Melanopsin is much more light sensitive than ChR2 but has much slower kinetics (melanopsin responses evolve over several seconds to tens of seconds compared to milliseconds for ChR2). Nevertheless, they were able to see improvements in pupillary light reflexes (PLR) and visually guided behaviour after ectopic expression of melanopsin.

Continuing their research into optogenetic retinal prosthesis, Tomita et al. (2009) were the first to use a transgenic rodent line, as opposed to a viral vector, to control ChR2 expression. This has the advantages that expression is more consistent between animals and promoter sizes are not limited by the packaging capacity of AAVs or other viruses, but is obviously inapplicable in a clinical setting. They used the *Thy1* promoter to restrict expression of ChR2 to RGCs (Arenkiel et al. 2007) of sighted rats and then used light damage to induce retinal degeneration, but light damaged rats with ChR2 still displayed VEPs and OKRs. Interestingly, Thyagarajan et al. (2010) crossed a transgenic line expressing ChR2 under this same promoter with *rd1* mouse, but found that the resulting mice fared no better than plain *rd1* controls in visually guided tasks, despite strong optogenetically evoked responses recorded from RGCs. Possible reasons for this include the low number of ChR2-expressing cells or the fact that *Thy1* is not specific to any subtype of RGC, so some OFF and ON-OFF cells may have been turned into ON cells.

Shortly after, Doroudchi et al. (2011) replicated the work of Lagali et al. (2008) using a more clinically relevant method of transfection (viral vector delivery as opposed to electroporation) and in multiple mouse models (*rd1*, *rd10*, and *rd16*). This time, the ChR2-expressing mice beat the sham-injected controls on a six alternative forced-choice (6AFC) visual water maze task. This is a harder version of the 2AFC visual water maze task used in Thyagarajan et al. (2010), but as noted the treated *rd1* mice in that study performed no better than controls. Doroudchi et al. (2011) attributed this to the lack of ON and OFF segregation in a general RGC targetting approach, whereas their ON bipolar cell-only approach maintains this separation. Furthermore, they were the first to show optogenetic visual restoration to be safe and stable long term (up to 10 months). Very recently, Macé et al. (2015) showed that targeting only ON bipolar cells can also restore OFF responses, most likely through rod bipolar cell input onto AII amacrine cells or electrical coupling of ON cone bipolar cells to AII amacrine cells.

Until this point, every attempt at an optogenetic retinal prosthesis targeted some form of inner retinal neuron, usually RGCs or bipolar cells. The first group to attempt optogenetic resensitisation of surviving photoreceptors was Busskamp et al. (2010). They chose HaloR on the basis that it has the same polarity as rhodopsin and the cone opsins, i.e. it hyperpolarises in response to light. Expressing this in surviving cones of *rd1* and *Cnga3*$^{-/-}$;*Rho*$^{-/-}$ mice, they demonstrated rescue of numerous features of inner retinal processing, including ON and OFF segregation, surround suppression and direction selectivity, as well as visually-guided behaviours. In another important first, they demonstrated viral transfection of cones in postmortem human retinas and were able to record HaloR-mediated photocurrents from these retinas.

With numerous proofs-of-concept having been demonstrated for different optogenetic retinal prosthetic strategies, researchers turned their attention to improving the designs. Al-Atabany et al. (2013) were the first to apply the concept of retina-mimicking encoders (having already been used in electrical prosthetics (Hornig et al. 2007)) to optogenetic retinal prosthetics. This idea was later duplicated by Nirenberg and Pandarinath (2012), who were able to demonstrate extremely high-fidelity optogenetically-evoked replications of RGC responses to natural scenes, as well as restoration of OKRs in the same mouse model in which Thyagarajan et al. (2010) failed to show optogenetic rescue of visually-guided behaviour. Reutsky-Gefen et al. (2013) combined a retina-mimicking encoder with a holographic projector, allowing patterned optogenetic stimulation with millisecond temporal precision and cellular resolution *in-vivo*.

Another major area of recent innovation in optogenetic retinal prosthetic designs has been improving the light sensitivity. As mentioned above, the first attempt at this was that of Lin et al. (2008), but they chose melanopsin, which is extremely sluggish. Wyk et al. (2015) improved on this approach by generating a chimeric protein, Opto-mGluR6, which combines the light-sensing part of melanopsin with the signal amplification cascade of the native ON bipolar cell receptor, mGluR6. The result is a fast, light-sensitive optogenetic protein constructed from native mammalian proteins. They expressed this protein in ON bipolar cells, which restored ON and OFF light responses to blind retinas, although with inverted polarities (mGluR6 is a sign-inverting receptor, so Opto-mGluR6 hyperpolarises in response to light; the ON bipolar cell to AII amacrine cell circuitry then carries this to native OFF RGCs, inverting the sign again to turn it into an ON response). Nevertheless, they were able to show optogenetically-evoked visually guided behaviour at much lower light intensities than those typically used in studies of optogenetic retinal prosthesis. Most recently, Cehajic-Kapetanovic et al. (2015) took this idea a step further by expressing human rhodopsin in the ON bipolar cells of *rd1* mice to restore a retinal responses and a variety of visually guided behaviour to these mice at light intensities almost an order of magnitude lower again than the lowest used by Wyk et al. (2015) (8×10^{11} photons·cm^{2}s^1 for the grating stimuli in Cehajic-Kapetanovic et al. (2015) versus 6×10^{12} photons·cm^{2}s^1 for the water maze in Wyk et al. (2015)).

In summary, the concept of optogenetic retinal prosthesis has been demonstrated to be feasible in a variety of animal models and using different opsins and target cell types. These studies are summarised in table 1.4.

						Improvements			
Reference	Opsins	Model	Cell Types	Method	Promoter	IV	ERG	VEP	Beh
Bi et al. (2006)	ChR2	*rd1*	Mostly RGCs	Viral	CAG	Yes	n.t.	Yes	n.t.
Tomita et al. (2007)	ChR2	RCS	Mostly RGCs	Viral	CAG	n.t.	Yes	Yes	n.t.
Lagali et al. (2008)	ChR2	*rd1*	ON BCs	Electroporation	*grm6*, *SV40*	Yes	n.t.	Yes	Yes
Lin et al. (2008)	Melanopsin	*rd1*	Mostly RGCs	Viral	CMV	Yes	n.t.	n.t.	Yes
Ivanova and Pan (2009)	ChR2	C57BL/6	Mostly RGCs	Viral	CAG	Yes	n.t.	n.t.	n.t.
Tomita et al. (2009)	ChR2	*rd1*	RGCs	Transgenic	*Thy1*	Yes	Yes	Yes	Yes
Zhang et al. (2009)	ChR2, HaloR	*rd1*	Mostly RGCs	Viral	CMV	Yes	n.t.	n.t.	n.t.
Busskamp et al. (2010)	HaloR	*rd1*, CRDKO, Human RP	Cones	Viral	hRO, mCAR	Yes	n.t.	n.t.	Yes
Ivanova et al. (2010)	ChR2	Marmoset	Mostly RGCs	Viral	CAG, CMV	Yes	n.t.	n.t.	n.t.
Thyagarajan et al. (2010)	ChR2	*rd1*	RGCs	Transgenic	*Thy1*	Yes	n.t.	Yes	No
Tomita et al. (2010)	ChR2	RCS	Mostly RGCs	Viral	CAG	Yes	Yes	Yes	Yes
Doroudchi et al. (2011)	ChR2	*rd1*, *rd10*, *rd16*	ON BCs	Transgenic	*grm6*, *SV40*	Yes	n.t.	n.t.	Yes
Greenberg et al. (2011)	ChR2, HaloR	*rd1*	RGCs	Biolistic	CaMKII	Yes	n.t.	n.t.	n.t.
Sugano et al. (2011)	ChR2	RCS	Mostly RGCs	Viral	CAG	n.t.	n.t.	Yes	n.t.
Nirenberg and Pandarinath (2012)	ChR2	*rd1*	RGCs	Transgenic	*Thy1*	Yes	n.t.	n.t.	Yes
Reutsky-Gefen et al. (2013)	ChR2	*rd1*	RGCs	Transgenic	*Thy1*	Yes	n.t.	n.t.	n.t.
Wu et al. (2013)	C57BL/6	*rd1*	Mostly RGCs	Viral	CAG	Yes	n.t.	n.t.	n.t
Cehajic-Kapetanovic et al. (2015)	Rhodopsin	*rd1*	ON BCs	Viral	*CAG*, *grm6*	Yes	n.t.	n.t.	Yes
Macé et al. (2015)	ChR2	*rd1*	ON BCs	Viral	*grm6*	Yes	n.t.	n.t.	Yes
Wyk et al. (2015)	Opto-mGluR6	*rd1*	ON BCs	Viral	*grm6*, *SV40*	Yes	Yes	Yes	Yes

Table 1.4: Summary of studies of optogenetic retinal prostheses conducted to date. Listed are the opsins used, animal models, expression method, target cell type, and whether visual improvements were reported by various measures. BCs = bipolar cells; BT = behavioural tests; CRDKO = $Cgna3^{-/-}$,$Rho^{-/-}$ double knock-out; ERG = electroretinograms; IV = *in-vitro*; n.t. = not tested; VEP = visual evoked potential in cortex. For details of promoters, see associated references.

Choice of Target Cell Type. As is evident from the studies described above, there are numerous ways of designing an optogenetic retinal prosthesis and different groups have succeeded with a variety of approaches. One consideration is the choice of cell to target. Many of the pros and cons are analogous to those in the debate between subretinal and epiretinal electronic prostheses (see section 1.3.1). Targeting bipolar cells (Lagali et al. 2008; Doroudchi et al. 2011; Macé et al. 2015; Wyk et al. 2015; Cehajic-Kapetanovic et al. 2015) or surviving cones (Busskamp et al. 2010) seeks to capitalise on the sophisticated inner retinal circuitry in the hopes that any remodelling that has taken place (Marc et al. 2003; Marc et al. 2007) will not interfere with normal processing too much. Targeting RGCs (Tomita et al. 2009; Thyagarajan et al. 2010), on the other hand, bypasses any dysfunctional circuitry, possibly at the expense of having to recreate it genetically (Greenberg et al. 2011; Wu et al. 2013) or computationally (Al-Atabany et al. 2013; Nirenberg and Pandarinath 2012; Reutsky-Gefen et al. 2013). Unlike with epiretinal and subretinal prostheses, surgical accessibility is less of a concern, as one only needs space for a needle to deliver the virus and not a whole implant, but the ability of one's chosen vector to penetrate into the retina is of concern. In particular, it may be difficult for standard viral vectors to penetrate the ILM of marmoset retinas (which have considerably smaller eyes than humans (Troilo et al. 1993; Marc 2006a)) to transfect RGCs (Ivanova et al. 2010). Another concern the possibility of immune responses to the chosen opsin, which could have severe consequences (up to and including death) if the RGCs are targeted. Fortunately, thus far no serious adverse events associated with retinal expression of optogenetic proteins have been reported in animal studies. Moreover, the problem can be side-stepped entirely by using mammalian opsins (Wyk et al. 2015; Cehajic-Kapetanovic et al. 2015) instead of bacterial or algal ones.

Unlike with electrical prostheses, with optogenetics the choice target cell population is more fine-grained than just RGCs versus photoreceptors and bipolar cells. In principle, one can target any class of cells for which one has a sufficiently selective promoter (Packer et al. 2013) or even different locations within cells (Greenberg et al. 2011; Wu et al. 2013). Early optogenetic retinal prostheses did not take advantage of this, using non-selective promoters that mostly drove expression in RGCs but also in other cell types

(Bi et al. 2006; Tomita et al. 2007; Lin et al. 2008; Ivanova and Pan 2009; Zhang et al. 2009; Ivanova et al. 2010; Tomita et al. 2010). Due to the diversity of cell types in the mammalian retina (Masland 2001b), each encoding distinct features of the visual scene (Azeredo da Silveira and Roska 2011), more targeted expression of optogenetic constructs is likely to be beneficial, and researchers quickly realised this. Most of the effort focussed on targeting optogenetic constructs to the ON bipolar cells (Lagali et al. 2008; Doroudchi et al. 2011; Macé et al. 2015; Wyk et al. 2015; Cehajic-Kapetanovic et al. 2015), most likely due to the ease of targeting these cells with the mGluR6 promoter. Although on the surface this seems like it should only restore the ON pathway, sufficiently high expression can also drive OFF responses (Macé et al. 2015), most likely through one or both of the AII amacrine cell pathways (Macé et al. 2015; Wyk et al. 2015). A few groups have also shown successful prosthetic designs targeting surviving cones (Busskamp et al. 2010) or RGCs (Tomita et al. (2009) and Nirenberg and Pandarinath (2012), although my own microscopy data as well as the work of Park et al. (2014) suggest that the *Thy1* promoter may also drive expression in amacrine cells).

Ultimately, the question of which cell type is best to target can only be answered empirically. Results from RGC targeting approaches have been mixed (compare Tomita et al. (2009, 2010) to Thyagarajan et al. (2010)). The most successful approaches have been those targeting bipolar cells or surviving cones (Lagali et al. 2008; Busskamp et al. 2010; Doroudchi et al. 2011; Macé et al. 2015; Wyk et al. 2015; Cehajic-Kapetanovic et al. 2015), although the heterogeneity of behavioural assays used makes it difficult to quantitatively compare approaches. (Light intensity requirements are not a good measure on which to compare difference cellular targets as this is also influenced by the choice of opsin (see section 1.3.2) and expression levels.) This suggests that, following photoreceptor death, the inner retina is not too degenerated to support useful vision and *in-vitro* data from Busskamp et al. (2010) seems to suggest that some normal processing is intact. There are some caveats to this conclusion, however. First, Busskamp et al. (2010) did not test the full suite of retinal processing. Even if they had, mice are not particularly known for their high resolution vision or sophisticated repertoire of visually guided behaviours, so more subtle deficits in visual processing due to inner retinal remodelling that could compromise a photoreceptor or bipolar cell targeting approach might only be revealed in large animal models such as cats (Narfstrom 1983), dogs (Aguirre et al. 1978), or pigs (Petters et al. 1997). (This would also be consistent with the fact that even high resolution subretinal electrical prostheses only restore modest visual function (Stingl et al. 2015).) Finally, RGC targeting approaches have not had a fair test, particularly against bipolar cell targeting approaches. The latter have had segregation of ON and OFF pathways as a primary concern from the beginning, whereas all RGC approaches to report behavioural results so far have used non-pathway-specific promoters, potentially converting diverse RGC types to a single ON type (Doroudchi et al. 2011). No group has reported behavioural results from an RGC targeting approach that separates ON and OFF pathways, but it is interesting to note that retina mimicking encoders restore behavioural responses in an RGC-targeting prosthetic (Nirenberg and Pandarinath 2012) where the naive optogenetic approach fails to restore behavioural responses to environmental light in the same mouse model (Thyagarajan et al. 2010). Thus at least some of the failure of RGC-targeting approaches so far may be due to higher visual centres being unable to interpret unnatural inputs, such as receiving ON input through both ON and OFF channels. Degenerate spontaneous hyperactivity (Stasheff 2008; Stasheff et al. 2011) might also hamper RGC targeting approaches more than bipolar cell or cone targeting approaches (see discussion in Choi et al. (2014)), but no-one has tested this directly.

Choice of Opsin. The choice of whether to use an excitatory opsin, such as ChR2, or an inhibitory opsin, such as HaloR, is mostly driven by the choice of target cell type: excitatory opsins for ON cells and inhibitory opsins for photoreceptors and OFF cells. Beyond that, most previous studies on optogenetic retinal prostheses have used fairly standard versions of ChR2 or HaloR. However, since their initial application to neuroscience (Boyden et al. 2005; Zhang et al. 2007; Han and Boyden 2007), geneticists and molecular biologists have developed a huge variety of new opsins with altered response kinetics, spectral sensitivities and modes of action (Zhang et al. 2011; Mei and Zhang 2012). There are a number of reasons one might want to use some of these improved optogenetic proteins in an optogenetic retinal prosthesis. Improving the response kinetics might allow more temporally precise retinal stimulation (Gunaydin et al. 2010). ChR2 and HaloR are extremely light-insensitive. To some extent this can be overcome with light amplification goggles, which might be necessary in any case if the prosthetic does any form of image processing (e.g. retinal encoding, Al-Atabany et al. (2013) and Nirenberg and Pandarinath (2012)), but alternatively variants with improved light sensitivity might be able to expand the dynamic range of an optogenetic prosthesis (Mutter and Münch 2013), ideally to the point that it works with ambient light. If a device is used to project light into the eye, red-shifted opsins such as ReaChR (Lin et al. 2013) or Chrimson (Klapoetke et al. 2014) might allow safer photostimulation than blue light (Degenaar et al. 2009). Multiple, spectrally distinct opsins might also be used to control distinct cell populations, for example to segregate ON and OFF pathways (Zhang et al. 2009; Greenberg et al. 2011; Wu et al. 2013) or as another strategy to expand the dynamic range of the prosthesis (Mutter and Münch 2013). Finally, mammalian opsins such as melanopsin (Lin et al. 2008; Wyk et al. 2015) or rhodopsin (Cehajic-Kapetanovic et al. 2015) might be preferred to algal or bacterial opsins, both for their several orders of magnitude increased light sensitivity and for the fact they are less likely to evoke an immune response, which is of particular concern for RGC-targeting prostheses.

1.4 Aims of the Thesis

In this chapter, I have provided an overview of retina, focussing on how it encodes visual information, and given a brief introduction to photoreceptor dystrophies and their treatments, with a special emphasis on optogenetic retinal prosthesis.

In section 1.1.3, I noted a number of open questions with regards to retinal encoding, in particular the extent to which RGCs can be considered independent encoders (or, indeed, what it even means to be independent), and whether rank-order coding, for all its theoretical justification, is plausible as a coding strategy employed by real mammalian retinas. The aim of chapter 3 will be to explore some of these issues.

In section 1.2.4, I described the spontaneous hyperactivity that arises in retinal degenerations and the possible underlying mechanisms, as well as noting that suppressing this activity can improve RGC responses to photoreceptor and electrical stimulation. Despite the considerable research effort that has gone into the development of optogenetic retinal prostheses over the past 10 years as described in section 1.3.2, this spontaneous activity has been completely ignored. The aim of chapters 4 and 5 will be to test whether dampening this activity can also improve RGC responses to optogenetic stimulation.

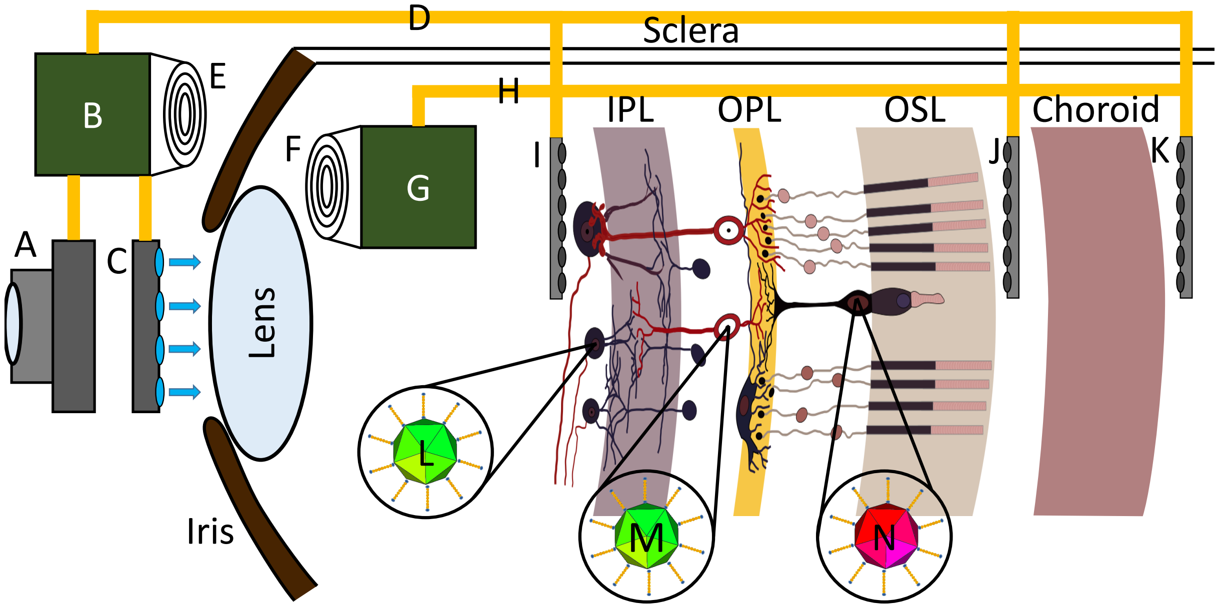

Figure 1.9: Diagram summarising the different components that may be incorporated in to common retinal prosthesis designs. An optional camera (A) captures the incoming light and sends it to a video processing unit (B). This unit may simply translate the scene directly into a pattern of stimuli, or it may do more sophisticated processing such as retinal encoding. In the case of a photovoltaic or optogenetic prosthesis, this information is displayed by a light emitter (C), such as a mini projector or microLED array. Otherwise, the information may be sent via a transcleral cable (D) to the implant, or wirelessly via a radio frequency or infrared transmitter (E) and receiver (F) to another unit (G) that transfers the information via an intraocular cable (H). The transcleral cable or wireless link can also provide power the electrodes from an external battery, which is usually placed subdermally and charged wirelessly. If there is an implant, it may be placed epiretinally (I), subretinally (J), or suprachoroidally (K). For an optogenetic prosthesis, common designs include expressing excitatory opsins such as ChR2 in the RGCs (L) or bipolar cells (M), or inhibitory opsins such as HaloR in surviving cones (N). Sufficiently sensitive optogenetic or photovoltaic protheses may forgo the external camera and use incoming light to stimulate the retina. IPL = inner plexiform layer, OPL = outer plexiform layer, OSL = outer segment layer. Retinal circuit diagram taken from https://commons.wikimedia.org/wiki/File:Retina-diagram.svg, licensed under the Creative Commons Attribution-Share Alike 3.0 Unported license. Virus image modified from http://openclipart.org/detail/179321/adenovirus-by-chatard-179321, which is in the public domain.

Chapter 2. Materials and Methods

2.1 Animals and Breeding

I used two main strains of mice: C57BL/6 (*wild-type*) for photoreceptor stimulation experiments (chapter 3), and for optogenetic stimulation experiments (chapters 4 and 5) I created a strain of congenitally blind mice with RGCs that express the light-sensitive cation channel *channelrhodopsin-2* (ChR2). I purchased C3H/HeNHsd mice (also known as *rd1*) from Harlan Laboratories (Indianapolis, USA). These mice express a naturally-occurring mutant $Pde6b^{rd/rd}$ allele of rod phosphodiesterase, which causes rapid rod death followed by secondary cone loss, with virtually no surviving rod photoreceptors by post-natal day 36 (P36; Carter-Dawson et al. (1978)). Staff at the Campus for Ageing & Vitality crossbred these mice with B6.Cg-Tg(Thy1-COP4/EYFP)9Gfng/J (*ChR2*) mice, purchased from the Jackson Laboratory (Bar Harbor, USA), which express ChR2 (Nagel et al. 2003; Boyden et al. 2005) under the control of the *Thy1* promoter in a number of cell types through the central nervous system, including about 40% of all RGCs (Arenkiel et al. 2007; Thyagarajan et al. 2010). Offspring of the initial and subsequent crosses were then crossed with C3H/HeNHsd mice again to ensure that some of the offspring were homozygous for $Pde6b^{rd/rd}$ (necessary for photoreceptor degeneration phenotype) and at least hemizygous for *ChR2* (sufficient for ChR2 expression). Mice with this genotype are referred throughout the text as *ChR2rd1*.

The *ChR2rd1* mouse is the same mouse model as was used by Thyagarajan et al. (2010), Nirenberg and Pandarinath (2012), and Reutsky-Gefen et al. (2013). Figure 2.1 shows a confocal microscope image—taken by Dr Gerrit Hilgen—from a typical *ChR2rd1* retina. ChR2 in these mice is tagged with enhanced yellow fluorescent protein (EYFP), so these cells show up in yellow. This retina has also been stained with the RGC marker RBPMS (Rodriguez et al. 2014). ChR2 is expressed in a considerable fraction of RGCs; I have not quantified this, but Thyagarajan et al. (2010) report expression in roughly 40% of RGCs. ChR2 in these mice is expressed through the cell—including soma, dendrites, and axon—

as is clear from figure 2.1. Additionally, I have taken fluorescence microscope images from a number of *ChR2* mice of a wide range of ages (from 1 to 20 months postnatal) and the pattern of ChR2 expression was consistent throughout all the images (e.g. figures 2.2 and 2.3).

Although expression of ChR2 under the control of the *Thy1* promoter is primarily restricted to RGCs, there is some evidence that a few amacrine cells are labelled as well (Park et al. 2014). Figure 2.4 shows an image created by merging two fluorescence microscope images I took from the inner nuclear and plexiform layers of a three month old *ChR2rd1* retina (I judged the depth based on the vertical orientation of the fixed retina and layers of DAPI-stained cell nuclei). There is a lone soma in the centre of the image, surrounded by part of the cell's dendritic arbor (and possibly some processes from other ChR2-expressing RGCs in the ganglion cell layer). Given the cell's location in the inner nuclear layer, it is most likely an amacrine cell, although a displaced RGC is not impossible. This was the only EYFP-labelled cell in the inner nuclear layer that I observed in 11 *ChR2* and *ChR2rd1* retinas, so if *Thy1* does drive transgene expression in amacrine cells it seems to be fairly rare.

Apart from figure 2.1, I took all images presented in this section using a Nikon Eclipse TE2000 microscope. Using ImageJ, I adjusted all images to remove background fluorescence, improved the contrast, recoloured the images to green, and a added scale bar.

Although virtually no rods survive past P36 in the *rd1* mouse, roughly a third of cone cells survive to at least this age (Carter-Dawson et al. 1978). This presents the possibility that putative ChR2 responses recorded in mature *ChR2rd1* retinas may in fact be cone-mediated light responses. This is unlikely in the experiments presented in chapters 4 and 5 for a number of reasons. First, Stasheff (2008) found no discernible light responses in any of hundreds of RGCs recorded from *rd1* retinas aged P21-29. One possible reason for this is the considerable morphological abnormalities in these retinas: Lin et al. (2009) found considerable proportions of surviving cones in P30 *rd1* retinas—especially short wavelength-sensitive cones in the ventral retina—but these cones displayed a loss of outer segments and opsin mislocalisation, which may greatly diminish their capacity to generate light responses. Moreover, cones in this study were virtually absent by P90 except in the

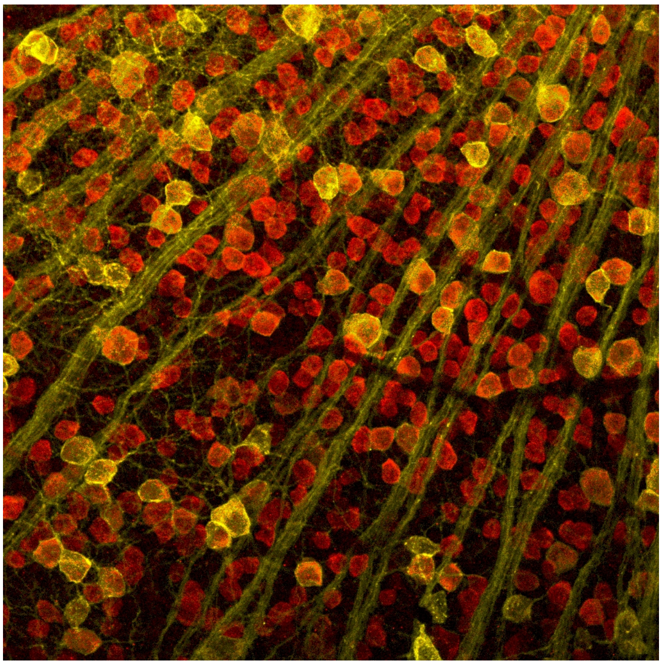

Figure 2.1: 40X magnification confocal microscope image of a *ChR2rd1* retina showing ChR2-EYFP fluorescence (yellow) and staining for RBPMS (red), which labels ganglion cells (Rodriguez et al. 2014). Image courtesy of Dr Gerrit Hilgen.

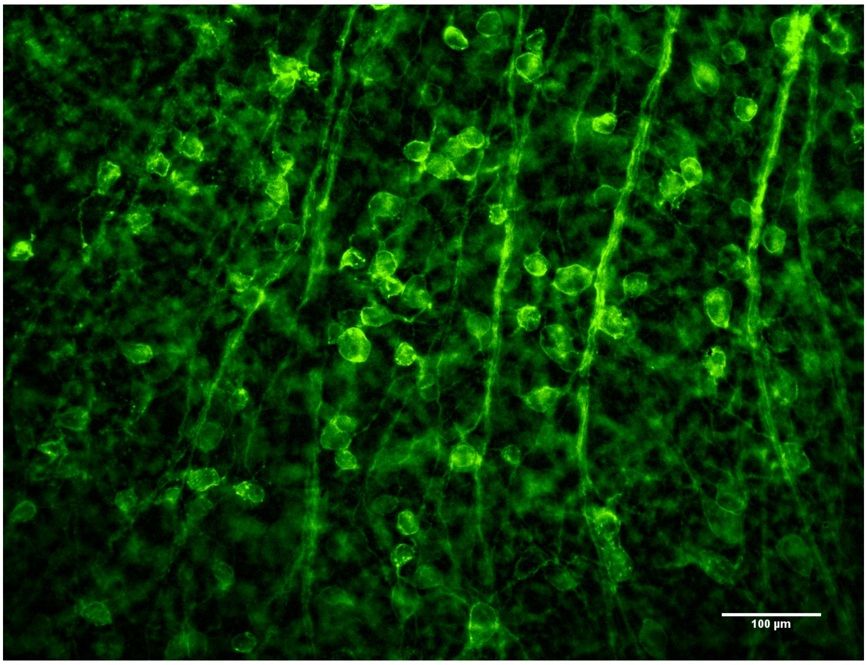

Figure 2.2: 20X magnification fluorescence microscope image from the ganglion cell layer of a 3 month old *ChR2rd1* mouse retina showing ChR2-EYFP expressing cells.

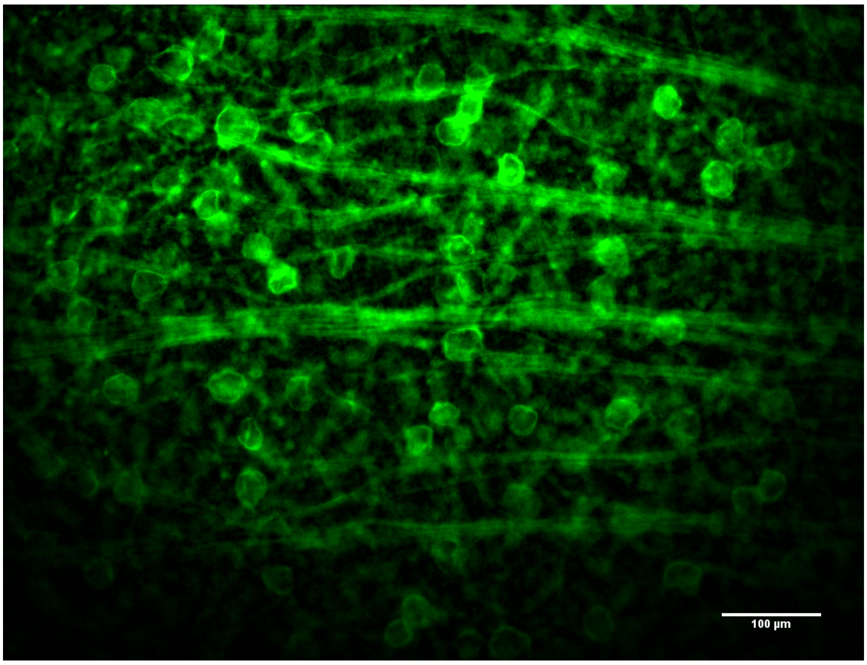

Figure 2.3: 20X magnification fluorescence microscope image from the ganglion cell layer of a 20 month old *ChR2* mouse retina showing ChR2-EYFP expressing cells.

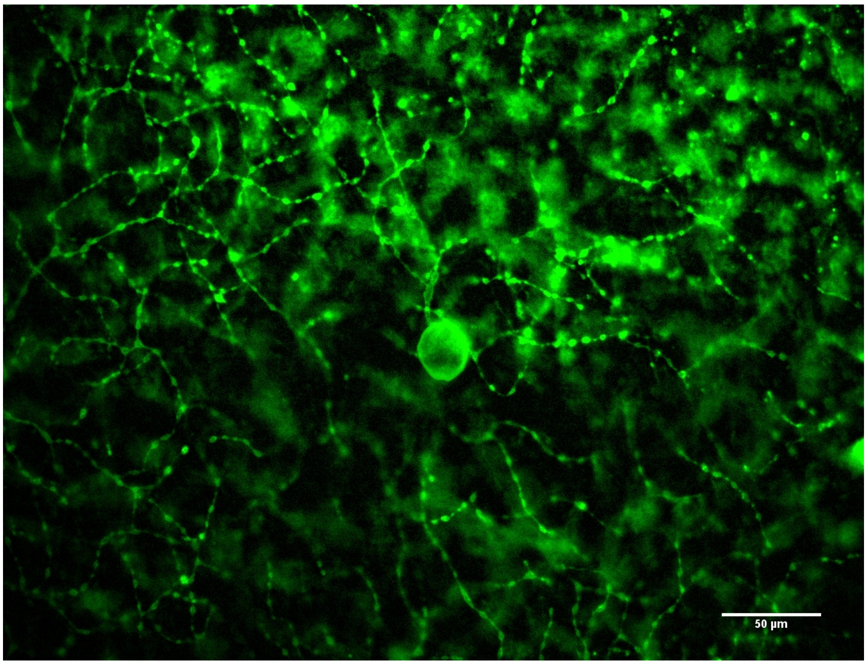

Figure 2.4: A possible ChR2-expressing amacrine cell from a 3 month old *ChR2rd1* mouse retina. This image is a combination of two 40X magnification fluorescence microscope images taken from the inner plexiform and nuclear layers, which I merged in Paint.NET following adjustment in ImageJ as for the previous two images.

far periphery, and the youngest *ChR2rd1* retina recorded from in either chapter 4 or chapter 5 was P93.

In contrast, Wyk et al. (2015) claim to have observed light responses in *rd1* retinas as old as postnatal week 20, but these results should be treated with caution. They show no examples of these supposed responses, the light stimulus they used to detect them was one to two orders of magnitude brighter than those used in chapters 4 and 5, and the statistical test they used to detect them was extremely liberal: a single statistically significant difference between any of 100 pairs of bins in the peristimulus time histogram was sufficient to be classified as a response, with no mention of the threshold for statistical significance nor whether any corrections were made for multiple comparisons. In any case, the majority of recordings presented in chapter 5 were made from retinas older than the P168 at which Wyk et al. (2015) saw no light responses.

Another consideration is that, if there are any surviving, functional photoreceptors in the retinas I used, the retinas were dissected under bright light and the intensity of light used for stimulation was very high compared to what is need to stimulate photoreceptors, so any photoreceptor-mediated responses are likely to have bleached very quickly and will very likely have been abolished long before the end of the experiments. For practical reasons, the recordings in control conditions are taken towards the beginning of each experiment, so this would favour improved responsiveness and signal-to-noise ratio of any surviving cone responses in control conditions, which would weaken any drug effects found in chapters 4 and 5.

Finally, I conducted a number of control experiments in *ChR2rd1* mice heterozygous for the *rd1* mutation—which therefore have no retinal degeneration—in which I stimulated the same retina before and after blocking photoreceptor responses with L-AP4 and DNQX. Responses to bright light persisted in the presence of the drugs in mice hemizygous for ChR2 but not in mice lacking ChR2 expression. In summary, it is extremely unlikely that the mice used in chapters 4 and 5 have working cone photoreceptors and so the recorded responses are almost certainly ChR2 mediated.

2.2 Electrophysiology

2.2.1 *Dissection*

At the start of each experiment, mice were killed by cervical dislocation and their eyes quickly enucleated and kept at room-temperature in artificial cerebrospinal fluid (aCSF) containing (in mM) 118 NaCl, 25 $NaHCO_3$, 1 NaH_2PO_4, 3 KCl, 1 $MgCl_2$, 2 $CaCl_2$, and 10 glucose, equilibrated with 95% O_2 and 5% CO_2. The cornea was pierced with a scalpel, a circular incision cut in the sclera and the lens extracted. Next, the cornea and RPE were peeled away from the retina and the vitreous humour carefully removed with fine forceps. A small amount of aCSF was gently blown onto the retina using a small Pasteur pipette and the retina drawn into and out of a pipette with a widened opening to dislodge any remaining pieces of vitreous. The isolated retina was then transferred to the well of the multielectrode array (MEA). Four radial incisions were made to facilitate flattening the retina, RGC layer facing down, onto the MEA. The MEA chamber was then drained, a small piece of polyester membrane filter (5 µm pores) (Sterlitech, Kent, WA, USA) and a diamond- or ring-shaped metal weight (Warner Instruments, Hamden, CT, USA) was placed onto the retina to improve coupling between the tissue and the electrodes, and then the chamber was refilled with aCSF. The retina on the MEA was then transferred to the electrophysiology rig, where it was heated to 32°C by a heating element and continuously perfused with aCSF heated to the same temperature at 1-2 ml/min. The retina was allowed to settle for 2 hours before any recordings were taken.

2.2.2 *MEA Systems*

Two MEA systems were used: a 60-channel conventional MEA system manufactured by MultiChannel Systems (MCS; Reutlingen, Germany) and a 4096-channel CMOS MEA system, the Biocam Active Pixel Sensor (APS) CMOS-MEA system (Maccione et al. 2014) manufactured by 3Brain (Landquart, Switzerland). The MCS system was used in chapters 3 and 4 and the APS in chapters 3 and 5. I performed the dissection and recordings for all experiments on the MCS system; Dr Gerrit Hilgen (GH) performed all experiments on the APS. Table 2.1 details the differences between each system and figure 2.5 shows a diagram of each system.

	MCS	APS
Electrophys. Channels	60	4095
Analog Inputs	3	1
Digital Inputs	3	0
Electrode Layout	8×8 square	64×64 square
MEAs	60MEA200/10iR-ITO	BioChip 4096S
Electrode Material	Titanium Nitride	Platinum
Electrode Readout	Indium Tin Oxide tracks	CMOS
Electrode Shape	Round	Square
Electrode Diameter	10µm	21µm
Electrode Pitch	200µm	42µm
Total Array Area	1.4mm × 1.4mm	2.67mm × 2.67mm
Amplifier	MEAInv-1060	Biocam APS
Acquisition Card	MC_Card	Camera Link frame grabber
Recording Software	MC_Rack	BrainWave
Sampling Rate	25000 Hz	Variable, ~7000 Hz
Heating Element	HE-Inv-8	Integrated
Temperature Control	TC02	Warner TC-324
Perfusion Heater	PH-01	Warner SH-27B

Table 2.1: Properties for each of the MEA systems used in my experiments.

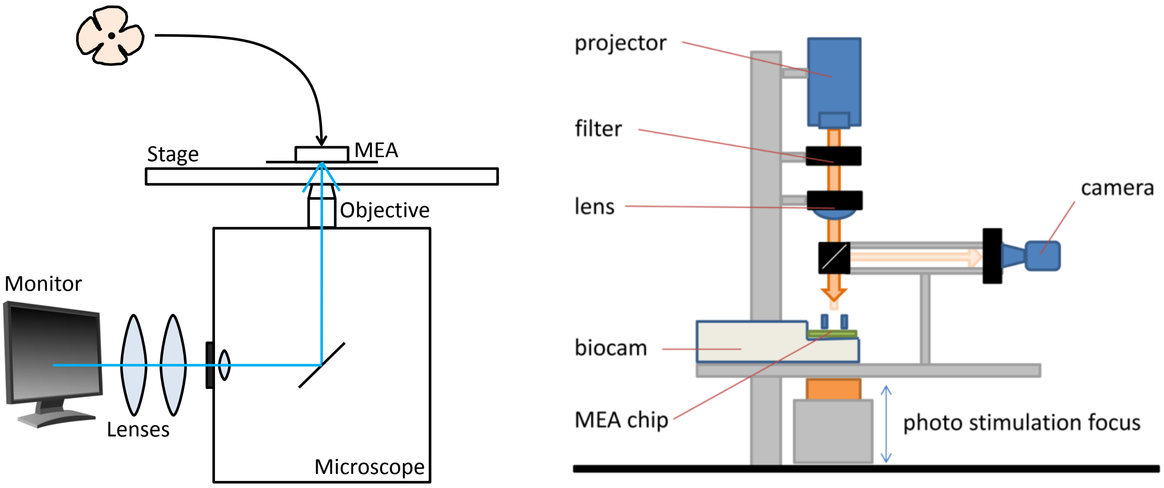

Figure 2.5: Diagrams of the two MEA systems. On the left is the MCS system. The MEA is mounted on the stage of an Olympus IX-71 microscope and light is projected onto the retina from below through the microscope objective, via the camera port. The light path is shown in blue. Projecting the light in this way mimics the way light reaches the retina naturally, as the light must first travel through the inner retina before reaching the photoreceptors. In chapter 4, the monitor and lenses are replaced with a microLED array that slots directly into the camera port. On the right is the APS system. In place of the microscope, there is a custom optomechanical setup that focusses light from the projector onto the MEA. Different neutral density filters can be placed in the light path (shown in orange) to control the light intensity. Unlike the MCS system, the light reaches the photoreceptors first, without having to be projected through the inner retina. This is the only way to get light to the retina, as the APS MEA chips are opaque. Monitor image is public domain clipart taken from http://openclipart.org/detail/4659/lcd-monitor-by-aquila. APS diagram courtesy of Dr Luca Berdondini and Dr Alessandro Maccione.

2.3 Analysis

2.3.1 *Spike Extraction and Sorting*

To extract spikes from MCS data, I first high-pass filtered each raw recording in MC_Rack using a 2nd order Butterworth filter with a cut-off of 300Hz. A possible spike was detected every time the voltage signal on a channel dropped below a certain threshold. To set this threshold, I took a 60 second baseline recording from MEA containing only aCSF at the beginning of each experiment, prior to mounting the retina on the array. The threshold on each channel was set at 6.5-8 standard deviations (depending on the quality of the recording) below a randomly selected 500ms segment of the baseline signal on that channel. I then adjusted thresholds for some channels manually if necessary to ensure as many spikes were detected as possible while minimising noise. In order to minimise waveform corruption by spikes from different cells occurring close together in time, the spike detector had a dead-time of 1ms, meaning no spikes were detected within 1ms following a spike. I extracted spike waveforms comprising 1ms before to 2ms after the time of threshold crossing. I then trimmed these waveforms to 16 samples (0.64ms) before and 32 samples after (1.28ms) the threshold crossing in Matlab, to minimise the amount of noise before and after each spike.

Spike extraction from APS data was done by GH using quantile-based event detection (Maccione et al. 2014).

For all MCS data and the APS data used in chapter 5, I imported the extracted spikes into Offline Sorter (Plexon, Dallas, USA) for spike sorting. (APS data from chapter 3 was sorted by GH). I then performed automatic spike sorting using T-distribution Expectation-Maximisation (Shoham et al. 2003) with 30 (MCS) or 50 (APS) degrees of freedom and 8 (MCS) or 4 (APS) seed clusters. (For MCS data, I aligned each spike waveform to its global maximum before this step). To ensure correct sorting, I then manually inspected either all channels (for MCS data) or only those channels with more than one unit found by automatic sorting (for APS data). The criteria I used were that each unit's average waveform should have a typical action potential shape, no unit should have more than 1% of spikes within 1ms of any other spike, different units should have visually distinct waveforms and form clusters with distinct modes in principal component space, and waveforms should remain stable over time except for possibly a change in amplitude due to either settling of the retina or run-down of the tissue.

Due to the high electrode density of the APS, the same unit is sometimes detected on multiple neighbouring channels. To avoid analysing the same unit multiple times, these redundant units were removed by grouping units on neighbouring electrodes with greater than 5% of spikes occurring within 2 samples (~0.3ms) of another unit's spikes, then iteratively removing units from each group until only the group with the highest spike count remains. This analysis was run by GH (chapter 3) or myself (chapter 5) using a Python script developed by Dr Mathias Hennig.

2.3.2 *Information Theory*

This section provides a brief introduction to information theoretic concepts, such as mutual information and Bayesian decoding, and their application to neural data. For a more thorough treatment, including other applications, the reader is invited to consult any standard information theory textbook, for example Cover and Thomas (2006).

Mutual Information for Discrete Random Variables. The entropy of a random variable is a measure of how much randomness is contained in that variable, or how much uncertainty there is about its value. It is given by:

$$H(X) = -\sum_{x \in \mathcal{X}} p(X = x) \log p(X = x)$$

where $\mathcal{X}$ is the support of X, i.e. the set of values it can take, and $p(X = x)$ is the probability that the discrete random variable X takes the value x. (In general throughout this thesis I shall use italicised capital letters to denote random variables and lower case italicised letters to denote the values they might take. Where the random variable or its value is explicitly a vector, I will use bold face in place of italics. For brevity I sometimes use $p(x)$ in place of $p(X = x)$; I shall always use $p(x)$ for the probability densities of continuous or mixed continuous-discrete random variables, as the actual probably $p(X = x)$ is vanishingly small for all x when X is continuous.) For example, a constant random variable—one which always takes the same value—has entropy zero and a uniformly distributed random variable—one which can take any of its values with equal probability—has the maximum entropy of any discrete random variable having the same number of possible values. Thus a uniformly distributed random variable with eight possible values has entropy $H(X) = -8 \times \frac{1}{8} \log \frac{1}{8} = 4.33$ nats (if the natural logarithm is used) or 3 bits (if the base of the logarithm is 2) of entropy.

The conditional entropy of one variable conditioned on another and the joint entropy of a pair of random variables are defined analogously:

$$\begin{aligned}
H(X|Y) &= -\sum_{x\in\mathcal{X}}\sum_{y\in\mathcal{Y}} p(X=x|Y=y)\log p(X=x|Y=y) \\
H(X,Y) &= -\sum_{x\in\mathcal{X}}\sum_{y\in\mathcal{Y}} p(X=x,Y=y)\log p(X=x,Y=y)
\end{aligned}$$

The mutual information between two random variables is the sum of their individual entropies less their joint entropy:

$$\begin{aligned}
I(X;Y) &= H(X) + H(Y) - H(X,Y) \\
&= H(X) - H(X|Y) \\
&= H(Y) - H(Y|X) \\
&= \sum_{x\in\mathcal{X}}\sum_{y\in\mathcal{Y}} p(X=x,Y=y)\log\frac{p(X=x,Y=y)}{p(X=x)p(Y=y)}
\end{aligned}$$

Mutual information is a measure of how much knowledge one gains (i.e. uncertainty one loses) about the value of X if one knows the value Y, and vice-versa. For example, if X and Y are independent and so their joint probability distribution is equal to the product of their individual marginal distributions, then $I(X;Y) = \sum\sum p(X=x,Y=y)\log 1 = 0$. Knowing the value of X tells us nothing about Y, and vice-versa. Alternatively, if the value of X is completely determined by the value of Y, then distribution of X conditioned on each value of Y is degenerate, so $H(X|Y) = 0$ and therefore $I(X;Y) = H(X)$. That is, knowing the value of Y tells us everything there is to know about X.

Mutual Information for Neural Data. Information theoretic tools such as mutual information have a long history of use in neuroscience, for example to assess how well neurons encode stimuli, to compare coding strategies, or to analyse neural networks (Quian Quiroga and Panzeri 2009; Timme et al. 2014). Often, neuroscientists are interested in computing the mutual information $I(S;R)$ between a variable S, representing the stimulus, and another variable R, representing the response of a neuron or a population of neurons. As only a finite number of stimuli can be presented in a given experiment, the stimulus variable S can often be treated as a discrete random variable (although in some cases it is useful to treat it as continuous, e.g. in cases where the stimulus is generated by some mathematical procedure). The nature of R, however, depends on how one assumes neurons encode information. Under spike count coding, all that matters is the number of spikes fired by a population of neurons in some fixed time window, hence R is discrete (e.g. Gollisch and Meister (2008)). Under other coding strategies, however, R may be continuous - for example under spike latency coding (Gollisch and Meister 2008), if one assumes all neurons fire in response to every stimuli - or even a mixed continuous-discrete random variable. An example of the latter is spike latency coding if one allows neurons not to fire: there is a discrete component (does the neuron fire?) and a continuous component (when does the neuron fire?). One approach to analysing the information content of entire spike trains also treats them as a mixture (Victor 2002): how many spikes were fired (discrete) and when (continuous)?

Mutual information is defined for continuous random variables by replacing sums over probability distributions with integrals over probability density functions (PDFs), e.g.:

$$I(X;Y) = \int_{-\infty}^{\infty} \int_{-\infty}^{\infty} p(x,y) \log \frac{p(x,y)}{p(x)p(y)} dxdy$$

for one-dimensional continuous random variables X and Y with infinite support. Various strategies are possible for estimating the underlying PDFs. If one has some intuition as to the form of the PDF, one can fit a model to the data and calculate the information analytically, as Gollisch and Meister (2008) do for their latency code in which they assume the latencies follow a normal distribution. Other approaches include discretising the data by binning (Panzeri and Treves 1996), kernel density estimation (Rosenblatt 1956; Parzen 1962) or methods based on nearest-neighbour distances (Kozachenko and Leonenko 1987; Victor 2002).

Regardless of the type of random variable, an important consideration in information theoretic studies of neural data is limited sampling bias, which arises whenever one tries to estimate probability distributions or PDFs from finite data (Panzeri and Treves 1996). Various methods have been proposed for dealing with this (for review see Panzeri et al. (2007)), but in my work I have mostly employed the subsampling method of Gollisch and Meister (2008) (described in detail in chapter 3) as it is easy to implement and applicable to any information estimation procedure.

2.3.3 *Bayesian Decoding*

Despite the various methods of bias correction for information estimates, it can still require prohibitively large amounts of data to obtain accurate information values, particularly for high-dimensional variables such as long spike trains and ensemble responses from multiple neurons. An alternative approach for assessing neural codes is Bayesian classification (Jacobs et al. 2009; Quian Quiroga and Panzeri 2009). Bayesian classifier performance (or the performance of any decoder) provides a lower bound on the information available in a neural response: by the data-processing inequality, the mutual information between a stimulus and any transformation of the response (such as a prediction of the stimulus that evoked it) can not be greater than the mutual information between the stimulus and the untransformed response (Quian Quiroga and Panzeri 2009).

A Bayesian classifier attempts to assign each observation of an random variable R to one of a set of classes $\{s_1, ..., s_k\}$, which form the support of a discrete random variable S. It achieves this using Bayes' rule to determine the most likely class $\hat{s}$:

$$\begin{aligned}\hat{s} &= \arg\max_s p(s|r) \\ &= \arg\max_s \frac{p(r|s)p(s)}{p(r)} && \text{by Bayes' rule} \\ &= \arg\max_s p(r|s)p(s) && \text{because the denominator doesn't depend on } s\end{aligned}$$

In most Bayesian classification tasks, R is in fact an ensemble $\mathbf{R}$ of random variables $R_1, ..., R_n$, where each individual random variable is referred to as a 'feature'. For example, each feature might be the responses of an individual neuron and the classes would be the stimuli that might have evoked that response. A naive Bayesian classifier is one that assumes each feature is conditionally independent of the others for each class, so

$$p(r_1, ..., r_n|s) = \prod_{i=1}^{n} p(r_i|s)$$

In practice, due to noise correlations and stimulus-driven correlations in the neural responses, this will not usually be the case. However, it has been shown in the retina and other systems that the performance of a naive Bayesian classifier approaches that of one that exploits the full correlation structure of neuronal responses (Latham and Nirenberg 2005; Jacobs et al. 2009) unless the population is very large (Schwartz et al. 2012a). This is fortunate, as it greatly reduces the amount of data needed to estimate the relevant probability distributions.

How are the probability distributions estimated? The stimulus distribution is known *a priori* as it is set by the experimenter. When each R_i is discrete, it can be estimated easily using histogram methods. For continuous R_i, the PDF $p(r_i|s)$ must be estimated somehow, just as for calculating continuous mutual information. Classical Bayesian classification assumes each $p(r_i|s)$ follows a Gaussian distribution, with its mean and variance estimated as those of the sample. Other assumptions can be made, as in the spike timing code of Jacobs et al. (Jacobs et al. 2009). Flexible Naive Bayes (John and Langley 1995) uses kernel density estimation to estimate the underlying PDF. For mixed continuous-discrete random variables, both the probability distribution of the discrete portion and the PDF of the continuous portion must be estimated. The only case I consider in my work is that in which the discrete portion is binary-valued (i.e. response or no response, and hence by necessity follows a Bernoulli distribution) and follows a one-dimensional continuous PDF whenever there is a response. Such a mixed continuous-discrete random variable has the following stimulus-conditional PDF:

$$p(r|s) = \begin{cases} q_s & \text{if } r = \infty \\ (1 - q_s)g(r|s;\theta_s) & \text{if } r < \infty \end{cases}$$

where $0 \leq q_s \leq 1$ and $\int g(r|s;\theta_s)dr = 1$. The parameters θ_s of the continuous PDF $g(r|s;\theta_s)$ can be estimated using any of the methods mentioned above. It is trivial to show that, given a sample $\{x_1, ..., x_m, y_1, ..., y_n\}$ (where $x_i = \infty$ for all $1 \leq i \leq m$ and $y_j \in \text{supp}\{g(r|s;\theta_s)\}$ for all $1 \leq j \leq n$) of observations from such a random variable, the maximum likelihood estimator (MLE) of q_s is $\frac{m}{m+n}$ and the MLE of θ_s is the same as if the random variable were purely discrete and one had only the samples $\{y_1, ..., y_2\}$.

Using all of the available data to estimate $p(\mathbf{r}|s)$ and then testing the classifier on the same data is an example of a statistical error known as double-dipping (Kriegeskorte et al. 2009) and is likely to overestimate the performance of the classifier. Thus, it is usual to partition the data into a training set, used to estimate $p(\mathbf{r}|s)$, and a test set, used to evaluate the classifier. This practice is known as cross-validation. Many forms of cross-validation are possible, but I used leave-one-out cross-validation, in which the size of the test set is always one, the training set is every trial apart from the test trial, and each trial is used as the test set exactly once. For a given instantiation of training and test set, if the stimulus presented on the test trial was $\bar{s}$, then the performance of the classifier is 1 if $\hat{s} = \bar{s}$ and 0 otherwise[1]. The average performance over all instantiations then gives an estimate of the classifier performance in general.

My motivation for using leave-one-out cross-validation is two-fold. First, it is a more naturalistic test of the neural code as, in a behaving animal, at any given moment the

---

[1] If multiple $\hat{s}$ are equally likely, then the performance is one over the number of most likely stimuli, as the best the classifier can do in this case is to randomly guess which is correct.

brain does not have access to multiple snapshots of the retinal output that it is trying to assign to various classes, but rather is trying to understand the information coming from the retina at that point in time. Secondly, and more pragmatically, leave-one-out cross-validation uses the maximum amount of both training and test data. The disadvantage is that it only gives a single, scalar estimate of the classifier performance, whereas other cross-validation methods can give estimates of higher-order statistics such as the variance. This is not an issue here, as I can aggregate across sub-populations of RGCs or across retinas, as appropriate, for comparing different classifiers.

Chapter 3. Comparison of Coding Strategies in the Healthy Retina

3.1 Introduction

3.1.1 *How Do Individual RGCs Encode Information?*

How RGCs encode visual information remains an open question. A classical assumption is that information about the visual scene is carried by changes in the firing rate of individual neurons (Meister and Berry 1999), but other coding strategies are possible. Gollisch and Meister (2008) found that, for fast-OFF RGCs in the salamander retina, the latency of the first spike following a stimulus carried more information than the number of spikes fired (spike count) and that the difference in latency between pairs of fast-OFF cells was more informative still. The principle advantage of a first spike latency code over spike count is speed and granularity. Assuming a given neuron has a maximum firing rate (which it necessarily does, due to the refactory period between action potentials), then the maximum number of spikes - which sets an upper limit on the number of stimuli that can be distinguished - is determined by the length of the response window. Thus there is an intrinsic trade-off between speed and precision in a spike count code: the quicker one wants to decode a stimulus, the fewer spikes are available to do so, and to decode a stimulus very precisely may mean waiting for a long time for the relevant spikes to occur. A first spike latency code avoids this: the precision of the code is limited only by the timing jitter from one neuron to the next and downstream neurons can process the information as soon as it becomes available, rather than waiting until a fixed response window has elapsed. Nevertheless, a single neuron first spike latency code has disadvantages as well: it needs an external reference time to give it meaning and is completely destroyed by high levels of spontaneous firing. Relative latencies between neurons potentially avoid some of these problems, but I will discuss ensemble and population codes in section 3.1.2.

Spike count and first spike latencies are simple codes in that they can be easily summarised by a single number. More sophisticated codes are possible, for example ones that consider the timing of individual spikes or inter-spike intervals within a spike train. Jacobs et al. (2009) compared spike count to two such codes: 'spike timing', which treats spikes as though they are generated by an inhomogeneous Poisson process whose rate function depends on the stimulus, and 'spike correlation', which is similar to spike timing except that the rate function also depends on the time since the last spike. Both of the spike timing and the spike correlation codes greatly outperformed the simpler count code in that study, but only the spike correlation code gave the same performance on a visual task as that achieved by an awake, behaving animal. These two codes are also more 'natural' than either count or latency in that they make sense outside the extremely artificial paradigm of static stimuli that appear from the void at known points in time. Although Jacobs et al. (2009) treat their stimulus-dependent rate functions as a set of distinct functions defined on some fixed interval following stimulus onset, one can readily generalise this to a rate function that is wholly or partially a function of some continuous incoming stimulus. Such codes thus fit naturally into frameworks such as general linear models that are popular for modelling retinal encoding (Chichilnisky 2001; Paninski et al. 2004, 2007).

3.1.2 *How Do Ensembles of RGCs Encode Information?*

The previous section only considers how individual RGCs encode information, but the vertebrate retina usually contains tens of thousands of RGCs. Is knowing how individual RGCs encode information sufficient to answer the question of how the whole population works together to encode the visual scene? There are numerous ways of answering this question. One can ask whether RGC responses are conditionally independent given the stimulus (S), i.e. for each response R_i from a population of n RGCs, does

$$p(R_1, ..., R_n|s) = \prod_{i=1}^{n} p(R_i|S)$$

It is difficult to answer such a question without knowing the full joint probability distribution of panretinal responses to any stimulus, but one can approach the answer information theoretically by computing the difference in mutual information, ΔI, between a stimulus and a set of RGC responses calculated either using the full joint response distribution or assuming that responses are conditionally independent:

$$\begin{aligned}\Delta I &= I(S;\mathbf{R}) - I_{ind}(S;\mathbf{R}) \\ &= \sum_{(S)}\sum_{\mathbf{R}} p(R_1,...,R_N,S)\log\frac{p(R_1,...,R_N,S)}{p(R_1,...,R_N),p(S)} \\ &\quad - \sum_{(S)}\sum_{\mathbf{R}}\left[\prod_{i=1}^{n} p(R_i,S)\right]\log\frac{\prod_{i=1}^{n} p(R_i,S)}{p(S)\prod_{i=1}^{n} p(R_1,...,R_N)}\end{aligned}$$

Nirenberg et al. (2001) found that ΔI was very small, hence they argued that RGCs act largely as independent encoders. However, later studies contradicted this. Pillow et al. (2008) found significantly increased decoding performance in a Bayesian framework using a general linear model that included coupling terms between neurons compared to one without coupling. Schwartz et al. (2012a) found similar performance between independent decoders and ones that exploit the full correlation structure of responses for small RGC populations, but for large populations the latter significantly outperformed the former.

Another way of analysing this question is in terms of synergy and redundancy (Schneidman et al. 2003; Latham and Nirenberg 2005; Timme et al. 2014). In this framework, RGCs are independent encoders if the information available in the population considered as a whole is the same as the combined information available by considering each RGC in isolation. Redundancy occurs when some of the same information is encoded by multiple RGCs. By contrast, synergy means that there is information available in the population response that can't be acquired by considering each RGC independently. Naively, one might attempt to measure quantify this as the mutual information between the stimulus and the population response less the sum of the mutual information between the stimulus and each RGC's response. This is sometimes referred to as a redundancy-synergy index (RSI; Timme et al. (2014)):

$$RSI = I(R_1,...,R_n;S) - \sum_{i=1}^{n} I(R_i;S)$$

If this value is positive, then it gives the amount of synergy in the population code. If negative, it gives the redundancy. For example, Schneidman et al. (2011) used the RSI to compare the amount of information carried by synchronous spikes fired by pairs of neurons versus spikes fired by one neuron of the pair when the other was silent. On average, they found that synchronous spikes were redundant, but the combination of one neuron firing when the other was silent carried slightly more information (in terms of bits per symbol) than that carried by the spikes of the first neuron and the silence of the second. In other words, the combination of spiking and silence was synergistic. However, Schneidman et al. (2011) only computed the information rate of particular symbols in individual spike trains and pairs of spike trains, not the total information rate (which would be the average symbol information rate weighted by the probability of each symbol), so it is impossible to conclude from their data whether paired spike trains are redundant or synergistic overall.

Moreover, the RSI breaks down if there is both synergy and redundancy in the code (Timme et al. 2014), which the results of Schneidman et al. (2011) suggest is the case. In 2010, Williams and Beer (2010) introduced the partial information decomposition (PID), which simultaneously quantifies the amount of synergy, redundancy and independent ('unique' in their terminology) information about one variable (e.g. a stimulus) encoded by an ensemble (of e.g. responses). This idea is shown graphically for the two variable case in figure 3.3. The two inner circles represent the information carried by each of R_1 and R_2; where they overlap is the redundancy. The outer circle represents the information in the pair response: that not covered by the two inner circles is the synergistic information. The RSI is the difference between the area of the outer circle and the sum of the areas of the two inner circles considered separately. As such, the area corresponding to redundant information is subtracted from the pair information twice. If this area is large and the outer circle only just larger than the two inner circles, the RSI may be negative even if there is synergy; similarly, if the outer circle is large and the overlap between the inner circles small, the RSI may be positive even if there is some redundancy. Thus the RSI can only tell us if there is net synergy or net redundancy. The PID, described in more detail in section 3.2.2, quantifies each area separately and thus measures redundancy, synergy and independent coding simultaneously. However, to date no-one has applied PID to the retina.

As well as analysing population coding by considering interactions between individual neurons' stimulus encoding in terms of synergy or the importance of correlations, one can also consider coding strategies that only make sense in the context of a population of neurons. One example of such a population code is rank-order coding (ROC), first proposed by Thorpe et al. (2001) in the context of rapid image classification. Under ROC, information is encoded by the relative firing order of a population of neurons. This is an extremely rich and efficient code: one could write the response of a population of n neurons as an n-element vector whose values represent the order in which each neuron fired its first spike following the stimulus. As such, there are $n!$ possible code-words but only one spike per neuron is required. Hence Thorpe et al. (2001) argued that such a code was ideal for discerning a lot of information about a visual scene very quickly, which the vertebrate CNS is obviously capable of doing, for example performing face recognition with presentation times as low as 150ms. They tested this using a simplified model of the retina, showing that ROC provided more information and enabled more faithful stimulus reconstruction than codes based on spike count or timing (Van Rullen and Thorpe 2001), but to date no-one has tested ROC in biological retinas.

3.1.3 *Aims*

The aim of the experiments presented in this chapter was to explore some of the questions outlined above in the mouse retina, in particular the extent, if any, of synergistic coding between RGC pairs and the plausibility of ROC as a coding strategy employed by the retina.

3.2 Specific Methods

The work presented in this chapter was part of a collaboration with Dr. Geoffrey Portelli (GP) and Dr. Pierre Kornprobst (PK) of the Neuromathcomp Team, INRIA Sophia Antipolis-Méditerranée, France. GP and PK designed the stimuli and GP conducted the Bayesian decoder analyses. Additionally, some of the recordings were performed by Dr Gerrit Hilgen (GH). All work performed by others is noted in the text; additionally, table 3.1 summarises who was responsible for each part of the work.

Dataset	Recordings	Preprocessing	PID Analysis	ROC Analysis
MCS	JB	JB	JB	GP
APS	GH	GH/GP	JB	GP

Table 3.1: Table summarising who was responsible for each part of the work presented here. Datasets: MCS = 10 retinas recording on MCS MEAs; APS = 2 retinas recorded on APS MEAs. Preprocessing refers to spike extraction, spike sorting and selecting responsive cells. JB = John Barrett, GP = Dr Geoffrey Portelli, GH = Dr Gerrit Hilgen.

3.2.1 *Visual Stimulation*

I projected stimuli onto the retina from a 6.5" LCD monitor (640x480px, 60Hz refresh rate), using a pair of lenses (Edmund Optics, Barrington, USA) and the 2X objective of an Olympus IX-71 inverted microscope (Olympus, Tokyo, Japan) to focus the image onto the RGC layer. Each pixel covered an area of 23.333μm by 23.333μm on the retina. I generated the stimuli in Matlab (MathWorks, Natick, USA) and controlled them using Psychtoolbox (Brainard 1997; Pelli 1997; Kleiner et al. 2007). To synchronise stimulation and recording, I reserved a 100×480-pixel area on the side of the screen that did not cover the retina to signal changes in the presented stimulus by alternating between black and white every time the stimulus changed. I placed a photodiode with built-in amplification (OPT101; Texas Instruments, Dallas, USA) over this area and connected it to one of the digital inputs of MC_Card so that the value on that channel toggled every time the stimulus updated. Figure 3.1 shows a circuit diagram describing the connection between the photodiode and the acquisition card and figure 3.2 shows an annotated photograph demonstrating how the photodiode is used to synchronise recording and stimulus.

The stimuli comprised flashed gratings of maximum contrast with bar widths of 8, 16, 32 and 64 pixels. As 30μm on the retina corresponds to one degree of visual angle, these bar widths correspond to spatial frequencies of 0.08, 0.04, 0.02 and 0.02 cycles per degree, respectively.

Each grating was presented at one of eight phases (equivalent to a shift of 1/4 the bar width), for a total of 4 frequencies × 8 phases = 32 stimuli per block. In each experiment, the stimuli were presented in 150 randomised blocks containing all 32 stimuli. Each trial comprised a 500ms presentation of a grating followed by a grey mask for 1000ms. The mask was also presented for 3 seconds prior to the first grating. The luminance of the

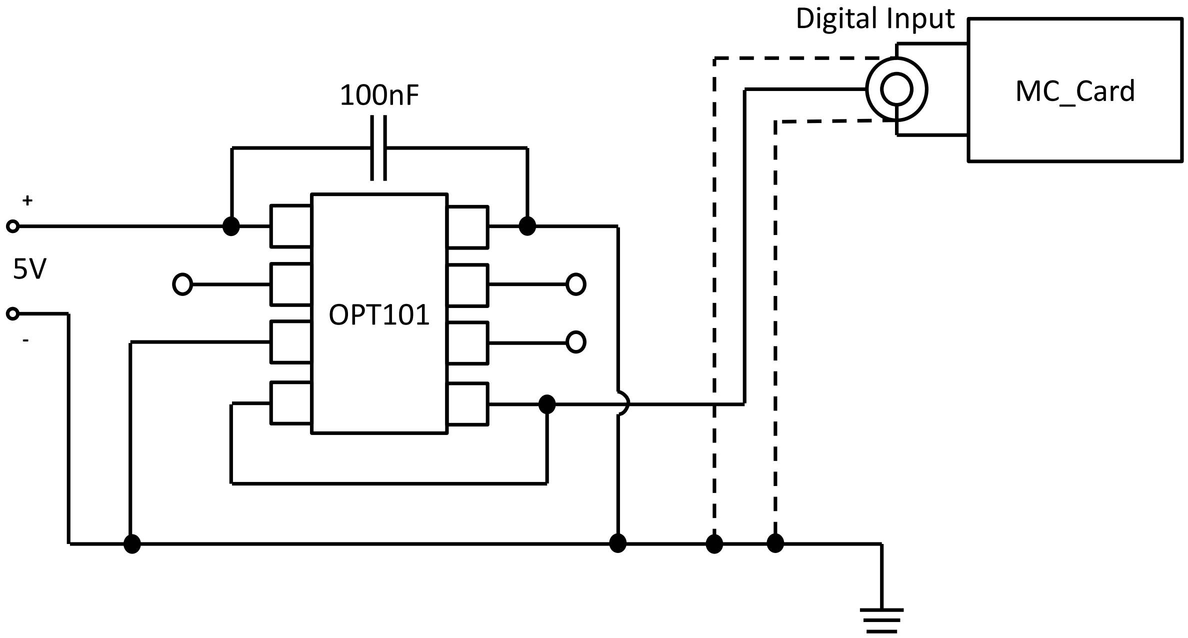

Figure 3.1: Circuit diagram showing how the photodiode and amplifier (OPT101) connects to MC_Card.

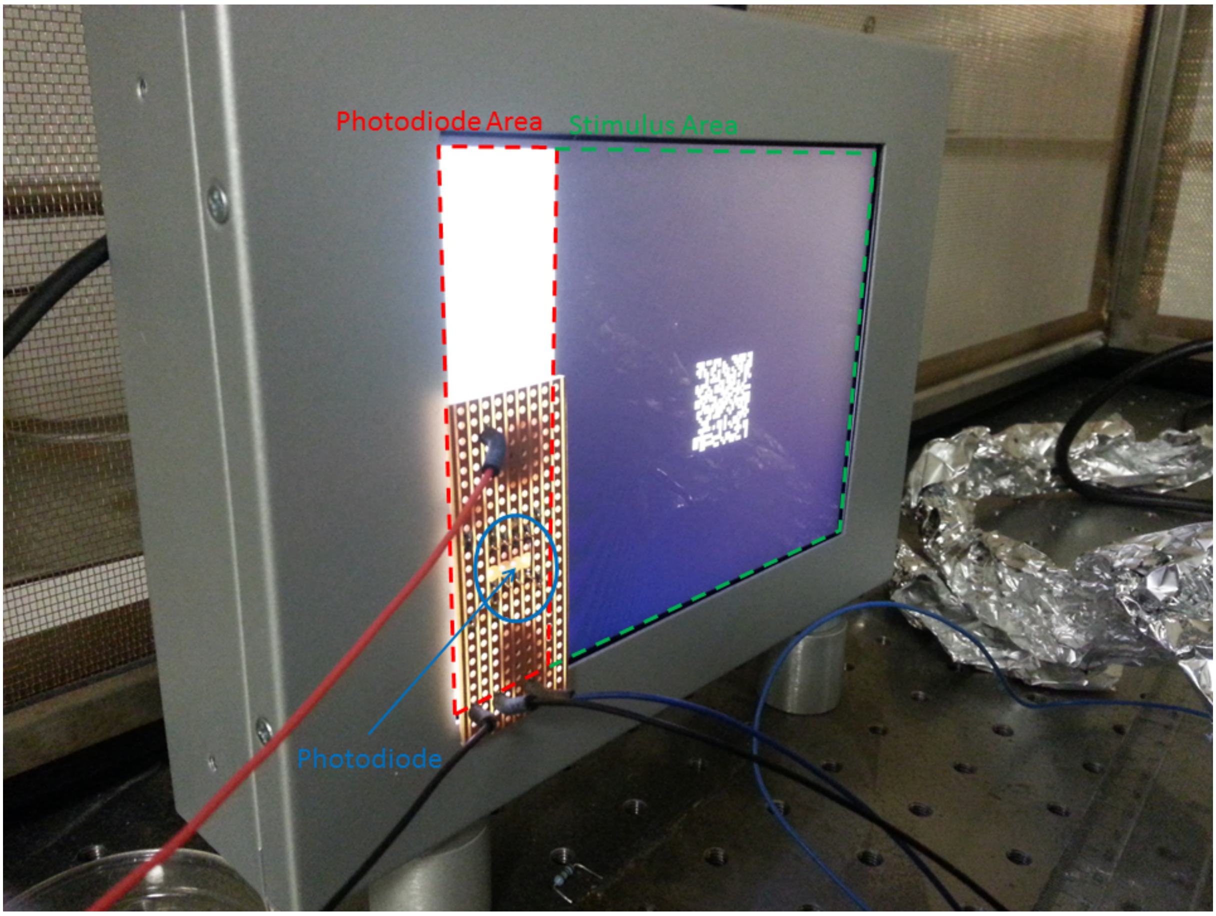

Figure 3.2: Photograph showing how the photodiode is used to synchronise stimulation and recording. Stimuli are presented in the green outlined area, of which only the central 60×60 pixels project onto the MEA. The red outlined area alternates between black and white every time the stimulus changes. The photodiode, circled in blue, is connected to one of the digital inputs of MC_Card.

mask was intended to be the same as the mean luminance of the gratings, but due to a lack of gamma correction there was an error of ~10% in all but one experiment.

3.2.2 *Data Analysis*

Responsive Cell Selection. As not all recorded RGCs in a given retina respond strongly to all stimuli, I selected a subset of RGCs for analysis as follows. First, I selected one sixth of the blocks (i.e. 25 trials per stimulus) to use for detection. From these blocks, I counted the total number of spikes fired by each cell in response to the second lowest-spatial frequency grating as a function of phase. (I chose the second lowest spatial-frequency gratings as these appeared, on visual inspection of the rasters, to evoke the strongest responses). Any cells whose total spike count for all phases was less than 13 (i.e. less than 50% chance of firing a spike in response to any grating) I excluded immediately. For the remaining cells, I tested whether they modulated their firing significantly with grating phase using the Rayleigh test for non-uniformity of circular data. Finally, I selected those cells whose p-value was significant at the $\alpha < 0.05$ level after false-discovery rate correction (Yoav and Hochberg 1995) for further analyses. So as to avoid double-dipping (Kriegeskorte et al. 2009), those blocks used for detection were excluded from further analysis, leaving 125 blocks per stimulus.

Partial Information Decomposition. To analyse information, redundancy, and synergy in RGC pairs, I calculated the PID of the mutual information between RGC pair spike counts and the stimulus (Williams and Beer 2010). I used PID for two reasons. First, it is asymmetric in that it quantifies mutual information between one random variable and an ensemble of random variables, making it a natural fit for experiments where one records responses of multiple neurons to a set of sequentially presented stimuli. Second, unlike many other synergy measures used in the neuroscience literature, it is guaranteed to be non-negative and is able to measure synergy and redundancy simultaneously (Timme et al. 2014).

The idea behind PID is to decompose information provided by an ensemble of random variables $\mathbf{R}$ (e.g. responses of individual neurons) about another variable S (e.g. a stimulus) into the information provided by each variable individually, by each subset of variables,

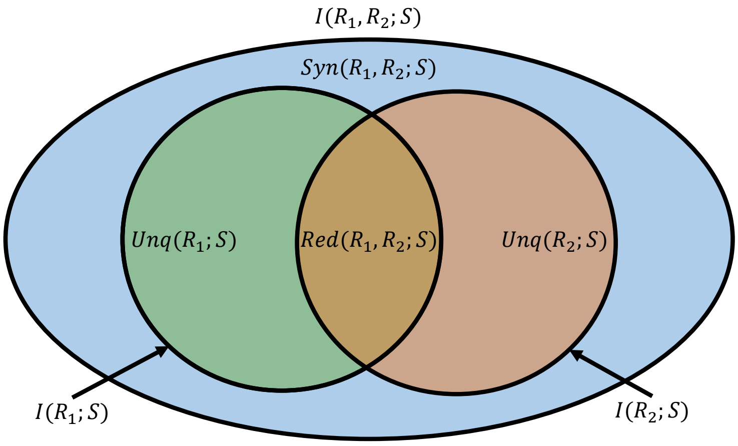

Figure 3.3: Partial information diagram for two variables, based on Figure 1 from Williams and Beer (2010). The two inner circles represent the mutual information between two variables, R_1 and R_2, and a third, S, considered separately. Where they overlap is the redundant information; where they don't is the unique information provided by each. The outer ellipse represents the mutual information between the pair (R_1, R_2) and S. The area not covered by the inner circles is the synergistic information.

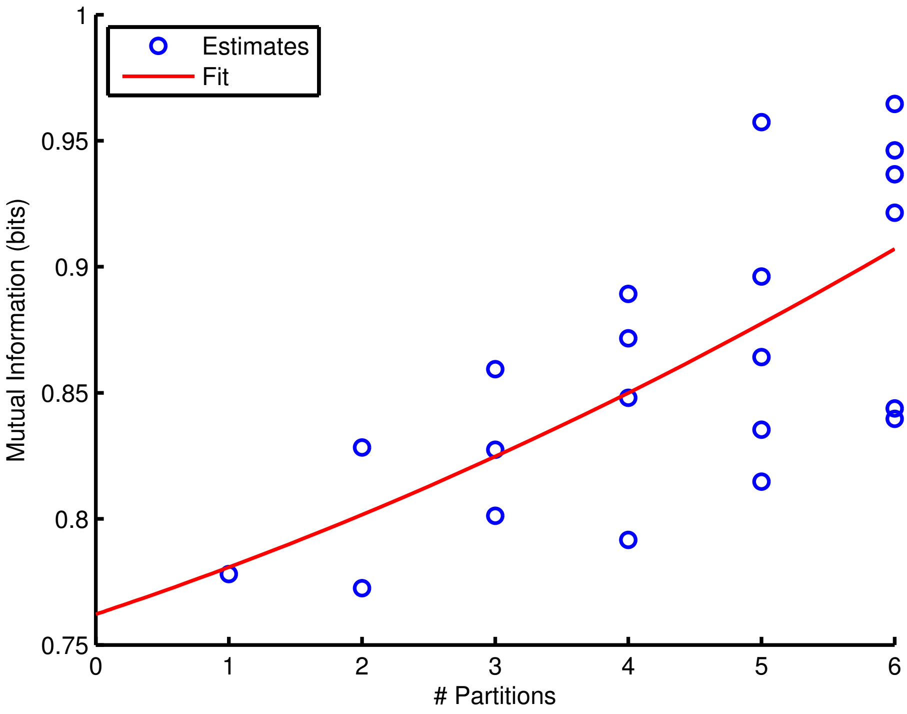

Figure 3.4: Example bias correction for mutual information between one neuron's response and the stimulus. Each blue circle represents the mutual information estimate from one partition after splitting the data into the number of partitions indicated on the X-axis. The red line is a second-order polynomial fit to the same data. The intercept of the red line represents the estimate one would obtain after splitting the data into no partitions, i.e. if one had infinite data, and thus does not suffer from limited sampling bias.

and by the whole ensemble. The full derivation of the PID is available in Williams and Beer (2010), but the calculation for the two-variable case ($\mathbf{R} = R_1, R_2$) is described below with the help of the partial information diagram in figure 3.3. The two inner circles represent the information carried by each individual variable about the stimulus:

$$I(S; R_i) = \sum_s \sum_{r_i} p(s, r_i) \log_2 \frac{p(s, r_i)}{p(s)p(r_i)} \quad \text{for } i = 1, 2$$

Where the two circles overlap is the redundant information between the two variables. To calculate the redundancy, the specific information provided by each variable R_i about a particular stimulus value s is first calculated as the Kullback-Leibler divergence between the distribution of R_i conditioned on s and the marginal distribution of R_i, i.e.

$$I(S = s; R_i) = D_{KL}(R_i | S = s || R_i) = \sum_{r_i} p(r_i | S = s) \log \frac{p(r_i | S = s)}{p(r_i)}.$$

The redundancy is then the sum over all stimulus values of the minimum specific information provided by either variable about that stimulus value, weighted by the stimulus probability, i.e.

$$R(S; R_1, R_2) = \sum_s p(s) \min_{i=1,2} I(S = s; R_i).$$

The unique information carried by each variable is the mutual information between that variable and the stimulus less the redundant information: $U(S; R_i) = I(S; R_i) - R(S; R_1, R_2)$. The outer ellipse in figure 3.3 represents the mutual information between the pair and the stimulus:

$$I(S; R_1, R_2) = \sum_s \sum_{r_1} \sum_{r_2} p(s, r_1, r_2) \log_2 \frac{p(s, r_1, r_2)}{p(s)p(r_1, r_2)}$$

Finally, the area of this ellipse not covered by the redundant or unique information is the synergistic information: $Syn(S; R_1, R_2) = I(S; R_1, R_2) - U(S; R_1) - U(S; R_2) - R(S; R_1, R_2)$. The PID can be defined similarly for larger ensembles, but the complexity of the corresponding partial information diagrams and the resulting expressions become excessively complex extremely quickly as the number of variables increases, so I decided to restrict my analysis to the two-variable case, i.e. pairs of neurons.

I took each R_i as the number of spikes fired by the ith neuron of a pair during the presentation of the stimulus. I calculated the PID for every pair of neurons that was unique up to ordering: that is, if the PID for a pair (i, j) was calculated, I did not calculate the PID for the pair (j, i). Due to the long presentation times (500ms), I deemed it unnecessary to include any of the period immediately following the stimulus, as 500ms is sufficient to capture the entire response of all but the most sustained of cells.

To correct for bias introduced by limited sampling of the data, I separately bias corrected each of $D_{KL}(R_i|S = s||R_i)$, $I(S; R_i)$ and $I(S; R_1, R_2)$ using the subsampling method of (Gollisch and Meister 2008). Briefly, after obtaining an estimate using the whole data set of N trials, I randomly partitioned the data into halves, thirds, and so on, and new estimates calculated for each of these partitions. I fit a second-degree polynomial to the estimate as a function of the number of partitions: the intercept of this polynomial corresponds to the estimate one would obtain with $N/0 = \infty$ samples and so I took this as an unbiased estimate of the true value (figure 3.4). I split the data up to six times and repeated this bias correction procedure 10 times for each pair, taking the average intercept as the final estimate. Using this procedure on simulated data for each of the simple, two-variable examples given in (Timme et al. 2014), the estimates converged to within a few percent of the true value after a few hundred samples from the relevant probability distributions.

The PID as presented in Williams and Beer (2010) is only defined for discrete random variables, which precludes its use for whole spike trains. The underlying information theoretic quantities, however, have equivalent definitions for continuous and mixed continuous-discrete variables (Nair et al. 2006). Thus, to apply the PID to spike trains, I developed a version of PID for the general case of a mixed continuous-discrete random variable (for details, see Appendix A). Using this spike train PID estimator, I also calculated the PID for whole spike trains fired by pairs of RGCs during the presentation of each stimulus.

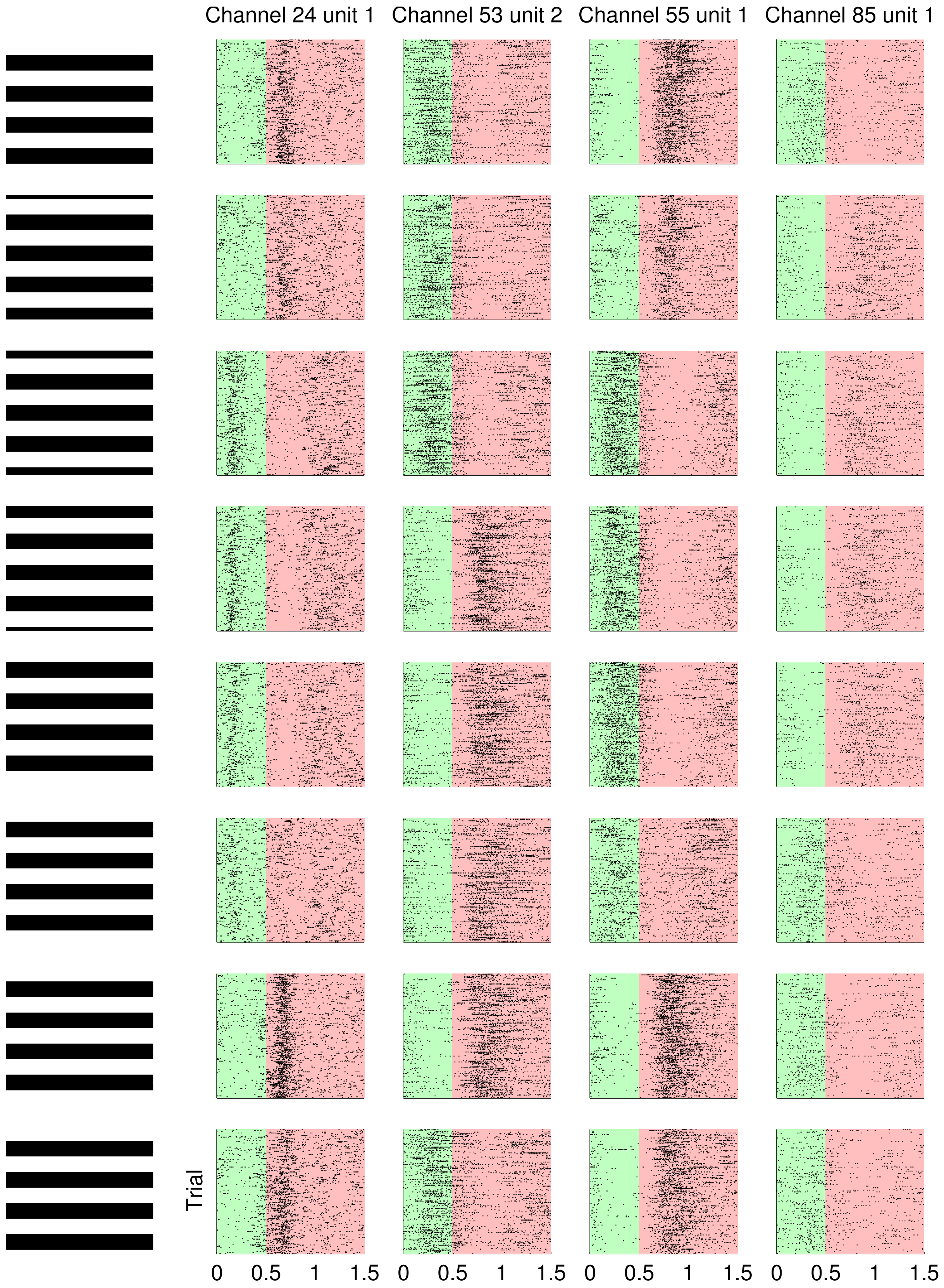

Figure 3.5: Raster plots from four example cells from one retina in response to flashed gratings at 800µm bar width. The grating was presented during the green shaded area and the mask during the red shaded area. Each column represents a different RGC and each row a different phase, as indicated by the example gratings in the left-most column.

3.3 Results

3.3.1 *Pairs of RGCs Encode Information Synergistically*

Using 60-channel MCS arrays, I recorded responses to gratings from ten retinas from ten C57BL/6 mice aged P19-46. Across all retinas, I selected a total of 258 cells for analysis according to the method described in section 3.2.2. Figure 3.5 shows responses of four example cells from one recording in response to the 800µm gratings. There is a clear modulation of firing rate with grating phase, but very little obvious change in latency. This pattern was consistent across all responsive cells in all retinas.

Across all ten retinas, the median RGC pair carried 0.26-0.32 bits of information (depending on the spatial frequency) about the stimulus in their combined spike counts and somewhat more (median 0.57-0.61 bits) in whole spike trains (figure 3.6, left). Note that the information carried by the spike count must be less than or equal to that in the whole spike train. This is a consequence of the data processing inequality: $\forall f. I(X; f(Y)) \leq I(X; Y)$, in other words no manipulation of a variable can increase the amount of information it carries about another variable (Cover and Thomas 2006; Quian Quiroga and Panzeri 2009), and one can trivially determine the spike count from a spike train by counting the spikes. About 65% of recorded RGC pairs respected the data processing inequality, meaning there was more information in the whole spike trains than just the spike counts (figure 3.6, right). The spike count information estimates are reasonably accurate, so the spike train information was likely underestimated in those pairs that showed less spike train information than spike count information. Figure 3.7 shows the results of three different measures of (non)independence: ΔI, RSI and PID. The former asks how much information is contained in correlations between neurons and the latter two test the amount of synergy, i.e. information available in the pair responses that is not available in the individual responses. All three measures represented a similar fraction of the pair information, with ΔI slightly less than PID synergy and RSI slightly lower still. I did not make a similar comparison for the spike train information, as the estimator I used to calculate the spike train PID (see Appendix A) operates on nearest-neighbour distances rather than estimating the underlying probability densities directly, so it is not

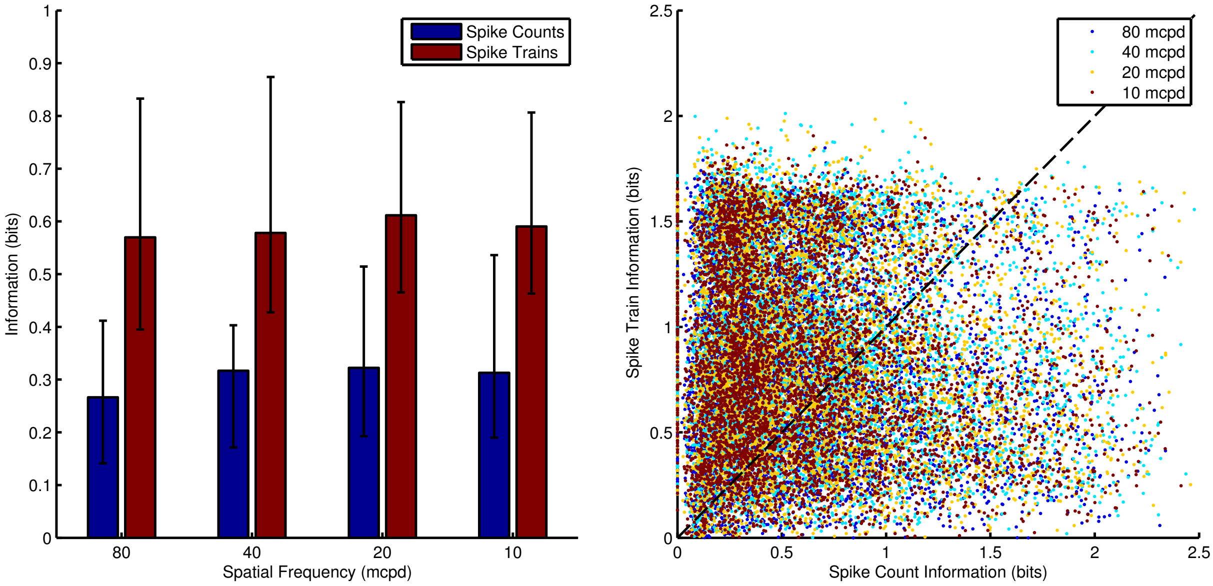

Figure 3.6: Left: median information carried by RGC pair spike counts (blue) and spike trains (red) for the 10 retinas recorded on 60-channel MCS arrays. Bar height represents the median taken first over all pairs within each retina and then between retinas. Error bars are IQR (inter-quartile range) between retinas. Right: information in spike count versus whole spike trains for all recorded pairs of neurons (only pairs within retinas, i.e. pairs from different retinas are not shown). The dashed line represents unity. Most (~65%) pairs lie above the diagonal, i.e. there is more information in the whole spike train than in the spike counts. mcpd = thousandths of a cycle per degree, e.g. 80 mcpd = 0.08 cpd.

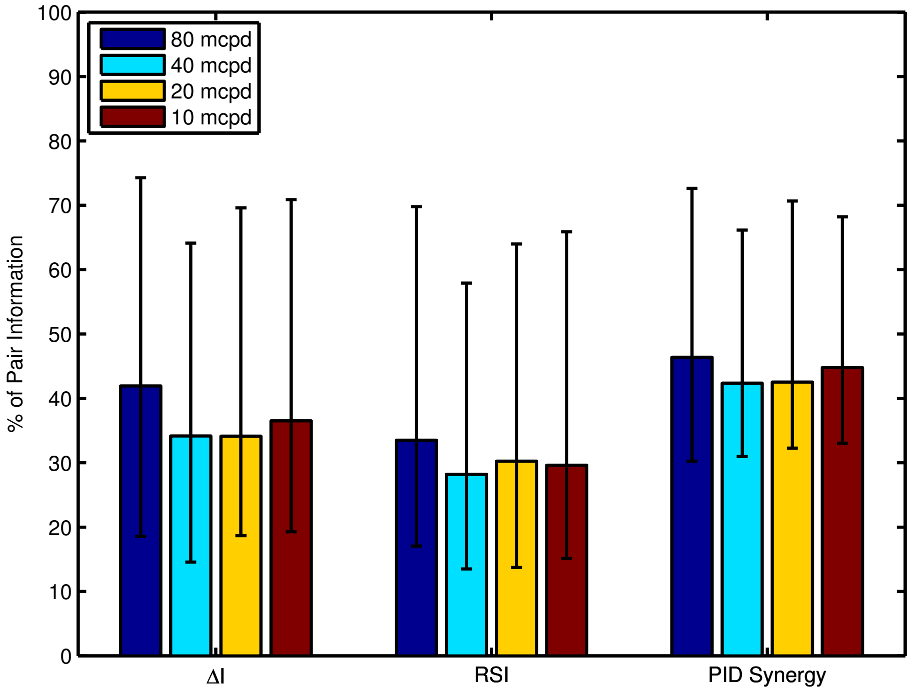

Figure 3.7: ΔI, RSI, and PID synergy as a percentage of pair information. Bar height represents the median taken first over all pairs within each retina and then between retinas. Error bars are IQR. mcpd = thousandths of a cycle per degree, e.g. 80 mcpd = 0.08 cpd.

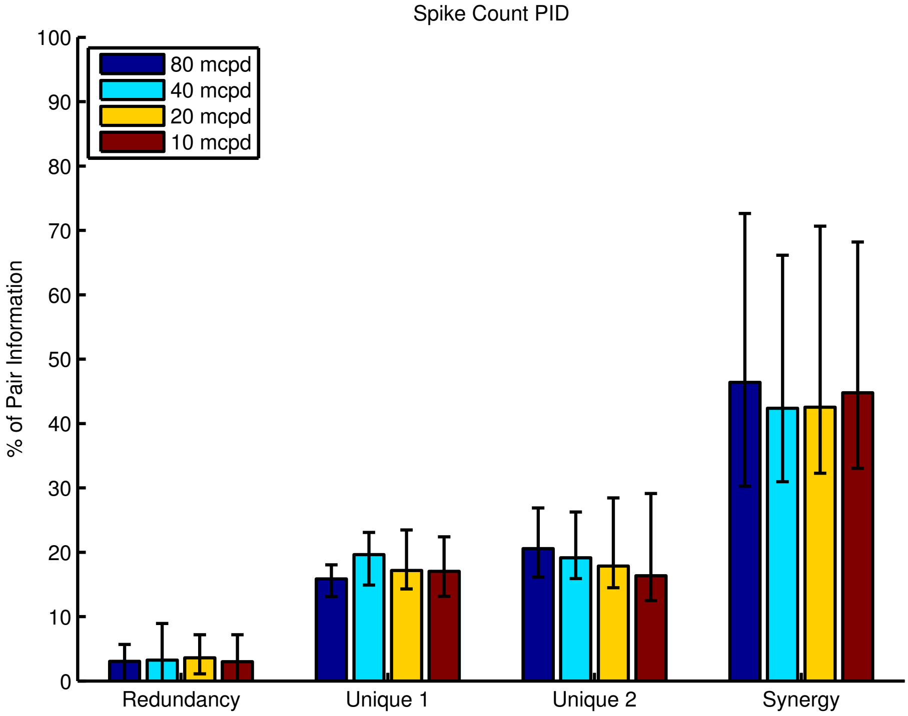

Figure 3.8: Median proportion of redundant, unique and synergistic information carried by RGC pair spike counts for the 10 retinas recorded on 60-channel MCS arrays. Unique 1 and unique 2 refer to the information carried by the first and second neuron of each pair. Bar height represents the median taken first over all pairs within each retina and then between retinas. Error bars are IQR. mcpd = thousandths of a cycle per degree, e.g. 80 mcpd = 0.08 cpd.

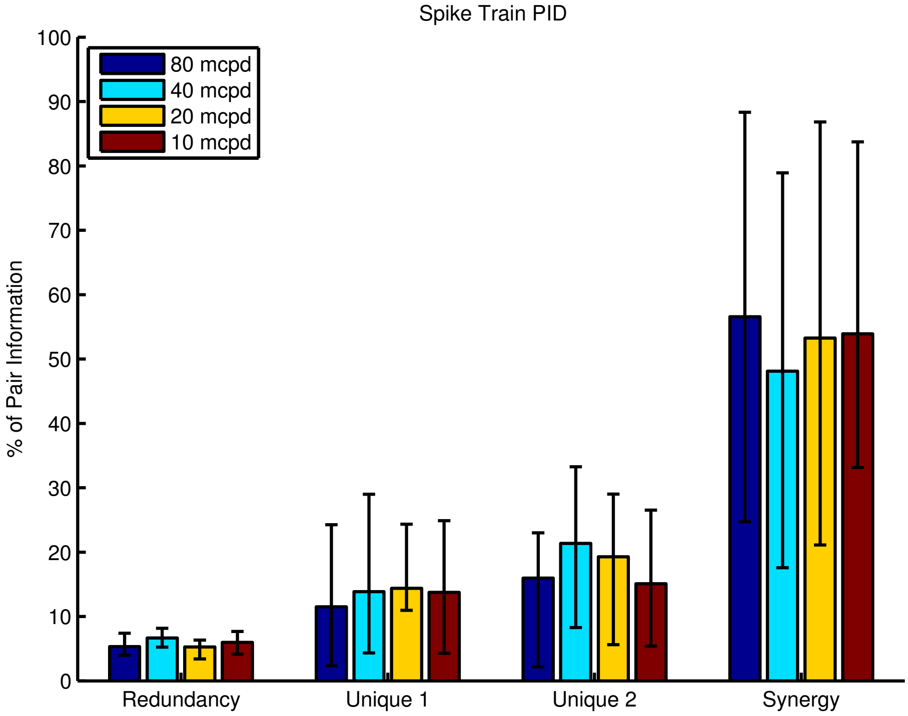

Figure 3.9: As figure 3.8, but for information contained in whole spike trains fired by RGC pairs.

immediately obvious how to incorporate it into the ΔI forumla.

Figure 3.8 shows the whole PID for the pair spike counts, including the proportions of redundant and unique information, as well as the synergistic information (which is the same as that shown in figure 3.7). The synergistic information comprised a large fraction of the total information, 42.4-46.4% on average, and there was very little redundancy. The pattern was similar regardless of spatial frequency. Figure 3.9 shows the results for the spike train PID. The pattern was similar, with synergy taking up 48.1-56.6% of the total information, although these results should be treated with caution (see Appendix A). For the spike counts, shuffling the data—either by shifting responses of one cell of a pair to the same stimulus by one trial or completely randomising the responses to each stimulus—had almost no effect on either the measured pair information values or pattern of synergy and redundancy.

3.3.2 *Spike Count Outperforms Spike Latency and Rank Order Code*

Using my data, GP compared three coding strategies by using Bayesian classification to decode the phase of the flashed grating at each spatial frequency. Figure 3.10 shows the performance of each code as a function of spatial frequency. At almost all frequencies, spike count was the best performing of the three codes, with ROC performing second best for high and low spatial frequencies and spike latency outperforming ROC at medium spatial frequencies. To examine the performance of each code as a function of time and population sizes, GP reran the Bayesian classifier for the 0.04 cpd gratings, separately varying the length of time after the stimulus over which the response is computed and the number of neurons included in the population. Changing the number of neurons did not change the pattern of results for each code at this spatial frequency (figure 3.11). When the length of the window used to define the response was varied, spike count performed the best at all time windows considered, while ROC performed second best initially but was overtaken by first spike latency with a time window between 200 and 250 ms (figure 3.12).

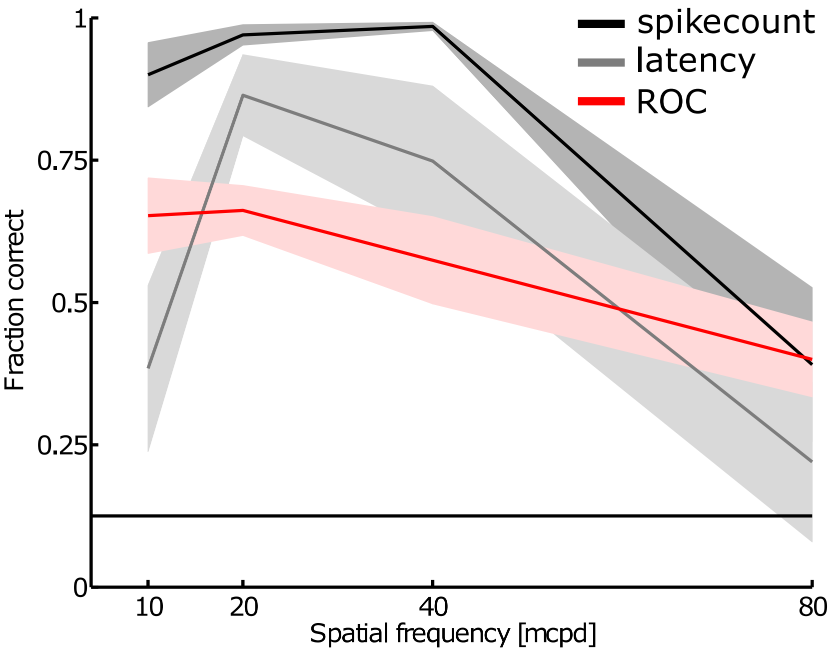

Figure 3.10: Bayesian decoder performance as a function of spatial frequency for each of spike count (black), first spike latency (grey) and ROC (red). Figure produced by GP.

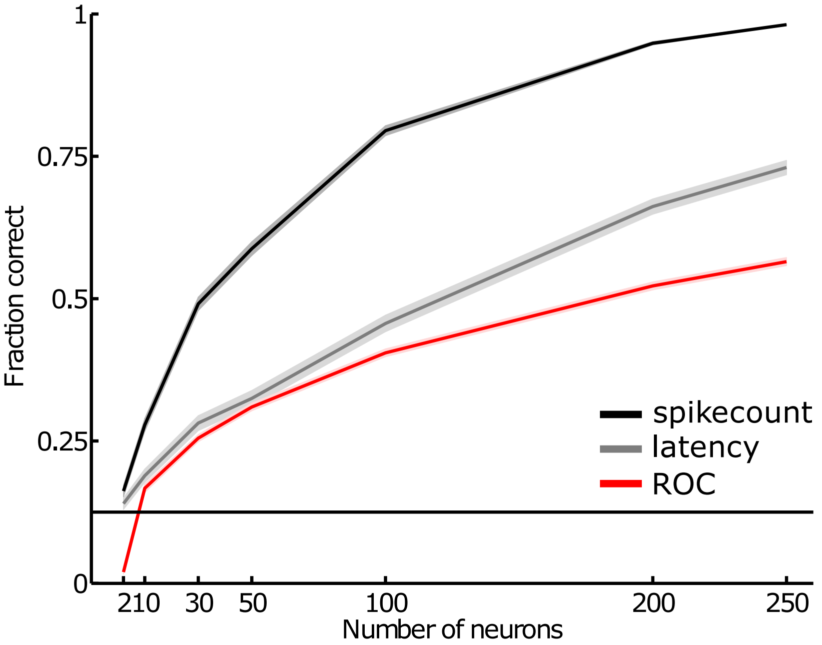

Figure 3.11: Bayesian decoder performance for the 0.04 cpd gratings as a function of the number of neurons used in the decoder for each of spike count (black), first spike latency (grey) and ROC (red). Figure produced by GP.

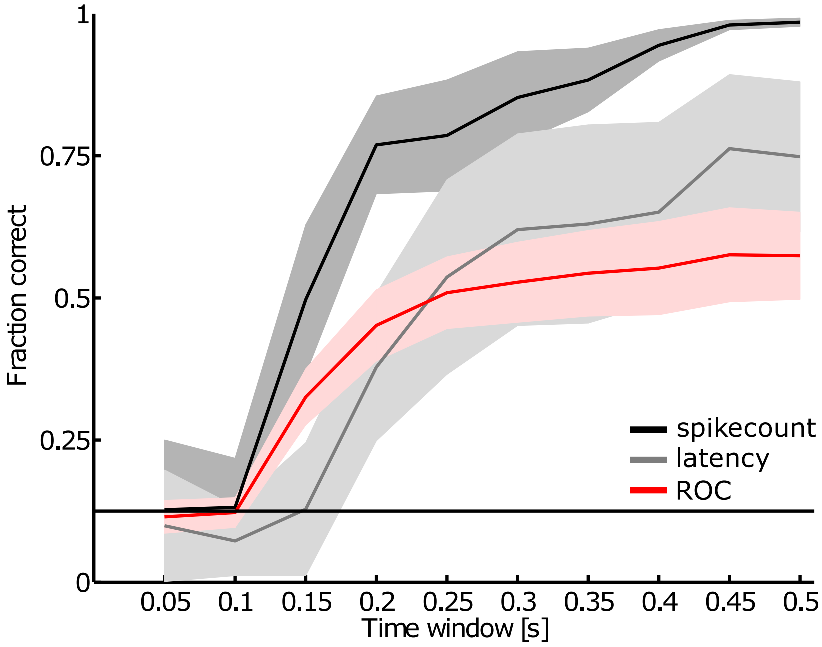

Figure 3.12: Bayesian decoder performance for the 0.04 cpd gratings as a function of the length of the time window used to define the response for each of spike count (black), first spike latency (grey) and ROC (red). Figure produced by GP.

3.3.3 *High-Density MEA Recordings*

To investigate how these results hold up in a larger RGC population, these experiments were replicated using the high-density APS MEA and a high-resolution projector (see section 2.2.2). GH recorded responses from two retinas, aged P39 and P52, on the APS MEA, from which GP selected 764 and 649 responsive RGCs, respectively, on the basis of their responses to full-field flashes and the quality of their receptive fields as recovered from reverse correlation of their responses to a white-noise stimulus.

Using these data, I analysed the proportion of redundant, unique and synergistic information using PID. For the P39 retina (figure 3.13), there were noticeable differences compared to the average pattern seen in retinas recorded using MCS arrays (figure 3.8). The first thing to note was that there was more information in RGC pairs on average—0.32-0.88 bits in the spike counts and 0.54-0.99 bits in the spike trains—and there was a much higher effect of spatial frequency, with information being highest for low spatial frequncies. There was still considerable synergy in the pair responses, but for the spike count the percentage was somewhat lower (32.5-37.9%), while amount in the spike trains (46.7-64.6%) was similar to that seen in the MCS recordings. Again, the PID was insensitive to shuffling of the data. There was also a greater discrepancy between the PID synergy and each of ΔI and RSI (figure 3.15), with the latter two being lower on average.

The pattern for the P52 retina was similar to that for the P39 retina, with the most noticeable differences being much lower pair information for the highest spatial frequency and an even smaller percentage of synergy for both spike counts and spike trains (figure 3.14). RGC pairs in this retina carried on average 0.26-1.08 bits of information in their spike counts and 0.62-1.33 bits in their spike trains. Synergy represented 25.7-27.0% of the spike count information and 20.7-31.8% of the spike train information. This pattern was unaffected by shuffling. Once again, there was considerable discrepancy between PID synergy and each of ΔI and RSI (figure 3.16), with the latter two being much lower.

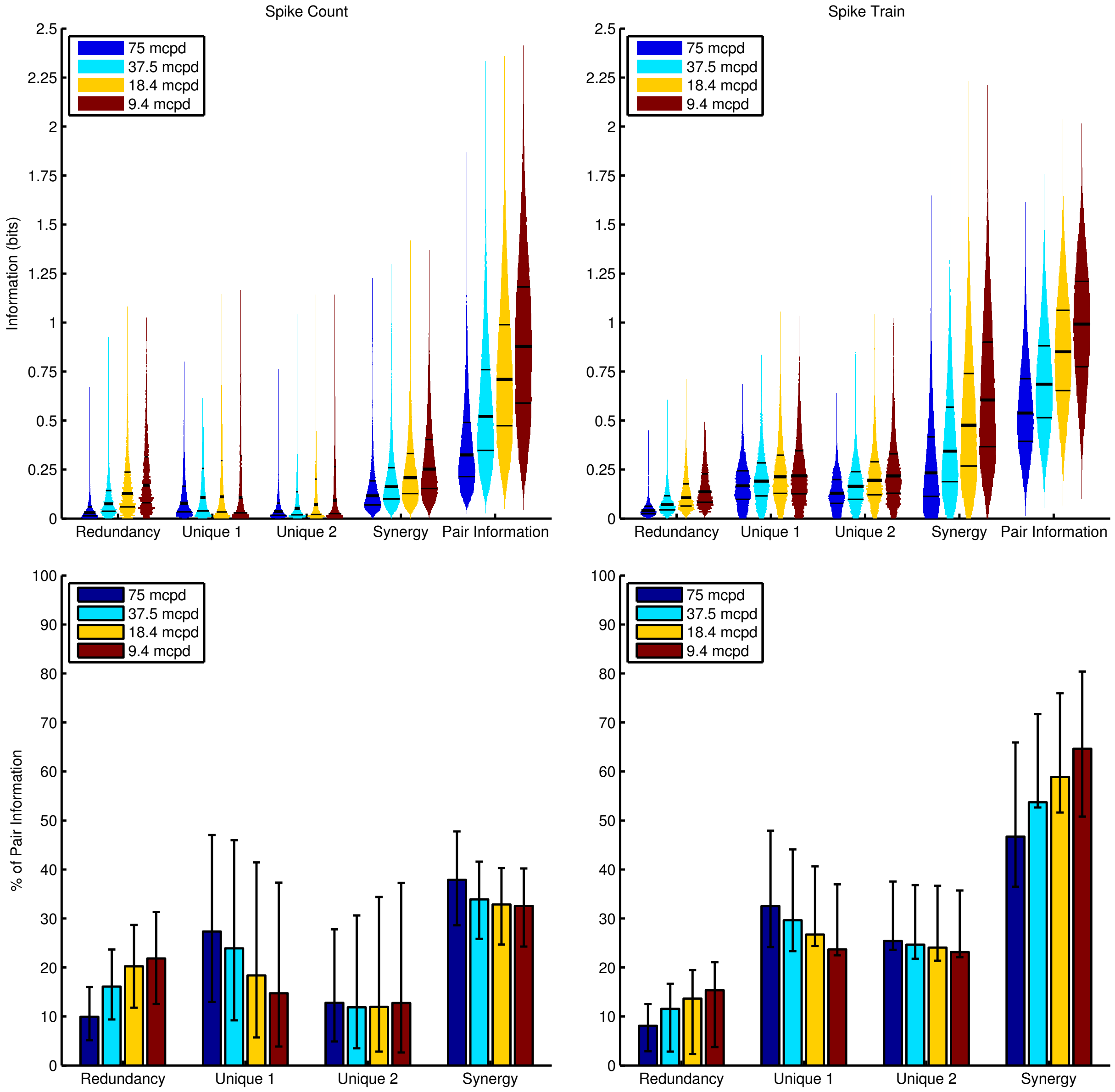

Figure 3.13: Top row: violin plots of redundant, unique, synergistic, and total information in RGC pair spike counts (left) and spike trains (right) for the P39 retina recorded on the APS. Thick black bars indicate the median and thin black bars the upper and lower quartiles. Thickness of the violin at each height represents the observed frequency of the corresponding information value. Bottom row: redundancy, unique information, and synergy as a percentage of pair information in spike counts (left) and spike trains (right) in the P39 retina, for comparison with figures 3.8 and 3.9. Bar height represents the median for all recorded RGC pairs and error bars IQR. mcpd = thousandths of a cycle per degree, e.g. 80 mcpd = 0.08 cpd.

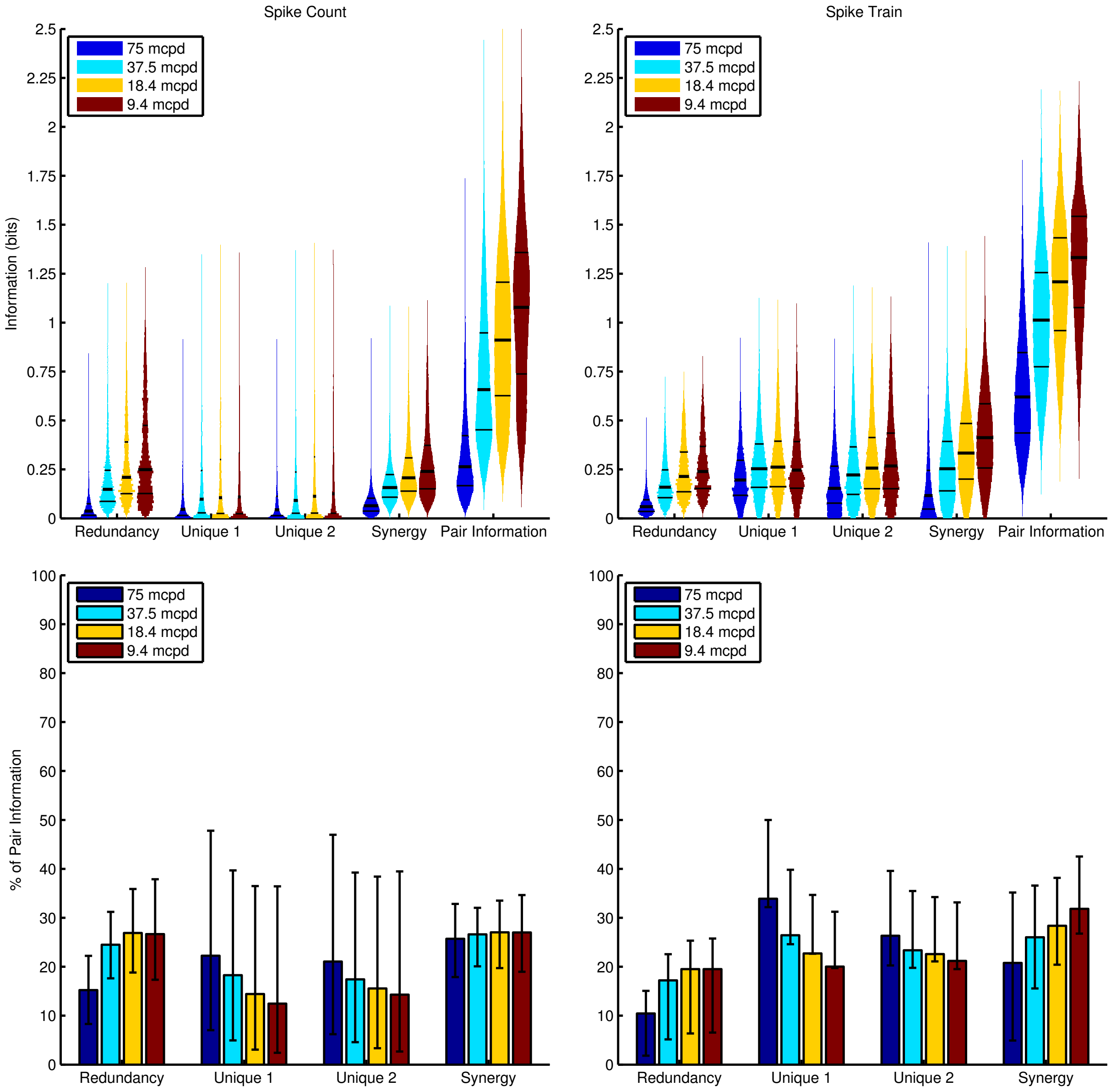

Figure 3.14: Top row: violin plots of redundant, unique, synergistic, and total information in RGC pair spike counts (left) and spike trains (right) for the P52 retina recorded on the APS. Thick black bars indicate the median and thin black bars the upper and lower quartiles. Bottom row: redundancy, unique information, and synergy as a percentage of pair information in spike counts (left) and spike trains (right) in the P52 retina, for comparison with figures 3.8 and 3.9. Bar height represents the median and error bars IQR. mcpd = thousandths of a cycle per degree, e.g. 80 mcpd = 0.08 cpd.

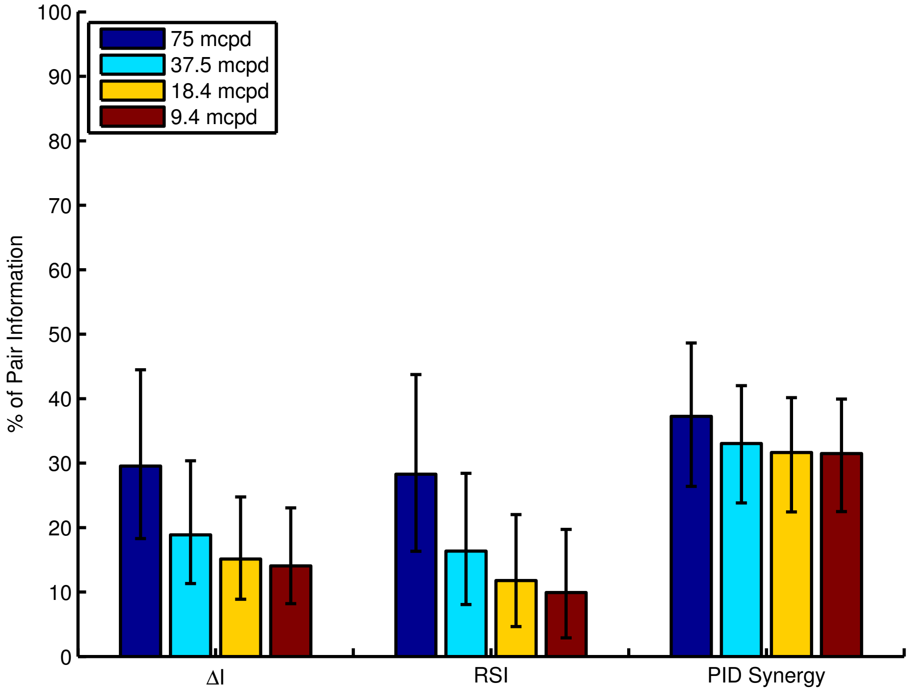

Figure 3.15: ΔI, RSI, and PID synergy as a percentage of pair information for the P39 retina. Bar height represents the median for all recorded RGC pairs in this retina and error bars are IQR. mcpd = thousandths of a cycle per degree, e.g. 80 mcpd = 0.08 cpd.

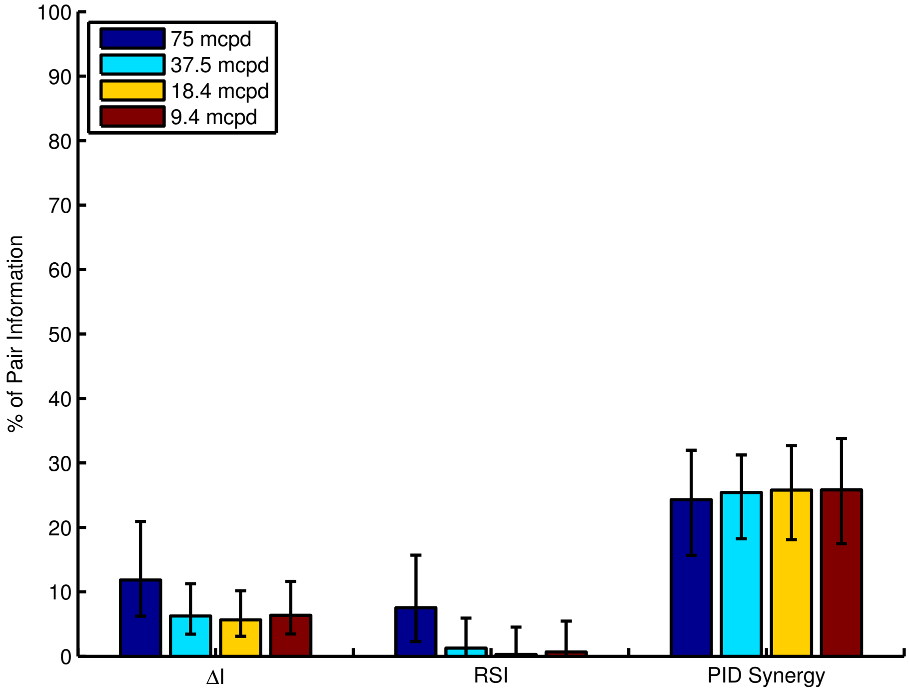

Figure 3.16: ΔI, RSI, and PID synergy as a percentage of pair information for the P52 retina. Bar height represents the median for all recorded RGC pairs in this retina and error bars are IQR. mcpd = thousandths of a cycle per degree, e.g. 80 mcpd = 0.08 cpd.

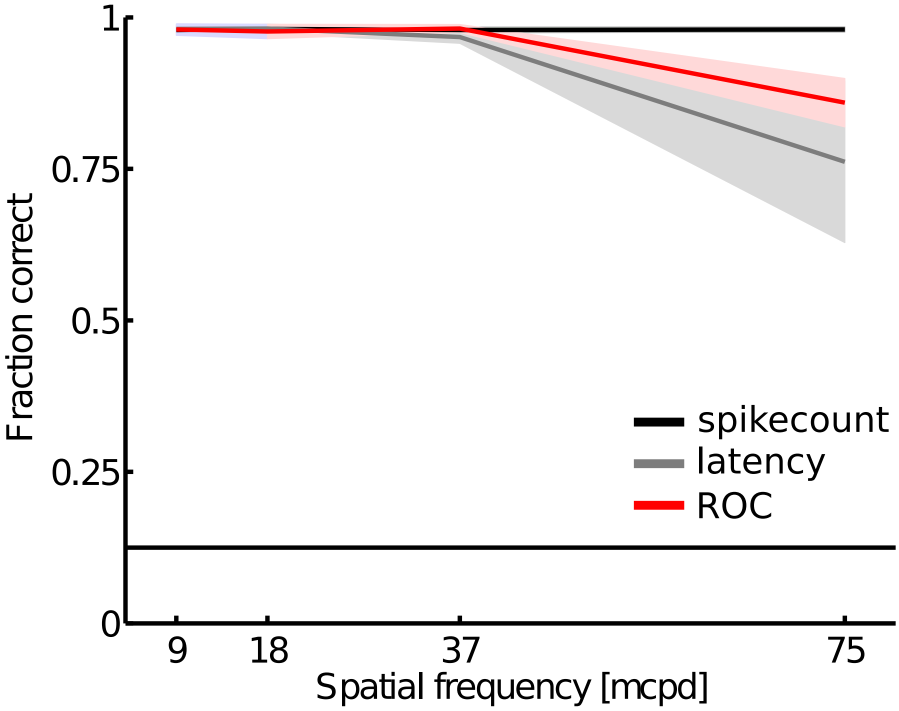

Figure 3.17: Bayesian decoder performance as a function of spatial frequency for each of spike count (black), first spike latency (grey) and ROC (red) in the P39 retina. Figure produced by GP.

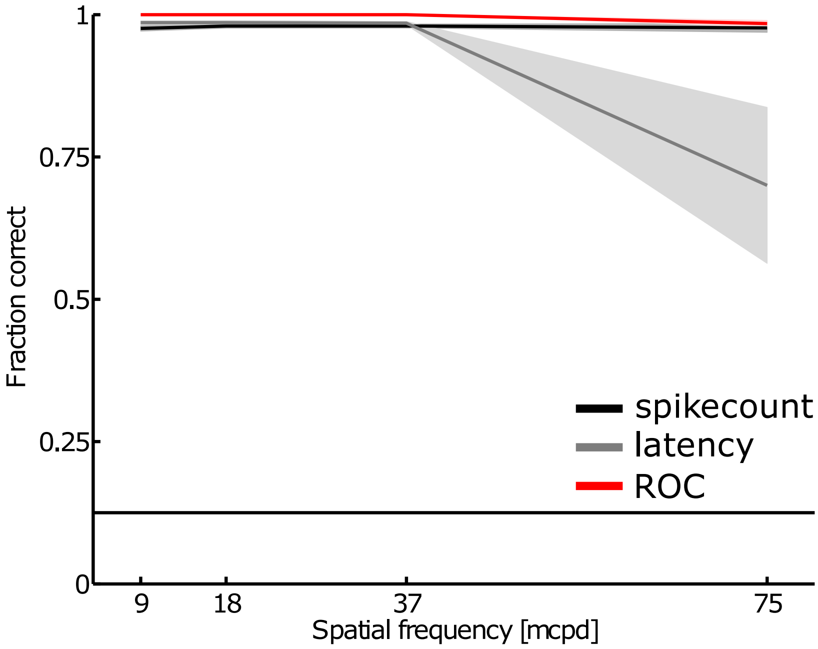

Figure 3.18: Bayesian decoder performance as a function of spatial frequency for each of spike count (black), first spike latency (grey) and ROC (red) in the P52 retina. Figure produced by GP.

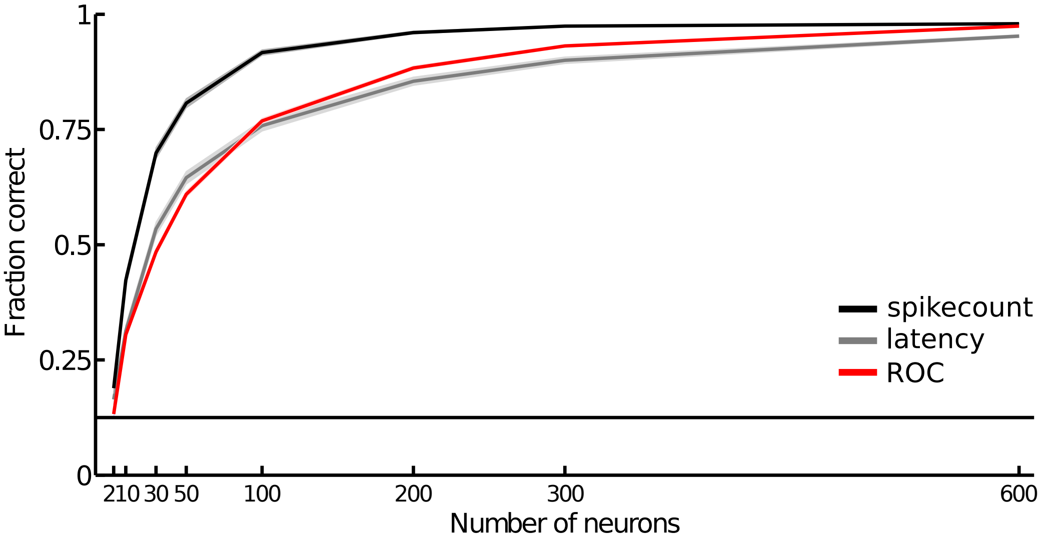

Figure 3.19: Bayesian decoder performance for the 0.037 cpd gratings as a function of the number of neurons used in the decoder for each of spike count (black), first spike latency (grey) and ROC (red) in the P39 retina. Figure produced by GP.

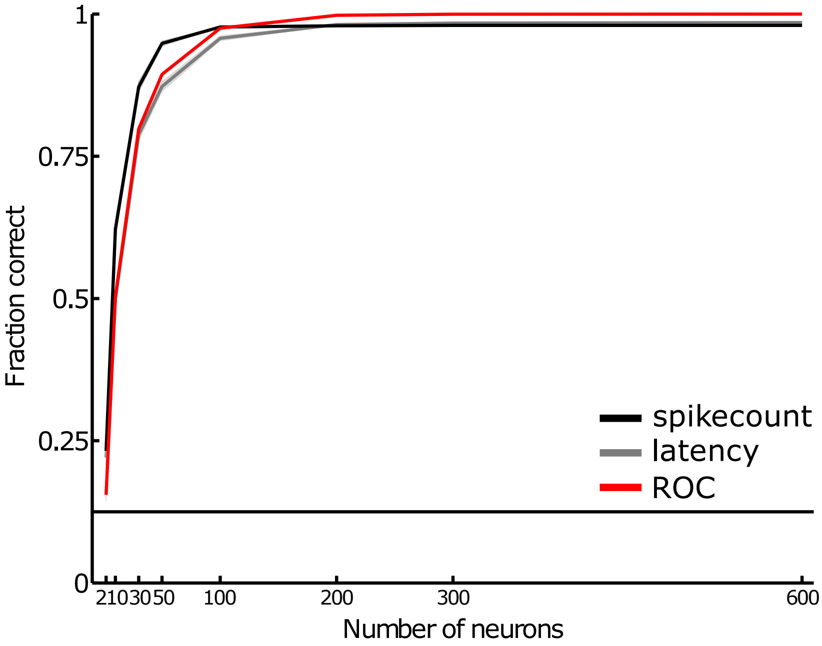

Figure 3.20: Bayesian decoder performance for the 0.037 cpd gratings as a function of the number of neurons used in the decoder for each of spike count (black), first spike latency (grey) and ROC (red) in the P52 retina. Figure produced by GP.

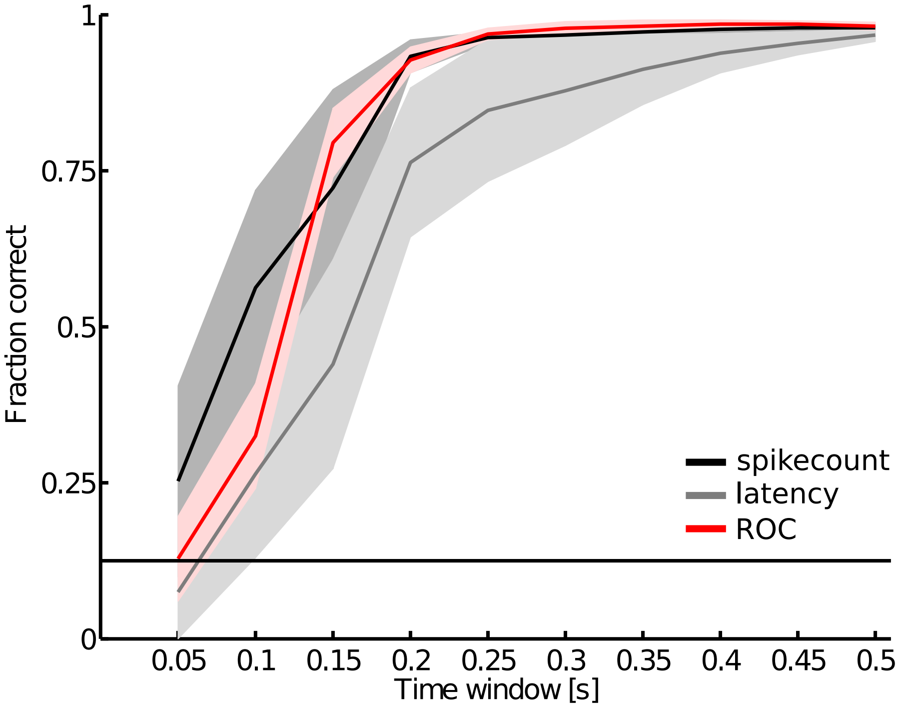

Figure 3.21: Bayesian decoder performance for the 0.037 cpd gratings as a function of the length of the time window used to define the response for each of spike count (black), first spike latency (grey) and ROC (red) in the P39 retina. Figure produced by GP.

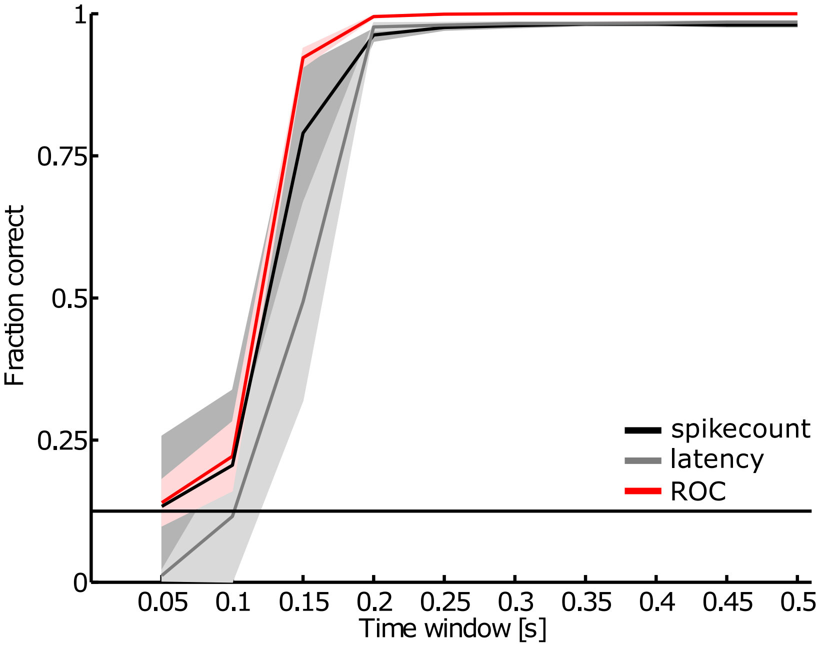

Figure 3.22: Bayesian decoder performance for the 0.037 cpd gratings as a function of the length of the time window used to define the response for each of spike count (black), first spike latency (grey) and ROC (red) in the P52 retina. Figure produced by GP.

3.4 Discussion

3.4.1 *Rank Order Coding in Large RGC Populations*

My results show that, at least for flashed grating stimuli, a considerable proportion (at least 20%, sometimes more than 50%) of the information carried by pairs of RGCs is synergistic. This is certainly true for pair spike counts and likely true for spike train pairs as well (but see Appendix A for caveats regarding the method used to estimate synergy in spike trains). However, according to GP's analysis of my data, a spike count code that treats neurons as independent outperforms rank order coding, which compares responses within a population of RGCs. This seems counter-intuitive.

One possible explanation is inadequate sampling of the RGC population by the 60-channel MCS array. GP also compared spike count, first spike latency and ROC using Bayesian classification on the two retinas recorded on the APS. His results are shown in figures 3.17 and 3.18. In the P39 retina, ROC outperformed the first spike latency and was as least as good as spike count for all but the highest spatial frequencies. In the P52 retina the difference was even more dramatic: ROC was the best performing code at all spatial frequencies. This finding is much more compatible with the degree of pairwise synergy revealed by the PID analysis. Further, it appears that the power of the ROC is revealed only when the sample of RGCs is sufficiently large, as is possible on high-density MEA systems such as the APS, but not on traditional low-density MEAs.

GP also analysed Bayesian decoder performance in these datasets as a function of either the size of the neural population used for decoding or the length of time window over which the response was considered. For the P39 retina, the pattern of performance versus number of neurons was reversed from that shown in the MCS data. With low numbers (<100) of neurons, latency coding outperforms ROC, then as the population size increases ROC overtakes latency (figure 3.19). For the P52 retina, ROC was as good as or better than latency at all population sizes and overtook spike count at around 100 neurons (figure 3.20). The change in performance with varying time windows in these retinas is more interesting. In both cases, the ROC reached its maximum performance faster than latency coding and at least as fast as spike count coding (figures 3.21 and 3.22). In particular, ROC reached it maximum performance between 150-250ms, which is consistent with its theoretical origins in the context of rapid image classification (Thorpe et al. 2001).

3.4.2 *Do RGCs Act as Independent Encoders?*

Using the PID, I found a considerable amount of synergy in the responses of RGC pairs: around 45% on average for pair spike counts among retinas recorded on 60-channel MCS arrays and between 20% and 30% on average for the two retinas recorded using the APS. Another measure of synergy, RSI, gave lower estimates of synergy, but as noted in section 3.1.2, this measure is confounded by simultaneous redundancy and synergy and the PID also revealed non-zero redundancy, so we would expect synergy as measured by RSI to lower in this case.

By contrast, Nirenberg et al. (2001) argued that RGCs act largely as independent encoders. They concluded this not by measuring synergy but by calculating a term they call ΔI, which measures the difference in information calculated using the full joint response distribution of RGC pairs versus assuming statistical independence. As such, it answers the question of whether correlations are important for decoding (Latham and Nirenberg 2005), whereas synergy measures ask whether there is information available in the population response that is not available in the individual responses. Nirenberg et al. (2001) found that ΔI was rarely more than 10% of the total information, whereas among my datasets the median ΔI was anywhere from just under 10% to more than 40%. This may reflect differences in both the particular stimuli used—square-wave gratings here versus uniform grey fields and natural scenes in Nirenberg et al. (2001)—and the different coding strategies considered: information in coarse spike counts using histogram methods versus information in discretised spike trains calculated using the direct method of Strong et al. (1998). In any case, here both ΔI and PID synergy are large fractions of the total pair information, so correlations are important for decoding and RGC pairs encode information about these stimuli synergistically in their spike counts. That does not imply that said synergy arises due to correlations, however. In fact, shuffling the data to destroy the correlation structure had almost no effect on the PID, suggesting that the synergistic information arises by means other than pairwise correlations. (Note that this result is not incompatible with large ΔI: as Nirenberg and Latham (2003) and Latham and Nirenberg (2005) note, the change in information due to shuffling can be zero when ΔI is non-zero and vice-versa.)

Other studies have also investigated the issue of (non)independence of RGC encoding, both in terms of the importance of correlations and the amount of synergy. In the former case, for example, Schwartz et al. (2012a) found that the difference in performance between a Bayesian decoder that uses the full response correlation structure (mixture decoders, in their terminology) versus ones that assume statistical independence (independent decoders) depends on the size of the population. For RGC pairs, in accordance with the results of Nirenberg et al. (2001), there was almost no difference, but for large populations mixture decoders greatly outperformed independent decoders. Moreover, this was true for a variety of different coding strategies. More in line with my own data, Pillow et al. (2008) found that including pairwise correlations in a generalised linear model of retinal encoding and using this to decode responses in a Bayesian framework allowed them to extract 20% more information than treating RGCs as independent. Schneidman et al. (2011) calculated the amount of synergy carried by different symbols in a neural code using RSI and found that synchronous spikes were generally redundant but the combination of spiking and silence was synergistic. If synchronous spikes are rare, then on average this would make pairs of spike trains synergistic, in accordance with the results presented here, but the proportion of synergy they observed was much lower than that seen here. However, as discussed above, simultaneous redundancy and synergy may confound RSI (see in particular figures 3.15 and 3.16), so Schneidman et al. (2011) may have underestimated the amount of synergy. Moreover, there were also differences in the stimuli used (gratings versus natural scenes and white noise) and coding strategies considered: where they used discretised spike trains, I used either coarse spike counts or continuous (up to measurement precision) spike trains.

In summary, the question of whether RGCs act as independent encoders or not is a complex one. Attempts to find a definitive answer are hindered by the variety of recording methods, stimuli, and analyses employed in this and other studies. In terms of stimuli, Nirenberg et al. (2001) used natural movies and spatially homogeneous temporal white noise, Pillow et al. (2008) used spatiotemporal binary white noise, Schneidman et al.

(2011) used spatiotemporal binary white noise and natural movies, Schwartz et al. (2012a) used black-and-white shapes, and here I used flashed square-wave gratings. As discussed below, different stimuli might lend themselves more or less well to synergistic coding. Different ways of interpreting retinal spike trains may lead to different conclusions about the amount of synergy and the importance of correlations. For example, Schwartz et al. (2012a) found that mixture decoders outperformed independent decoders for large RGC populations for all codes they tested, but the size of the improvement varied considerably between different codes. Similarly, here I found there was generally more synergy in whole spike trains than coarse spike counts (but see Appendix A for caveats regarding the calculated PID values here). The spatial sampling of the recorded RGCs may also affect the results: Nirenberg et al. (2001), Pillow et al. (2008), and Schwartz et al. (2012a) all sampled RGCs from small areas and thus with short distances between their receptive fields, where as my recordings and those on APS include RGCs from much larger retinal areas. Finally, there may be species differences: I used mice, as did Nirenberg et al. (2001), whereas Pillow et al. (2008) used primate retinas, Schwartz et al. (2012a) used salamander retinas, and Schneidman et al. (2011) used salamander and guinea pig retinas (although the latter found remarkably similar results across the two species they considered).

3.4.3 *Future Work*

As described above, a number of questions arise from my data. First, rank order coding performs very well in the retina, at least if the RGC population is adequately sampled, but how is this code generated and is the information accessible to the brain? Secondly, although I noted considerable synergy in RGC responses to flashed gratings, this synergy was not affected by shuffling of responses to destroy the correlation structure, so how does it arise?

Cell Types. There are many types of RGCs in the mammalian retina (Masland 2001a), each encoding distinct features of the visual scene (Azeredo da Silveira and Roska 2011). In the data presented here, neither I nor anyone else involved in these experiments has attempted any detailed classification of the recorded RGCs into defined subtypes. In their studies of relative latency coding in the salamander, Gollisch and Meister (2008)

S	ON	OFF	P(S,ON,OFF)
0	0	1	1/3
1	1	1	1/3
2	1	0	1/3

Table 3.2: Joint probability distribution for simple ON and OFF cells (as described in the text and figure 3.23) responding to a black (0), split black and white (1) or white (2) field.

and Gütig et al. (2013) focussed on the responses of a single class of RGC: the fast-OFF cell. The data presented here demonstrate the effectiveness of a population-wide relative lantency code, the ROC, in large, heterogeneous RGC populations. To what extent does cell type interact with this code? This is important, as different cell types are known to project to distinct areas of higher visual centres. A classic example is the parvo-, magno- and koniocellular layers of the primate lateral geniculate nucleus (Clay Reid 1999; Kandel et al. 2000). More recently, different types of direction selective RGCs have been shown to project to either the superior colliculus or the medial terminal nucleus of the accessory optic system (Gauvain and Murphy 2015). If the ROC only functions in a heterogeneous RGC population, it will be destroyed by such segregation of RGC efferents and the wealth of information it carries will never leave the retina. (However, there is emerging evidence that certain LGN cells receive input from multiple distinct RGC cell types (Roska 2014).) Thus, an important subject for future work will be to investigate how well the ROC functions within RGCs of the same type versus between different types.

Different RGC types may also play a role in synergistic coding in the retina. As a toy example, imagine a situation in which a grey mask might be followed with equal probability by a black full field stimulus, a white field or a black and white split field. The task is to determine which stimulus was presented from the responses of two RGCs whose receptive field centre is located in the middle of the field. These RGCs maybe of two types: an ON type that fires if and only if there is a light increment in any part of its receptive field and an OFF type that fires if and only if there is a light decrement in any part of its receptive field. Figure 3.23 illustrates the circuitry involved in this example and table 3.2 details the joint probability distributions of the stimulus and the two types of response.

If one has two cells of the same type, we gain 0.9183 bits of information about the stimulus from the responses. For example, with two ON cells, one can distinguish the black field

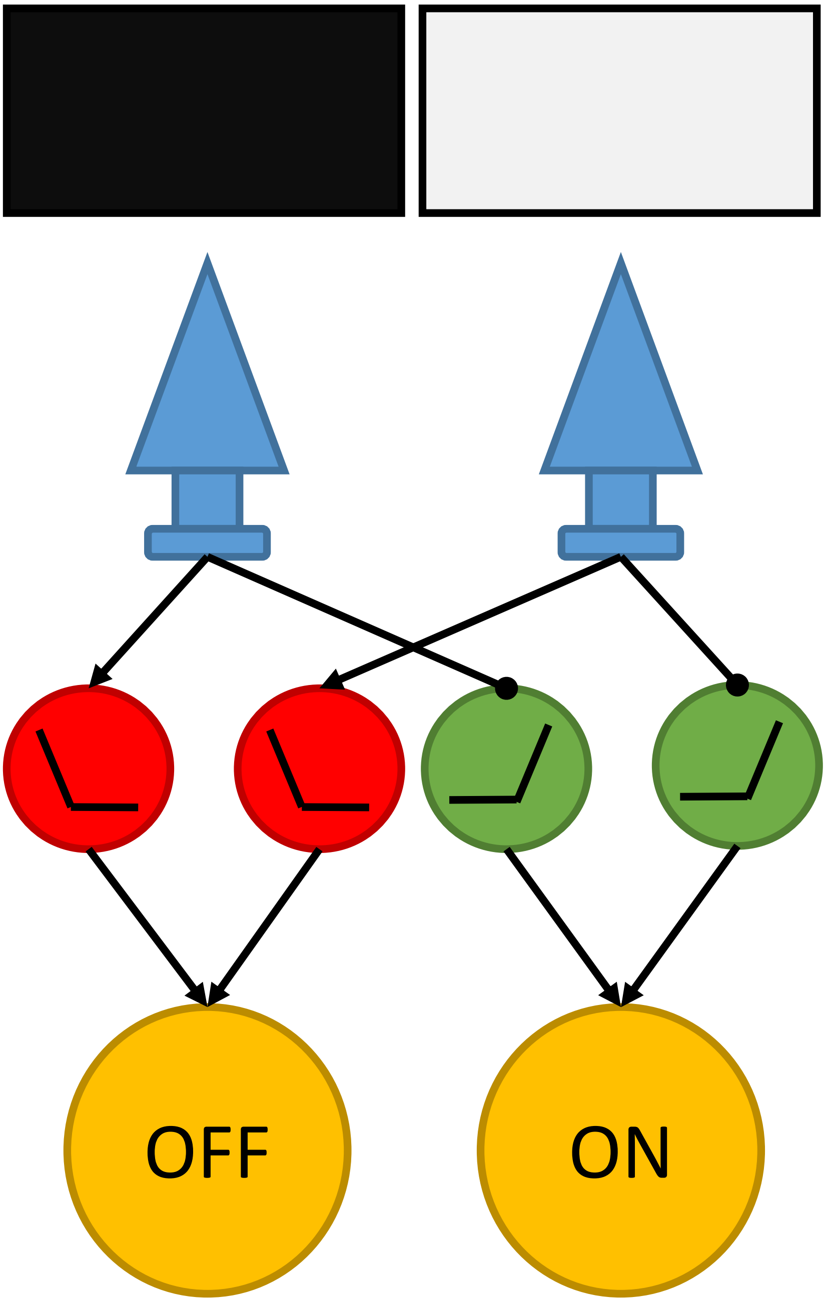

Figure 3.23: Simple retinal circuit diagram with two photoreceptors (blue), two ON bipolar cells (green), two OFF bipolar cells (red), and an ON and an OFF RGC (yellow). Pointed arrows denote sign-conserving synapses and rounded arrows denote sign-inverting synapses (recall that photoreceptors hyperpolarise in response to a light increment). Lines inside bipolar cells depict the shape of the rectifying nonlinearity at the bipolar cell to ganglion cell synapse. In this example, the left photoreceptor receives a light decrement and the right photoreceptor a light increment, so the left most and right most bipolar cells depolarise and the inner bipolar cells do nothing. The RGCs fire if they receive input from either bipolar cell, so both RGCs fire.

from the split field or the white field, but not the split field and the white field from each other. According to the PID, all of the information provided by the two cells is redundant. However, if one has an ON and an OFF cell, one can distinguish all three stimuli and thus the RGCs provide the full 1.585 bits of information. Computing the PID reveals that 0.585 bits of the information is redundant, each cell provides 0.333 bits of unique information and the final 0.333 bits is synergistic. However, ΔI in this system is zero, so absolutely no information is lost by ignoring correlations. A full derivation of these results is given in Appendix B.

The above example, though incredibly simplistic compared to the full suite of retinal processing, demonstrates how different RGC types may give rise to synergy by providing complementary information about a stimulus, without requiring strong pairwise correlations. As part of the RGC selection for the APS data, GH calculated a bias index for each cell (Carcieri et al. 2003) that gives the relative strength of that cell's ON and OFF responses. Using this information, I classified each cell as ON (bias index >0.3), OFF (bias index <-0.3) or ON-OFF (otherwise) and thus each pair into one of six categories (ON/ON, ON/ON-OFF, ON/OFF, ON-OFF/ON-OFF, ON-OFF/OFF, OFF/OFF). However, I did not see systematic difference in the proportion of synergy between the different pair categories (data not shown), but this is an extremely simple classification scheme. A better approach would be to compare synergy in pairs of RGCs that have been classified more precisely, e.g. using a wider variety of stimuli for functional classification (e.g. Carcieri et al. (2003) and Zampaglione et al. (2014)), genetic labelling, or morphological analysis of recorded cells using fluorescent proteins or dyes (e.g. Li et al. (2015)).

Other Stimulus Classes. The type of stimulus and the task that is asked of the retina can also affect the degree of synergy present. In the simple example system described above, imagine there are now four equiprobable stimuli: a black field, a white field, and two mirror-image black and white split fields. Further suppose that one has two ON (or two OFF) cells with receptive fields on either side of the split. If the task is to tell whether the stimulus is a split field or a full field, then the solution is simple: it is a split field if one neuron or the other fires, but not both. If neither or both neurons fire, it is a full field.

S	ON	OFF	T	P(S,ON,OFF)
0	0	0	0	$1/4$
1	0	1	1	$1/4$
2	1	0	1	$1/4$
3	1	1	0	$1/4$

Table 3.3: Joint probability distribution for two simple ON cells responding to a black full field (0), split field with white over the first cell's receptive field (1), split field with white over the second cell's receptive field (2), or a white full field (2). The task variable, T, represents whether the stimulus is a full (0) or split (1) field.

This is equivalent to a XOR gate in digital logic: as described in Timme et al. (2014), each neuron individually gives no information about the stimulus, but the pair gives one bit of synergistic information.

Now consider a direction selective cell that fires two spikes in response to a bar moving in its preferred direction (PD) or one spike to bars moving perpendicularly to its PD, but does not fire when a bar moves opposite to its PD. Suppose that one has two such cells whose PDs are e.g. northerly and easterly, and one wants to distinguish bars moving in the four cardinal compass directions with equal probability. According to PID, the two neurons provide 1 bit of redundant information (is the bar moving latitudinally or longitudinally?) and each neuron provides 0.5 bits of unique information: once one knows the axis, one cell says whether the bar is northerly or southerly and the other whether it is moving easterly or westerly. None of the information is synergistic. A full derivation of these results is given in Appendix B.

The above examples demonstrate how the proportion of synergy can vary considerably depending on the stimulus and the task: from 100% synergy in the second version of the split-field task to none whatsoever in the direction selectivity task. Though simplistic, these examples are inspired by real features of retinal processing. Thus it is not a stretch to imagine that the proportion of synergy present in retinal responses also varies with the stimulus and the task. The experiments presented here only used one set of stimuli (flashed gratings of varying phase), so it is impossible to conclude anything from these results about how much synergy is present in retinal responses in general. Further studies should investigate this using a wider variety of stimuli, in particular natural scenes.

3.4.4 *Conclusion*

I have shown that a considerable proportion of the information available in RGC pair responses is synergistic, although the precise amount is uncertain and how this synergy arises remains to be seen. Moreover, although my data suggested that rank-order coding does not work terribly well in the retina, further analysis showed that in fact it does perform extremely well, but this is only revealed in high-density MEA recordings that sample a significantly larger number of RGCs.

Chapter 4. Pharmacology of Degenerate Spontaneous Activity and Optogenetic Stimulation

4.1 Introduction

As discussed in section 1.2, retinitis pigmentosa (RP) is a retinal dystrophy characterised by progressive photoreceptor death, starting with the rods, causing night-blindess and a loss of peripheral vision, followed eventually by total blindness as the cones start to degenerate as well (Berson 1993; Hartong et al. 2006; Heckenlively et al. 1988). It has a global prevalence of approximately one in 4000 (Hartong et al. 2006). At present, the only clinically available treatment capable of restoring vision in RP (as opposed to slowing or halting progression of visual loss) is retinal prosthesis. Current retinal prostheses use implanted electrodes in combination with photovoltaics (Mathieson et al. 2012; Stingl et al. 2013) or an external light sensor (Dorn et al. 2013) to deliver patterned electrical stimulation to the retina and evoke a visual percept (Margalit et al. 2002), but thus far such devices have only managed to restore crude vision (Dorn et al. 2013; Stingl et al. 2013). Possible reasons for this include limited resolution due to the low number of electrodes (presently 60-1500 (Dorn et al. 2013; Stingl et al. 2013)), lack of control over the spatial spread of charge, lack of cell-type specificity, and the ability to provide excitatory but not inhibitory stimulation (Barrett et al. 2014). Optogenetics, in which neurons are engineered to express light-sensitive ion channels to enable optical control of membrane potential (Bernstein and Boyden 2011; Boyden et al. 2005; Deisseroth 2011; Fenno et al. 2011), may be able to overcome many of these limitations of electrical prostheses. Thus the past decade has seen considerable progress in the development of optogenetic retinal prostheses, in which surviving inner retinal neurons are made light sensitive to restore vision (for review, see section 1.3.2, as well as Barrett et al. (2014), Busskamp et al. (2012), Busskamp and Roska (2011), Cepko (2012), and Sahel and Roska (2013)).

However, an often overlooked problem of retinal degenerations in retinal prosthetic research is the extensive remodelling of the inner retina that follows photoreceptor death (Marc et al. 2003; Jones and Marc 2005; Marc et al. 2007), which results in slow local field potential (LFP) oscillations in the inner retina and rhythmic bursting of RGCs (see sections 1.2.3 and 1.2.4). This pathological hyperactivity is observed in numerous animal models of photoreceptor dystrophy, including the *rd1* mouse (Stasheff 2008), the *rd10* mouse (Stasheff et al. 2011; Goo et al. 2011), the CRX mouse (Soto et al. 2012; Maccione et al. 2014), and the P23H rat (Sekirnjak et al. 2009). In the *rd1* mouse, lack of photoreceptor input results in the AII amacrine cells becoming tonically hyperpolarised, revealing intrinsic, low-frequency (~10Hz) oscillations in these cells (Choi et al. 2014) that then spread via gap junctions through the AII-ON bipolar cell network (Menzler and Zeck 2011; Trenholm et al. 2012), resulting in RGC bursting. Similar oscillations are observed in wild-type mouse after blocking photoreceptor to bipolar cell synapses (Trenholm et al. 2012; Choi et al. 2014). Oscillations in the *rd10* mouse are slightly lower frequency than the *rd1* but are pharmacologically similar (Biswas et al. 2014), suggesting a similar underlying mechanism. In summary, low frequency oscillations and increased spontaneous RGC firing are found in numerous mouse models of photoreceptor dystrophy and appear to share are common origin.

As a result, any signal delivered prosthetically may be more difficult to distinguish against this background of higher and more bursty spontaneous firing of RGCs in the degenerate retina. Recently, Toychiev et al. (2013) demonstrated that blocking this pathological spontaneous activity with the gap junction blocker meclofenamic acid (MFA) improves the signal-to-noise ratio (SNR) of surviving photoreceptor responses and responses to electrical stimulation in the *rd10* mouse retina (Toychiev et al. 2013; Ivanova et al. 2015). Here, I set out to determine if the same principle works in other models of retinal degeneration, specifically the fast-degenerating *rd1* model, and for optogenetic stimulation. Additionally, Toychiev et al. (2013) considered only responses to full-field illumination, so I sought to investigate the effects of reducing spontaneous activity on responses to spatiotemporally patterned stimulation using a novel 256-pixel microLED (µLED) array (Grossman et al. 2010; Al-Atabany et al. 2013). Finally, I tested a number of drugs with different mechanisms of action to ascertain whether specific blockade of gap-junctions is sufficient and necessary to block these pathological oscillations or whether general reduction in spontaneous activity can achieve the same results.

4.2 Specific Methods

4.2.1 *Drugs*

I used three drugs in the experiments presented here. MFA is a gap-junction blocker (Pan et al. 2007; Veruki and Hartveit 2009) that has previously been shown to improve SNR of light and electrical responses of RGCs in dystrophic retinas (Toychiev et al. 2013; Ivanova et al. 2015). Flupirtine is a Kv7 potassium channel opener (Martire et al. 2004; Wladyka and Kunze 2006; Yeung et al. 2007) that has recently been shown to block spontaneous activity in degenerate retinas by dampening intrinsic oscillations in the AII amacrine cell (Trenholm et al. 2012; Choi et al. 2014). MFA also affects the same potassium channel (Peretz et al. 2005; Yeung et al. 2007), so I also tested a second gap-junction blocker, 18-β-glycyrrhetinic acid (18BGA) (Davidson et al. 1986; Pan et al. 2007; Sun et al. 2008; Syed et al. 2004), that to the best of my knowledge has no effect on the Kv7 channel. Both 18BGA and the closely related compound carbenoxolone have been shown to dampen *rd1* spontaneous activity (Menzler and Zeck 2011; Trenholm et al. 2012). MFA and 18βGA were purchased from Sigma-Aldrich (St Louis, USA); Flu from Abcam (Cambridge, UK). I took recordings in control conditions, once at each drug concentration (10, 20, 40 and 80μM) and again after washout. I added drugs to the perfusing aCSF, maintaining separate reservoirs for each drug concentration. I allowed 30-45 for the drug to take effect after each increase in concentration and I waited between 1 and 3 hours after applying the final drug concentration for the drug to wash out. Only one drug was used on any given retina.

4.2.2 *Quantification of Oscillations and Spontaneous Activity*

I recorded five minutes of spontaneous activity before the first stimulation recording at each drug concentration. To analyse LFP oscillations, I imported raw MC_Rack data into Matlab (The MathWorks, Natick, USA) using the FIND toolbox. I extracted roughly one minute of data (specifically 83.88 seconds, i.e the number of samples ($2^{21} = 2097152$) equal to the next integer power of two greater than one minute of recording at 25kHz) from the middle of each spontaneous activity recording to compute the power spectrum on each channel. To quantify oscillation strength, I calculated the area under the peak of the power spectrum over the full width at half maximum, then normalised the oscillation strength on each channel at each concentration by dividing by the oscillation strength in control conditions. To compare retinas, I took the median value over all channels for each retina.

To analyse spontaneous firing, I extracted spikes from each spontaneous activity recording as described in section 2.3.1. I counted all spikes fired on each channel during each recording, without sorting spikes into units. I normalised the spontaneous firing rates as a function of drug concentration and averaged within each retina exactly as for oscillation strength, except that I necessarily excluded channels on which no spikes were detected in control conditions.

4.2.3 *Optogenetic Stimulation Using MicroLED Arrays*

I presented stimuli using a custom-made, 256-pixel, Gallium Nitride microLED (µLED) array (Grossman et al. 2010; Al-Atabany et al. 2013) developed by Pleun Maskaant of the Tyndall National Institute. Stimuli were controlled using custom software I wrote in C$^\sharp$ to communicate with an mbed control interface developed by Kamyar Mehran. Light from the µLED array entered through the camera port of an Olympus IX-71 inverted microscope (Olympus, Tokyo, Japan) and was projected through a 2X objective, which I used to focus the image of the array onto the RGC layer. Each pixel covered an area of approximately 62.5µm on the retina and hence the whole array covered an area of roughly 1mm^2. Before the first recording from each retina, I positioned the array so as to cover either the central 6×6 electrodes or the set of electrodes showing the strongest electrophysiological activity. I made no attempt to block surviving photoreceptor responses. All retinas used in this chapter were from mice aged P93-175; at these ages virtually all rods are dead (Carter-Dawson et al. 1978) and the few surviving cones are morphologically degenerated and unlikely to be capable of normal light responses (Lin et al. 2009). Accordingly, in one experiment using a plain *rd1* mouse, I saw no responses to stimulation with the µLED array (data not shown). Hence I assumed all light responses seen in this chapter to be ChR2 mediated (in all cases they were too fast and transient to be mediated by melanopsin). For a more detailed discussion, see section 2.1.

4.2.4 *Stimuli*

I used three sets of stimuli in this chapter: full-field flashes with durations of 5, 10, 25, 50, 75 or 100 ms presented every 2 seconds; flashing squares of 1×1, 2×2 or 4×4 pixels presented for 100ms each; and bars of width 2 pixels moving in the 8 cardinal and ordinal compass directions at speeds of one pixel every 50 or 100ms (1250µm/s or 625µm/s) presented every 4 seconds. I presented all stimuli in control conditions and at the highest drug concentration. Additionally, I presented the full-field flashes at all intermediate drug concentrations and again after washout. Each set of stimuli at a given drug concentration was presented in randomised blocks: 20 blocks for the full-fields and 10 blocks each for the flashing squares and moving bars. Using a Newport 1918-R optical power meter (Newport Spectra-Physics Ltd, Didcot, UK) equipped with a Newport 818-UV/DB photodiode, I measured the total power transmitted from the µLED array to the retina as 25.5µW . Averaged over the entire (approximately 1mm^2) image this corresponds to an irradiance of 25.5µW/mm^2. In practice due to the separation between individual LEDs there will be regions of zero irradiance and regions of higher irradiance (equal to the average irradiance divided by the fill factor). In one experiment, I accidentally set the power output to 21.0µW, but the results from this experiment were not qualitatively different from the rest and so I included them in all analyses presented here. Despite the high irradiance, the µLEDs did not appear to induce photoelectric artefacts on ITO MEAs, as I never observed any when shining the LEDs onto empty MEAs nor on electrophysiologically quiet channels when stimulating retinas. (By contrast, during experiments conducted as part of my Master of Research degree, I did notice photoelectric artefacts when projecting light from an arc lamp onto empty MEAs with titanium nitride electrode contacts and tracks.)

Detecting Optogenetically Responsive Cells. All the analyses of optogenetic responses described below used spike sorted data, where I performed spike sorting as in section 2.3.1.

Not all RGCs in these retinas express ChR2, so I used responses to the longest-duration full-field flashes to detect RGCs that responded to optogenetic stimulation. First, I bootstrapped a spontaneous firing distribution by dividing the 1 second periods before each flash into 100ms bins (equal to the length of the longest flash), computing the median number of spikes in 10 randomly selected bins and repeating this procedure 10000 times. I used this distribution to assign one-sided p-value to the median number of spikes fired by a cell in response to 100ms flashes, under the null hypothesis that the cell does not respond to stimulation. I took those cells within a recording having $p < 0.05$ after false-discovery rate correction (Yoav and Hochberg 1995) as responsive. To avoid double-dipping (Kriegeskorte et al. 2009), I only used odd-numbered trials of the full-field flashes to detect responsive cells and used the even-numbered trials to calculate thresholds and SNR (see below).

Stimulation Threshold and Signal-to-Noise Ratio. For each cell that was responsive in both control conditions and at the highest drug concentration, I calculated the stimulation threshold and SNR as follows. I calculated the response probability as a function of flash duration by counting the number of trials on which the number of spikes fired in the 100ms following the onset of a flash exceeded the median number of spikes fired in any 100ms period of spontaneous activity. I fit this response probability function with a sigmoid function using the `lsqcurvefit` function in Matlab:

$$p(t) = \frac{1}{1 + e^{-\frac{t-b}{a}}}$$

The parameter b gives the flash duration with a 50% probability of evoking a response, which I took as the threshold for a given cell. The SNR is commonly defined as the mean of the signal divided by the standard deviation of the noise. The signal I am interested in here is those spikes evoked by the µLED flash, but it is impossible to distinguish stimulus-evoked spikes from spontaneous spikes that happened to be fired immediately after a stimulus, hence I estimated the SNR for a given cell as

$$SNR = \frac{\mu_{signal+noise} - \mu_{noise}}{\sigma_{noise}}$$

Where $\mu_{signal+noise}$ is the mean number of spikes (spontaneous and evoked) fired in the

100ms following any even-numbered flash, μ_{noise} is the mean number of spikes fired in any 100ms bin of spontaneous activity and σ_{noise} is the standard deviation of the number of spikes fired in any 100ms bin of spontaneous activity. Some RGCs in each recording only fired immediately following a flash and so their SNR was immeasurably high: I assigned these cells an SNR of infinity.

Spike Triggered Averaging and Receptive Field Measurement. I used responses to the 2x2 and 4x4 pixel flashed squares to construct spike-triggered averages (STAs) for each cell (the 1x1 pixel flashes were found to produce very weak responses, if any, and so were excluded from the STA). First, I instantiated a 16×16 matrix of zeros - one entry per µLED pixel - for each cell. For each frame of each stimulus, I counted the number of spikes fired by that cell during presentation of that stimulus frame and added this number to those matrix entries corresponding to the pixels that were on during that frame. Finally, I divided each entry in the matrix by the number of stimulus frames in which the corresponding pixel was on. I fit each spike-triggered average with a raised two-dimensional Gaussian function using Matlab's lsqcurvefit function:

$$\begin{aligned} a &= \frac{\cos^2\theta}{2\sigma_x^2} + \frac{\sin^2\theta}{2\sigma_y^2} \\ b &= -\frac{\sin 2\theta}{4\sigma_x^2} + \frac{\sin 2\theta}{4\sigma_y^2} \\ c &= \frac{\sin^2\theta}{2\sigma_x^2} + \frac{\cos^2\theta}{2\sigma_y^2} \\ RF(x,y) &= Ae^{-(a(x-x_c)^2+2b(x-x_c)(y-y_c)+c(y-y_c)^2)} + B \end{aligned}$$

I then calculated the receptive field radius as the geometric mean of the semimajor and semiminor axes of the 1-SD contour of the fitted Gaussian, i.e. $r = \sqrt{\sigma_x\sigma_y}$. This corresponds to the radius of a circle having the same area as the fitted receptive field. I calculated the receptive field eccentricity as $e = \sqrt{1 - \left(\frac{\min(\sigma_x,\sigma_y)}{\max(\sigma_x,\sigma_y)}\right)^2}$.

Moving Bars. To estimate the instantaneous firing rate (IFR), I convolved each cell's spike train during the presentation of the moving bar stimuli with a one-dimensional Gaussian function with a standard deviation of 25ms. I calculated the time to peak firing on each trial as the time between the appearance and disappearance of the bar that the IFR reached its maximum value, relative to bar onset. If a cell only fires when a sufficient amount of light falls within its receptive field, this time to peak firing should provide a reliable estimate of the point along the bar's trajectory at which it entered the cell's receptive field. If the cell's receptive field is not exactly in the middle of the array, this will also give some information as to the direction of travel of the bar.

To quantify how well the population of optogenetically sensitive cells in a given retina encodes stimulus direction, I trained a modified naive Bayesian classifier to determine bar direction, as described in section 2.3.3. I took $p(r_i|s)$ as following a mixed Bernoulli-Gaussian distribution:

$$p(r|s) = \begin{cases} q_s & \text{if } r = \infty \\ (1 - q_s) g(r; \mu_s, \sigma_s) & \text{if } r < \infty \end{cases}$$

where r is the time to peak firing of the cell, s is the bar direction, and $g(r; \mu_s, \sigma_s)$ is a Gaussian probability density function with mean μ_s and variance σ_s^2. I estimated q_s as the number of trials with no response divided by the total number of trials and μ_s and σ_s as the mean and standard deviation of the peak firing latency on those trials in which the cell responded.

Statistical Analysis. All analyses presented in this chapter are non-parametric repeated measures designs with drug concentration as the within-subjects factor, so I used the Friedman test to analyse the effect of drug concentration. I used the different retinas as the blocking factor except where noted in the text. Where multiple measurements were taken from a single retina (i.e. multiple channels or multiple cells), I used the median value for each retina in the analysis. As the Friedman test operates on ranks, infinite SNR values were assigned the mean of the rank they would have been assigned had they been finite, monotonically increasing values greater than any measurable SNR value. Due to the uneven number of retinas used for each drug for some analyses, I had to use separate tests for each drug and so I could not make any direct statistical comparisons between drugs (and in any case the Friedman test does not assess the significance of between-subject effects). All p-values are reported uncorrected, but all those significant at the $p < 0.05$ level remained significant after Holm-Bonferroni correction for multiple comparisons with an α level of 0.05.

4.3 Results

4.3.1 *Spontaneous Activity*

Figure 4.1 shows a portion of the raw trace recorded from one channel in control conditions and in the presence of 20µM and 80µM MFA, as well as the power spectra from this same channel at each drug concentration. There is a clear decrease in oscillatory activity and spontaneous firing as the drug concentration increases. This pattern held across all retinas for all three drugs tested. Each drug significantly reduced the strength of LFP oscillations (Friedman test: 18BGA $n = 7, p = 2.5 \times 10^{-5}$; Flu $n = 7, p = 0.0001$; MFA $n = 7, p = 6 \times 10^{-6}$) and spontaneous RGC firing (Friedman test: 18BGA $n = 7, p = 1.1 \times 10^{-5}$; Flu $n = 7, p = 6 \times 10^{-6}$; MFA $n = 7, p = 1.5 \times 10^{-5}$). Figure 4.2 shows the effect of each drug on oscillation strength and spontaneous firing rate relative to control conditions averaged across all recorded channels for all retinas. Flu has a stronger effect at low concentrations, consistent with a previous study showing that 10µM Flu blocks spontaneous activity (Choi et al. 2014), but for all three drugs spontaneous firing is almost completely abolished at 80µM. There is substantial recovery of oscillations and spontaneous firing after washout of Flu and MFA, consistent with previous reports (Menzler and Zeck 2011; Trenholm et al. 2012; Choi et al. 2014), but not with 18BGA, the effects of which are known to be irreversible at concentrations above 75µM (Rozental et al. 2001).

4.3.2 *ChR2 Responsiveness and Signal-to-Noise Ratio*

Lowering spontaneous activity has the potential to improve SNR, but not if it comes at the expense of the ability to stimulate RGCs optogenetically. Figure 4.3 shows the number of cells that respond to the longest full-field µLED array flash at each drug concentration, relative to control conditions. All three drugs significantly affected the number of respon-

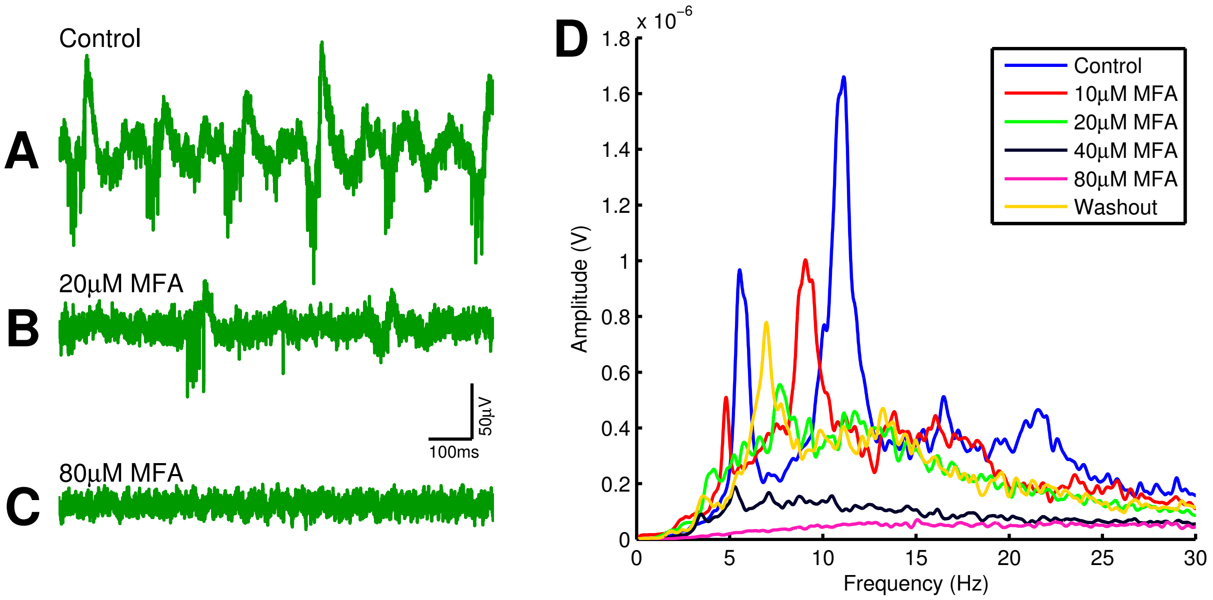

Figure 4.1: A-C: raw electrode trace on one channel for an example retina in control conditions (A), with 20µM MFA (B), and with 80µM MFA (C). Note the decrease in both oscillations and level of spontaneous firing as the drug concentration increases. D: power spectra recorded on the same channel in control conditions, at each drug concentration, and after washout. Notice the overall decrease in LFP power as the drug concentration increases and the recovery upon washout.

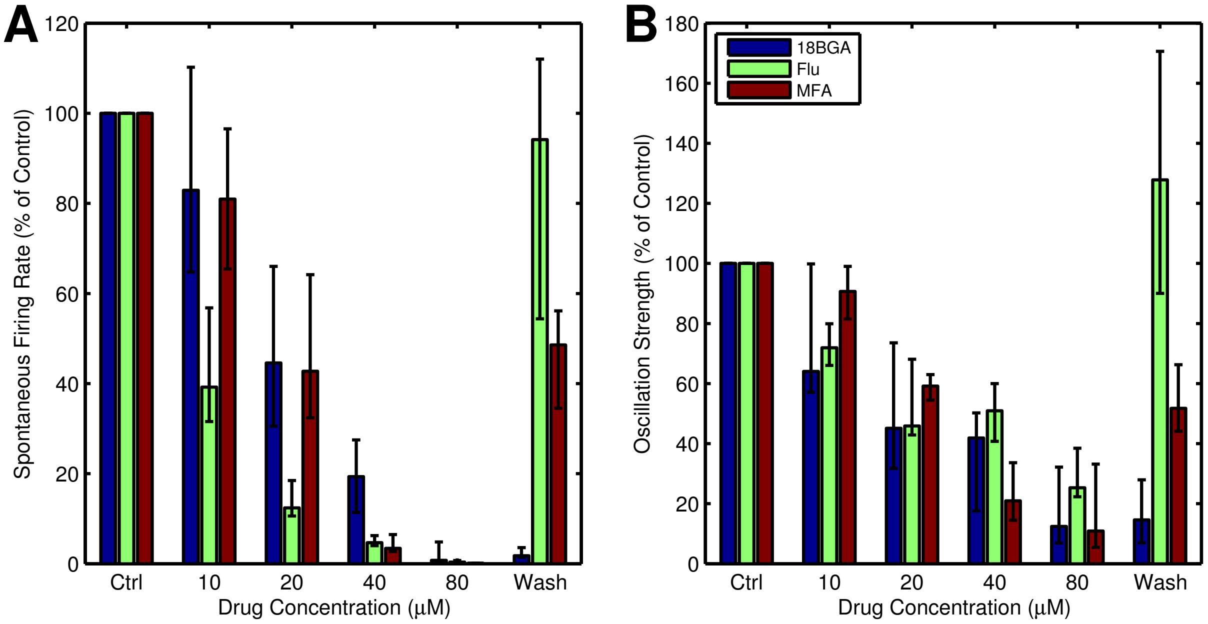

Figure 4.2: A: Spontaneous firing rate as a percentage of control conditions for each concentration of all three drugs, averaged over all channels with recorded spikes and all retinas. B: Oscillation strength as a percentage of control conditions for each concentration of all three drugs, averaged over all recorded channels and all retinas. For both figures, error bars show the interquartile range (IQR).

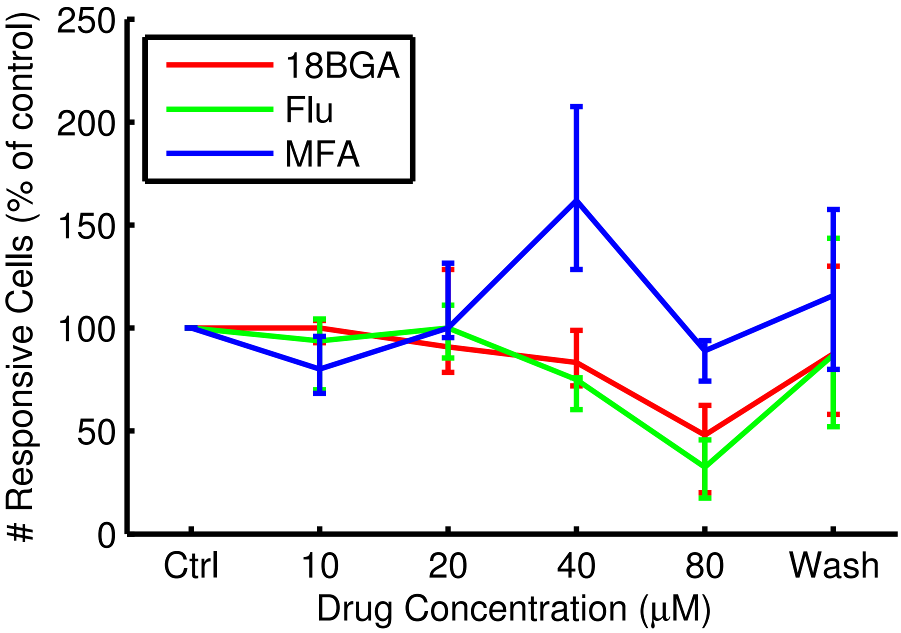

Figure 4.3: Number of cells responding to the longest µLED array flash at each drug concentration as a percentage of control conditions, averaged over all retinas.

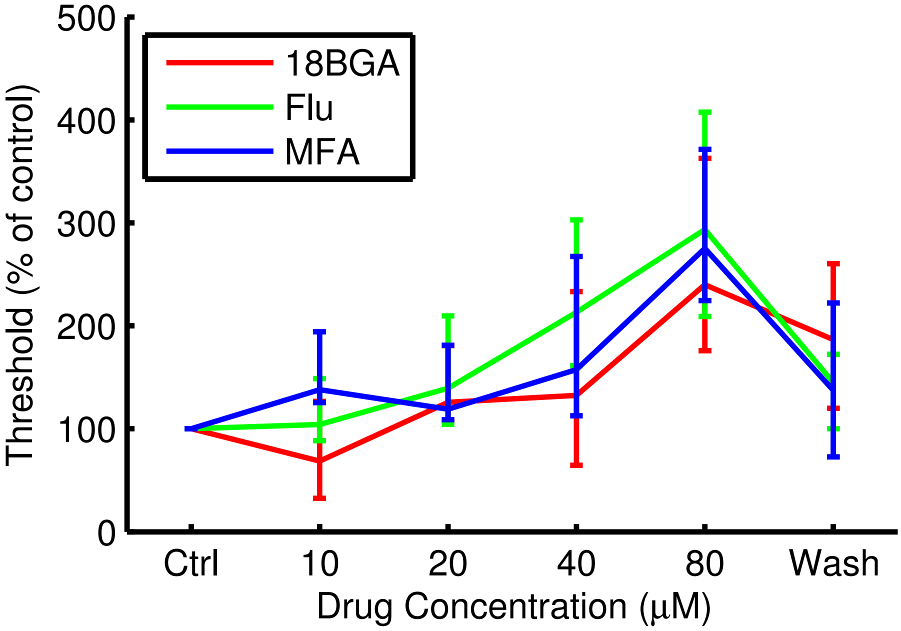

Figure 4.4: Threshold flash duration for optogenetically sensitive cells at each drug concentration as a percentage of control conditions. Data points are median over all retinas of the median threshold of all cells that respond in both control conditions and at 80µM drug. Error bars are IQR for all retinas.

sive cells (18BGA $n = 7, p = 0.0037$; Flu $n = 7, p = 0.0019$; MFA $n = 7, p = 0.0058$). 18BGA and Flu both caused a dose-dependent decrease in the number of responsive cells (in one experiment for each, there were no responding cells left at 80µM and so these experiments were excluded from the threshold and SNR analyses). The pattern for MFA is more complicated: at most concentrations, the number of responsive cells was similar to control conditions, but the number of responsive cells appears to increase at 40µM before returning to baseline at 80µM. Figure 4.4 shows the response thresholds for those cells that responded to optogenetic stimulation in both control conditions and at the highest drug concentration, relative to control conditions. All three drugs appear to cause a dose-dependent increase in stimulation thresholds (18BGA $n = 6, p = 0.0097$; Flu $n = 6, p = 0.0002$; MFA $n = 7, p = 0.0087$). Taken together, these results suggest that 18BGA and Flu hinder optogenetic stimulation of RGCs, whereas MFA has a mixed effect, increasing the number of responsive cells at the expense of increasing the stimulation threshold.

Figure 4.5 shows raster plots and PSTHs from an example cell in response to the longest flash in control conditions and at the highest drug concentration. It is very difficult to distinguish the cell's response from the high level of spontaneous activity in control conditions, but the response to light is very distinct once the spontaneous activity is abolished. Figure 4.6 shows SNR as a function of drug concentration for those cells that responded at 0µM and 80µM drug, relative to control conditions. Cells with infinite SNR were excluded from figure 4.6 (although they were included in statistical analyses, see section 4.2.4). Such cells represented more than half of all responding RGCs at 80µM Flu and MFA, so the median SNR over all retinas in these two conditions was infinity. All three drugs significantly increased SNR (Friedman test, flash duration as blocking factor: 18BGA $n = 6, p = 0.0004$; Flu $n = 6, p = 1.2 \times 10^{-7}$; MFA $n = 7, p = 3.7 \times 10^{-7}$).

4.3.3 *Spatiotemporally Patterned Stimulation*

Figure 4.7 shows example STAs recovered from responses to flashing squares in control conditions and at a drug concentration of 80µM. In both cases, a clear hotspot is observed, presumably corresponding to those pixels within the cell's receptive field, but the surrounding pixels are slightly noisier in control conditions. This pattern was similar

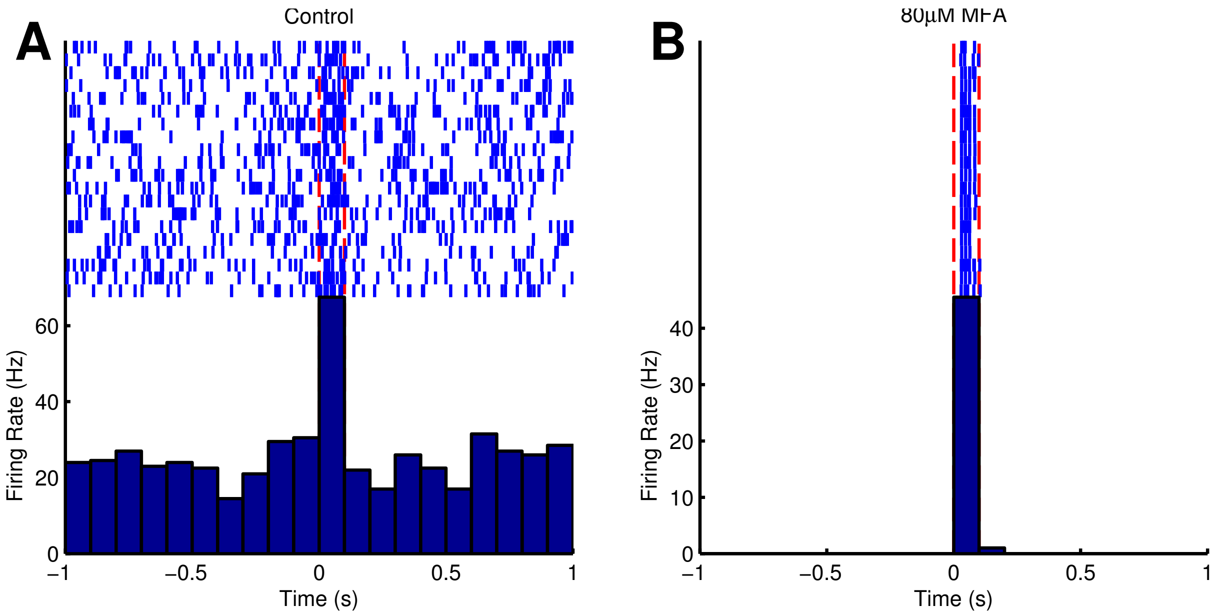

Figure 4.5: A: raster plot and PSTH of an example cell in response to 100ms full-field μLED flashes in control conditions. The light is on between the red dotted lines. The response is barely discernible above the background noise. B: raster plot and PSTH of the same cell in response to the same stimulus in the presence of 80μM MFA. Note the greatly decreased spontaneous activity.

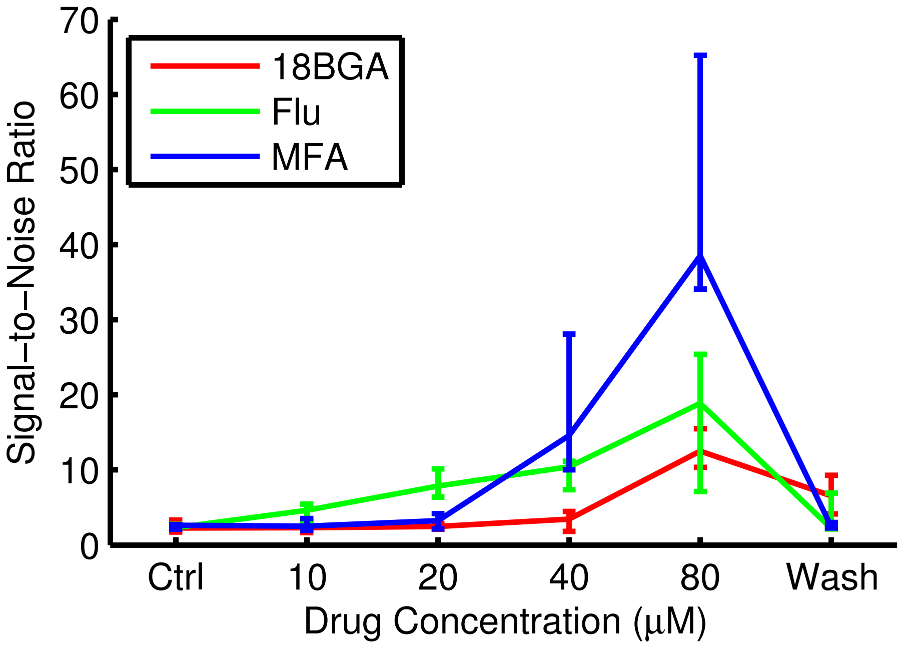

Figure 4.6: Signal-to-noise ratio for responses to the longest μLED array flash at each drug concentration as a percentage of control conditions. Data points are median over all retinas of the median SNR of all cells that respond in both control conditions and at 80μM drug and had measurable (i.e. non-infinite) SNR values. Error bars are IQR for all retinas.

across all cells for which responses to flashing squares were successfully recorded. The median receptive field diameter was 245.2µm in control conditions and 219.8µm in the drug condition, but this difference was not significant. In both control and drug conditions the median receptive field eccentricity was around 0.5. ChR2 in these retinas is expressed throughout the cell (figures 2.2 and 2.3, see also Thyagarajan et al. (2010)), including soma, dendrites and axons. The size and shape of the ChR2 receptive fields is consistent with ChR2 activation in the soma and dendrites being primarily responsible for spike generation, rather than axonal stimulation, even though the light had to pass through the nerve fibre layer before reaching the RGCs.

Figure 4.8 shows responses of an example cell to four directions of the moving bar stimulus, in control and drug conditions. It is difficult to discern the response to the bar in the presence of spontaneous hyperactivity, but there is a clearly distinguishable peak in the cell's firing when the bar enters its receptive field in the drug condition. Nevertheless, the Bayesian classifier was modestly successful in decoding stimulus direction in control conditions, achieving correct decoding roughly 40-70% of the time on average (figure 4.9, blue bars). After applying the drug, the decoder performance is improved, with the classifier decoding the stimulus direction correctly 70-100% of the time on average (figure 4.9, red bars). This difference was significant for MFA (Friedman's test, bar speed as blocking factor: $n = 7, p = 0.0001$) but not Flu ($n = 7, p = 0.44$) or 18BGA ($n = 7, p = 0.57$).

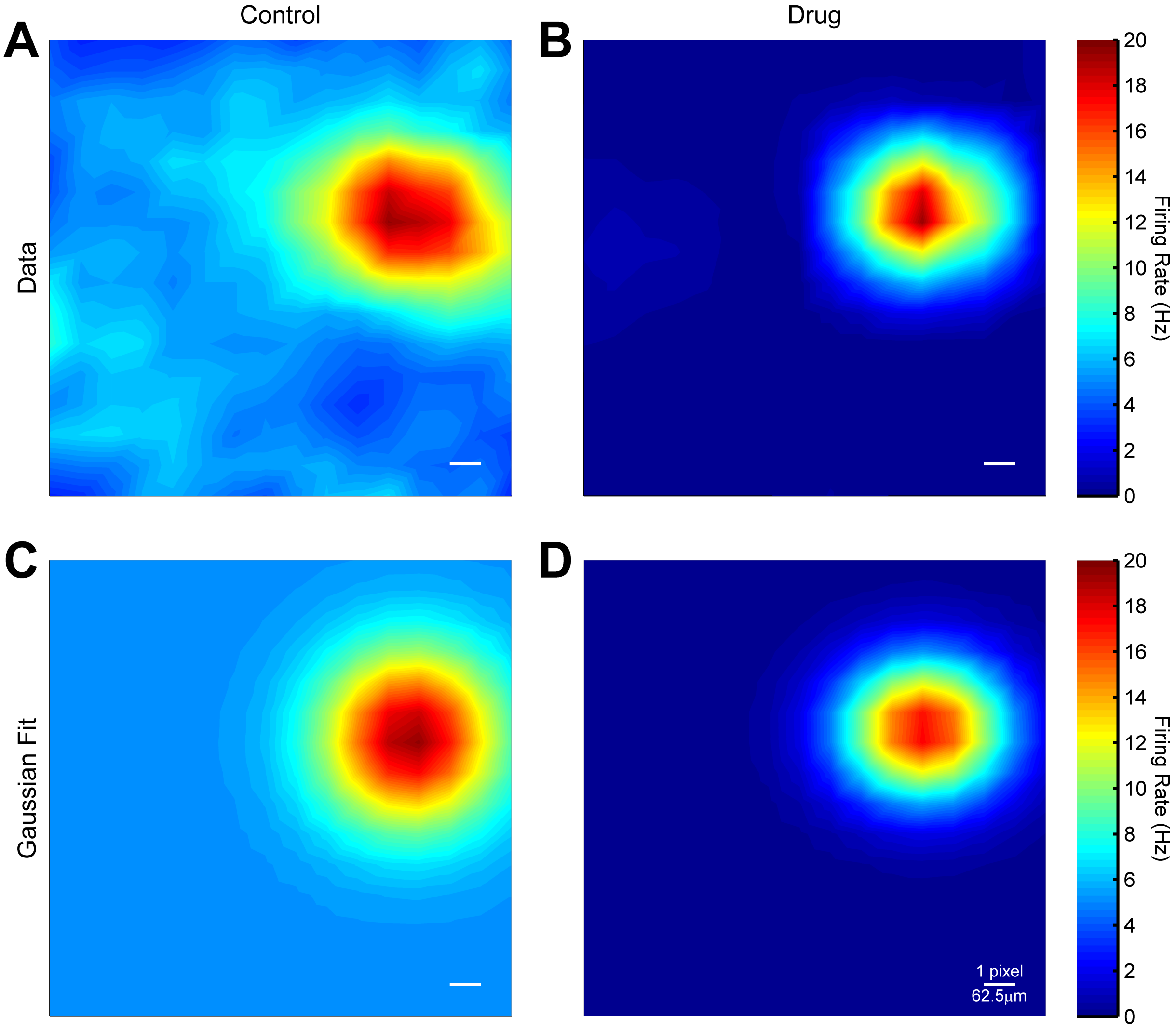

Figure 4.7: A: spike triggered average for an example RGC in control conditions. B: spike triggered average for the same cell in the presence of 80µM MFA. C-D: Gaussian fits to the data in A-B. The scale bar in each panel is one µLED array pixel or approximately 62.5µm in length.

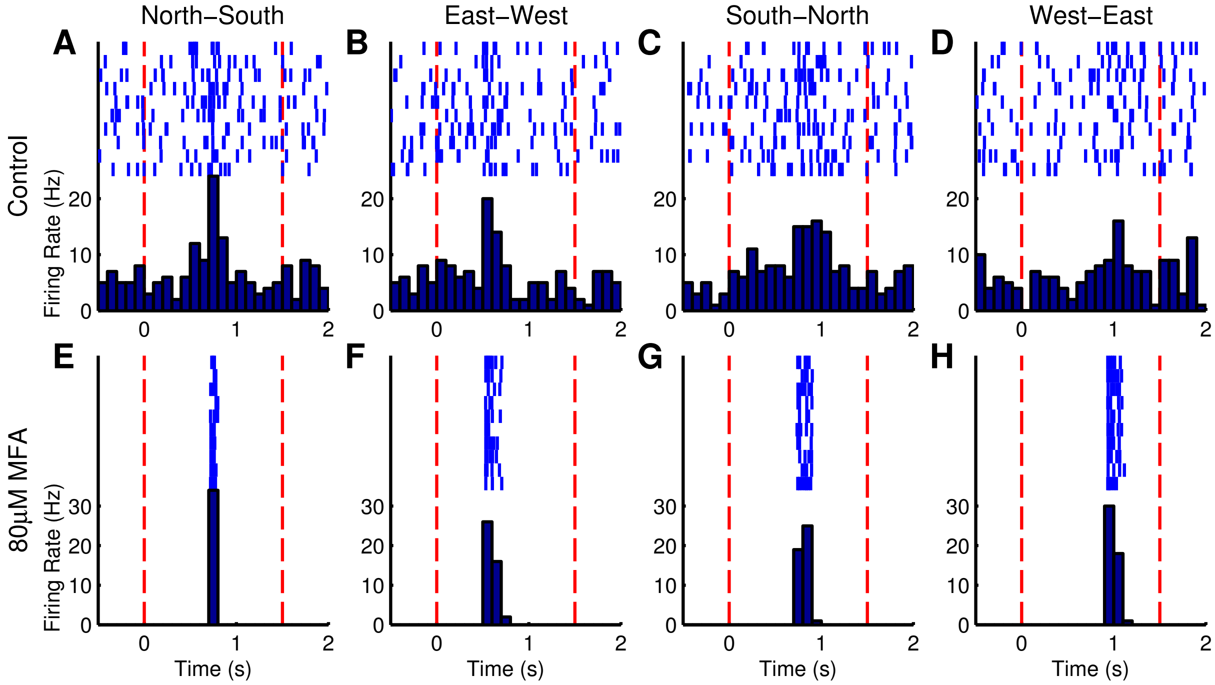

Figure 4.8: Raster plots and PSTHs for an example RGC in response to bars moving in the four cardinal compass directions at 625µm/s in control conditions (A-D) and in the presence of 80µM MFA (E-H). The bar appears at the first red dotted line, sweeps across the array, and disappears at the second red dotted line. In control conditions it is difficult to isolate the response to the bar from the high spontaneous activity and the peak of the PSTH is broad. After blocking the spontaneous activity it is easy to see when the bar enters the cell's receptive field and there is a sharp peak in the PSTH. This cell was located fairly centrally along the Y-axis of the array, so there is little difference in time to peak firing between bars originating in the north or south of the array (A,C,E,G), but as the cell was located close to the east side of the array the cell fires much earlier for a bar originating in the east (B,F) than the west (D,H).

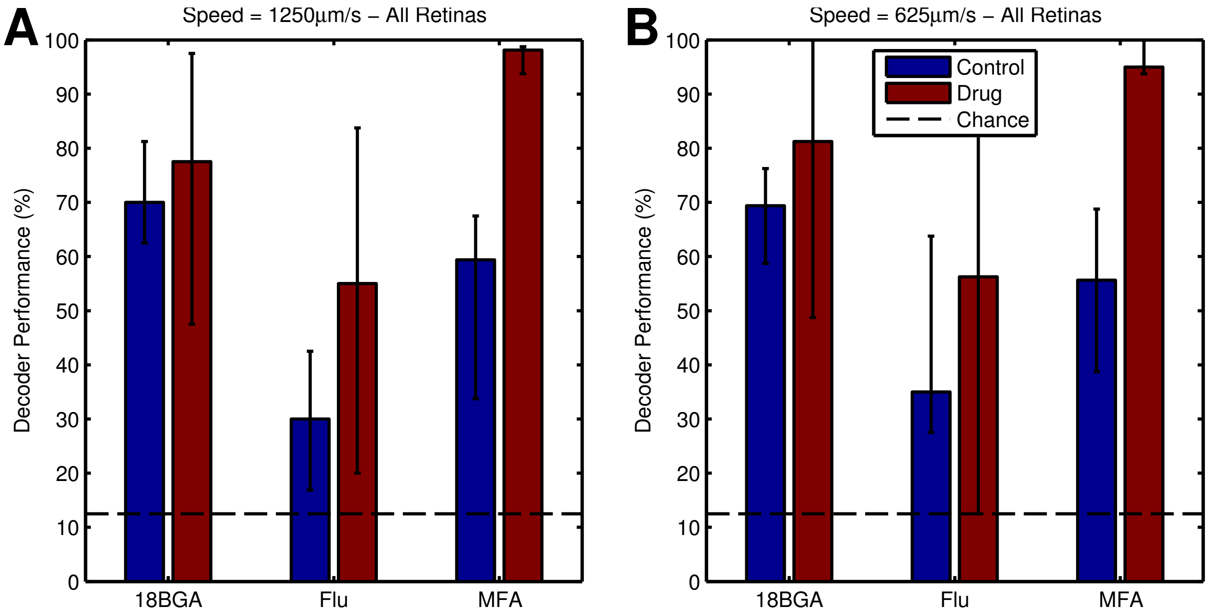

Figure 4.9: A: Bayesian decoder performance for responses to the 1250µm/s bars in control conditions (blue bars) and in the presence of 80µM of each drug (red bars). Decoder performance is much higher in the presence of the drug. Dotted line indicates chance level performance. B: the same plot for the 625µm/s bars. For both panels, data points are medians over all retinas and error bars are IQRs.

4.4 Discussion

4.4.1 *Blocking spontaneous activity improves SNR regardless of the the mechanism of action*

It has been shown recently that blocking spontaneous activity with MFA improves the SNR of residual photoreceptor responses and responses to electrical stimulation in the *rd10* mouse (Toychiev et al. 2013; Ivanova et al. 2015). My results show that this principle also holds for optogenetic stimulation in the *rd1* mouse. Spontaneous activity in degenerate retinas is believed to originate in the AII amacrine cell (Trenholm et al. 2012; Choi et al. 2014) and propagate through the retinal network via gap junction coupling between AII amacrine cells and other cell types, such as ON-cone bipolar cells (Menzler and Zeck 2011; Trenholm et al. 2012; Yee et al. 2012). These oscillations can be strengthened or dampened by altering the potassium conductance of AII cells (Choi et al. 2014), and prevented from spreading by blocking gap junctions (Menzler and Zeck 2011; Trenholm et al. 2012; Toychiev et al. 2013; Biswas et al. 2014).

MFA is both a gap-junction blocker (Pan et al. 2007) and a modulator of Kv7 potassium channels (Peretz et al. 2005; Yeung et al. 2007), so it is not clear which of these mechanisms is responsible for its effects on spontaneous hyperactivity. In principle, it should not matter for improving SNR, but to confirm this I tested two additional drugs: Flu, which is a powerful Kv7 potassium channel opener (Martire et al. 2004; Wladyka and Kunze 2006; Yeung et al. 2007) that has recently been shown to block *rd1* spontaneous activity (Choi et al. 2014); and 18BGA, another gap junction blocker (Davidson et al. 1986). As expected, all three drugs significantly reduced spontaneous firing and improved the SNR of optogenetic responses, at least for those cells that were still sensitive to ChR2 stimulation. These results demonstrate that being able to suppress the pathological spontaneous activity, rather than the specific approach to do so, is the key requisite to enhance the SNR during electrical or optogenetic stimulation. In principle, any other means of blocking spontaneous activity, for example blocking synaptic input onto RGCs (Biswas et al. 2014; Borowska et al. 2011; Menzler and Zeck 2011; Trenholm et al. 2012), should also improve the SNR of optogenetic responses, although I have not tested this.

4.4.2 *Effects on Stimulation Efficiency of ChR2 RGCs*

Increasing the SNR of individual cells by decreasing spontaneous activity may not lead to improved prosthetic signal transmission through the retina if the method of decreasing spontaneous activity also leads to fewer cells responding to stimulation. Hence, I measured the number of cells responding to stimulation and their stimulation threshold as a function of drug concentration. Both 18BGA and Flu appear to lead to a dose-dependent decrease in the number of cells responding and an increase in stimulation thresholds. In the case of Flu, this may be because it acts by increasing the conductance of the Kv7 potassium channel (Peretz et al. 2005; Yeung et al. 2007; Choi et al. 2014). If these potassium channels are present on RGCs, application of Flu could lead to a lower resting membrane potential and a decrease in excitability, which would explain the observed effects. This is consistent with the result in chapter 5 that increasing RGC excitability by raising the extracellular potassium concentration increases the number of optogenetically responsive cells. Why 18BGA should also increase stimulation thresholds is not clear, but as well as blocking gap junctions it affects a number of other ion channels (Juszczak and Swiergiel 2009; Rozental et al. 2001) and possibly one of these effects is responsible for the increase in thresholds. 18BGA is also apparently cytotoxic at concentrations above 75µM (Rozental et al. 2001), although this would not explain the dose-dependent increase in thresholds. MFA has mixed effects on stimulation efficiency of ChR2-expressing RGCs. Like 18BGA and Flu, it increases thresholds in a dose-dependent manner, but at 40µM it increases the total number of cells with detectable responses. At this concentration, the threshold increase is modest (median 150% of control) and therefore moderate concentrations of MFA (similar to those used by Toychiev et al. (2013)) seem to offer the best trade-off between improving SNR by decreasing spontaneous activity and not hindering ChR2 stimulation too badly.

4.4.3 *Spatiotemporally Patterned Stimulation of Optogenetically Sensitive Retinas*

The above analyses concern responses to wide-field, spatially homogenous flashes, which are not particularly perceptually interesting stimuli. Most visual tasks involve discerning information from a scene in which the pattern of light is varying in both space and time. Hence I also investigated, for the first time, the effects of decreasing spontaneous activity on spatiotemporally patterned optogenetic stimulation.

First, I mapped the receptive fields of ChR2-sensitive RGCs using spike-triggered averaging, or reverse correlation, of responses to small (2x2 or 4x4 pixels), brief flashes. Limitations of the stimulation device prevented the use of more typical reverse correlation stimuli, such as white noise (Chichilnisky 2001), but nonetheless I was able to capture clear receptive fields in both control conditions and after blockade of spontaneous activity. The similarity of the recovered receptive fields in both conditions is more likely a testament to power of reverse correlation as a technique than evidence against the hypothesis that blocking spontaneous activity improves prosthetic responses. The recovered receptive fields were unipolar (as expected, since ChR2 is purely excitatory), slightly elliptical, and had an average diameter of 200-250µm, which is on par with typical RGC dendritic arbor sizes (Sun et al. 2002). This is unsurprising: expression of ChR2 in the RGCs of this particular mouse line is throughout the cell membrane, including soma, dendrites and axons (figures 2.2 and 2.3; see also Thyagarajan et al. (2010)). One would thus expect the amount of depolarisation caused by ChR2 stimulation to be proportional to the total cell surface area covered by the light stimulus, hence the response would be strongest when the light covers the soma and dendrites.

In terms of assessing the effect of spontaneous activity on prosthetic vision, a more important question to ask is how well does the RGC population encode stimulus features after blockade of spontaneous activity compared to control conditions. Bayesian decoding has been established as a useful framework for assessing the performance of different retinal coding strategies (Jacobs et al. 2009) and comparing them to behavioural performance. Here I use it to ask a slightly different question: assuming a fixed coding strategy, how well does the retina encode stimulus properties in different conditions? As an example, I chose decoding motion direction of a moving bar. Given that all ChR2 RGCs can encode is the amount of light falling in their receptive field, the most natural coding strategy for determining motion direction is the latency of each cell relative to the stimulus: those cells whose receptive field the bar enters first will fire most strongly earlier than those whose receptive field the bar enters later. Under this strategy, the retina did indeed encode motion direction better when there was less spontaneous activity, confirming that this strategy improves encoding of spatiotemporal stimulus information. This improvement was statistically significant for MFA, but not 18BGA or Flu. A possible explanation for this is the reduction in optogenetically responsive cells at high concentrations of the latter two drugs: having more cells with less distinct responses might encode visual information just as well as a few cells with very sharp responses. Flupirtine is effective at lower concentrations than 18BGA or MFA (figure 4.6; see also Choi et al. (2014)), so in one experiment I recorded moving bar responses at 0µM and 20µM Flu, but despite vastly reduced spontaneous activity, the decoder performance was virtually identical (data not shown).

4.4.4 *Implications for Treatment of Retinal Degenerations*

This study adds more evidence to the idea that reducing spontaneous hyperactivity in degenerate retinas could potentially improve the quality of vision returned by retinal prosthetics and that this is a worthwhile avenue to pursue in the search for improved treatments for retinal dystrophies such as RP. Further, by investigating a number of drugs I have provided information as to the best choice of drug if a pharmacological strategy is chosen to reduce spontaneous activity in retinal prosthetic patients (but see chapter 6). Flu is an analgesic, anticonvulsant, and muscle relaxant that is currently being investigated for possible neuroprotective effects (Friedel and Fitton 1993; Klawe and Maschke 2009; Szelenyi 2013); MFA is a non-steroidal anti-inflammatory drug and analgesic (Juszczak and Swiergiel 2009); and 18BGA is a flavouring agent derived from licorice (Asl and Hosseinzadeh 2008). Thus all three drugs are at least safe for human consumption and, in the case of Flu and MFA, already clinically approved drugs. However, given the apparent negative effects of 18BGA and Flu on ChR2 stimulation, MFA is probably the best candidate, at least where optogenetic retinal prostheses are concerned. There is some evidence that MFA is retinotoxic (Sun et al. 2013), but only at concentrations much higher than those used in this study. In particular, concentrations of around 40-50µM seem to be effective at improving prosthetically-evoked responses without adverse effects either on optogenetic stimulation or the retina itself.

4.4.5 *Conclusions*

I have demonstrated that reducing spontaneous activity works as a strategy to improve the quality of optogenetically-evoked retinal responses, increasing the signal-to-noise ratio of optogenetic responses and improving the ability to determine stimulus properties from RGC firing. Morever, of the drugs tested so far, I have shown that MFA is the most promising in terms of decreasing spontaneous activity without hampering optogenetic stimulation. This provides important information and guidance for future research into improving the quality of vision returned by retinal prosthetics.

Chapter 5. Improving Optogenetic Responses by Dampening Spontaneous Activity

5.1 Introduction

In chapter 4, I demonstrated that reducing spontaneous RGC hyperactivity improves the SNR of RGC responses to optogenetic stimulation in the *rd1* model of retinitis pigmentosa (RP). A variety of drugs had the same effect, but this came at the expense of increased stimulation thresholds and, with the exception of moderate (40µM) concentrations of meclofenamic acid (MFA), reduction in the total number of responding cells. This is consistent with the results of Toychiev et al. (2013) and Ivanova et al. (2015), who found that 50µM MFA improved RGC responses to stimulation of residual photoreceptors and electrical stimulation in the *rd10* mouse. Further, I demonstrated that, in the specific case of decoding direction of a moving bar from RGC population responses using latency coding, blocking spontaneous activity with MFA (but not other drugs) improves the amount of information in optogenetic responses.

The logical extension of these results is to ask whether they extend to other stimulus classes. In particular, I decided to focus on stimuli inspired by those typically used to assess vision in the clinic and in vision research. For example, one standard method for testing visual acuity is the logMAR chart (Bailey and Lovie 1976); and discrimination of gratings from a flat background, pioneered by Arden and Jacobson (1978), is a popular method for testing contrast sensitivity. Applying such tests *in-vitro* facilitates comparison with current clinical trials of electrical prostheses that make use of similar tests, for example visual tests used by Stingl et al. (2015) included Landolt Cs, and both Stingl et al. (2015) and Ho et al. (2015) also included gratings in their visual testing. Such tests also enable comparison with existing behaving animal tests of optogenetic retinal prosthetic function: one popular test in such studies is optokinetic reflex testing, in which a mouse's head naturally tracks a drifting grating (e.g. Lagali et al. (2008), Tomita et al. (2009, 2010), Busskamp et al. (2010), and Wyk et al. (2015)). Similarly, Cehajic-Kapetanovic et al. (2015) used a modified open-field test in which a mouse is placed into a box with two halves, the sides of which were illuminated by a computer monitor, both initially displaying a flat grey screen. When the stimulus presented in one of the halves is changed, a significant change in the mouse's locomotor activity indicates they have perceived the change. Among the stimuli they used were stationary flickering gratings of varying contrast and spatial frequency.

Although the stimuli described above would provide a useful test of whether blockade of spontaneous hyperactivity has the potential to improve retinal prosthetic vision in practice, they cannot be employed with the µLED array used to deliver stimuli in chapter 4. This is due to its low pixel count, which limits the spatial frequency and complexity of stimuli, and binary pixels, which do not allow manipulation of contrast. A standard computer monitor or projector provides much a higher resolution display with variable contrast, at the cost of refresh rate (typically around 60Hz, whereas the µLED array can theoretically update itself at submillisecond time scales). Unfortunately, the monitor used in chapter 3 is almost certainly too dim to stimulate ChR2 once light losses between monitor and MEA are taken into account. However, in the APS experiments also described in chapter 3, the light from the projector was attenuated more than 30000-fold using a neutral density filter in order to bring the incident light into the mesopic range for stimulation of rods and cones in the normal retina. With less drastic light attenuation, the APS projector might be capable of stimuluating ChR2. Thus, my aims in the experiments presented in this chapter were two-fold. First, to test whether the APS projector could successfully stimulate ChR2 and, if so, at what intensities and on what spatial and temporal scales. Secondly, to test whether spontaneous activity blockade using MFA can improve the spatial acuity and contrast sensitivity of optogenetic retinal responses.

5.2 Specific Methods

All recordings described in this chapter were performed by Dr Gerrit Hilgen, who also extracted spike times and waveforms. Otherwise, the experimental design and all analysis, including spike sorting and the analyses described below, was my own work.

5.2.1 *Visual and Optogenetic Stimuluation using a DLP Projector and Recording from a Large Scale MEA*

All data presented in his chapter was recorded on the APS MEA (section 2.2.2). The APS in our lab is equipped with a lightCrafter DLP projector (Texas Instruments, Dallas, TX, USA) and a custom optomechanical setup to facilitate focusing the light from the projector onto the MEA. This projector system provides 664x664 pixels of spatiotemporally patterned stimulation over the area of the MEA with 4µm spatial resolution, a refresh rate of 60Hz, and full, independent control over the brightness and colour of each pixel. Stimuli are controlled with custom software to allow presentation of sequences of stimuli with microsecond temporal precision; this software also enables synchronising stimulation and recording by means of TTL pulses delivered to the analogue input of the Biocam (MEA amplifier) every time the display updates.

The projector is also very bright, with a maximum irradiance on the MEA of 0.13W/cm^2. Unfortunately, as the MEA is made of silicon and lacks a light-shielding metal layer, incident light causes a photoelectric artefact that, at high intensities, can saturate the amplifier. This limits the brightness of the light that can be used while reliably recording RGC activity. In practice, attenuating the light from the projector with neutral density filters in the range ND 1.9 (irradiance 1.65mW/cm^2) to ND 2.2 (irradiance 0.87mW/cm^2)—depending on the spatial extent of the stimulus—allows most spikes to be recorded while keeping the artefact manageable. On most channels, the artefact takes the form of a negative boxcar function with a height that varies with the stimulus intensity and width corresponding to the length of the stimulus. On some channels the amplifier temporarily saturates during the stimulus, but such periods are few and brief.

There is the possibility that the negative deflection at the beginning of the artefact could be detected as a spike[1]. In practice, this does not appear to present a problem. Firstly, such artefactual spikes would have a distinct shape, similar to a time-reversed Heaviside step, which could be easily recognised and excluded during spike sorting, but I saw no clusters of such spikes. Secondly, if such spikes were detected and not excluded during

---

[1] Saturations are never detected as spikes because these are positive deflections but the spike detection algorithm looks for negative voltage deflections.

spike sorting, these would appear in the rasters as a single spike fired reliably on every trial at time zero relative to stimulus onset. I did not see any such precisely time-locked spikes in any of the many thousands of rasters I inspected from the datasets presented in this chapter. Another possibility is that the increase in variance of the electrode trace around the artefact could cause spikes to be missed. If this does happen, it does not appear to present a serious problem, as in many cases I saw cells with a sharp, low-latency, transient increase in firing in response to stimulation. Such responses would be less distinct if the artefact caused the spike detection algorithm to miss spikes the beginning and the end of the artefact. Alternatively, if the artefact caused spikes to be missed throughout its length, then this would create spurious OFF-like responses in cells with very steady firing, as the firing rate would appear to decrease while the stimulus was on and return to baseline when it was turned off. Again, such responses were never observed. In summary, the artefact does not appear to pose significant problems for spike detection or sorting. Occasionally, the tail end of spike waveforms are corrupted by saturation periods that happen to occur just after a spike. In most cases, Offline Sorter leaves these spikes unsorted and where it does attempt to sort them it appears to assign them to the correct unit. Such instances are rare, however: most channels show no such corrupted waveforms and those that do usually only have one or two even if tens or hundreds of thousands of spikes were recorded. Thus missed spikes due to Offline Sorter not assigning saturation-corrupted waveforms to any unit will not serious affect the analysis. Finally, note that none of these considerations apply to the APS recordings in chapter 3, as the much lower light intensities used for photoreceptor stimulation in those experiments do not induce noticeable artefacts.

5.2.2 *Experimental Design*

Most of the experiments described in this chapter fall into one of two designs: stimulus decoding or a simulated two-alternative forced choice (2AFC) task. All stimuli in a given recording were presented in randomised blocks, wherein each unique stimulus is presented exactly once in random order, before moving onto the next block. All sets of stimuli were presented once each in control conditions and again in the presence of 40μM MFA (allowing at least one hour for the drug to take effect). For each set of stimuli there was a preprocessing step to detect responsive cells, similar to that used in Chapter 4.

Detecting Responsive Cells. First, on certain trials a 250ms white or black (i.e. no stimulus) full field was presented (one trial each per block in stimulus decoding experiments, two each in 2AFC experiments). I used responses to the black stimulus to bootstrap a spontaneous activity distribution by dividing the entire trial into 50ms bins and then calculating the mean number of spikes in a number of randomly selected bins equal to the number of presentations of the black stimulus. 10000 samples were taken. Next, I constructed a PSTH with a bin width of 50ms from the responses to the white stimulus. I excluded cells that fired on average less than one spike per trial immediately. For each remaining cell, I assigned a one-tailed p-value to the bin with the most spikes using the spontaneous activity distribution bootstrapped previously. Finally, I selected cells with a Bonferroni-corrected p-value less than 0.05 as responsive.

There are a few notable differences between this procedure and the one used in chapter 4. First, instead of one bin for the entire detection stimulus, I used multiple bins. This is due to the increased diversity of response types observed in these experiments. Whereas responses to the 100ms µLED flash could be accurately captured with a single bin, responses to the 250ms projector flash were more varied: from slight, sustained increases in firing rate, to more transient bursts, or even down to single stimulus-evoked spikes. Using a single wide bin obscures the responses of transient cells, but on the other hand, using too narrow a bin biases the selection procedure against cells with weak but sustained responses: I chose 50ms as a compromise after manual investigation of different bin widths. Further, using a fixed bin to evaluate responses risks missing responsive cells, as the latency of responses varied considerably between cells, so I used the bin with the maximum firing rate during stimulus presentation to assign the p-value. Finally, visual inspection of rasters suggested the false discovery rate correction used in chapter 4 was too liberal for recordings with many hundreds of recorded cells, so I used Bonferroni correction instead.

Stimulus Decoding Experiments. Two sets of flashed gratings and one set of flashed letters were presented in a stimulus decoding paradigm. In this paradigm, the goal of the analysis was to decode a certain property of the stimulus (target variable) from the RGC population response while controlling for the effect of one or more other stimulus properties (confounding variables). Stimuli were presented in randomised blocks, once at every level of target and confounding variables. Then, within each level of the confounding variables, I trained a Bayesian classifier to determine which level of the target variable was presented on each trial, as described in section 2.3.3. In all cases, I took each cell's response as the number of spikes fired during presentation of the stimulus, so $p(r_i|s)$ by necessity follows a categorical distribution.

Simulated Two-Alternative Forced Choice Task. In the simulated 2AFC task paradigm, instead of a single stimulus being presented on each trial, each trial follows this sequence: either a stimulus or an isoluminant mask is presented for 250ms, followed by 250ms of a black full field, then which ever of the mask or the stimulus was not presented previously is presented for 250ms. Finally, a black full field is presented for 750ms before the next trial begins. Otherwise, this paradigm is very similar to the stimulus decoding paradigm, except that the target variable is which of the grating or mask was presented first and all other stimulus properties are treated as confounders. Following Jacobs et al. (2009), the Bayesian classifier is awarded a success on each trial if

$p(\text{grating}|r_g) > p(\text{grating}|r_m)$

where r_g is the response of the RGC population to the grating and r_m is the response to the mask. (If both posteriors are equal, the classifier is awarded half a success.) Only gratings were used in the 2AFC paradigm and, again, I took the response as the number of spikes fired by each cell during presentation of each stimulus.

5.2.3 *Stimuli*

Table 5.1 details the main stimuli used in the experiments presented in this chapter. The letters were presented as white stimuli on a black background; gratings were stationary spatial square waves aligned to horizontal axis of the MEA. The two largest sizes of letter were large enough to cover most of the MEA and so were presented centred. The smallest and second smallest were presented in a 3 × 3 and 2 × 2 grid pattern, respectively, and letter position was treated as an additional confounding variable nested in letter size. For training the Bayesian classifier for these sizes of letter, I also divided the MEA into matching grids and only used cells recorded on electrodes in the corresponding grid cell to decode letters presented in each position. The separation between letters was always larger than the average ChR2 RGC receptive field (see chapter 4) so it was unlikely that any cells were stimulated by multiple letters on the same trial.

Also note that in one experiment the letters were presented at a different set of sizes (384, 576, 1056 and 1920 µm letters in a 4×4, 3×3, 2×2 or 1×1 grid), but classifier performance for both the 384µm and 576µm letters was around chance, so I decided to exclude those and use only the larger size letters for all subsequent experiments. Results from the first letters experiment are not included in the results presented in this chapter.

5.2.4 *Psychometric Function Fitting*

I analysed the results of the the letters experiments using the Matlab toolbox `psignifit` (version 2.5.6), a tool for fitting psychometric functions to nAFC data (Wichmann and Hill 2001a,b) (although I included the letters experiment in the stimulus decoding paradigm, it can also be thought of as a 10AFC task). A psychometric function $\Psi(x; \mathbf{\Theta})$ gives the performance of a subject in some task as a function of some property x of the stimulus. Here, the 'subject' is the Bayesian classifier for each retina in each condition, the task is the letters task, and x is the feature size of the letters. $\mathbf{\Theta}$ is a parameter vector that controls the shape of the function. `psignifit` uses maximum likelihood inference to fit curves to data, which I will describe briefly here.

Maximum likelihood estimation fits curves to data by finding the set of parameters $\hat{\mathbf{\Theta}}$ that maximises the likelihood of the $\mathbf{\Theta}$ given the data D, which is identical to the probability of the data according to the model with those parameters:

$$\hat{\mathbf{\Theta}} = \arg\max_{\mathbf{\Theta}} \mathcal{L}(\mathbf{\Theta}|D) = \arg\max_{\mathbf{\Theta}} p(D|\mathbf{\Theta})$$

As an extension to this, `psignifit` optionally allows the user to specify prior distributions for each parameter, which are used to weight the likelihood function. In other words, given a set of priors $p(\mathbf{\Theta})$, `psignifit` attempts to maximise

Stimulus	Reps	Property	Values
Contrast Gratings (SD)	50	**Phase**	$(0..7)\pi/4$
		Michelson Contrast	7.8%, 15.5%, 23.0%, 86.6%, 91.0%, 93.2%
		Average Irradiance	0.71, 0.71, 0.71, 0.23, 0.34, 0.45 mW/cm^2
		Bar Width	640 µm
Frequency Gratings (SD)	50	**Phase**	$(0..7)\pi/4$
		Bar Width	48, 192, 384, 624, 912, 1248 µm
		Michelson Contrast	93.2%
		Average Irradiance	0.45 mW/cm^2
Sloan Letters	25	**Letters**	C, D, H, K, N, O, R, S, V, Z
		Height	576, 1056, 1632, 2304 µm
		Letter Irradiance	1.65 mW/cm^2
Contrast Gratings (2AFC)	50	Phase	$(0..3) \times \pi/2$
		Michelson Contrast	10.4%, 20.5%, 30.9%, 40.6%, 50.6%, 60.04%
		Average Irradiance	0.53 mW/cm^2
		Bar Width	640 µm
Frequency Gratings (2AFC)	50	Phase	$(0..3)\pi/2$
		Bar Width	48, 192, 384, 624, 912, 1248 µm
		Michelson Contrast	60.04%
		Average Irradiance	0.54 mW/cm^2

Table 5.1: Stimulus properties for the main stimuli used in the experiments in this chapter. Bolded property value names represent the target variable for stimulus decoding experiments. Note that for the 2AFC stimuli, the number of repetitions listed includes both grating-first and mask-first conditions. Also note that irradiance and contrast cannot be separated: where multiple values are listed for both, gratings of each contrast were presented at the corresponding irradiance, not at every possible contrast × irradiance pair. Reps = repetitions, SD = stimulus decoding paradigm, 2AFC = simulated two-alternative forced-choice task paradigm.

$$\mathcal{L}(\boldsymbol{\Theta}|D)p(\boldsymbol{\Theta}) = p(D|\boldsymbol{\Theta})p(\boldsymbol{\Theta})$$

Although Wichmann and Hill (2001a) do not state this explicitly, this essentially turns the maximum likelihood procedure into a Bayesian inference, as by Bayes' rule

$$p(\boldsymbol{\Theta}|D) = \frac{p(D|\boldsymbol{\Theta})p(\boldsymbol{\Theta})}{p(D)}$$

But since $p(D)$ is the same for all $\boldsymbol{\Theta}$ for a given set of data, maximising the numerator on the right hand side maximises the whole expression. Unlike in traditional Bayesian inference, however, `psignifit` only provides point estimates of the posterior distribution $p(\boldsymbol{\Theta}|D)$, whereas Bayesian inference usually attempts to estimate the posterior probability density over a range of possible parameter values. Point estimates are fine for the purposes for which I am attempting to fit curves to the letter performance data here (see section 5.2.5).

Specifying priors provides two benefits over traditional maximum likelihood estimation. First, it allows completely nonsensical values to be excluded (e.g. negative visual angles). Second, if the user has some intuition as to which parameter values are more likely than others, they can express this in the prior distribution. For the first purpose, `psignifit` allows the user to specify the prior implicitly by providing upper and lower limits for the parameter under consideration, in which case the prior is the uniform probability distribution within those limits; for the second, the user can specify the prior explicitly by selecting from a limited number of standard probability distributions and specifying the necessary parameters, or providing their own prior probability distribution programmatically.

Like many maximum likelihood methods, `psignifit` in fact maximises the log-likelihood ($\log(\mathcal{L}(\boldsymbol{\Theta}|D)p(\boldsymbol{\Theta})) = \log\mathcal{L}(\boldsymbol{\Theta}|D) + \log p(\boldsymbol{\Theta})$). It does so using the Nelder-Mead simplex search algorithm (Wichmann and Hill 2001a; Press et al. 2007).

Psychometric functions in `psignifit` have the following form:

$\Psi(x; m, w, \lambda, \gamma, \alpha) = \gamma + (1 - \gamma - \lambda)F(x; a, b, \alpha)$

Where $F(x)$ is a function that spans the range [0,1], hence $\Psi(x)$ goes from γ to $(1-\gamma-\lambda)$. γ corresponds to the 'guess rate', i.e. the performance one would expect by chance, and is thus fixed at $^1/_n$ for an nAFC task. Normally, λ is the 'lapse rate', i.e the rate at which the observer misses the stimulus and is forced to guess. However, the 'observer' in this case is a machine and cannot lapse. More generally, this parameter can be interpreted as controlling the maximum possible performance, however given the limited range of letter sizes used here, in practice this parameter is not well constrained by the data, particularly in control conditions, so I chose to fix it at zero[2], i.e. a theoretical maximum performance of 100%. a controls the midpoint of the psychometric curve, i.e. the point where performance is halfway between the minimum and maximum. b controls the slope of the curve and is inversely related to the gain: as b approaches zero, the curve becomes a step function, and as b increases the curve gets wider and shallower.

`psignifit` provides a variety of forms of $F(x)$, mostly sigmoid in shape. The precise choice of model function has little influence on the resulting parameters (Wichmann and Hill 2001a); I chose the logistic function, which is parameterised in `psignifit` as follows:

$$F(x; a, b, \alpha) = \frac{1}{1 + e^{-\frac{x-a}{b}}}$$

This equation can be reparameterised in terms of the the midpoint, m, and width w, of the sigmoid as follows:

$$\begin{aligned} m &= a \\ w &= F^{-1}(1-\alpha) - F^{-1}(\alpha) = 2b \log\left(\frac{1}{\alpha} - 1\right) \end{aligned}$$

In this form, m gives the stimulus value that gives a performance halfway between the maximum and minimum ($\frac{1+0.1}{2} = 55\%$ for a 10AFC) and w gives the width of the sigmoid as the performance above chance rises from α to $1-\alpha$, i.e. 10% to 90% if $\alpha = 0.1$.

---

[2] This is why I used the older `psignifit` 2.5.6 and not the newer version 3.0, which among other changes does not allow the user to fix the λ parameter.

As stated, `psignifit` allows the user to optionally specify Bayesian priors to constrain the values of each parameter of the psychometric function. For the reasons mentioned above, I fixed λ at zero. m and w are expressed in units of degrees of visual angle, thus values less than zero or greater than 360 are nonsensical. As such, I constrained b to lie within in the range 0 to $2 \times 360 \log \left(\frac{1}{0.1} - 1 \right) = 81.9215$ with a flat prior within this range. The midpoint should be greater than zero and less than the feature size corresponding to a letter that covers the entire retina, as one would expect performance to plateau or even drop off once the letter no longer fits onto the retina. The mouse retina covers approximately 160 degrees of the eyeball (Marc 2006b) and since the relevant features for discrimination in Sloan letters are one fifth the size of the letters themselves (Sloan 1959), this corresponds to a feature size of 32 degrees. Moreover, the midpoint is likely to be closer to the middle of this range than either of these extremes. Thus, for a I used a Gaussian prior with mean 16°and standard deviation 8°: in other words, the midpoint is probably somewhere in the middle of the range of plausible feature sizes and unlikely to be less than zero degrees (mean minus 2 S.D.) or greater than 32 (mean plus 2 S.D.). I also tested a variety of other priors, but these largely did not affect the conclusions (see section 5.4.2).

5.2.5 *Simulated LogMAR Testing*

Using the results of the letter experiments and the fitted psychometric function, I derived a visual acuity rating for each *ChR2dr1* retina before and after application of MFA using a simulated logMAR (logarithm of the Minimum Angle of Resolution) test. In a traditional logMAR test, the patient is presented with a chart of Sloan letters, five to a row, where each row subtends a visual angle 0.1 decadic log units smaller than the row above (visual angles are given in minutes of arc, i.e. 1⁄60 of a degree). The patient is then asked to read each row and given a visual acuity score VA using the following formula (Carlson and Kurtz 2012):

$$VA = logMAR_1 + 0.1 - 0.02N$$

where $logMAR_1$ is the logMAR value of the first row of letters and N is the total number of letters correctly identified across all rows.

Normally, the largest letters on the chart subtend 10 minutes of arc (Bailey and Lovie 1976), i.e. a logMAR score of 1, but a *ChR2rd1* mouse is likely to have worse visual acuity than a normally sighted human. Hence, for my simulated logMAR test, I set the largest row size to the angle subtended by the entire mouse retina (approximately 160 degrees or 9600 minutes of arc). Since the features needed to distinguish Sloan letters are one fifth the size of the letters themselves (Sloan 1959), the features in the largest row subtend 1920 minutes of arc, corresponding to a logMAR score of about 3.3. I kept the change in size between subsequent rows at 0.1 decadic log units. At each row size, I estimated the number of letters 'read' by each retina in each condition as five times the decoder performance (because each row has five letters), calculated using the fitted psychometric function. The test continued until the performance dropped below one letter read, i.e. below 20%. I then gave each retina in each condition a visual acuity score in logMAR units using the formula above. These can be converted into a Snellen fraction S using the formula $S = 20/(20 \times 10^{VA})$.

5.2.6 ***Statistical Analysis***

I tested the distribution of decoder performances for normality at each spatial frequency, contrast or letter size tested in each condition (control or drug) using the Shapiro-Wilk test. This test was significant ($p < 0.05$) in only 4 out of 56 cases (12 each for the four sets of gratings and 8 for the letters). In other words, for the most part decoder performances were normally distributed within each level of each stimulus in both control and drug conditions. Hence, to test the effect of stimulus properties and drug I used a repeated measures ANOVA with frequency, contrast or letter size (as appropriate) and condition (control versus drug) as within-subjects factors. Degrees of freedom and p values reported in the text are after applying the Greenhouse-Geisser correction for violations of sphericity, but the overall pattern of results was largely the same regardless of whether sphericity was assumed or which correction was applied (Greenhouse-Geisser, Huynh-Feldt, or lower-bound[3]). Normality testing and ANOVAs were conducted in SPSS 21.

---

[3] Although with the lower-bound correction for violations of sphericity, the interaction effects for the 2AFC gratings experiments were no longer significant.

None of fitted psychometric function parameters or estimated visual acuity scores from the letter experiments deviated significantly from normality (Shapiro-Wilk test, $p > 0.05$), so I tested differences in these values using paired t-tests.

5.3 Results

5.3.1 *Successful Optogenetic Stimulation Using the APS Projector*

GH successfully recorded optogenetic responses from 14 *ChR2rd1* retinas and retinas from two mice hemizygous for ChR2 under the control of the Thy1 promoter and heterozygous for the *rd1* mutation of the *Pde6b* gene (*ChR2rd1 hetero*). As the *rd1* mutation is recessive, the *ChR2rd1 hetero* mice had ChR2-expressing RGCs, functional photoreceptors and no retinal degeneration.

First, it was necessary to confirm that the APS projector is bright enough to stimulate ChR2 without evoking unmanageable stimulation artefacts. To do this, GH recorded and I analysed responses to 30 repetitions of two-second full-field white flashes presented at a rate of 0.25 Hz in two *ChR2rd1 hetero* mice in the absence and presence of 20μM DNQX, an ionotropic glutamate receptor antagonist, and 20μM L-AP4, an mGluR6 agonist. This cocktail of drugs blocks the photoreceptor to bipolar cell synapses, leaving only melanopsin- and ChR2-expressing RGCs able to respond to light (but melanopsin responses can be distinguished from ChR2 responses easily by the former's extremely high latency and prolonged duration compared the latter). To quantify responses to these stimuli, I calculated the peak firing rate of each cell in any 100ms bin during (ON responses) or between (OFF Responses) the white flashes, divided its spontaneous firing rate. Spontaneous firing rates for each cell were calculated separately for each set of flashes (to account for non-stationary firing rates) as the number of spikes fired between the end of preceding set of stimuli and the beginning of the next, divided by the time between stimulation runs (for the first run I used the time between the beginning of the recording and the presentation of the first stimulus). Figure 5.1 shows the results of this analysis for 133 RGCs (142 selected according to the method described in section 5.2.2 less 9 cells excluded due to having zero spontaneous firing rate) recorded in a P95 *ChR2rd1 hetero* mouse retina before and after photoreceptor blockade and at two different light intensities.

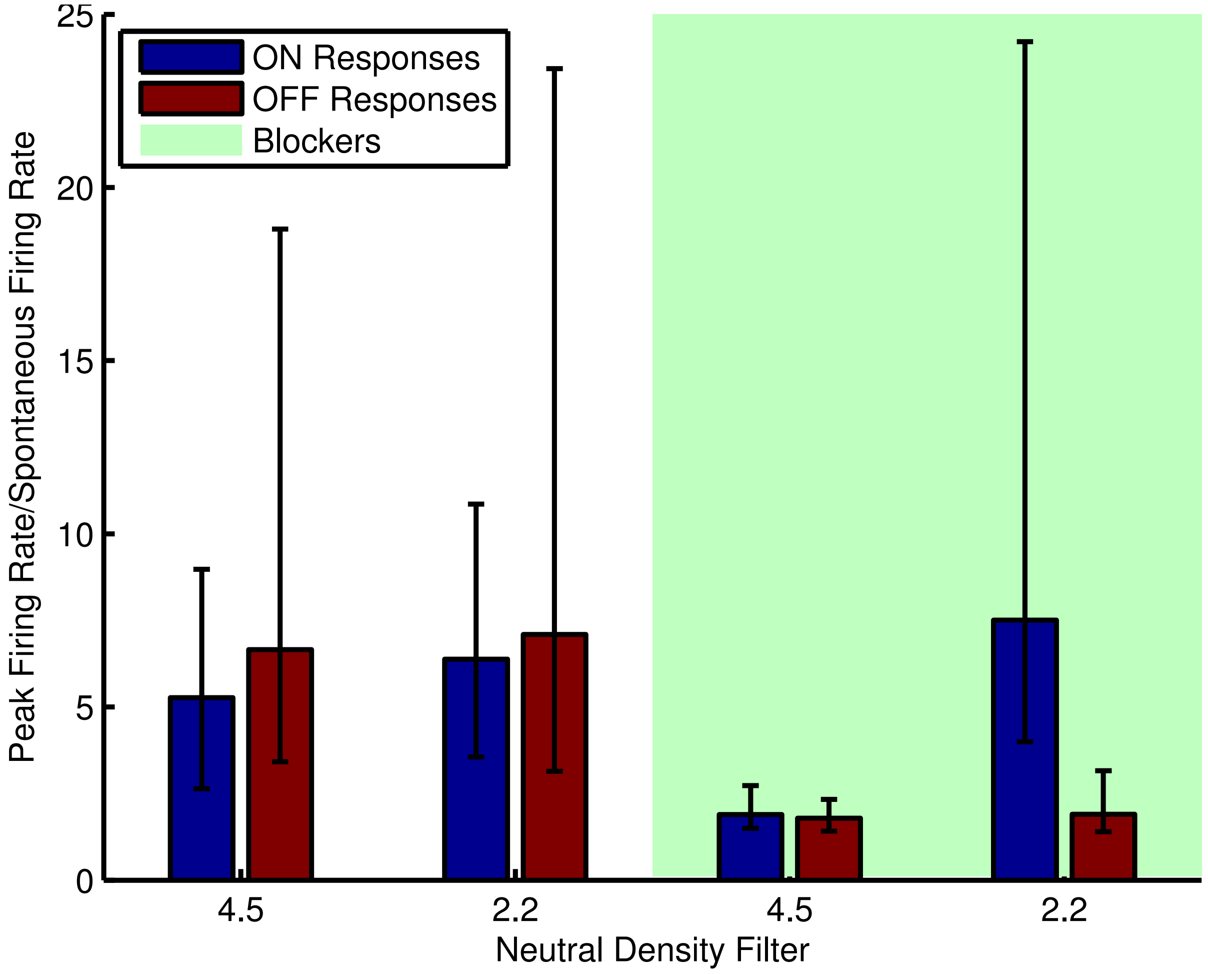

Figure 5.1: Median normalised peak firing rate in any 100ms bin following a two second white (blue) or black (red) full field flash for 133 cells recorded from a P95 *ChR2rd1 hetero* mouse retina in control conditions (white background) or in the presence of DNQX and L-AP4 (green background) at two different light intensities. Error bars are inter-quartile range (IQR). X-axis units are decadic log units, e.g. 4.5 means the light is attenuated roughly 31000-fold.

Endogeneous retinal photoreceptors are extremely sensitive to light and RGC responses to photoreceptor stimulation can be divided into ON (responses to light increment) and OFF (light decrement) pathways. Thus, for photoreceptor stimulation, one would expect both ON and OFF responses to light and these responses would be stronger the brighter the light. ChR2 is relatively light insensitive and purely excitatory, so for ChR2 stimulation one would expect to see only ON responses to bright but not to dim light and no OFF responses at all. The pattern in figure 5.1 matches the expected pattern for photoreceptor stimulation in control conditions and that expected for ChR2 stimulation after applying the blockers. A very similar pattern was observed in two more retinas from a different *ChR2rd1 hetero* mouse (data not shown). Thus, it appears that, at ND2.2 or an irradiance of approximately 0.9mW/cm^2, the APS projector is bright enough to excite ChR2, at least in healthy retinas.

To confirm this was also true for blind, ChR2-expressing retinas, GH recorded and I analysed (in the same manner as for the P95 retina) responses to the same stimulus (at ND2.2) in a P96 *ChR2rd1* retina. Figure 5.2 shows the results of this analysis for 244 cells (305 selected according to the method in section 5.2.2 less 61 excluded due to having zero spontaneous firing) in control conditions and in the presence of 40µM MFA and at varying K$^+$ concentrations.

Virtually all photoreceptors should have degenerated by P96 in an *rd1* retina (Carter-Dawson et al. 1978; Lin et al. 2009), so one would expect only ChR2-mediated ON responses in these retinas. However, there was little evidence of ON or OFF responses in control conditions and it was difficult to discern if the retina was sensitive to ChR2 stimulation by visual inspection of the rasters. After applying 40µM MFA, which has been shown to reduce *rd1* spontaneous activity and increase the signal-to-noise ratio of ChR2 responses (chapter 4), there was very little change in the size of responses to light increase or decrease. Thus, in an effort to improve the responsiveness of the ChR2 RGCs by increasing membrane excitability, GH increased the extracellular potassium concentration (from 3 to 9mM), which causes membrane depolarization. This caused a dramatic, dose-dependent increase in normalised peak firing for ON responses, suggesting successful ChR2 stimulation. This was confirmed by visual inspection of the rasters. One example is shown

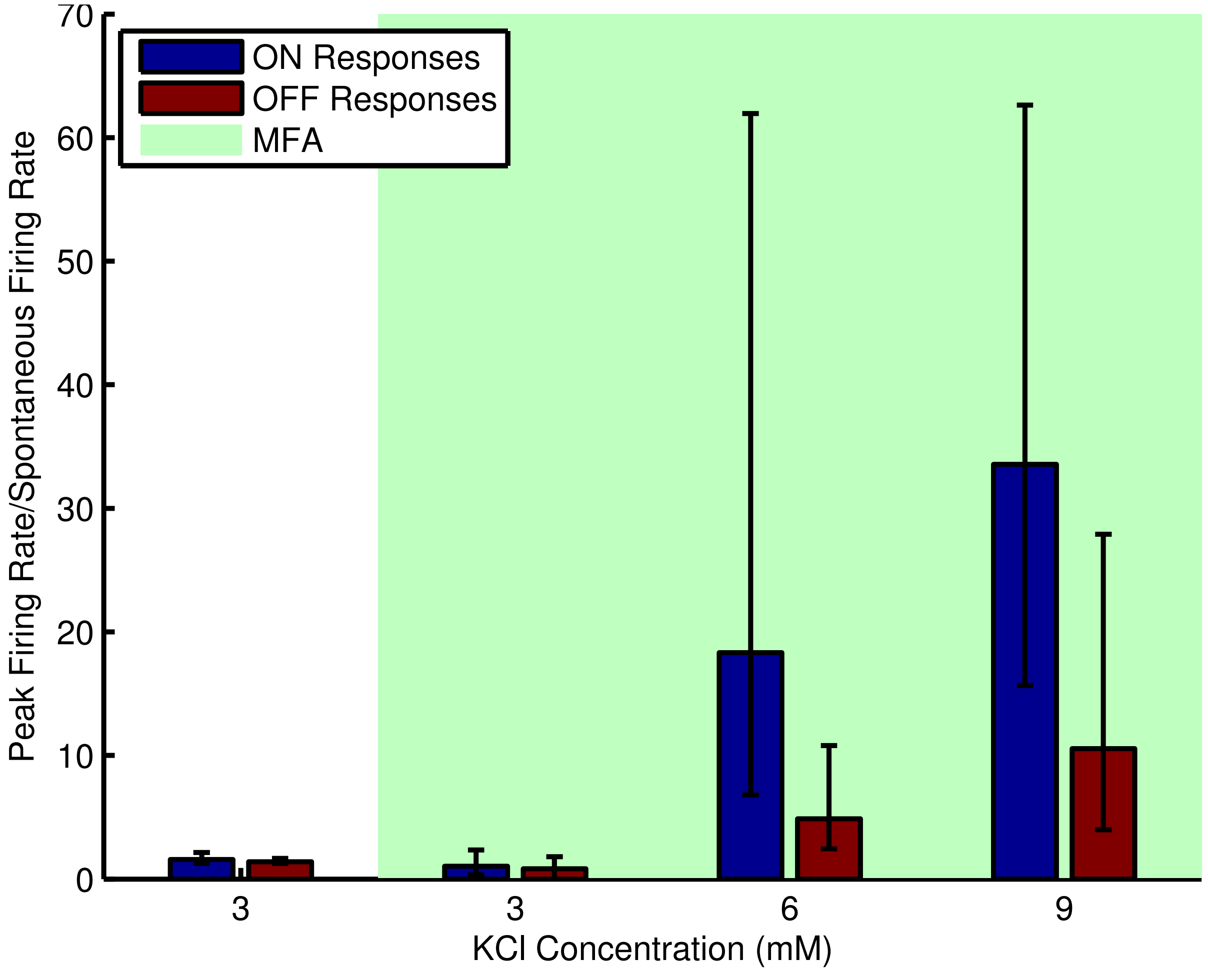

Figure 5.2: Median normalised peak firing rate in any 100ms following a two second white (blue bars) or black (red bars) full field flash at ND2.2 for 244 cells recorded in a P96 *ChR2rd1* mouse retina in control conditions (white background) or in the presence of 40μM MFA (green background) at varying K^+ concentrations. Error bars are IQR.

in figure 5.3, although there was incredible variety in the strength and temporal pattern of responses. Interestingly, OFF responses were also apparently improved, albeit to a lesser extent. However, on visual inspection of all 1450 raster plots of RGC firing from this retina between flashes, I did not observe a single response resembling anything like a photoreceptor-mediated OFF response. Thus the apparent increase in OFF responses figure 5.2 is not due to ChR2 stimulation but some other effect, for example increased burstiness of low firing rate cells. Some cells showed a decrease in firing immediately following light off (e.g. figure 5.3), but in almost all cases this was seen in cells with high maintained firing during light on and thus likely represents suppression due to sudden removal of ChR2-mediated excitation rather than a result of surviving cone pathways.

These results demonstrate that it is possible to evoke RGC responses optogenetically using the APS projector, although in order to see significantly stronger and more numerous responses, it is necessary to increase the extracellular potassium concentration above physiological levels in the *rd1* homozygous retina. As such, all data presented in the remainder of this chapter is taken from recordings conducted with an aCSF potassium concentration of 9mM (as opposed to the usual 3mM), where the potassium concentration was increased after the retina had been allowed to settle onto for two hours but before any recordings were taken. Additionally, two control experiments (not presented here) were conducted using 3mM potassium, wherein a subset of the stimuli used in the main experiments of this chapter were presented to the retina before and after applying MFA. The overall pattern of results was similar to those shown below, apart from a lower number of responsive cells.

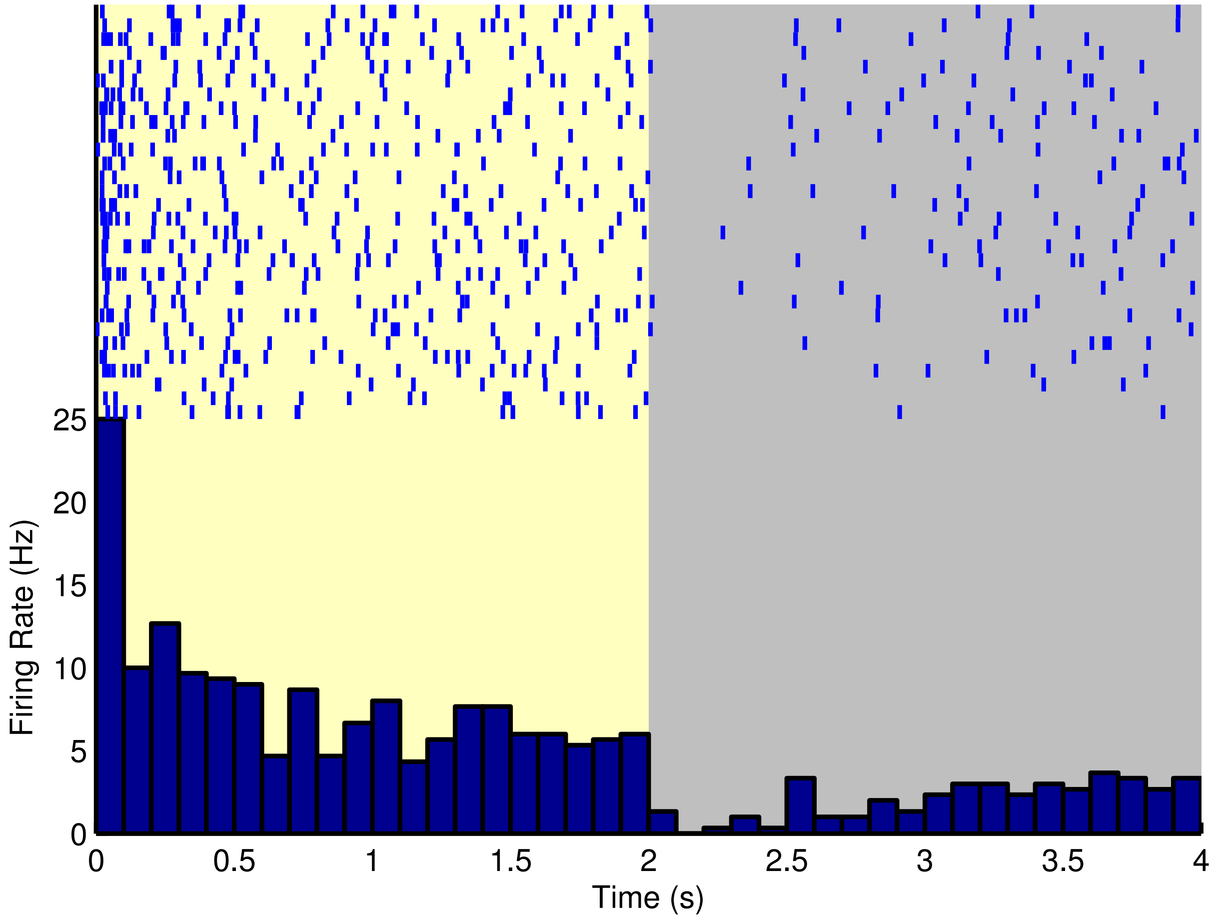

Figure 5.3: Raster plot and PSTH for an example RGC recorded from a P96 *ChR2rd1* mouse retina in response to 2s alternating white and black full fields in the presence of 40µM (green background) with 9mM KCl. The light is on during the yellow background and off during the grey background. There is no gap between trials: each line of the raster follows immediately from the line below. When the light comes on, there is a sharp, transient burst of action potentials followed by a sustained slight increase in firing. When the light goes off, there is a brief suppression of firing followed by recovery to baseline.

5.3.2 *Blockade of Spontaneous Activity Facilitates Decoding of Stimulus Properties*

Having established the ability to evoke RGC responses optogenetically using the APS projector, I set out to extend the results of chapter 4 using richer stimuli than are possible using the 256 binary pixels of the µLED array. Figure 5.4 shows the average performance of a Bayesian classifier in decoding the phase of flashed, maximum contrast gratings of varying spatial frequency from the RGC population response. This analysis was performed separately for five retinas, both in control conditions and in the presence of 40µM MFA. There was an improvement in performance at all spatial frequencies, with the gain being especially dramatic at low spatial frequencies. Spatial frequency (repeated measures ANOVA: $n = 5, F(1.224, 4.897) = 31.278, p = 0.002$), drug ($F(1, 4) = 22.936, p = 0.009$) and their interaction ($F(1.585, 6.339) = 12.879, p = 0.007$) all significantly affected the decoder performance.

Figure 5.5 shows similar results when the spatial frequency of the gratings was held constant and the contrast varied instead. Contrast was varied in two ways: in the high contrast, low average irradiance condition, the dark bars were black and the light bars varied from mid-grey to white, whilst in the the low contrast, high irradiance condition, the bars were two different shades of grey. In both conditions performance was very poor at all contrasts. Within each condition, performance seemed to increase slightly with increasing contrasts, and there also appeared to be a slight improvement in performance after applying MFA. Analysis of variance on these data revealed a significant effect of contrast (repeated measures ANOVA: $n = 5$, $sF(2.727, 10.908) = 9.976$, $p = 0.002$) but not drug ($F(1, 4) = 1.77$, $p = 0.253$) or the interaction between contrast and drug ($F(1.902, 7.609) = 0.423$, $p = 0.66$).

5.3.3 *Blockade of Spontaneous Activity Improves Spatial Acuity*

The results above for the frequency gratings corroborate the finding from chapter 4 that moderate concentrations of MFA improve the decoding of stimulus properties from optogenetic RGC responses, using a different feature (phase of a grating versus direction of a moving bar) and code (spike count versus latency) and over a range of spatial scales. One

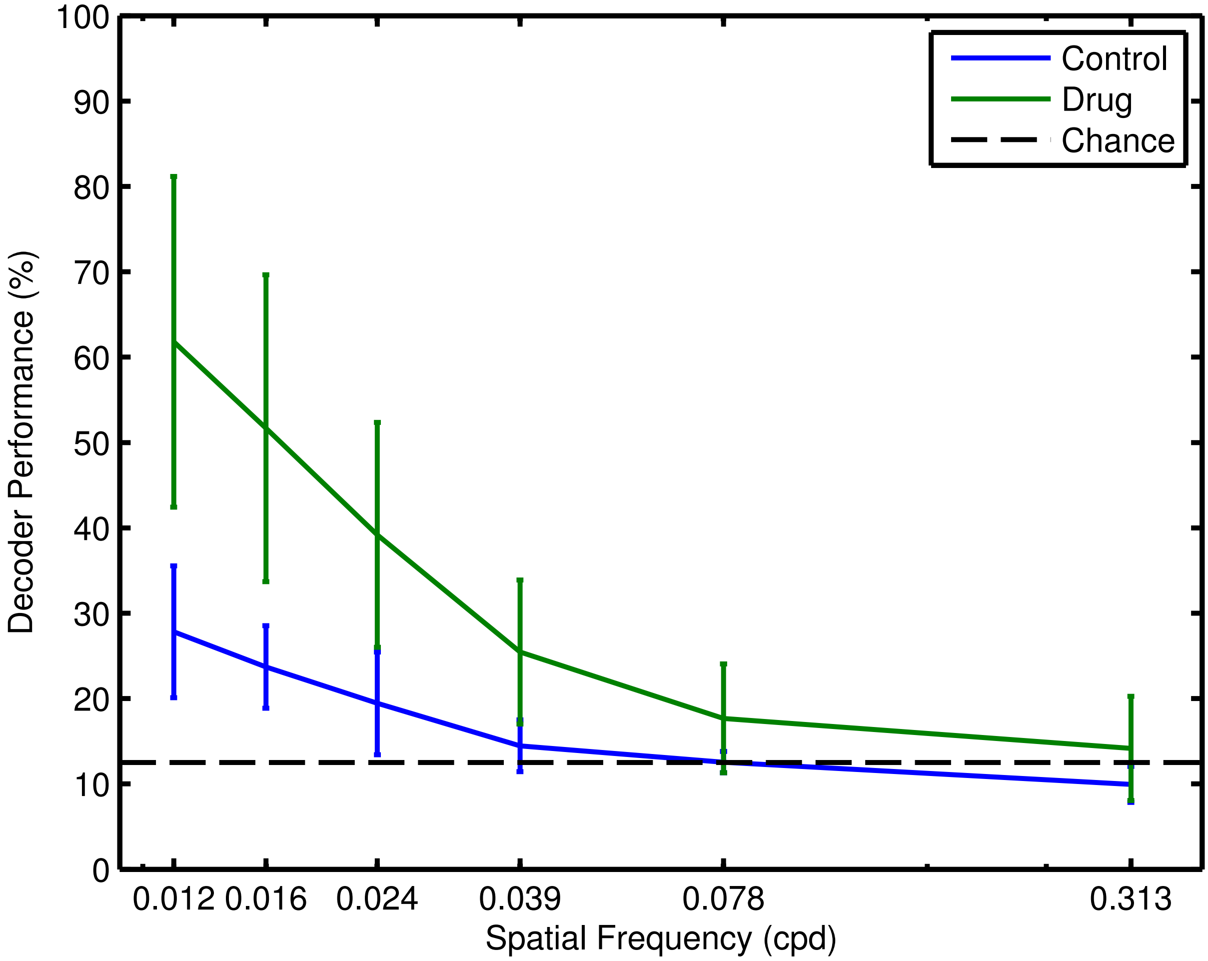

Figure 5.4: Average over five retinas of Bayesian classifier performance in decoding the phase of a flashed grating from the optogenetically-sensitive RGC population, as a function of spatial frequency. Blue lines denote performance in control conditions and green in the presence of 40µM MFA. Error bars are the mean over five retinas ± the standard deviation. The dotted black line denotes the performance expected by chance (12.5%).

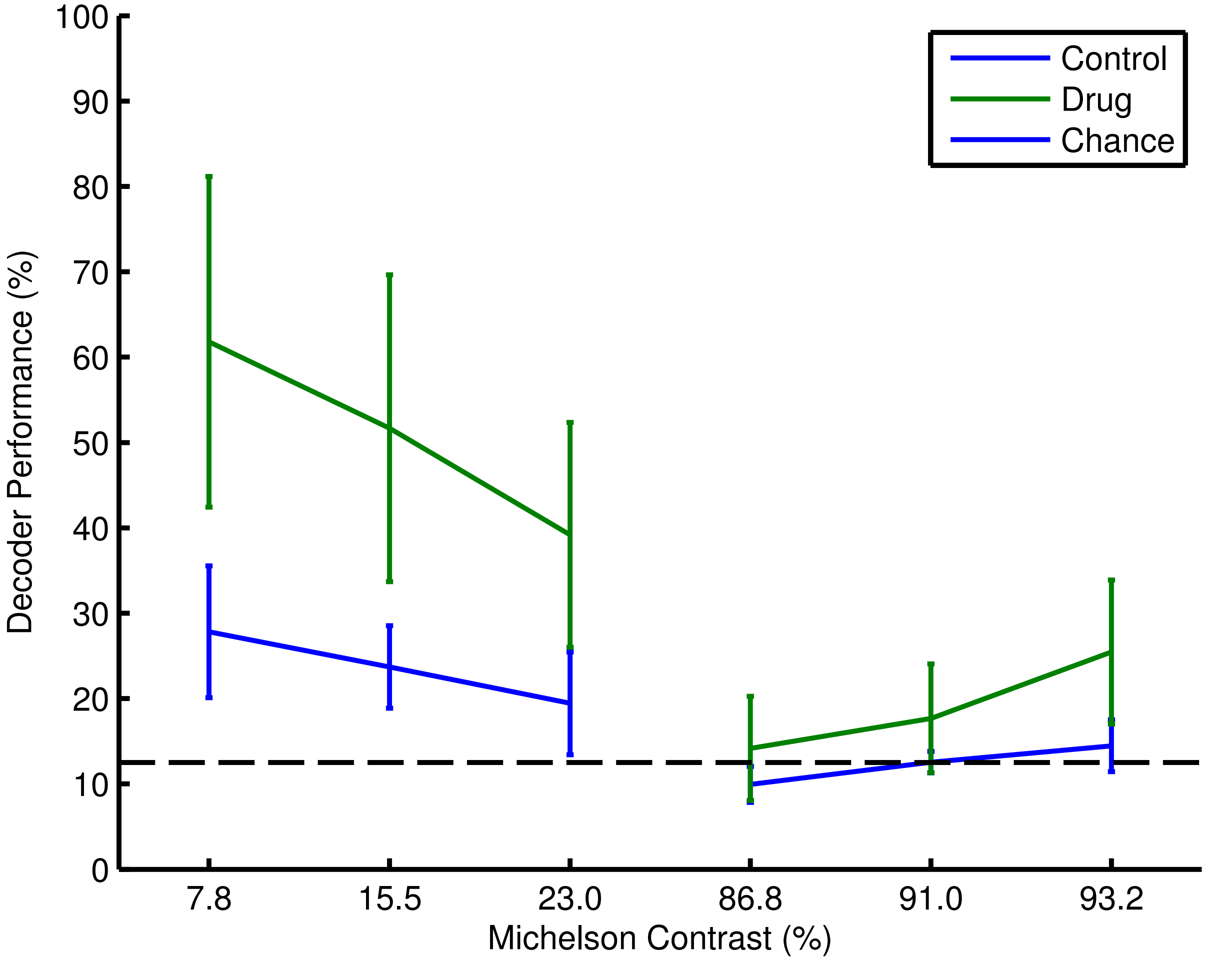

Figure 5.5: Average over five retinas of Bayesian classifier performance in decoding the phase of a flashed grating from the optogenetically-sensitive RGC population as a function of contrast. Blue lines denote performance in control conditions and green in the presence of 40µM MFA. Error bars are the mean over five retinas ± the standard deviation. The dotted black line denotes the performance expected by chance (12.5%).

logical conclusion of this is that reducing spontaneous activity improves the spatial acuity of optogenetic responses. To test this, I modified the grating experiment to simulate a two-alternative forced choice task in which the goal was to distinguish between a grey full field and an isoluminant grating. In each retina, before and after applying MFA, I trained a Bayesian classifier to guess which of the two stimuli, presented in rapid succession, was the grating.

Figure 5.6 shows the results of this experiment averaged over six retinas. Gratings were presented at a variety of phases and spatial frequencies: the results are shown averaged over phase (to control for uneven distribution of ChR2 responsive cells over the MEA) and as a function of spatial frequency. The decoder performance was scarcely above chance at all spatial frequencies in control conditions, but performance was much better after applying 40µMFA, confirming that reducing spontaneous activity improves spatial acuity. Statistical analysis showed significant effects of spatial frequency (repeated measures ANOVA: $n = 6$, $F(2.613, 13.066) = 23.1$, $p < 0.001$), drug ($F(1, 5) = 79.87$, $p < 0.001$) and their interaction ($F(2.052, 10.258) = 4.255$, $p = 0.044$) on decoder performance.

As another test of this, I also trained a Bayesian classifier to identify the ten Sloan letters, commonly used in optometry to measure patients' spatial acuity, from optogenetically evoked RGC population responses. The results are shown in figure 5.7. The pattern is very similar to that for the gratings: in control conditions, performance was poor for all but the largest letters and even for these the average performance was 30%, but after applying 40µMFA, the performance was higher at all sizes and over 80% on average for the largest letters. The effects of letter size (repeated measures ANOVA: $n = 7$, $F(1.497, 8.983) = 128.743$, $p < 0.001$) and drug ($F(1, 6) = 75.885$, $p < 0.001$) on decoder performance, as well as their interaction ($F(1.672, 10.033) = 48.519$, $p < 0.001$), were all highly significant.

To estimate visual acuity more directly, I fit the performance of the letter decoder as a function of feature size with a logistic function for each retina in each condition (see section 5.2.4). Table 5.2 gives the parameters of the fitted sigmoids. After applying MFA, the midpoint of the performance function was at a significantly lower feature size (paired t-test: $n = 7$, mean ± S.D. control $= 17.05 \pm 1.18$, drug $= 11.15 \pm 1.66$, $t(6) =$

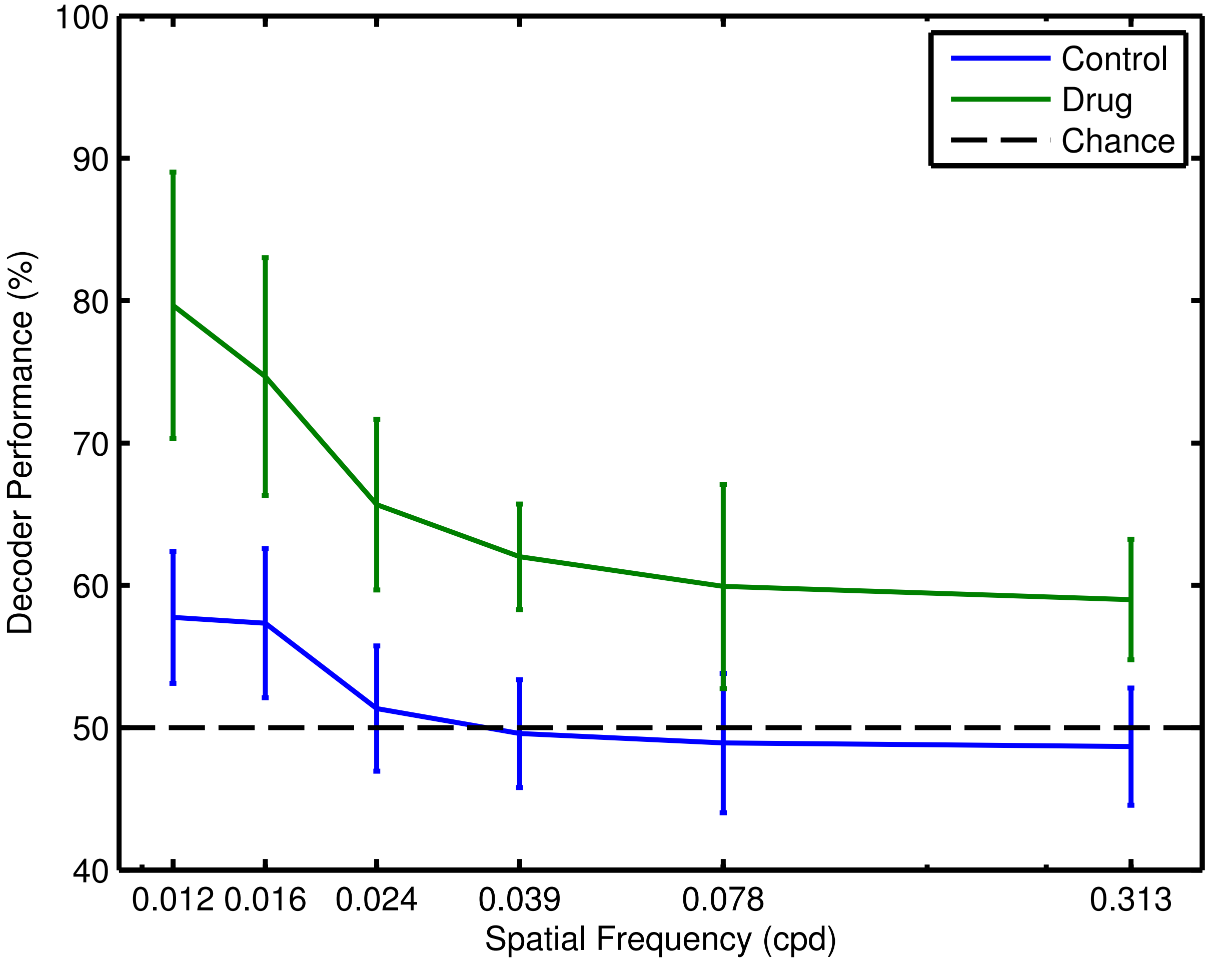

Figure 5.6: Average over four phases and six retinas of Bayesian classifier performance in distinguishing flashed gratings from an isoluminant mask using the optogenetically-sensitive RGC population response, as a function of spatial frequency. Blue lines denote performance in control conditions and green in the presence of 40µM MFA. Error bars are the mean ± the standard deviation between retinas. The dotted black line denotes the performance expected by chance (50%).

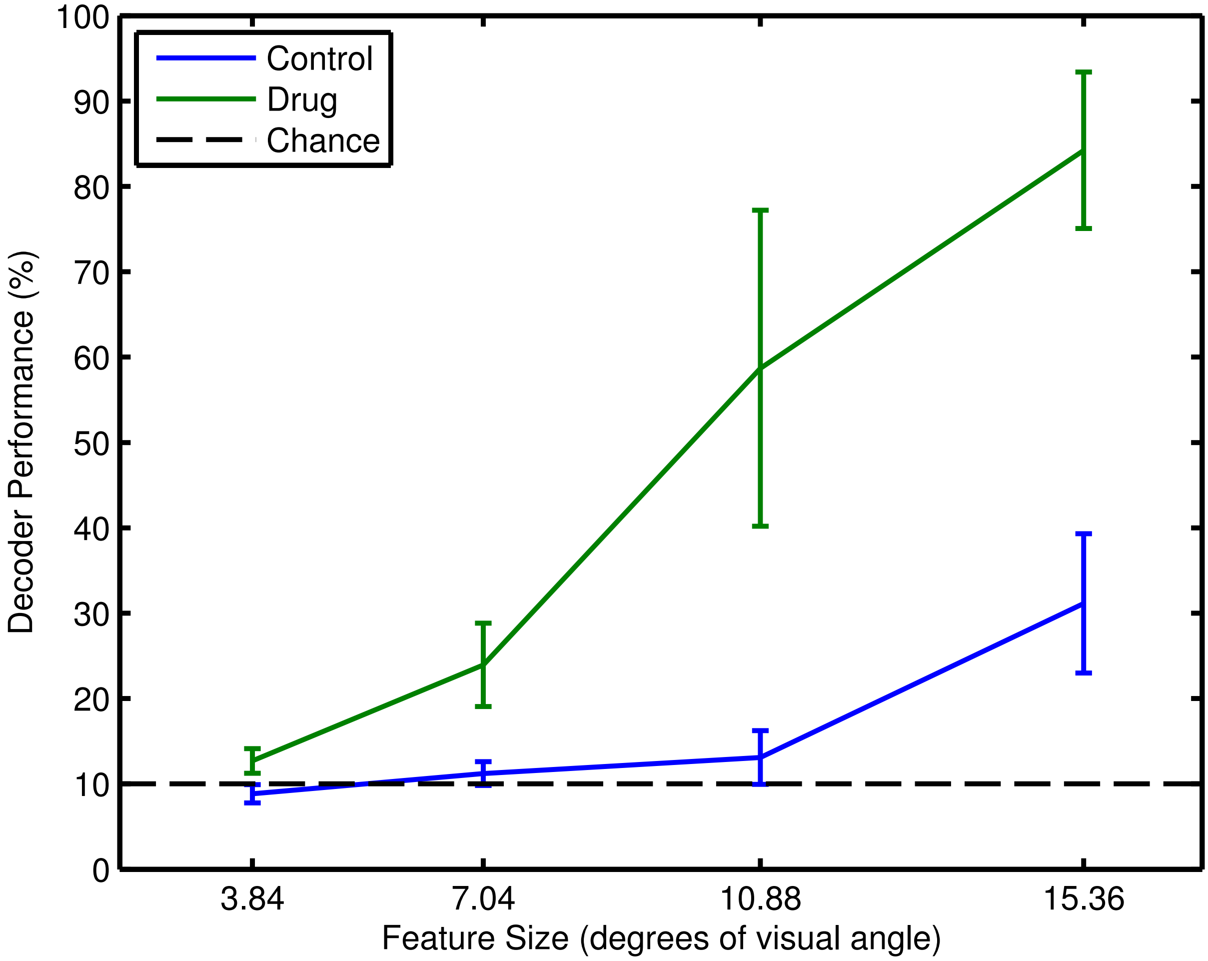

Figure 5.7: Average over seven retinas of Bayesian classifier performance in identifying flashed Sloan letters using the optogenetically-sensitive RGC population response, as a function of feature size. Feature size is the size of the features needed to distinguish one letter from another, i.e. one-fifth the height of the letter. Blue lines denote performance in control conditions and green in the presence of 40µM MFA. Error bars are the mean ± the standard deviation between retinas. The dotted black line denotes the performance expected by chance (10%).

Retina	Control m	Control w	Control VA	Control S	MFA m	MFA w	MFA VA	MFA S
1	15.98	5.51	3.03	20/21660	11.94	10.28	2.88	20/15087
2	15.91	0.92	3.00	20/20110	10.11	10.05	2.80	20/12625
3	17.77	7.78	3.07	20/23599	11.79	9.53	2.87	20/14933
4	18.59	10.97	3.09	20/24629	9.68	8.00	2.78	20/12177
5	15.76	1.94	3.01	20/20475	10.39	8.95	2.81	20/12892
6	18.20	9.52	3.08	20/24149	9.83	9.78	2.77	20/11794
7	17.16	8.81	3.04	20/22031	14.31	12.47	2.96	20/18293
Mean	17.05	6.49	3.05	20/22318	11.15	9.87	2.84	20/13972
S.D.	1.18	3.85	0.03	-	1.66	1.38	0.07	-

Table 5.2: Parameters for the logistic function fit to the decoder performance data from the letters task for each retina in control conditions and after application of 40µM MFA. m = midpoint of the function in degrees of visual angle (halfway between chance and maximum performance), w = width of the function in degrees of visual angle as it rises from 10% to 90% of the maximum performance above chance, VA = estimated visual acuity score in logMAR units (see section 5.2.5), S = estimated visual acuity score as a Snellen fraction (20/20 corresponds to normal human vision). S.D. = standard deviation. Mean S values are calculated from the mean VA scores and so standard deviations are not reported.

$7.66, p = 5.8 \times 10^{-6}$). The width of the psychometric function was significantly larger on average after applying MFA (mean ± S.D. control = 6.49 ± 3.85, drug = 9.87 ± 1.38, $t(6) = -2.18, p = 0.0498$), in other words the gain was lower, although this finding should be treated with caution given the lack of constraint on this parameter due to the low performance in control conditions (section 5.4.2).

Additionally, I used the fitted performance function to estimate the visual acuity of each retina before and after MFA using a simulated logMAR test (see section 5.2.5). The results of this test are also shown in table 5.2. The average visual acuity was significantly better (smaller logMAR score) after application of MFA (paired t-test: $n = 7$, mean ± S.D. control = 3.05 ± 0.03, drug = 2.84 ± 0.07, $t(6) = 7.22, p = 1.1 \times 10^{-5}$). This corresponds to a 23.5% improvement in visual acuity on average.

5.3.4 *Blockade of Spontaneous Activity Improves Contrast Sensitivity*

Finally, I decided to test if the same approach could improve contrast sensitivity as well as spatial acuity. Using the same simulated 2AFC task design, I trained a Bayesian decoder to distinguish flashed gratings of varying contrast from an isoluminant mask. Unlike in the previous contrast gratings experiment, I held the average irradiance constant and varied the contrast linearly over the range 10% to 60%. To avoid the poor performance seen in the previous contrast grating experiments, the value I chose for the average irradiance was deliberately set to one I found reliably evoked ChR2 responses from many RGCs in preliminary experiments. This value was brighter than 50% grey, hence why I was not able to reach the projector's maximum contrast of ~93%.

Figure 5.8 shows the results of these experiments. Decoder performance was significantly affected by contrast (repeated measures ANOVA: $n = 5$, $F(1.6, 6.401) = 50.943$, $p < 0.001$), drug ($F(1, 4) = 13.022$, $p = 0.023$) and their interaction ($F(2.070, 8.279) = 7.354$, $p = 0.014$). However, the pattern is slightly more complicated than for the frequency gratings or the letters. In both control and drug conditions, there appears to be a similar threshold at which performance increases above chance, and above this threshold the performance was higher in the presence of MFA. However, counter-intuitively, performance peaked just above this threshold and then dropped off again as contrast increased. Possible reasons for this are discussed in section 5.4.1.

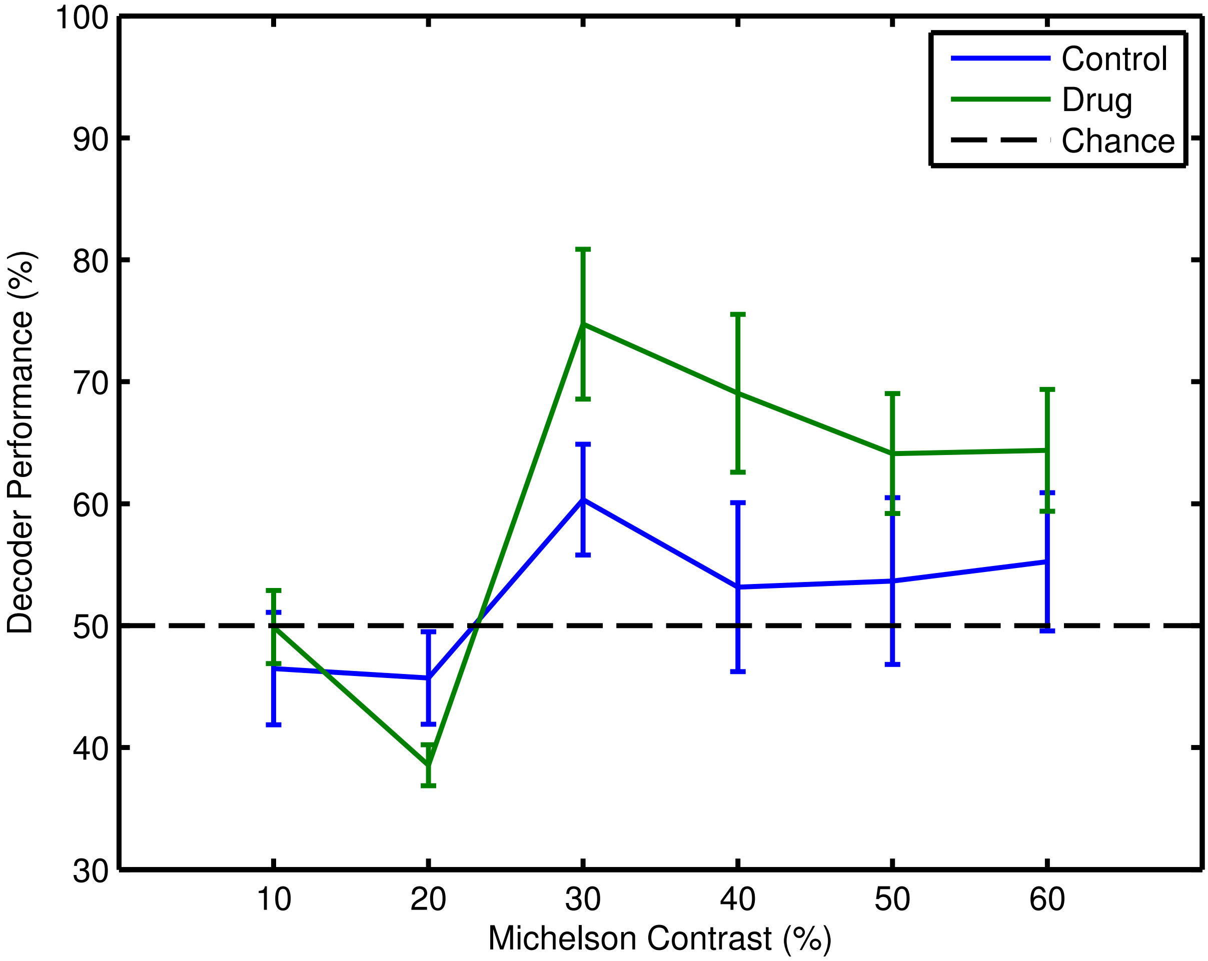

Figure 5.8: Average over four phases and six retinas of Bayesian classifier performance in distinguishing flashed gratings from an isoluminant mask using the optogenetically-sensitive RGC population response, as a function of contrast. Blue lines denote performance in control conditions and green in the presence of 40µM MFA. Error bars are the mean ± the standard deviation between retinas. The dotted black line denotes the performance expected by chance (50%).

5.4 Discussion

The above results demonstrate that, in line with the results in chapter 4 and those of Toychiev et al. (2013) and Ivanova et al. (2015), blocking spontaneous pathological oscillatory activity in dystrophic retinas with MFA improves prosthetic responses to a variety of stimuli across a range of spatial scales and contrasts. Further, the results from the 2AFC frequency grating and letters experiments show this results in an improvement in spatial acuity. The results from the two sets of contrast gratings experiments are slightly more equivocal and harder to interpret, but at certain combinations of irradiance and contrast there is a clear improvement in the information content of optogenetic retinal responses after application of MFA.

As noted in section 5.3.1, the main experiments in this chapter were conducted with a much higher than usual circulating potassium concentration (9mM as opposed to 3mM). This was done to increase the excitability of the RGCs and thus increase the number of cells with detectable responses. I do not believe this affects the strength of the conclusions from these data for two reasons. First, both control and MFA recordings were taken at this higher potassium concentration. Hence, the only difference between the two conditions is the absence or presence of MFA[4], hence any differences are due to the MFA and not the increased potassium concentration. Secondly, increasing the potassium concentration also exacerbates the spontaneous activity, so the number of responsive cells increases but their signal-to-noise ratios may in fact decrease, hence it is not immediately obvious that higher potassium should improve the quality of the responses in and of itself. Finally, two similar experiments were conducted with 3mM potassium and, apart from fewer responsive cells overall, the pattern of results in these experiments was similar to that seen above. Thus, the conclusions drawn from the data presented in this chapter still hold, regardless of the unusual recording conditions.

For the remainder of this chapter, I shall first discuss possible explanations for the contrast gratings data and the robustness of the results from the letter experiments, then conclude

---

[4] Also the time of the recording, but both *rd1* spontaneous activity and ChR2 responses are stable over several hours. Moreover, due to the difficulties in washing out MFA (see chapter 4), this was the only practical way to conduct these experiments.

by comparing the results here to results from studies of healthy mouse vision, mouse prosthetic vision and human prosthetic vision.

5.4.1 *Interaction Between Optogenetic Responses and Contrast*

Figure 5.8 shows that application of MFA improves sensitivity of RGC optogenetic responses to gratings with Michelson contrasts above 30%. What is not clear, however, is why the performance *decreases* as a function of contrast above this threshold. Intuitively, one would expect higher contrast gratings to be more distinguishable than lower contrast gratings and thus the performance should increase.

One possible way this behaviour could arise is due to the integration of ChR2-mediated photocurrents over space when the light intensities used are, due to the limitations of experimental setup, close to the ChR2 stimulation threshold. In particular, consider a ChR2-expressing RGC whose receptive field contains an edge between a white and a black bar. Further suppose that the irradiance needed to evoke an appreciable photocurrent is just below that of the mask. At low contrasts, the mask, light bar, and dark bar all excite ChR2 and the average irradiance over the receptive field is roughly the same for grating and mask, so it is difficult to distinguish the two stimuli by the cell's responses. However, at a certain contrast, the irradiance provided by the dark bar drops below the ChR2 threshold, so only the light bar evokes a photocurrent. If the light bar covers less than half of the cell's receptive field, the total irradiance provided the grating is now significantly less than that provided by the mask. As such, the responses of the cell to the grating are, on average, weaker than those to the mask. However, as the contrast increases, so too does the total irradiance provided by the grating over the cell's receptive field, hence the responses to the grating become stronger, until they are once again indistinguishable from those to the mask. Alternatively, if at medium contrasts the combination of light and dark (but still above threshold) bars evokes a stronger response than the mask, it is possible that increasing the contrast so that the irradiance of the dark bar drops below the ChR2 threshold would weaken the grating response, again bringing it closer to the mask response.

More concretely, suppose each ChR2 RGC is modelled as a nonlinear-linear-poisson (NLP)

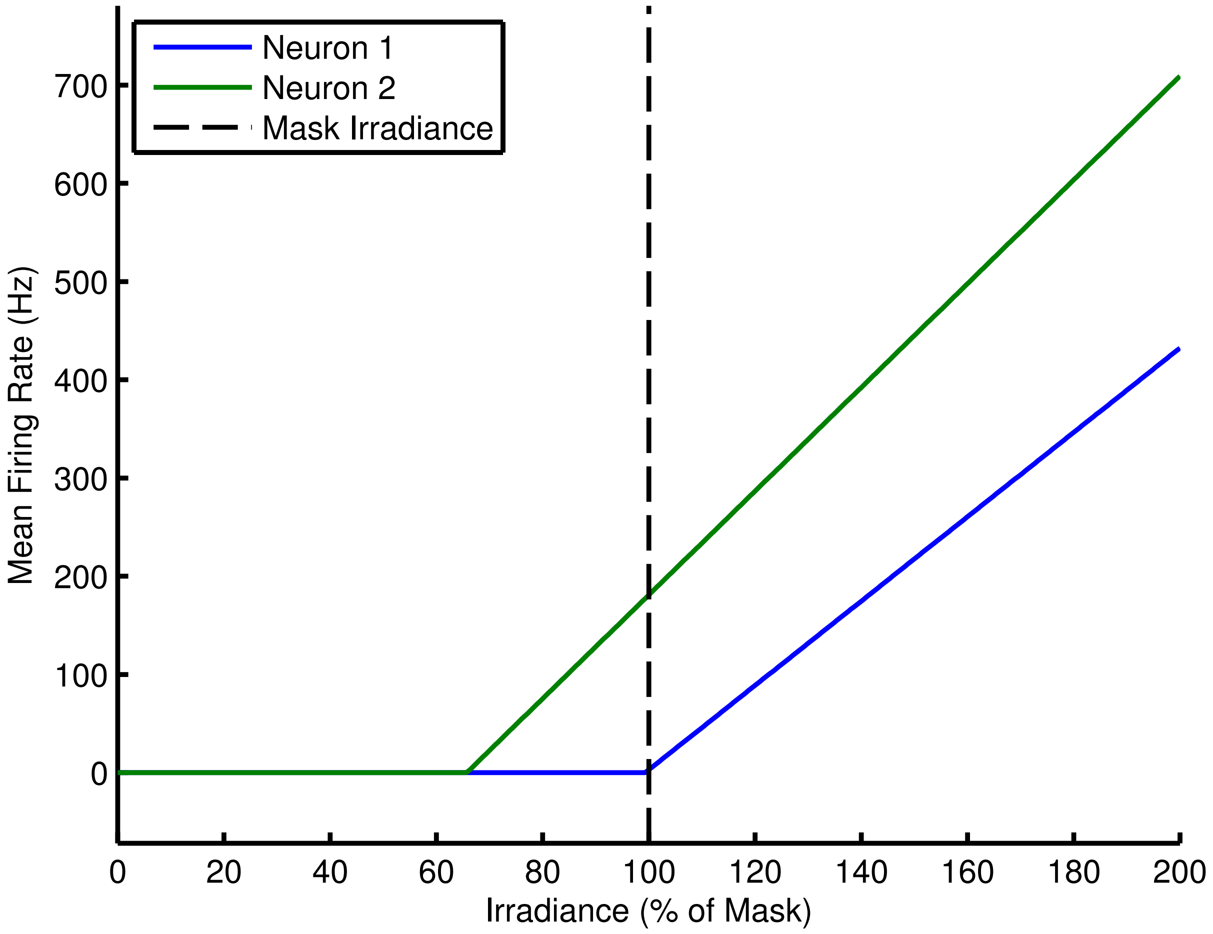

Figure 5.9: Response functions for the two model ChR RGCs. The first neuron (blue) only responds to irradiances greater than or equal to that of the mask. The second neuron (green) has a lower threshold and a slightly higher gain.

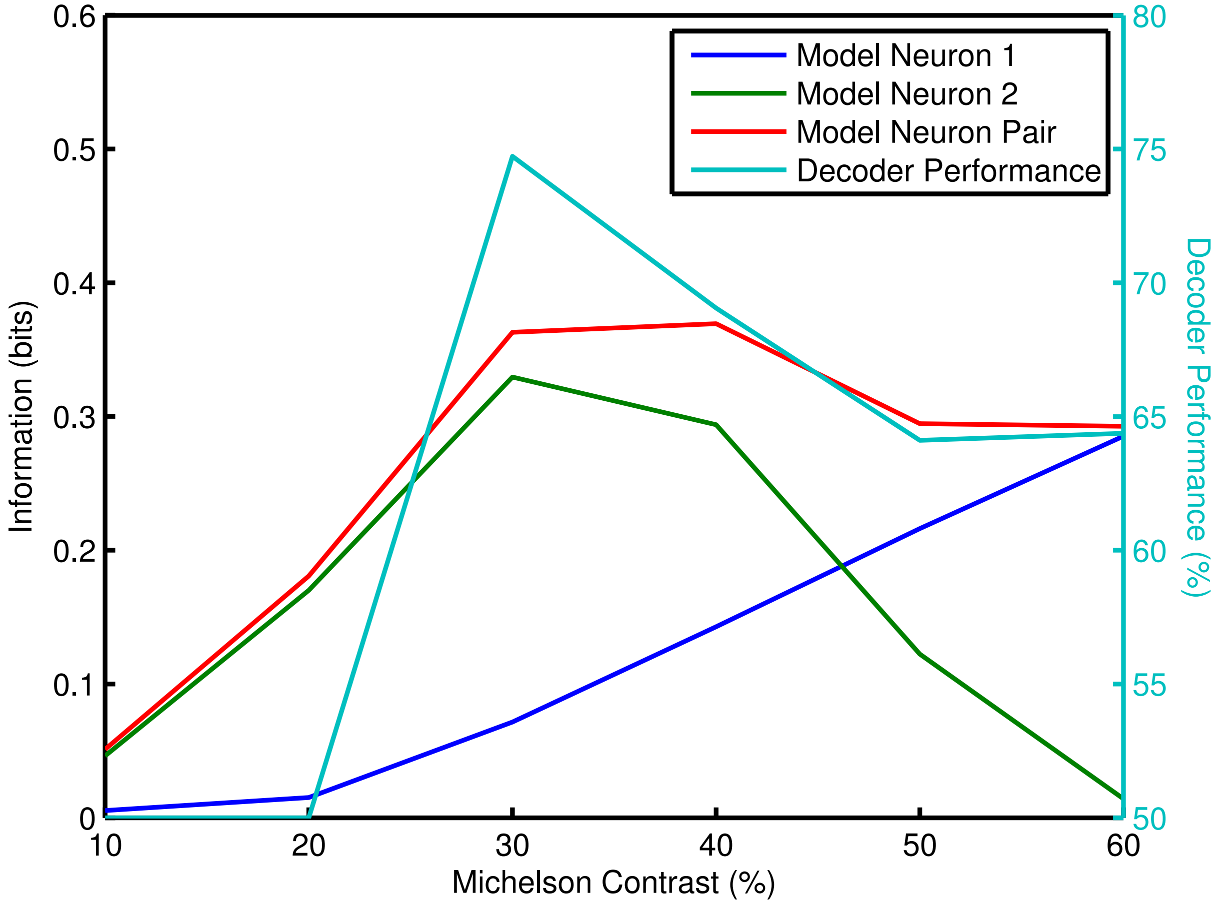

Figure 5.10: Average decoder performance in the 2AFC contrast gratings task after application of MFA (teal) and information provided by each model neuron individually (blue, green) or as a pair (red) as a function of contrast. The model behaviour is qualitatively similar to that observed in real retinas.

cascade. The response of the ChR2 channels as a function of irradiance is modelled as a simple rectifying nonlinearity, ChR2 photocurrents are integrated linearly over space, and the result is used as the rate function of a Poisson process. (This is a reversal of the standard LNP models of RGCs, but placing the nonlinear step first is justified if the nonlinearity is assumed to arise due to the properties of the ChR2 channel, whereas in typical RGC models the nonlinearity usually represents integration of synaptic inputs and the linear stage represents the processing that occurs presynaptic to the RGC.) The shape of the receptive field and the spatial distribution and weighting of ChR2 channels is left unspecified, except that the integral of their density over the receptive field is arbitrarily defined to be equal to unity.

For a spatially uniform stimulus (e.g. a mask) with irradiance I_{mask}, the firing rate λ of such a model neuron at time τ is thus given by:

$\lambda(t) = a \max(0, I_{mask} - I_0) + b$

where I_0 represents the ChR2 threshold, a controls the gain of the nonlinearity, and b determines the minimum firing rate. Alternatively, if some fraction c of the receptive field receives an irradiance of I_{light} and the rest I_{dark} (as in a grating where the edge falls within the receptive field), the firing rate is given by:

$\lambda(t) = a(c \max(0, I_{light} - I_0) + (1 - c) \max(0, I_{dark} - I_0)) + b$

The probability of the neuron firing k spikes in the interval $(a, b]$ is given by:

$p(N(a, b] = r) = \frac{\left[\int_a^b \lambda(t) dt\right]^r}{r!} e^{-\int_a^b \lambda(t) dt}$

As such, the probability of the neuron firing r spikes in response to some temporally invariant stimulus s that evokes an instantaneous firing rate λ_s and is presented at time t_s for a duration T is:

$p(r|s) = p(N(t_s, t_s + T] = r) = \frac{(\lambda_s T)^r}{r!} e^{-\lambda_s T}$

Recall that the performance of any decoder is bounded by the mutual information about the stimulus in the response (Quian Quiroga and Panzeri 2009). Denoting the random variable governing the response of an ensemble of n NLP neurons as $\mathbf{R} = \{R_1, ..., R_n\}$, one can calculate the mutual information between a random stimulus S and the neurons' responses as:

$I(S;\mathbf{R}) = H(\mathbf{R}) - H(\mathbf{R}|S)$

If each neuron is statistically independent conditional on the stimulus, then:

$$\begin{aligned}
H(\mathbf{R}|S) &= \sum_{s\in\mathcal{S}} p(s) H(\mathbf{R}|S=s) \\
&= -\sum_{s\in\mathcal{S}} p(s) \sum_{\mathbf{r}\in\mathbb{N}_0^n} p(\mathbf{r}|s)\log_2 p(\mathbf{r}|s) \\
&= -\sum_{s\in\mathcal{S}} p(s) \sum_{\mathbf{r}\in\mathbb{N}_0^n} \left(\prod_{i=1}^{n} p(r_i|s)\right) \log_2 \left(\prod_{i=1}^{n} p(r_i|s)\right)
\end{aligned}$$

(Where $\mathcal{S}$ is the set of possible stimuli, $\mathbf{r} = \{r_1, ..., r_n\}$, and $\mathbb{N}_0$ is the set of natural numbers including zero.) Conditional independence does not guarantee statistical independence, but nevertheless $H(\mathbf{R})$ can be calculated from the stimulus-conditional response distributions as follows:

$$\begin{aligned}
H(\mathbf{R}) &= -\sum_{\mathbf{r}\in\mathbb{N}_0^n} p(\mathbf{r})\log_2 p(\mathbf{r}) \\
H(\mathbf{R}) &= -\sum_{\mathbf{r}\in\mathbb{N}_0^n} \left(\sum_{s\in\mathcal{S}} p(s)p(\mathbf{r}|s)\right) \log_2 \left(\sum_{s\in\mathcal{S}} p(s)p(\mathbf{r}|s)\right) \\
H(\mathbf{R}) &= -\sum_{\mathbf{r}\in\mathbb{N}_0^n} \left(\sum_{s\in\mathcal{S}} p(s)\left(\prod_{i=1}^{n} p(r_i|s)\right)\right) \log_2 \left(\sum_{s\in\mathcal{S}} p(s)\left(\prod_{i=1}^{n} p(r_i|s)\right)\right)
\end{aligned}$$

Using the model and information formulae described above, I set out to reproduce the observed Bayesian decoder performance on the 2AFC contrast gratings task after application of MFA. First, I thresholded, shifted and scaled the average Bayesian decoder performance p over all retinas in the drug condition (figure 5.8, green curve) to cover the range [0,1]:

$p' = max(0, p - 50)/50$

Thus a performance of 50% or below gives a value of 0 and 100% gives the value 1. As the stimulus entropy in a 2AFC task is 1 bit, this conversion is equivalent to saying that 100% classification accuracy means the RGC population response provides perfect information about the stimulus and a performance no better than chance means the responses provide no information about the stimulus. This transformation is not strictly mathematically rigorous: for example, a decoder that always gives the wrong answer (performance of 0%) also provides complete information about the stimulus, as an observer could always recover the correct stimulus by assuming the exact opposite of whatever the decoder tells them (this is a special case of the scrambled decoder described by Schneidman et al. (2003)). However, it suffices for my purposes here.

Next, I used the Global Optimisation Toolbox in Matlab to minimise the mean squared error between the scaled and shifted performance and the information provided by two model neurons responding to a mask with irradiance $I_{mask} = 1$ or a grating with light and dark bars having irradiances $I_{light} = 1 + k$ and $I_{dark} = 1 - k$ for $k \in \{0.1, 0.2, 0.3, 0.4, 0.5, 0.6\}$ (to give the same range of contrasts used in the experiments), each presented for $T = 250$ms. The two neurons were constrained to have the same value of b, but a, c, and I_0 were allowed to vary separately for each.

The above model was able to approximately reproduce the observed behaviour with $a_1 = 429.4, a_2 = 528.1, t_1 = 0.99, t_2 = 0.66, c_1 = 0.05, c_2 = 0.35$, and $b = 0.1$ (where subscripts denote different fitted parameters for each of the two model neurons). The rate functions for each of the model neurons are shown in figure 5.9. The first neuron has a threshold almost identical to the mask irradiance, so that it effectively only responds to the light bar of the grating stimulus. (Interestingly, the optimiser assigned it a c value such that the light bar covers only 5% of its receptive field. Most likely it chose this value to slow the growth of the information provided by this neuron as a function of contrast, so that it did not dominate the pair information.) The second neuron has a lower threshold, so that at low contrasts it responds to both the light and dark bars at low contrasts but only the light bar at high contrasts, and the light bar covers roughly one third of its receptive field.

Figure 5.10 shows the mutual information provided by the each of the model neurons individually and as a pair in comparison to the average decoder performance across all retinas, demonstrating that the model roughly reproduces the observed behaviour. When the contrast is low, the pair of neurons provides very little information about the stimulus. As the contrast increases, the pair responses provide steadily more information about the stimulus until reaching a plateau between 30 and 40% contrast, after which the information drops off slightly. Looking at the information provided by each model neuron individually provides clues as to how this behaviour arises. For the first neuron, the information increases monotonically with contrast, as one might intuitively expect. However, the information provided by the second neuron peaks somewhere between 30 and 40% contrast, then starts to *decrease* as contrast increases.

Yet more insight into how this behaviour arises can be obtained by inspecting the number of spikes fired by each neuron in response to the mask or the grating as a function of contrast, as show in figure 5.11. For the first neuron, the number of spikes fired increases steadily as the contrast increases, with the grating response distribution getting progressively further from the mask response distribution. The second neuron is more interesting. At low contrasts, the average irradiance in the neuron's receptive field is similar between grating and mask and so too are the responses. However, as the contrast increases and the irradiance of the dark bar dips below the neuron's ChR2 threshold, the grating response gets weaker, until it is distinguishable from the mask response. However, as the contrast increases further, the light bar gets brighter and so the grating response gets stronger, until once again its distribution overlaps that of the mask response.

Looking at the response of the second model neuron (figure 5.11, left), one might expect that if the contrast were increased further, the grating response would eventually become stronger than the mask response and the information provided would start to increase again. Extrapolating out to 100% contrast, this turns out to be exactly the case (figure 5.12). After reaching a trough around 60% contrast, the information provided by this neuron starts to climb again until it provides a similar amount of information at 100% contrast as it does at 30%. Due to my choice of mask irradiance, I was unable to use contrasts greater than 60%. Had I been able to, perhaps the Bayesian decoder performance would have started to climb again, instead of petering out as it appears to in figure 5.8.

The above model is not intended as a definitive explanation for the pattern of decoder performances versus contrast seen in figure 5.8, but merely one possible explanation as to what might cause the information contained in the RGC population response to vary non-monotonically with contrast. Additionally, in the experiments presented in this chapter there were generally many dozen to a few hundred cells included in the decoder with a variety of different patterns of responses; some more similar to the first model neuron, others more similar to the second (for an example, see figure 5.13), yet others with patterns not elucidated here, and finally some neurons that do not respond to the gratings despite responding vigorously to full field stimulation. Hence the interaction between gratings, contrast, and information will be vastly more complicated than the simple two neuron model described here.

Moreover, each neuron will show different patterns of responses to the different phases of each grating as the percentage of the receptive field covered by light versus dark bars varies. However, if it is the interaction between ChR2 nonlinearity and the spatial structure of the stimulus that results in the decrease in performance of the decoder at high contrasts, as this model suggests, then future experiments examining contrast sensitivity in *ChR2rd1* retinas should use stimuli with simpler spatial structures.

5.4.2 *Quality and Stability of* `psignifit` *Fits*

The estimated visual acuities in table 5.2 rely on well-fit psychometric functions relating the feature size to decoder performance. `psignifit` assesses goodness of fit by calculating the deviance, which is the log of the ratio of the likelihood of a model that perfectly fits the data to that of the maximum likelihood model (Wichmann and Hill 2001a). It then bootstraps the expected deviance distribution for the fitted model and assigns a p-value to the observed deviance. There was no evidence of overdispersion (right-tailed $p > 0.05$), indicating good fits of the model to the data.

As described in section 5.2.4, `psignifit` allows the user to specify prior distributions for all parameters to be estimated. If the parameters are well constrained by the model, these priors should exert little influence on the resulting parameter estimates and serve mainly to exclude nonsensical values. However, if the model parameters are not well constrained by the data, the final parameter estimates may be extremely sensitive to the exact choice of prior.

In both conditions, the estimates of m were largely unaffected by the choice of prior: as well as the Gaussian prior, I also used a uniform prior on the interval [0,32] and various Beta distributions scaled to cover this interval where I either skewed the distribution to one extreme or the other or kept the mode at 16 and adjusted the kurtosis up and down. In most cases, the fitted values for m were similar to those listed in table 5.2. I explored a similar range of priors for w: in the MFA condition, the fitted values were again largely insensitive to the choice of prior unless it was extremely skew. By contrast, non-flat priors tended to bias the value of w control conditions to the mode of the prior, indicating that this parameter was not well constrained by the data. In particular, when decoder performance is very low at all letter sizes, the resulting data can be consistent with anything from a step function centred at just above the largest letter size to an extremely shallow curve (figure 5.14). This is a known problem in psychometric function fitting: Wichmann and Hill (2001a) demonstrated that low performance values constrain the model less tightly than high performance values. However, it is important to note that in my explorations almost no choice of priors was able to reverse the overall pattern of results. Regardless of the choice of priors, there was an improvement in visual acuity with application of MFA and in many cases this improvement was larger than the 23.5% reported here. Combined with the results from the 2AFC frequency gratings experiment, this suggests that the conclusion that MFA improves visual acuity of optogenetical retinal prosthetic responses *in-vitro* is supported by the data and not merely an artefact of poor fits or carelessly chosen priors.

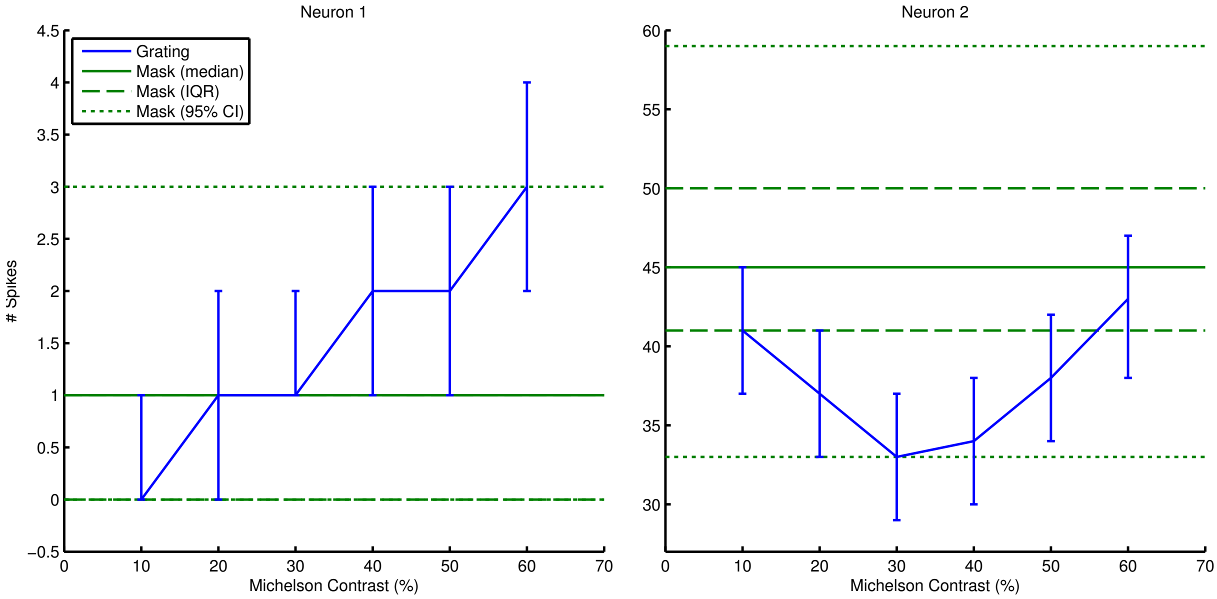

Figure 5.11: Distribution of number of spikes fired by each model neuron in response to the grating (blue) or the mask (green) as a function of contrast. The first neuron's response curve is shown on the left and the second's on the right. For the grating responses, the curve plots the median number of spikes fired on each presentation and the error bars represent the inter-quartile range. For the mask responses, the solid line shows the median, the dashed lines the IQR, and the dotted lines the 2.5th and 97.5th percentiles. Percentiles are calculated directly from each neuron's stimulus-conditional cumulative probability distribution at each contrast.

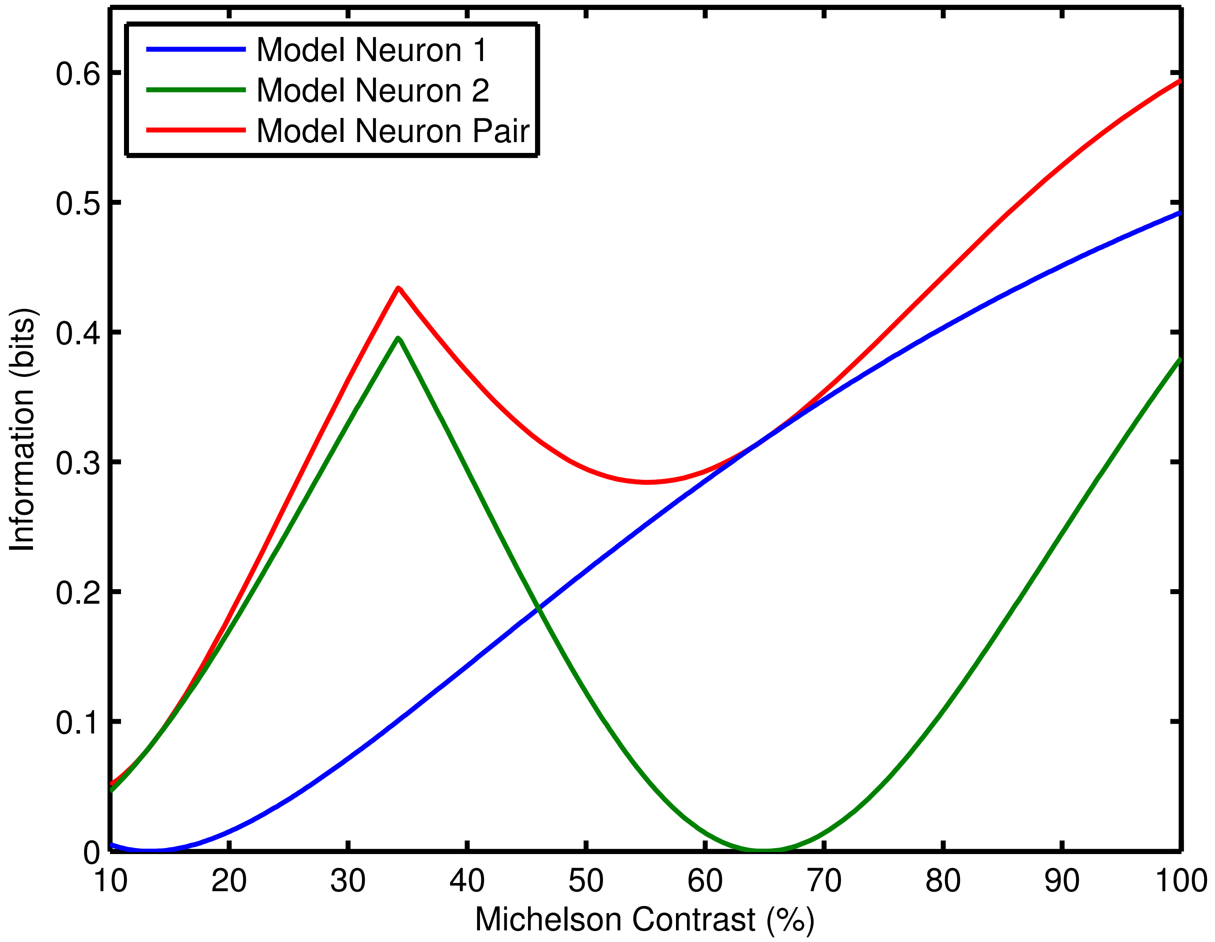

Figure 5.12: Mutual information contained in the responses of model ChR2 RGCs individually (blue, green) and as a pair (red) as contrast ranges continuously from 10 to 100%.

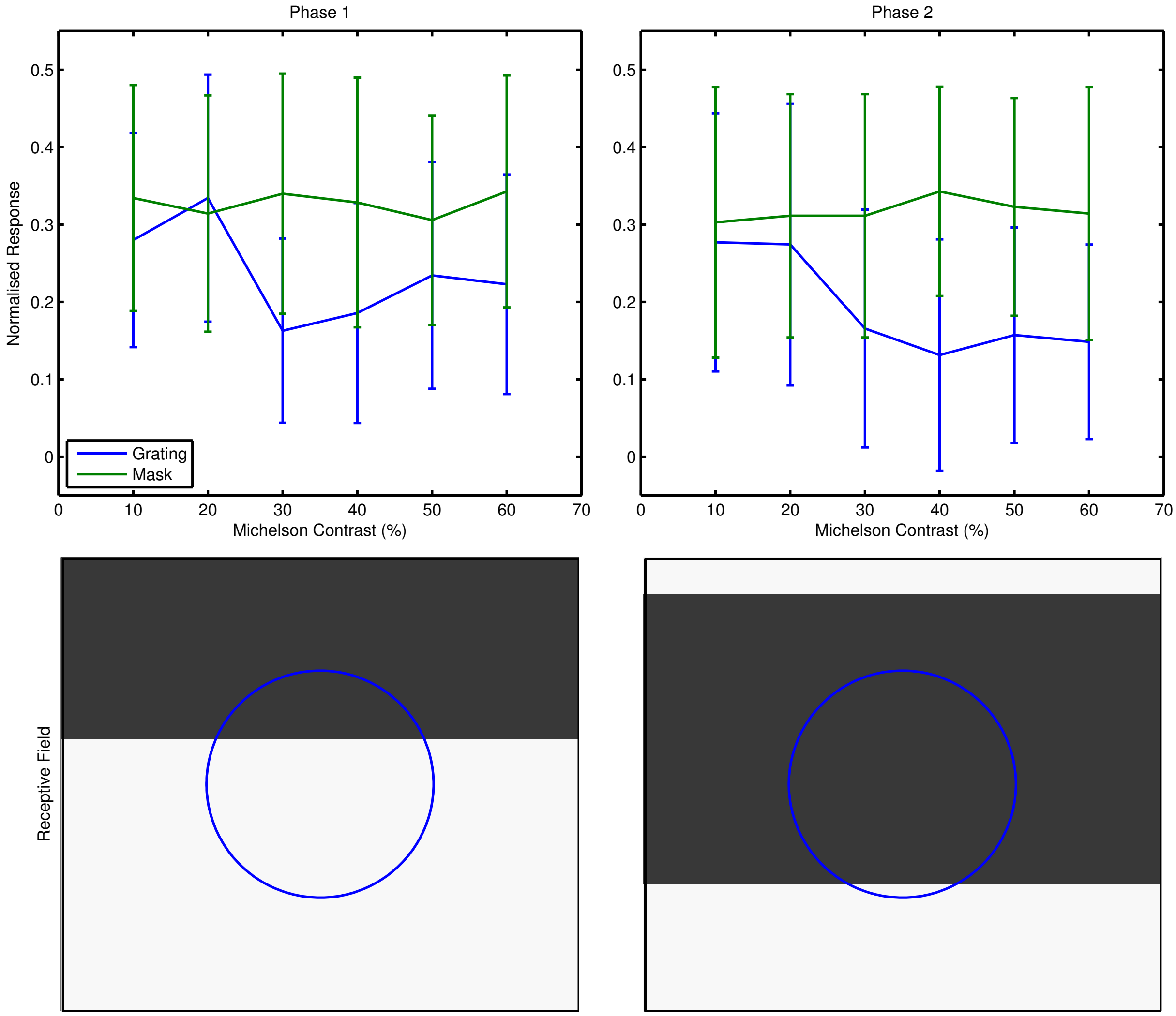

Figure 5.13: Example of a real ChR2 RGC that responds similarly to the second model neuron. The top row shows the mean response of the cell to two different phases of the grating (blue) at different contrasts and accompanying presentations of the mask (green). Error bars are one standard deviation. The bottom row shows the approximate size and location of the cell's receptive field relative to the grating. The blue circle shows the 2SD contour of a two-dimensional Gaussian with a standard deviation of 125µm (equal to the mean ChR2 RGC receptive field radius found in chapter 4) centred on the electrode on which the cell was recorded. For the first phase (left), the cell sees both the light and dark bars. At low contrasts, it responds to grating and mask similarly. Then, as the contrast increases, the response to the grating weakens, presumably due to the dark bar being too dim to stimulate ChR2. However, as the light bar brightens, the response to the grating gets stronger, bringing it closer to the mask response. For the second phase (right), however, the cell's receptive field is almost entirely occupied by the dark bar. Hence the response to the grating gets progressively weaker with contrast, bottoming out when the bar is too dim to excite ChR2.

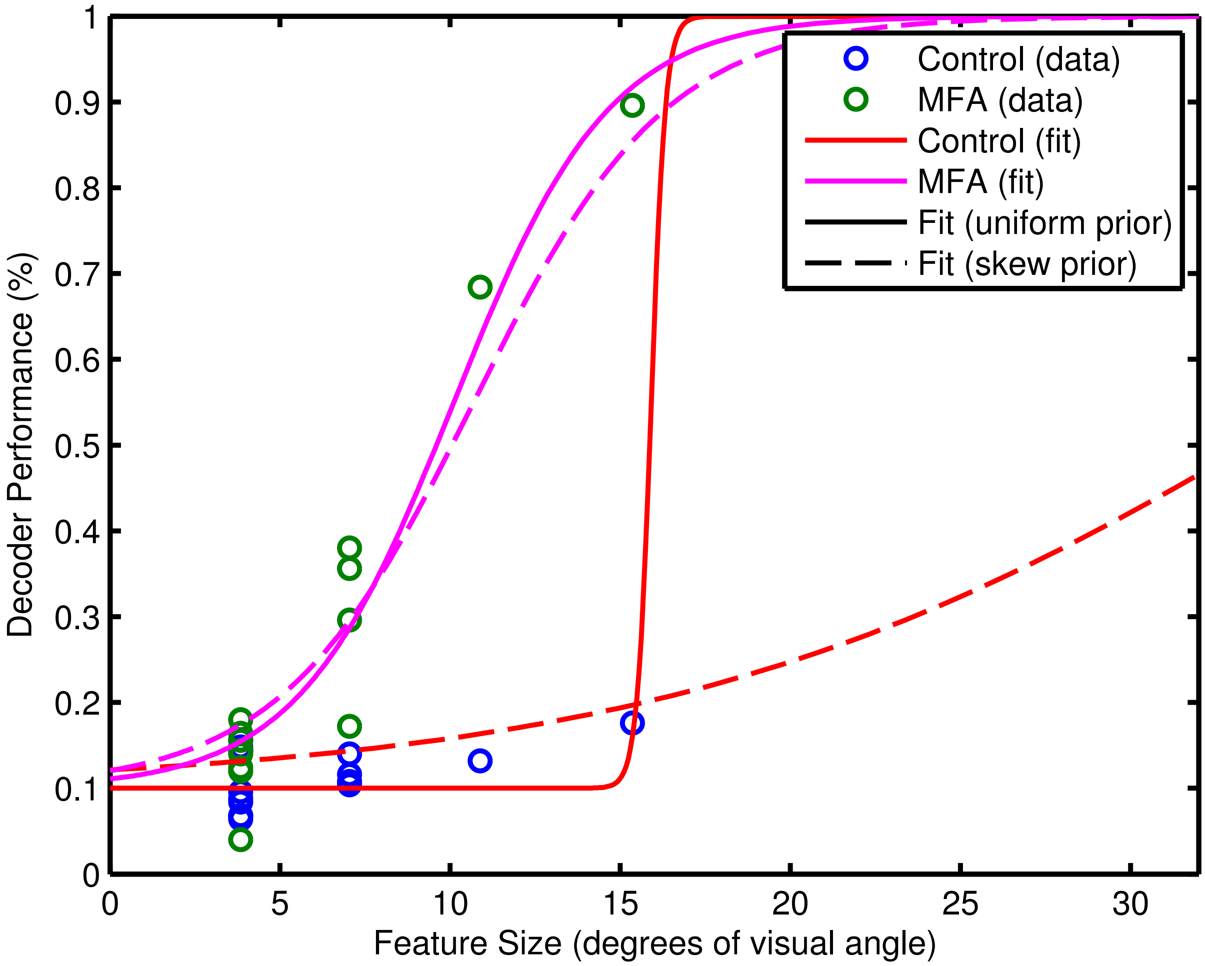

Figure 5.14: Example of how the choice of prior influences the fitting of the psychometric function in control versus MFA conditions. Open circles represent measured decoder performance for retina 2 in table 5.2 in control (blue) and drug (green) conditions. Multiple points for the same feature size represent performance measured at different grid locations. Solid lines are fits to the data using the priors described in section 5.2.4; in particular, the prior on w is the uniform distribution on the interval [0,360]. Dashed lines are the fits if the prior is changed to a beta distribution with $\alpha = 10, \beta = 2$, scaled to cover the interval [0,32]: this distribution has a mode of 28.8. Red lines are fits to the control data and magenta to the MFA data. Note how strongly the control data is influenced by the choice of prior compared to the MFA data.

5.4.3 *Comparison to Healthy Retina Performance*

The 2AFC task using frequency gratings is very similar to the task used by Jacobs et al. (2009) to compare retinal readout under different coding strategies to behavioural performance in the mouse, in that both involved distinguishing gratings of varying spatial frequency to an isoluminant full-field. There are some slight differences: they used sine wave gratings as opposed to square waves, which would most likely render the task harder due to the more subtle variations in contrast, and they permitted their decoder multiple 'looks' at the stimulus, to make it more comparable to the behavioural task.

In their experiments, freely behaving mice could distinguish mask from grating perfectly up to 0.313 cycles per degree (cpd), after which performance fell off roughly linearly with spatial frequency. Expecting that weakly stimulated *ChR2rd1* retinas would not perform as well as behaving animals, I did not test spatial frequencies higher than 0.313 cpd. This turned out to be correct: from figure 5.6 we see that at this spatial frequency the decoder performed scarcely above chance in control conditions. MFA improved matters, but to nowhere near perfect performance: average performance at this spatial frequency was around 60%. Even at spatial frequencies lower than those tested by Jacobs et al. (2009), the performance was less than 60% in control conditions and around 80% with MFA. However, this is comparing a spike count based decoder applied to *in-vitro* recordings to an awake behaving animal. Jacobs et al. (2009) found that such decoders failed to replicate behavioural performance, with their spike count decoder performing no better than chance above around 0.2 cpd. Thus, at the highest spatial frequency tested here the amount of information carried by the spike counts of ChR2 RGCs is actually higher than in wild-type retinas.

5.4.4 *Comparison to Electrical Prostheses in Clinical Trials*

In a recent report on a clinical trial of the Alpha IMS retinal prosthetic (Retina Implant AG, Reutlingen, Germany; Stingl et al. (2015)), patients receiving the device had their visual acuity tested using the Landolt C test, which involves identifying the orientation of the gap in C-shaped rings of different sizes. Most (86%) patients did not have measurable visual acuity using the Landolt C test; those that did had a visual acuity in the range

20/2000-20/546, expressed as a Snellen fraction. Here, I analysed responses of *ChR2rd1* retinas presented with Sloan letters, which give comparable visual acuity measures to the Landolt C (Sloan 1959), and used them to estimate visual acuity scores for each retina in control conditions and after application of MFA (section 5.2.5).

The first thing to note is that MFA improved visual acuity across the board: in every single retina, estimated visual acuity was higher after application of the drug. On average, there was a 23.5% improvement between conditions. However, even the best visual acuity score achieved by any *ChR2rd1* with MFA was almost an order of magnitude worse than the worst measured Landolt C visual acuity in Stingl et al. (2015). This might be a result of testing procedure. The authors do not state what range of sizes of Landolt C rings they used, but a Snellen fraction of 20/2000 (corresponding to a logMAR score of 2) is at the edge of the range of near-blindness and anything less than this is considered blind (International Council of Ophthalmology 1988), so this is likely the largest size they used. More patients had measurable light perception than succeeded on the Landolt C test, so had they used larger rings or a shorter testing distance, they may have been able to measure visual acuity scores in more patients. Unfortunately, there is no way of knowing what these scores might have been.

That said, there is no reason to expect a mouse to perform as well on a visual acuity test as a human. For a number of reasons, the letters task used in my experiments is much harder than the task of a patient asked to read a visual acuity chart. First, the patient is permitted as long as they need to read each row; here, each retina is permitted a single 250ms 'look' at each letter. Further, the C rings used in Stingl et al. (2015) were effectively much brighter than the letters used here. The irradiance of the letters in this experiment was roughly 1.6 times the threshold grey level for ChR2 activation found in preliminary experiments. By contrast, the ratio of the brightest black used in Stingl et al. (2015) to the darkest white level was two[5]; the ratio of the minimum black level to the maximum white level was 25000. Finally, the Alpha IMS provides a higher pixel count (1500) and theoretical maximum spatial resolution (0.25 degrees of visual angle) than was available to the decoder in my experiments. At best, the decoder had a few hundred ChR2

---

[5] Black and white levels were calibrated for each patient: the range of contrasts is not reported, but the range of black levels and white levels are reported separately

cells available with which to identify each letter. Assuming a regular grid arrangement of responsive cells over an area of 2.67x.267mm, this corresponds to an average separation of 4.5 degrees (in practice the cells will be arranged unevenly and so there will be regions of smaller and larger separation). If the letters had been brighter, the responses to multiple trials used in the decoder, and more cells had responded to stimulation, the estimated visual acuity scores for the *ChR2rd1* retinas may have been even higher.

5.4.5 *Comparison to Previous Studies on Optogenetic Prostheses*

Of the studies conducted so far on optogenetic retinal prosthesis in rodents, six have used the optokinetic reflex test as an outcome measure (Lagali et al. 2008; Tomita et al. 2009; Busskamp et al. 2010; Tomita et al. 2010; Nirenberg and Pandarinath 2012; Wyk et al. 2015), although one of these (Nirenberg and Pandarinath 2012) does not provide sufficient detail in the methods to allow meaningful comparison with other studies. The optokinetic reflex test makes use of rodents' instinctive tendency to track a drifting grating pattern by rotating their heads in the direction of the drift and can be used to measure spatial acuity. Table 5.3 details the spatial frequencies and light intensities tested in these studies at which blind rodents optogenetically engineered to have light sensitive retinas were able to follow the grating pattern.

To summarise table 5.3, blind mice and rats expressing traditional optogenetic proteins (ChR2 or an enhanced halorhodopsin) in their retinas were able to follow gratings with spatial frequencies between 0.05 and 0.5 cycles per degree at brightnesses on the order of 10^{14}-10^{15} photons·cm^{-2}s^{-1}. (The mice in Wyk et al. (2015) were able to follow much dimmer gratings, but they were transfected with a chimeric protein specifically engineered for greater light sensitivity.)

In control conditions, my *ChR2rd1* retinas were unable to distinguish gratings of these spatial frequencies from isoluminant gratings (decoder performance was no different than chance, figure 5.6) and so are likely to have failed the optokinetic reflex test. Application of MFA improved detection of gratings, with performance increasing to around 60% at these spatial frequencies, although it is not obvious whether this is sufficient to induce measurable optokinetic responses. The average irradiance of the 2AFC contrast gratings in

Reference	Species & Strain	Opsin	Target	Photon Flux (ph·cm^{-2}s^{-1})	Spatial Frequency (cpd)
Lagali et al. (2008)	*rd1* mouse	ChR2	ON BCs	1.0×10^{13}	N/A
				3.0×10^{15}	0.13-0.26
Tomita et al. (2009)	LIRD Wistar rat	ChR2	RGCs	4.5×10^{14}*	0.06-0.5
Busskamp et al. (2010)	*rd1* mouse	eNpHR	Cones	1.8×10^{15}**	0.13
	Cnga3$^{-/-}$,*Rho*$^{-/-}$ mouse	eNpHR	Cones	1.8×10^{15}**	N/A
Tomita et al. (2010)	RCS rat	ChR2	Mainly RGCs	1.2×10^{15}	N/A
				2.3×10^{15}	0.05
Wyk et al. (2015)	*rd1* mouse	Opto-mGluR6	ON BCs	5.6×10^{13}	0.17

Table 5.3: Table listing stimulus intensities and spatial frequencies at which rodents had measurable optokinetic responses (OKRs) in previous rodent studies of optogenetic retinal prosthesis, as well as tested stimulus intensities at which no OKRs were seen (indicated by N/A in spatial frequency column). ChR2 = channelrhodopsin-2; eNpHR = enhanced *Natronomonas pharaonis* halorhodopsin; Opto-mGluR6 = chimeric protein comprising the intracellular domains of the metabotropic glutamate receptor, mGluR6, and the light-sensing domains of melanopsin. LIRD = light-induced retinal degeneration. *Tomita et al. (2009) report the light intensity in the centre of their optokinetic drum as 100 lux, which is a photometric unit and not readily convertible to radiometric units. However, in a later publication Tomita et al. (2010) report that 500 lux in their optokinetic drum corresponds to ~2.25×10^{15} ph·cm^{-2}s^{-1}. **Busskamp et al. (2010) also report light intensities in lux, but in this case they used a single LED light source, so the value here was converted to photons·cm^{-2}s^{-1} using the standard photopic luminosity function assuming all light was emitted at the LED's peak emission wavelength.

my experiments was 0.53mW/cm^2, however, the projector was a standard RGB projector, so much of the light emitted will have been at wavelengths too long to excite ChR2. By convolving the emission spectra of the LEDs in the projector with the relative absorption spectrum of ChR2 (see Appendix C for details) I calculated the equivalent photon flux to be around 3.3×10^{14} photons·cm^{-2}s^{-1} at 450nm; lower than every light intensity at which OKRs were restored using algal or bacterial opsins in the studies listed in table 5.3. Thus, it is possible that blockade of spontaneous activity may permit measurable optokinetic responses at lower light intensities than have previously been reported in the literature.

In addition to the above, one other study has investigated spatial acuity in mice with optogenetic retinal prostheses. Cehajic-Kapetanovic et al. (2015) used a modified open field test in which they placed mice in a box with transparent end walls. Behind each wall was a computer monitor and they compared locomotor activity before and after they switched the monitors from displaying a grey screen to a drifting square-wave grating. In their study, *rd1* mice transfected with human rhodopsin were able to perform the task with 0.04 cpd gratings but not 0.08 cpd gratings. In the experiments presented here, the decoder could not distinguish gratings from an isoluminant grey screen at either of these spatial frequencies (or very similar frequencies: 0.039 and 0.078 cpd), but application of MFA enabled the decoder to distinguish both sets of gratings from the mask better than chance. The gratings used in Cehajic-Kapetanovic et al. (2015) were of much lower photon flux (around 8×10^{11} photons·cm^{-2}s^{-1}) than those used here (equivalent to around 3.3×10^{14} photons·cm^{-2}s^{-1} at 450nm—see Appendix C for details), but human rhodopsin is much more sensitive to light (it can detect luminance changes of one photon) compared to ChR2.

5.4.6 *Conclusions and Future Work*

The results presented here and in chapter 4 add yet more evidence to support the hypothesis that reducing spontaneous activity in degenerate retinas improves the amount of information available in prosthetic responses. A few questions remain as yet unresolved, however.

Foremost is the unusual pattern of responses to gratings of varying contrast, wherein decoder performance is highest for relatively low contrasts (around 30%), then drops off as contrast increases (figure 5.8). Possible reasons for this are discussed in section 5.4.1, but a more thorough explanation may require experiments in which contrast and irradiance are varied simultaneously to see how each affects the amount of information contained in *ChR2rd1* RGC responses. Further, as contrast sensitivity varies as a function of spatial frequency in both normal and prosthetic vision (Tomita et al. 2009), it would be worthwhile to repeat the gratings experiments while varying both frequency and contrast of the gratings (such experiments were not performed here mostly to limit the length of each recording and hence keep the size of the resulting data files manageable).

Another aspect of vision not investigated here is how spontaneous activity affects temporal aspects of vision. All of the stimuli presented here used a fixed presentation time of 250ms, which was chosen as it was found in preliminary experiments to evoke clear ChR2 responses in large numbers of cells. Many cells here and in chapter 4 responded to much briefer stimuli, however, so an interesting experiment might be to investigate how the number of responding cells and the strength of their responses evolves as a function of stimulus duration in control conditions and in the presence of MFA. Alternatively, one could examine how the information contained in the response to a fixed, long-duration stimulus increases with the length of the analysis window after stimulus onset, as in chapter 3. A related factor to investigate is how the temporal frequency of the stimulus and the level of spontaneous activity interact. Possible predictions include that reducing spontaneous activity may increase the temporal frequency of stimulus changes that can be reliably signalled by *ChR2rd1* RGCs (subject to the limitations imposed by the temporal kinetics of ChR2 itself (Boyden et al. 2005; Gunaydin et al. 2010)) or that the periodic nature of *rd1* spontaneous activity (Stasheff 2008) might selectively interfere with stimuli that vary with a temporal frequency of around 10Hz in control conditions but less so after application of MFA.

Additionally, although I have now tested a number of stimulus classes (full-field flashes, flashed squares, flashed gratings, moving bars, and letters) and found reducing spontaneous activity improves the encoding of all of them, there are many more stimuli one could present to the retina. One important stimulus class that has been investigated in previous optogenetic retinal prosthetic studies is that of natural scenes and movies (Nirenberg and Pandarinath 2012; Cehajic-Kapetanovic et al. 2015), but to date no-one has investigated how manipulating the level of spontaneous activity affects the encoding of such stimuli in optogenetically resensitised retinas.

Finally, all work so far investigating the effect of spontaneous hyperactivity on prosthetic responses (here, chapter 4, Toychiev et al. (2013) and Ivanova et al. (2015)) has reached its conclusions based on statistical and information theoretic analyses of electrophysiological data. While the results so far are encouraging, before they can be translated to the clinic they must first be validated behaviourally. As will be discussed in section 6.2, delivering MFA to the retina *in-vivo* and ensuring a steady, sufficiently high retinal exposure to the drug might be a considerable biomedical engineering challenge. As such, perhaps the easiest approach to test the behavioural effects of reducing spontaneous activity in prosthetic vision would be to adapt the approach used in Ivanova et al. (2015), i.e. to compare the performance of an optogenetically resensitised blind mouse strain in some visual task with the same strain crossed with the *Cx36*$^{-/-}$ connexin-36 knock-out mouse, which lacks retinal gap junctions and so exhibits much lower spontaneous activity when crossed with a retinal degeneration model.

Chapter 6. General Discussion

The main results of chapter 1 were twofold. First, I demonstrated the presence of synergistic information in paired spike counts and spike trains of RGCs in the wild-type mouse retina. Secondly, rank-order coding—a coding strategy that considers the relative order of firing of a large population of neurons—outperformed a latency code based on treating RGCs independently.

Chapters 4 and 5 explored the effect of dampening spontaneous hyperactivity on optogenetically evoked RGC responses in dystrophic retinas. Chapter 4 compared different drugs that affect spontaneous activity using responses to full-field flashes and simple spatiotemporally varying stimuli, and found that MFA was the best drug for blocking spontaneous activity without hindering stimulation, consistent with previous results using photoreceptor and electrical stimulation (Toychiev et al. 2013; Ivanova et al. 2015). I extended this result in chapter 5 by showing that blocking spontaneous activity increases the amount of information contained in optogenetically-evoked RGC population responses at a variety of spatial scales and contrasts, as well as increasing the spatial acuity of retinal prosthetic responses.

In the first part of this discussion chapter, I shall attempt to tie these themes together by considering how the results of chapter 3 might affect retinal prosthetic strategies. Following that, I shall consider ways in which the results of chapters 4 and 5 might be translated to the clinic.

6.1 Retinal Coding: Implications for Prosthetic Design

As discussed in section 1.3, there are two broad strategies for retinal prosthesis. In the terminology used for electrical prostheses, these are the subretinal approach—stimulating the outer retina to activate bipolar cells or surviving cones—and the epiretinal approach—stimulating the inner retina to activate RGCs. These terms refer to the location of an implanted device and so do not strictly apply to optogenetic prostheses or other kinds of prostheses, such as those based on chemical photoswitches (Tochitsky et al. 2014), but nevertheless in this chapter I shall use this terminology for all retinal prostheses, regardless of stimulation method.

The usual assumption in subretinal designs is that inner retinal processing remains intact (Margalit et al. 2002), in which case the prosthesis need only stimulate the retina in accordance with the spatiotemporal pattern of incoming light and the retina will do all the work of encoding this information and sending it to the brain. This seems unlikely, given the extent of inner retinal remodelling that occurs in retinal dystrophies, particularly in advanced stages (Marc et al. 2003; Marc et al. 2007). There have been few direct experimental tests of these questions. Rodent models of subretinal prosthesis usually show improvements in vision (Doroudchi et al. 2011; Cehajic-Kapetanovic et al. 2015; Lorach et al. 2015), but mice's natural vision is considerably worse than humans to begin with; by contrast, the quality of vision returned by subretinal prostheses in humans remains poor (Stingl et al. 2015). Toychiev et al. (2013) and Ivanova et al. (2015) have shown how spontaneous hyperactivity arising from retinal degenerations can lower the overall signal-to-noise ratio of RGC responses to photoreceptor stimulation and electrical stimulation of presynaptic bipolar cells, which is what subretinal electrical stimulation achieves if stimulation parameters are set appropriately (Boinagrov et al. 2014). However, they only consider responses to incredibly simple stimuli (full-field flashes, current steps). By contrast, Busskamp et al. (2010) applied a variety of stimuli to dystrophic retinas in which surviving cones were transfected with halorhodopsin and showed that some basic aspects of inner retinal processing were preserved. Thus the extent of the effect of inner retinal remodelling on information processing remains uncertain.

One possible reason for the failure of the first spike latency code in chapter 3 is the high degree of spontaneous activity in the mouse retina as compared to the salamander retina (Gollisch and Meister 2008). Similarly, in chapter 4 I showed how degenerate spontaneous activity can disrupt a different latency code based on times to peak firing. Hence, latency coding is likely to perform even poorer in the degenerate retina than in the wild-type retina. The rank-order code was more robust to levels of spontaneous activity seen in wild-type retinas, but it is not clear whether it remains stable as both the strength and variability of spontaneous activity increases, as in the degenerate retina (Stasheff 2008; Stasheff et al. 2011; Goo et al. 2011). This might be an interesting question to investigate, for example using simulations or by increasing the spontaneous activity level in wild-type retinas by raising the extracellular potassium concentration.

The epiretinal design, on the other hand, bypasses all retinal layers and stimulates the RGCs directly. Ideally, an epiretinal prosthesis would incorporate a retina-mimicking encoder in order to provide information in a way that higher visual areas can understand (Hornig et al. 2007; Al-Atabany et al. 2013; Nirenberg and Pandarinath 2012). The results in chapter 3 show that synergy is a feature of RGC pair responses and that rank-order coding can be used to extract information from RGC population responses. The fact that information *can* be extracted from the retinal output in a certain way does not entail that the brain *does* extract information from the retinal output in that way (Jacobs et al. 2009), but let us assume for the sake of argument that synergy and rank-order coding are important features of retinal responses. In that case, any prosthetic encoder would have to replicate these features.

First, let us consider rank-order coding. To produce an independent latency code is simple, as it simply requires an encoding model that, for each neuron, relates the stimulus intensity in its receptive field to the time of the first spike (Gollisch and Meister 2008; Gütig et al. 2013). However, given that rank-order coding outperforms independent latency coding, such an encoder is clearly insufficient. More likely, the encoder would have to reproduce stimulus-driven correlations in firing latencies between all neurons of the population, reminiscent of the spike latency mixture decoder of Schwartz et al. (2012a), which was one of the best performing codes in their study.

In the case of synergy, how easy this is depends on how synergy arises. The results of Nirenberg et al. (2001) and Schwartz et al. (2012a) suggest that pairwise correlations are unlikely to be a significant source of synergy (but see Pillow et al. (2008)). This is good news: so long as the encoder can accurately reproduce the marginal stimulus-conditional statistics of RGC responses, then it will not lose too much information about the stimulus (although the results of Schwartz et al. (2012a) suggest that for large RGC populations, as opposed to pairs, correlations can carry a large amount of information, in which case this conclusion no longer holds). Further, if the amount of synergy depends solely on the stimulus (see section 3.4.3), then any decoder that accurately reproduces the population response to arbitrary stimuli will produce synergistic responses as a side-effect with no extra design effort. However, as discussed in section 3.4.3, synergy can also arise as a result of different cell types encoding different information about the visual scene. In this case, the task of the encoder is much harder. By definition, RGCs in a blind retina can not be functionally classified based on their responses to light (Carcieri et al. 2003; Li et al. 2015). Thus the only ways of classifying them are by their morphology (Rockhill et al. 2002)—which in the clinical setting would require subcellular resolution of the dendritic arbors of densely packed, unlabelled cells through a funduscope—or genetic labelling (Packer et al. 2013). Even if this were possible, the prosthetic would then have to encode the scene separately for each cell type under consideration, which would increase its complexity linearly with the number of cell types included. Further, in the case of prostheses involving projecting the processed image into the eye to stimulate photodiodes (Lorach et al. 2015) or optogenetically labelled cells (Al-Atabany et al. 2013; Nirenberg and Pandarinath 2012; Reutsky-Gefen et al. 2013) using an external projector, the encoder would also need to keep track of the identities of each cell as they move with respect to the prosthetic as a result of eye movements.

6.2 Dampening Spontaneous Activity in the Clinic

In Chapters 4 and 5 I showed how dampening spontaneous activity in the degenerate retina using MFA can improve optogenetically-evoked responses to a variety of stimuli, regardless of how performance is measured (signal-to-noise ratio, Bayesian decoder performance, spatial acuity). This adds to the growing body of evidence suggesting that this is a worthwhile consideration in retinal prosthetic design (Toychiev et al. 2013; Ivanova et al. 2015). In this section, I shall consider ways of applying this in the clinical setting, how the prosthetic strategy affects the validity of the approach and whether it applies to other treatments, and finally the implications for how much light (and by extension power, depending on the prosthetic design) is needed to drive responses.

6.2.1 *Strategies for Dampening Spontaneous Activity*

In my experiments, I added MFA directly to the perfusant. The equivalent delivery mechanism in a clinical context would involve systemic oral administration, so that MFA enters the bloodstream, which then carries it to the retina. This is undesirable for a number of reasons. Firstly, patients may not want or be able to take pills all day, every day just to make their prosthetic work better, particularly if the improvement in vision is modest. More importantly, gap junctions are expressed throughout the body, not just in the retina, and MFA can have a number of unpleasant side effects (Juszczak and Swiergiel 2009), including abdominal pain, nausea, diarrhoea, vomiting, skin rash, headache, drowsiness, and dizziness. Thus a more targeted intervention is likely to be desirable. One possibility is intravitreal injection, but this relies on MFA being able to penetrate the ILM and, once there, remain in the retina. Moreover, *in-vitro*, MFA washes out in a matter of hours; if the time course is similar *in-vivo* then this would necessitate multiple intravitreal injections daily, which is obviously impractical. A better solution might be to create an implant or other drug delivery system that remains in the eye and delivers MFA continuously in controlled doses. Similar systems have been developed for anti-VEGF drugs for the treatment of AMD, for example, and a few are currently in human trials (Santarelli et al. 2015). Potentially, such systems could be adapted to deliver MFA instead.

Alternatively, non-pharmacological strategies to decrease spontaneous activity might also improve vision, while avoiding the challenges described above, especially given that there are multiple ways of blocking spontaneous activity in the degenerate retina (see chapter 4 as well as section 1.2.4 for a discussion of previous literature on this subject). For example, if increasing the potassium conductance of AII amacrine cells decreases spontaneous activity (Choi et al. 2014), then gene therapy to increase Kv7 potassium channel expression in AII amacrine cells or introduce a modified form of the channel with higher conductance might have a similar effect to Flu or MFA. Moreover, if the chosen promoter is selective for AII amacrine cells, then it would avoid the decrease in responsiveness observed with high concentrations of Flu. Genetic knock-out of gap junctions could also work (Ivanova et al. 2015), but it would be better to restrict the knock-out to AII amacrine cells rather than pan-retinally as gap-junctions play a number of important roles in vision (Bloomfield and Völgyi 2009). Alternatively, in the case of an optogenetic retinal prosthesis, one could envisage expressing an inhibitory opsin with a distinct absorption spectrum, such as halorhodopsin, in the AII amacrine cells and using a steady background light to hyperpolarise them and dampen the oscillations. However, this would increase the power consumption of the prosthetic device.

6.2.2 *Generalisability*

The results from chapters 4 and 5, combined with the work of Toychiev et al. (2013) and Ivanova et al. (2015), suggest that blocking spontaneous activity to improve prosthetic vision works as a general strategy, somewhat independently of the means of vision restoration. It has now been shown to work for residual photoreceptor responses, electrical stimulation, and optogenetic stimulation. Thus this strategy should be effective for electrical prostheses, optogenetic prostheses and even non-prosthetic strategies such as strategies to halt photoreceptor death (e.g. Cuenca et al. (2014)) or replace them with exogenously grown or endogenously regenerated photoreceptors (e.g. Jayakody et al. (2015)). However, the method of vision restoration has some implications for the choice of strategy for blocking spontaneous activity. Blocking gap-junctions with MFA is fine for an epiretinal prosthesis, as in this case we are bypassing the inner retina and so it is irrelevant whether our method of dampening spontaneous activity interferes with normal retinal processing. However, subretinal prostheses, as well as approaches that aim to halt degeneration or transplant replacement photoreceptors, rely on an intact inner retina to encode the visual scene in a way the brain can understand. Whether or not this is a valid assumption is discussed at length in chapter 1 and briefly above, but setting that aside for now, both amacrine cells (Masland 2012) and gap junctions (Bloomfield and Völgyi 2009) have important roles in normal visual function. As such, interfering with them to reduce spontaneous activity may corrupt the visual signal sufficiently to bring no net gain in quality of restored vision. Although Toychiev et al. (2013) and Ivanova et al. (2015) showed improvements in signal-to-noise ratio of surviving photoreceptor stimulation, they only considered responses to full-field stimulation, which will not reveal deficits in processing of more complex stimuli induced by gap-junction blockade. Choi et al. (2014)

suggest that restoration of photoreceptor light responses or light-sensitisation of bipolar cells might bring the AIIs into a more depolarised, non-oscillating regime and thus remove the spontaneous activity (which is consistent with the rasters shown in Busskamp et al. (2010), but that could also be the result of cherry-picking). However, this depends on the amount of depolarisation introduced by the light sensitisation. Hence whether spontaneous activity reduction, by gap-junction blockade or otherwise, truly improves the quality of vision restored by subretinal prostheses or photoreceptor replacement remains an open question.

6.2.3 *Light Intensity and Power Requirements*

Retinal degenerate spontaneous hyperactivity has been largely overlooked in previous studies of optogenetic retinal prostheses. One possible explanation for this is the light intensities used. Most reports are accompanied by dramatic rasters of light responses, where the peak in the PSTH towers above what appears to be an insignificant baseline firing rate (Bi et al. 2006; Busskamp et al. 2010; Doroudchi et al. 2011; Lagali et al. 2008; Zhang et al. 2009). The average irradiance at the level of the retina in chapter 4 was around 25µW/mm^2 or approximately 6.3×10^{15} photons·cm^{-2}s^{-1} at 490nm (the peak of the µLED array emission spectrum), which is at the lower end of light intensities typically used in studies of optogenetic retinal prostheses using algal or bacterial opsins (although, as noted in section 4.2.3, the peak irradiance at the retinal level in chapter 4 will have been higher than this, but not by more than half a log unit). In chapter 5, the light intensities used were even lower: 8.74µW/mm^2 for the grating stimuli and 16.50µW/mm^2 for the letters; equivalent to 5.5×10^{14} photons·cm^{-2}s^{-1} and 1.0×10^{15} photons·cm^{-2}s^{-1} at 450nm (the peak of the ChR2 absorption spectrum, see Appendix C for details), respectively. The implications for this are two-fold. Firstly, being able to evoke visual responses with lower light intensities lowers the overall power requirements of retinal prosthetic designs involving light amplification or projection of a preprocessed image onto the retina (Al-Atabany et al. 2013; Nirenberg and Pandarinath 2012; Reutsky-Gefen et al. 2013; Lorach et al. 2015). Moreover, if a prosthesis needs to drive the retina very strongly to produce a reliable percept, then this suggests that it will only be able to transfer information about high-contrast visual features, making them no better than currently available devices and necessitating image processing strategies to improve scene contrast (Al-Atabany et al. 2013). Decreasing the amount of spontaneous activity may allow lower-contrast visual features to be perceived (but see section 5.4.1), improving the dynamic range of retinal prosthetic devices. Ultimately psychophysical studies in prosthetic patients will be needed to determine whether this is indeed the case.

Appendix A. Development of a Partial Information Decomposition for Spike Trains

A.1 Introduction

This appendix details the development and validation of a partial information decomposition (PID) for spike trains. Developed by Williams and Beer (2010), the PID attempts to break down the mutual information[1] between one random variable, S, and an ensemble of random variables, $\mathbf{R}$, into the portions of information provided redundantly, uniquely and synergistically by each subset of $\mathbf{R}$. Williams and Beer (2010) only define the PID for discrete random variables, such as spike counts. Whole spike trains are not discrete, however: they contain a mixture of discrete information (the number of spikes) and multidimensional continuous information (the location of each spike in time). Thus the PID in its original form cannot be applied to ensembles of spike trains.

However, inspection of the definition of PID reveals that it is mostly comprised of standard information theoretic quantities. First, there is the mutual information between S and each subset $\mathbf{A}$ of $\mathbf{R}$:

$$I(\mathbf{A}; S) = \sum_{\mathbf{a} \in \mathbf{A}} \sum_{s \in S} p(\mathbf{a}, s) \log \frac{p(\mathbf{a}, s)}{p(\mathbf{a})p(s)}$$

Secondly, there is the redundancy, which is defined in terms of the specific information provided by an ensemble $\mathbf{A}$ about a particular state s of S:

$$I(\mathbf{A}; S = s) = \sum_{\mathbf{a} \in \mathbf{A}} p(\mathbf{a}|S = s) \log \frac{p(\mathbf{a}|S = s)}{p(\mathbf{a})}$$

Note, however, that the specific information is identical to the Kullback-Leiber divergence (KLD) between the distribution of $\mathbf{A}$ conditioned on $S = s$ and the marginal distribution of $\mathbf{A}$. The discrete KLD from one distribution X to another distribution Y is given by:

---

[1] For a brief introduction to the information theoretic concepts discussed in this appendix see section 2.3.2 or, for a more comprehensive discussion, see for example Cover and Thomas (2006)

$$D_{KL}(X||Y) = \sum_{x \in X} p(x) \log \frac{p(x)}{p(y)}$$

The remaining quantities in the PID are derived by simple arithmetic on mutual informations and KLDs. The expressions for the two variable case $\mathbf{R} = \{A, B\}$ are as follows:

$$\begin{aligned}
Red(A, B; S) &= \sum_{s \in S} p(s) \min_{R=A,B} I(R; S = s) \\
Unq(R; S) &= I(R; S) - Red(A, B; S) \quad \text{where } R = A \text{ or } B \\
Syn(A, B; S) &= I(A, B; S) - Unq(A; S) - Unq(B; S) - Red(A, B; S)
\end{aligned}$$

Continuous analogues of discrete mutual information and KLD are derived easily by replacing probability mass functions with probability density functions and finite sums with definite integrals. Related quantities can also be defined for mixtures of discrete and continuous variables (Nair et al. 2006). Thus the strategy for defining a spike train PID is simple: the equations remain the same, except that the discrete mutual information and KLD are replaced with their mixed discrete-continuous analogues. The only difficulty is in choosing a suitable estimator for these two quantities.

A.2 A Binless PID Estimator

It is possible to esimate entropy without binning using nearest-neighbour distances between points in a sample. Such methods, first developed by Kozachenko and Leonenko (1987), are asymptotically consistent and unbiased. In their original form they can only be used to for estimating quantities relating to purely continuous random variables, but Victor (2002) showed how they can be extended to estimate the mutual information between a mixed discrete-continuous random variable, such as a spike train, and a discrete stimulus random variable. Briefly, his method involves decomposing the information carried by the spike train into two parts: a discrete part corresponding to the information available by considering the number of spikes, and a continuous part corresponding to the information carried by each spike's location in time:

$$I(S;R) = I_{count}(S;R) + I_{continuous}(S;R)$$

The first quantity, as it is discrete in nature, can be estimated directly using histogram methods:

$$\begin{aligned}
I_{count}(S;R) &= \sum_s \sum_{k=0}^{\infty} p(S=s, K=k) \log \frac{P(S=s, K=k)}{P(S=s)P(K=k)} \\
\hat{I}_{count}(S;R) &= \sum_s \sum_{k=0}^{\infty} \frac{N_{s,k}}{N} \left(\log \frac{N_{s,k}}{N} - \log \frac{N_k}{N} - \log p(S=s) \right)
\end{aligned}$$

where K is the random variable governing the number of spikes in the response, $\hat{I}_{count}$ is an estimate of the mutual information, $N_{s,k}$ is the number of spike trains with k spikes in the sample fired in response to stimulus s, N_k is the number of spike trains with k spikes fired in response to any stimulus, and N is the total number of recorded spike trains. (The probability, $P(S=s)$, of each stimulus s is known *a priori* as it is set by the experimenter).

$I_{continuous}(S;R)$ is estimated by further decomposing it into the information carried by the timing of each spike in the train, conditional on there being k spikes in the train, for every value of k from zero up to the maximum number of spikes we observe. The total information can then be estimated using the chain rule for information:

$$\begin{aligned}
I(S;R) &= I_{count}(S;R) + \sum_{k=0}^{\infty} P(K=k) I(S;T|K=k) \\
\hat{I}(S;R) &= \hat{I}_{count}(S;R) + \sum_{k=0}^{k_{max}} \frac{N_k}{N} \hat{I}(S;T|K=k)
\end{aligned}$$

where T is the random variable governing the timing of each spike, k_{max} is the length of the longest spike train in the sample. The estimate of the timing information, $\hat{I}(S;T|K =$

k), for each k is calculated using a binless method related to that of Kozachenko and Leonenko (1987). However, to improve the performance of the estimator, a time-warping transformation based on ranked spike times is applied to ensure spike times are uniformly distributed on the interval [-1,1] and then each spike train is embedded into a Euclidean space of dimension $r = \min(k, D)$, where D is the maximal embedding dimension, which is the one free parameter in the method. The estimator is then calculated as

$$\hat{I}(S;T|K=k) = \frac{r}{N_k}\sum_{j=1}^{N_k}\log\left(\frac{\lambda_j}{\lambda_j^*}\right) - \sum_s \frac{N_{s,k}}{N_k}\log\frac{N_{s,k}-1}{N_k-1}$$

where λ_j is the distance between the jth spike train and its nearest neighbour in the embedding space and λ_j^* is the distance between the jth spike train and its nearest neighbour evoked by the same stimulus.

Additionally, there are extra steps for dealing with the cases where two spike trains are identical up to measurement precision (in which case λ_j is zero) or that only one spike train is available for particular combinations of k and s (in which case λ_j^* is undefined). For details, the reader is referred to Victor (2002). Optionally, spike trains with D or more spikes can be treated as having the same number of spikes; this improves the precision of estimate because for large k there may only be a few spike trains available in the sample, at the expense of a small downward bias in the estimated value.

Victor (2002) further showed that this estimator performs well for data sets of the size typically available in neurophysiological experiments, i.e. a few hundred to a few thousand spike trains per neuron. Thus, this is the method I used for calculating the mutual information between the stimulus and the spike trains of individual neurons.

This leaves two quantities left to estimate to construct the PID: mutual information between the stimulus and pairs of spike trains, and the specific information provided by each neuron's spike trains about each level of the stimulus. For the former, Victor (2002) sketches an extension of the method described above for spike trains fired by ensembles of neurons. In this case, each neuron's spike trains are embedded separately and $I_{continuous}$ is conditioned on the number of spikes fired by all neurons in the ensemble. For example, for pairs of neurons:

$$I(S;R) = I_{count}(S;R) + \sum_{k=0}^{\infty}\sum_{l=0}^{\infty} P(K=k, L=l) I(S;T|K=k, U|L=l)$$
$$\hat{I}(S;R) = \hat{I}_{count}(S;R) + \sum_{k=0}^{k_{max}}\sum_{l=0}^{l_{max}} \frac{N_{k,l}}{N} \hat{I}(S;T|K=k, U|L=l)$$

where K and L are now the random variables governing the number of spikes fired by the two neurons of the pair, T and U are the random variables governing the timing of each neuron's spikes, and $N_{k,l}$ is the number of pairs of spike trains in the sample where the first neuron fires k spikes and the second l spikes.

An important detail of the extension to the multi-neuron case that Victor (2002) does not specify is how to combine the nearest-neighbour distances λ_j and λ_j^* for each neuron. One possibility is the root mean square over neurons (Jonathan D Victor, personal communication), e.g. for the two neuron case:

$$\lambda_j = \sqrt{\frac{1}{2}\left(\lambda_{j,1}^2 + \lambda_{j,2}^2\right)}$$

where $\lambda_{j,i}$ is the nearest-neighbour distance for the the jth spike train fired by the ith neuron. Each λ_j^* is estimated similarly.

This leaves the specific information about each stimulus value provided by each neuron's spike trains as the only quantity left to estimate. As there is a chain rule for KLD similar to that for mutual information (Cover and Thomas 2006), the stratification and embedding method of Victor (2002) can be used here if a suitable estimator of continuous KLDs is available. Nearest-neighbour estimators for the KLD are well-studied; to date, the best performing estimator in the literature is that of Wang et al. (2009), so this is the one I used. This estimator calculates the KLD, $D_{KL}(P||Q)$ between two random variables P and Q using the nearest neighbour distances within a sample from P and the distance from each point in the sample of P to its nearest neighbour in a sample from Q. However, because I am calculating $D_{KL}(R|s||R)$, the first sample will always be a subset of the second. Thus the latter distances will always be at least as large as the former, which introduces a severe downward bias in the estimate, often to the point of being negative (which is impossible for a KLD). To avoid this problem I divide each dataset in two, giving one half as the sample from R and splitting the other into samples from $R|s$ for each s. I then repeat this with the partitions the other way round, then take the average of the two estimates for each $D_{KL}(R|s||R)$.

A C-based implementation of the method of Victor (2002) for single neurons with Matlab interfaces is available in STAToolkit (Goldberg et al. 2009). To extend it to the multineuron case, I reimplemented the calculation of the binless estimator in Matlab, checking my implementation gave numerically identical results to those given by the implementation in STAToolkit for a number of test datasets taken from my own experiments. I used the routines in STAToolkit for time-warping and embedding spike trains in their original form. I wrote my own implementation of the KLD estimator of Wang et al. (2009) from scratch in Matlab, using STAToolkit warped and embedded spike trains as input.

A.3 Evaluation

A.3.1 *Generating Simulated Spike Train Data*

To test the spike train PID estimator outlined above, I generated simulated spike trains for pairs of neurons responding to eight equiprobable stimuli (to match the task used in chapter 3), i.e. $p(s) = 1/8$ for all s. Each simulated neuron was modelled as a Poisson process with a rate parameter λ_s that depends on the stimulus. Using a known, fixed distribution to generate the spike trains allowed me to calculate exact PID values for each pair (see section A.3.2). For a trial of length T on which stimulus s was presented, the number and location of spikes fired by a particular neuron was governed by:

$$P(N \text{ spikes in the interval } [0,T]|s) \sim \text{Poi}(\lambda_s T) = \frac{(\lambda_s T)^N}{N!} e^{-\lambda_s T}$$
$$P(t_{i+1} = t_i + \tau | t_i, s) \sim \text{Exp}(\lambda_s) = \lambda_s e^{-\lambda_s \tau}$$

where t_j is the time of the jth spike fired during the trial. For numerical convenience, I set $T = 1$. I generated each spike train by randomly drawing values from an exponential distribution to determine the inter-arrival time of each spike (with the first such random value giving the time of the first spike after the beginning of the trial) until the sum of all inter-arrival times equalled or exceeded T (spikes with time greater than T were not included). I generated k such spike trains in response to each stimulus for each neuron, for a total of $n = 8k$ trains per neuron, with values of k ranging logarithmically from 1 to 1250 (i.e. n from 8 to 10000).

Values of λ_s for each neuron were generated according to:

$$\lambda_s = A \left(\frac{\cos(\pi * (s - x)/4) + 1}{2} \right) \text{ for } s = 0..7$$

where x is the neuron's preferred stimulus and lies on the interval [0,8) and A controls the neuron's maximum firing rate. Thus each neuron's average firing rate in response to each stimulus varies sinusoidally between 0 and A. I generated 50 pairs of neurons with preferred stimuli x, y randomly generated such that $x - y$ is uniformly distributed on the interval [-4,4), i.e. if s is interpreted as the phase of some periodic signal then the differences in preferred directions are circularly uniform. I chose five fixed values of A (10 pairs each per value) spaced logarithmically between 1 and 100 to reflect different strengths of firing rate tuning to the stimulus. This scheme was chosen to superficially resemble one of the possible patterns of responses of RGCs to grating stimuli, i.e. sinusoidal modulation of firing rate with phase of grating, and to see how the strength of the tuning affects the reliability of the spike train PID estimator.

Finally, I repeated the above ten times each for every pair of neurons. Spike trains were generated independently for each neuron, hence each neuron's stimulus-conditional firing distribution was independent from the other neuron in the pair, i.e. $p(r_1, r_2|s) = p(r_1|s)p(r_2|s)$ for spike trains r_1 and r_2 fired by different neurons on the same trial. Note that this does not imply that the marginal distributions of each neuron's spike trains were statistically independent, i.e. $p(r_1, r_2) \neq p(r_1)p(r_2)$ in general. As a trivial example, consider one neuron with $x = 0$ and another with $x = 4$, so that the first neuron's preferred stimulus is the other's null stimulus and vice versa. Even if spike trains for each stimulus are generated independently on each trial as described above, averaged over all stimuli the two neurons' responses will be anti-correlated, as the first neuron will tend to fire many spikes when the second fires few and vice versa.

A.3.2 *Direct PID Calculation for Stimulated Poisson Neurons*

As the stimulus-conditional probability distribution of each neuron's spike trains are known, it is possible to calculate the PID directly for each pair as follows. First, I calculated the mutual information between each neuron and the stimulus as

$$\begin{aligned} I(S;R) &= H(R) - H(R|S) \\ &= H(R) - \sum_s p(s)H(R|s) \end{aligned}$$

Following (McFadden 1965), to calculate each of these entropies I decomposed the random processes R (corresponding to the response of a neuron to any stimulus) and $R|s$ (corresponding to the response of a neuron to a stimulus s) into a numerical component, governing the number of spikes, and a locational component, governing the timing of each spike. The probability of a spike train given a stimulus is thus:

$$p(r|s) = p(n,t|s)k_n(\mathbf{u},t|s)dv_n$$

where $p(n,t|s)$ is the probability of observing n spikes in the interval (0,t] given a stimulus s:

$$p(n,t|s) = \frac{(\lambda_s t)^n}{n!}e^{-\lambda_s t}$$

$k_n(\mathbf{u},t|s)$ is the probability of observing the spike train $\mathbf{u} = t_1, ..., t_n$:

$$k_n(\mathbf{u},t|s) = \frac{n!}{t^n}$$

and dv_n is an infinitesimal n-dimensional volume. $H(R|s)$ can then be calculated using the standard formula for entropy:

$$
\begin{aligned}
H(R|s) &= -\sum_{n=0}^{\infty} \int_{R_n(t)} p(n,t|s) k_n(\mathbf{u},t|s) \log\left[p(n,t|s) k_n(\mathbf{u},t|s)\right] dv_n \\
&= -\sum_{n=0}^{\infty} p(n,t|s) \log p(n,t|s) - \sum_{n=1}^{\infty} p(n,t|s) \int_{R_n(t)} k_n(\mathbf{u},t|s) \log k_n(\mathbf{u},t|s) dv_n \\
&= H_N(R|s) + H_L(R|s)
\end{aligned}
$$

where $R_n(t)$ is the region $0 < t_1 < ... < t_n \leq t$. A more detailed derivation is available in McFadden (1965). The calculation of $H(R|S)$ follows a similar logic, except now we replace the conditional distributions with the corresponding marginal distributions:

$$
\begin{aligned}
p(n,t) &= \sum_s p(s) p(n,t|s) \\
k(\mathbf{u},t) dv_n &= \sum_s p(s) k(\mathbf{u},t|s) dv_n \\
&= \sum_s p(s) \frac{n!}{t^n} \\
&= \frac{n!}{t^n} \sum_s p(s) \\
&= \frac{n!}{t^n} \\
&= k(\mathbf{u},t|s) dv_n
\end{aligned}
$$

Following a similar logic as that used for the conditional entropy, $H(R)$ is given by:

$$
\begin{aligned}
H(R) &= -\sum_{n=0}^{\infty}\int_{R_n(t)}\left[\sum_s p(s)p(n,t|s)k_n(\mathbf{u},t|s)\right]\log\left[\sum_s p(s)p(n,t|s)k_n(u,t|s)\right]dv_n \\
&= -\sum_{n=0}^{\infty}\int_{R_n(t)}\frac{n!}{t^n}\left[\sum_s p(s)p(n,t|s)\right]\log\left[\frac{n!}{t^n}\sum_s p(s)p(n,t|s)\right]dv_n \\
&= -\sum_{n=1}^{\infty}\left\{\sum_s p(s)p(n,t|s)\int_{R_n(t)}\frac{n!}{t^n}\log\frac{n!}{t^n}dv_n\right\} \\
&\quad -\sum_{n=0}^{\infty}\left\{\left[\sum_s p(s)p(n,t|s)\right]\log\left[\sum_s p(s)p(n,t|s)\right]\int_{R_n(t)}\frac{n!}{t^n}dv_n\right\} \\
&= H_L(R)+H_N(R)
\end{aligned}
$$

However, note that

$$
\begin{aligned}
H_L(R) &= -\sum_{n=1}^{\infty}\left\{\sum_s p(s)p(n,t|s)\int_{R_n(t)}\frac{n!}{t^n}\log\frac{n!}{t^n}dv_n\right\} \\
&= -\sum_s\left\{\sum_{n=1}^{\infty}p(s)p(n,t|s)\int_{R_n(t)}\frac{n!}{t^n}\log\frac{n!}{t^n}dv_n\right\} \\
&= -\sum_s p(s)\left\{\sum_{n=1}^{\infty}p(n,t|s)\int_{R_n(t)}\frac{n!}{t^n}\log\frac{n!}{t^n}dv_n\right\} \\
&= \sum_s p(s)H_L(R|s) \\
&= H_L(R|S=s)
\end{aligned}
$$

In other words, the locational entropy component is identical for both the stimulus-dependent process and the process averaged over stimuli, so these terms cancel out in the mutual information calculation. Further note that $\int_{R_n(t)}\frac{n!}{t^n}dv_n = 1$, so the mutual information can be written as:

$$
\begin{aligned}
I(R;S) &= H_N(R) - H_N(R|S) \\
&= -\sum_{n=0}^{\infty} \left\{ \left[\sum_s p(s)p(n,t|s) \right] \log \left[\sum_s p(s)p(n,t|s) \right] \right\} \\
&\quad + \sum_s p(s) \sum_{n=0}^{\infty} p(n,t|s) \log p(n,t|s)
\end{aligned}
$$

The calculation of the mutual information between pairs of simulated neurons and the stimulus proceeds similarly, except that $p(r|s)$ is replaced with $p(\mathbf{r}|s) = p(r_1|s)p(r_2|s)$. As noted, the two neurons' responses are conditionally independent, so the probability of a pair of spike trains is the product of the probabilities of the individual spike trains. The specific information can be calculated very similarly by writing the KLD as the cross entropy between the stimulus-conditional and marginal response distributions less the conditional entropy:

$$
D_{KL}(R|s||R) = H(R|s,R) - H(R)
$$

where a discrete cross-entropy is given by

$$
H(X,Y) = -\sum_x p(X=x) \log \frac{p(X=x)}{p(Y=x)}
$$

and is defined analogously for the continuous and mixed discrete-continuous cases.

Using the above method and the PID equations given in section A.1, I numerically calculated precise PID values in Matlab for each of the 50 pairs of simulated neurons.

A.3.3 *Calculating and Evaluating Estimated PID Values*

Let $\mathbf{t}_{i,j,k,l}$ be the ith set of spike trains ($1 \leq i \leq 10$) generated for the jth pair of neurons ($1 \leq j \leq 50$) with k stimuli per trial and $A = l$. As described above, I can calculate the PID for the jth pair exactly from each neuron's stimulus-conditional firing distribution. For example, I can calculate the mutual information between the paired spike trains and the stimulus, $I_j(R_1, R_2; S)$ (where R_1 and R_2 are the responses of the two neurons of the pair). I can also estimate this value by feeding $\mathbf{t}_{i,j,k,l}$ into the spike train PID estimator described in section A.2. Let the resulting estimate be denoted $\hat{I}_{i,j,k,l}(R_1, R_2; S)$. The error between this estimate and the true value is calculated as:

$$E_{i,j,k,l} = \frac{\hat{I}_{i,j,k,l}(R_1,R_2;S)}{I_j(R_1,R_2;S)} - 1$$

Averaging these errors for each simulation and each pair gives the error as a function of trials per stimulus and strength of tuning:

$$E_{rel}(k,l) = \left\langle \langle E_{i,j,k,l} \rangle_i \right\rangle_j$$

where $\langle ... \rangle_x$ denotes averaging over the variable x. If this value is positive, then the pair information is consistently overestimated and likewise if it is negative then the pair information is consistently underestimated. If it is close to zero, then there is no bias in the estimate in either direction. Alternatively, taking the absolute value before averaging gives a measure of the precision of the estimate:

$$E_{abs}(k,l) = \left\langle \langle |E_{i,j,k,l}| \rangle_i \right\rangle_j$$

(The smaller E_{abs}, the more precise the estimate.) I calculated $E_{rel}(k,l)$ and $E_{abs}(k,l)$ for each of the directly calculated (redundancy, individual information, pair information) and derived (unique information, synergy) PID quantities.

A.4 Results

Figure A.1 shows the PID values for 50 pairs of simulated Poisson neurons that fire with a rate that depends sinusoidally on the stimulus, calculated according to the formulae in section A.3.2. These 50 pairs are divided into five groups of 10 with different maximum firing rates. Unsurprisingly, the higher the maximum firing rate, the more information about the stimulus is contained in the responses, with pairs of neurons with 100Hz maximum firing rates providing almost perfect information about the stimulus (eight equiprobable stimuli means $H(S) = -\log_2 \frac{1}{8} = 3$). For low firing rates, the pair information is roughly equally distributed between redundancy, unique information, and synergistic information, not unlike the pattern for the P52 retina in chapter 3, albeit with a much lower average pair information.

The left hand side of figure A.2 shows how the fraction of redundancy and synergy varies

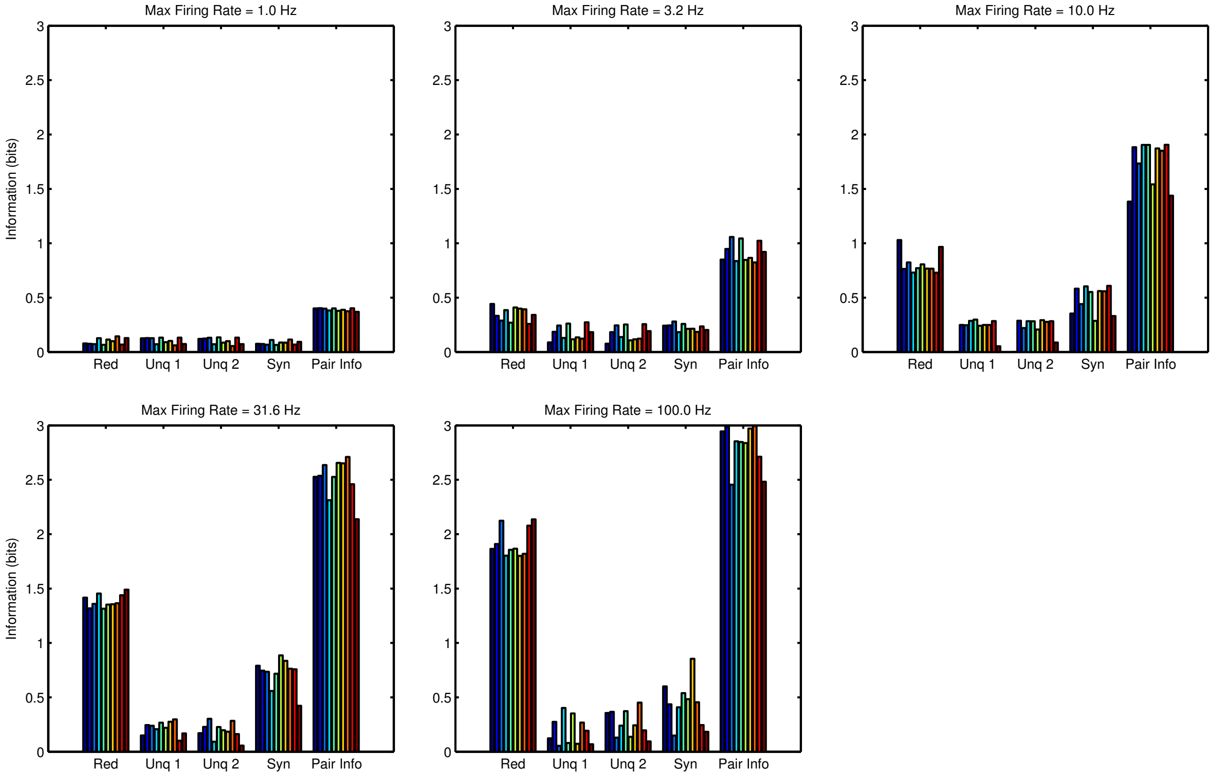

Figure A.1: Actual PID values for 50 pairs of simulated neurons. The 50 pairs are divided into five groups of 10 pairs with different maximum firing rates; each group is shown in a separate subfigure. Different colours within each subfigure correspond to different pairs.

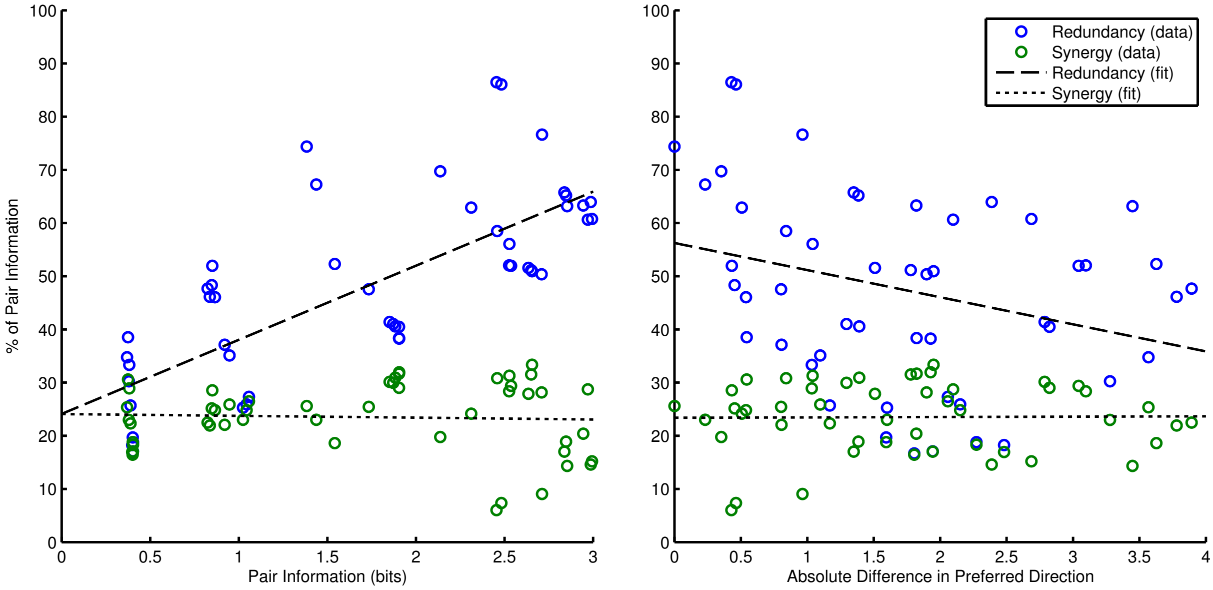

Figure A.2: Left: percentage of redundancy (blue) and synergy (green) in 50 pairs of simulated neurons as a function of the amount of information provided by each pair. Black lines are the line of best fit for the redundancy (dashed) and synergy (dotted) data. Right: percentage of redundancy (blue) and synergy (green) in 50 pairs of simulated neurons as a function of the absolute value of the difference in preferred stimulus of each neuron of the pair. Black lines are the line of best fit for the redundancy (dashed) and synergy (dotted) data.

with the total amount of information provided by each pair. As the pair information increases, the fraction of redundant information increases and the fraction of synergy remains roughly constant. There was a modest but significant correlation between pair information and fraction of redundant information (Pearson's product-moment correlation $R^2 = 0.55, p = 7.9 \times 10^{-10}$) and no correlation between pair information and fraction of synergy ($R^2 < 0.01, p = 0.74$).

The 50 pairs of neurons each had distinct preferred stimuli, randomly assigned such that the differences between their preferred stimuli were circularly uniform. Intuitively, one might expect more redundancy the closer the two neuron's preferred stimuli and more synergy the further apart their preferred stimuli. Accordingly, there was a weak but significant negative correlation between fraction of redundancy and the absolute difference between each neuron's preferred stimuli ($R^2 = 0.09, p = 0.03$). However, no correlation with difference in preferred stimulus was observed for synergy ($R^2 < 0.01, p = 0.94$). These results are shown in figure A.2 (right).

Having calculated the correct PID values and generated different numbers of simulated spike trains for each of the 50 pairs of neurons in response to the eight stimuli, I estimated the information contained in each individual neuron's spike trains, that contained in the paired spike trains, and the redundant information in paired spike trains using the estimators described in section A.2 and tested how closely the estimated values matched the true values. Ideally, the estimator should be accurate (E_{rel} close to zero) and get more precise as the number of trials per stimulus k increases ($\forall A. \lim_{k \to \infty} |E_{abs}(k, A)| = 0$).

Figure A.3 shows the average absolute percentage error E_{abs} between the estimated and actual information values (redundancy, single neuron information, and pair information) for the 50 pairs of neurons as a function of trials per stimulus (along the x-axis) and maximum firing rate (in different subfigures). The average is taken first within then between pairs; the pattern is similar if the averaging is done the other way around but the error bars are smaller (data not shown), suggesting that the estimates are stable across multiple samples from the same system. It is clear that the estimator is not very precise: even with over a thousand trials per stimulus, the average absolute error ranges from around 10% for single neuron pair information when the maximum firing rate is around

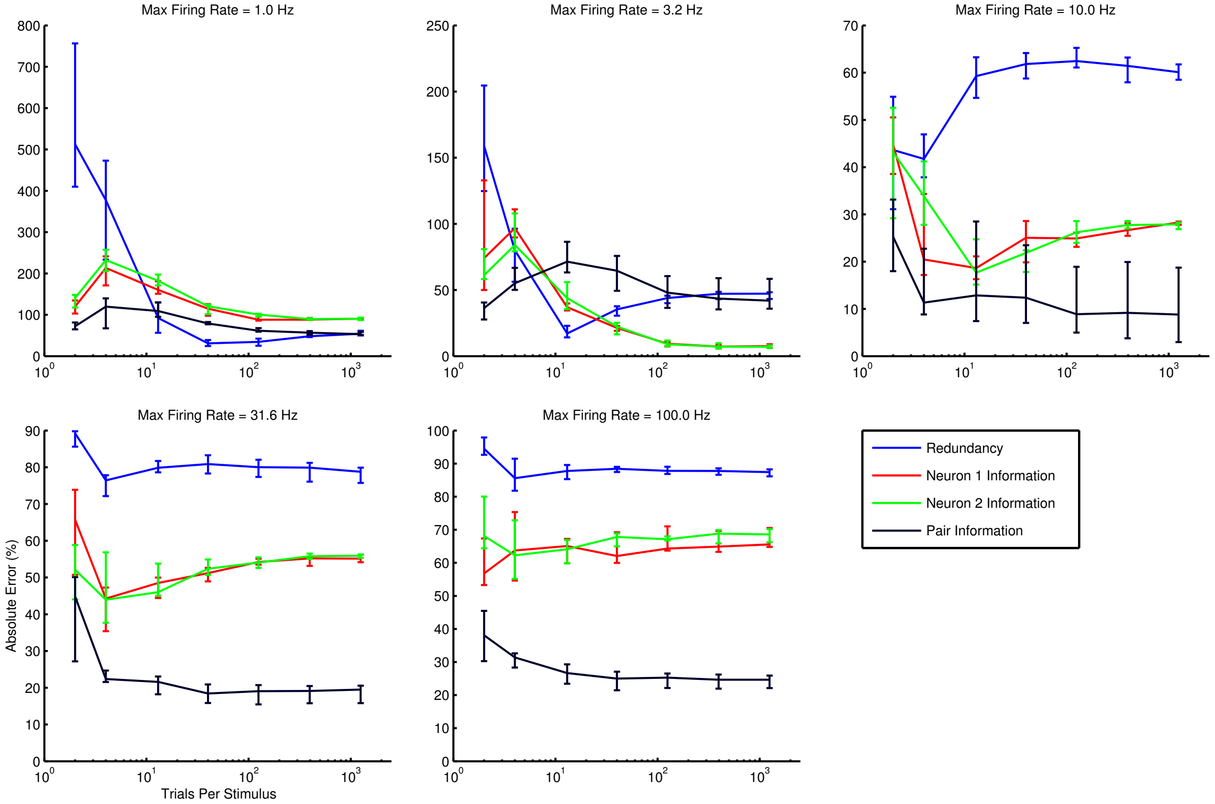

Figure A.3: Absolute percentage error between the estimated and correct values of the redundancy (blue), single neuron information (red and green), and pair information (black) for 50 pairs of simulated neurons. Each subfigure represents a group of 10 pairs of neurons having the same maximum firing rate. Medians are taken first over multiple samples from the same pair and then across different pairs with the same maximum firing rate. Error bars are interquartile range (IQR) across pairs.

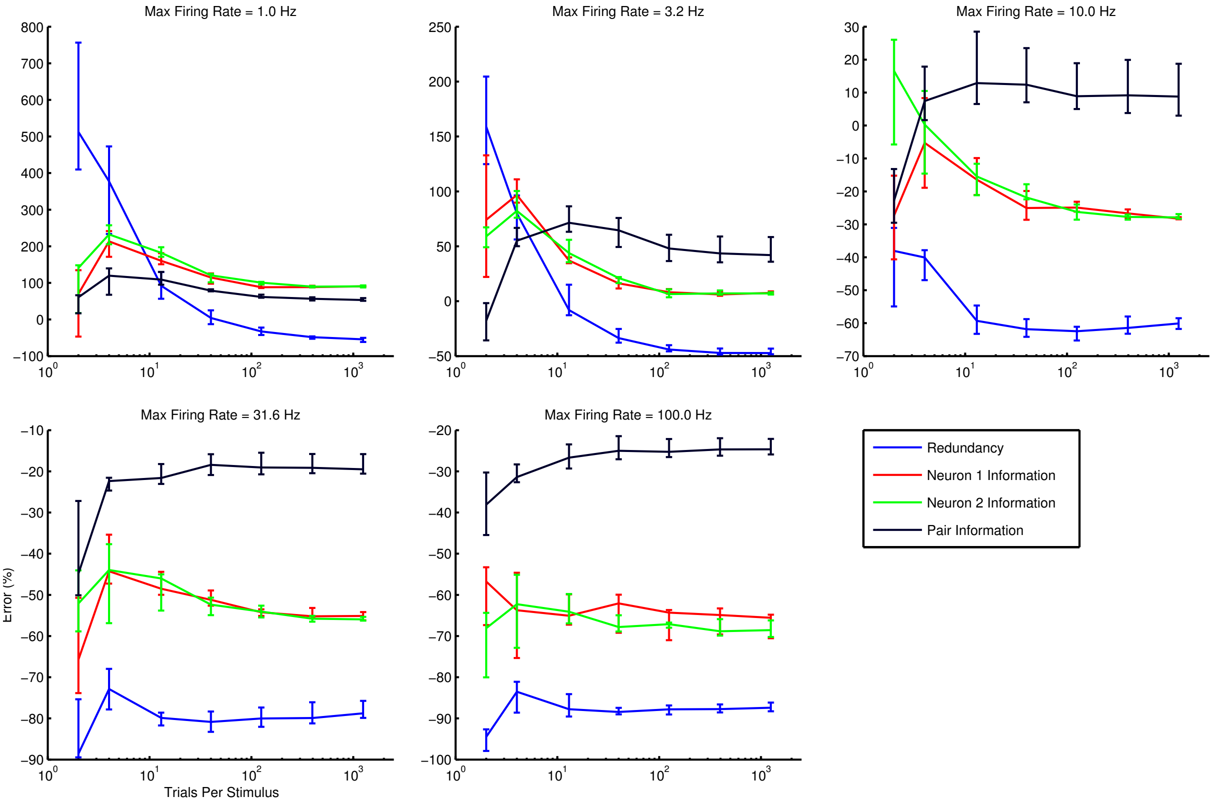

Figure A.4: Signed percentage error between the estimated and correct values of the redundancy (blue), single neuron information (red and green), and pair information (black) for 50 pairs of simulated neurons. Each subfigure represents a group of 10 pairs of neurons having the same maximum firing rate. Medians are taken first over multiple samples from the same pair and then across different pairs with the same maximum firing rate. Error bars are interquartile range (IQR) across pairs.

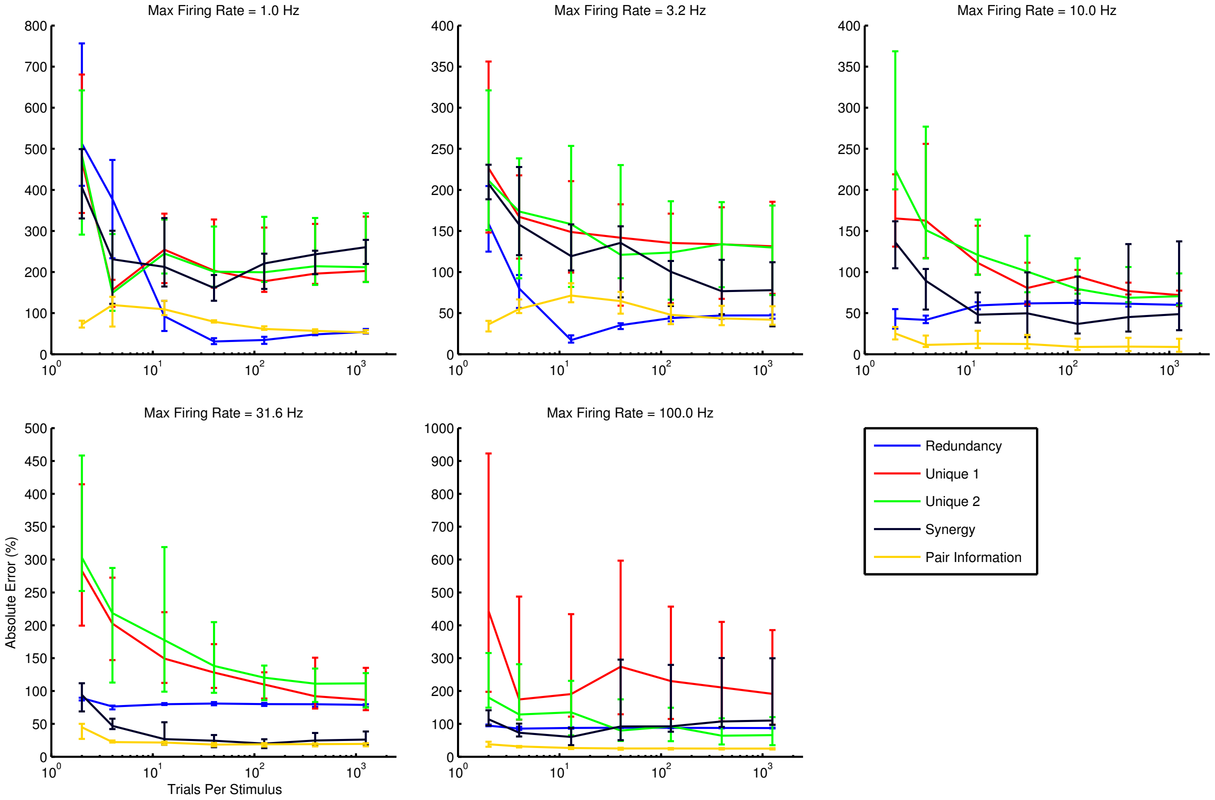

Figure A.5: Absolute percentage error between the estimated and correct values of the redundancy (blue), unique information carried by each neuron (red and green), synergy (black), and pair information (yellow) for 50 pairs of simulated neurons. Each subfigure represents a group of 10 pairs of neurons having the same maximum firing rate. Medians are taken first over multiple samples from the same pair and then across different pairs with the same maximum firing rate. Error bars are interquartile range (IQR) across pairs.

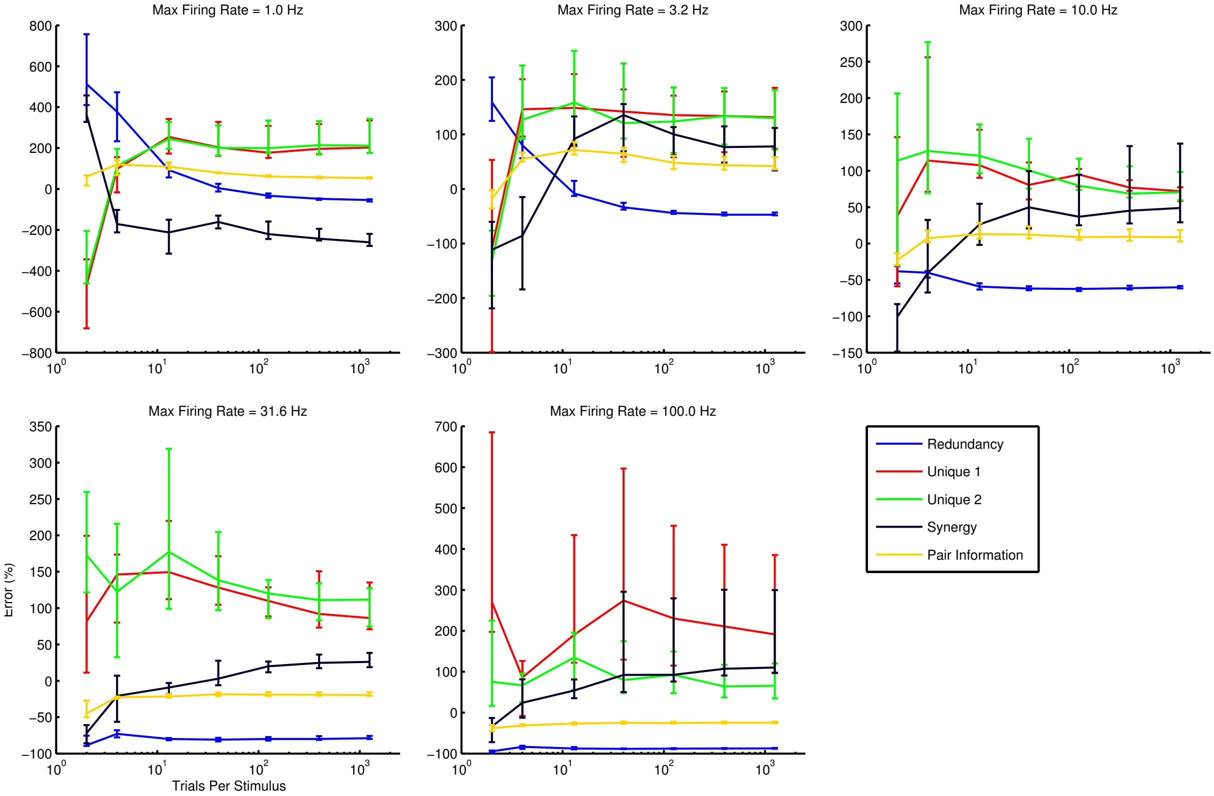

Figure A.6: Signed percentage error between the estimated and correct values of the redundancy (blue), unique information carried by each neuron (red and green), synergy (black), and pair information (yellow) for 50 pairs of simulated neurons. Each subfigure represents a group of 10 pairs of neurons having the same maximum firing rate. Medians are taken first over multiple samples from the same pair and then across different pairs with the same maximum firing rate. Error bars are interquartile range (IQR) across pairs.

3 Hz to almost 90% for redundancy for pairs of neurons with high maximum firing rates.

Even if an estimator is imprecise, it may nevertheless be accurate if there is no systematic bias in the estimates. In this case, E_{rel} will be close to zero as the positive and negative errors should cancel out. Unfortunately, figure A.4 confirms that this is not the case. It shows the (signed) average percentage error E_{rel} for the quantities in figure A.3 as a function of trials per stimulus and maximum firing rate. For large samples, the single neuron information is overestimated when the firing rates are low ($<$ 10Hz) and underestimated above this. The same is true for the pair information, except the switch from over- to underestimation happens at higher maximum firing rates (between 10 and 30 Hz). Finally, for all but the smallest samples and lowest firing rates, the redundancy tends to be underestimated.

The two variable PID comprises the redundancy and the pair information along with three derived quantities: the unique information carried by each neuron of the pair (the single neuron information less the redundant information), and the synergistic information (the pair information less each single neuron's information plus the redundant information). For unbiased estimates, summing and subtracting different estimates in this way should tend to decrease the precision of the estimates, but if the estimates are biased then the biases may cancel out or exacerbate each other depending on their direction.

Figure A.5 shows E_{abs} for the PID estimated from the simulated spike trains by combining the estimates of redundancy, single neuron information and pair information. For low firing, the pattern is as one would expect: the precision of the derived quantities (synergy and unique information) is generally lower than that of the directly estimated quantities (redundancy and pair information). Above 10Hz, however, the synergy is actually estimated more accurately than the redundancy. Looking at figure A.4 explains why this is: redundancy, single neuron information, and pair information are all systematically underestimated, but because the single neuron information is subtracted from the sum of the pair information and the redundancy, the biases partially cancel. This is seen most dramatically for the 31.6Hz maximum firing rate group, where sum of the downward biases in the redundancy (~80% for large samples) and the pair information (~20%) are close to twice the downward bias in each single neuron's information (~55% each), so they cancel to only a ~10% overestimate.

Even so, the estimates of the derived PID quantities are still imprecise: even with large samples, the average absolute error ranges from 10% to 200% for synergy and from 100% to 400% for the unique information, depending on the maximum firing rate of the pairs. (That unique information is generally estimated less precisely than synergy despite involving fewer arithmetic operations is likely a combination of redundancy being extremely poorly estimated and the unique information being generally the smallest quantity in each of the PIDs.) Figure A.6 shows E_{rel} for each of the PID estimates. The derived PID quantities, unique information and synergy, are generally overestimated for all but the smallest sample sizes and lowest firing rates.

A.5 Discussion

The spike train PID estimator developed in this appendix is based on mathematically sound estimators of spike train information (Victor 2002) and continuous KLDs (Wang et al. 2009) that appear to perform well in the tests shown by their respective authors. However, it performs disappointingly poorly, with the average absolute error for any quantity rarely dropping below 10% and in many cases quantities are overestimated by more than 100% of the analytically computed values, even when the sample size is impractically large for many neuroscientific experiments (1250 trials per stimulus or 10000 trials total for an experiment with 8 stimuli). Further, the magnitude and direction of the errors depends in a complicated way on the number of sampled spike trains and the maximum firing rate. Moreover, to keep things simple only one style of responses (sinusoidally-tuned Poisson neurons) was considered, but beyond this the possibilities are almost boundless: other forms of tuning, varying amounts and distributions of spontaneous activity, different types of point process, inhomogeneous rate functions, etc. This makes the results pertaining to synergy contained in spike trains in chapter 3 hard to interpret.

Why does the estimator perform so badly? Wang et al. (2009) do not report percentage errors for their estimators, only errors in nats; moreover, the scale bars on their graphs make it hard to determine the magnitude of these errors. Nevertheless, they appear to be much smaller than the errors observed here, suggesting that the extra error is due to the stratification method, adapted from Victor (2002), used to apply the continuous KLD estimator to spike train data. Additionally, as noted above, the KLD estimator is designed for use on samples from two distinct distributions, not a marginal distribution and the same distribution conditioned on another. Despite ensuring the two samples given to the estimator were distinct, this may still explain some of the increased error.

The estimates for single-neuron and pair information are more precise than the estimates of redundancy, but still poor. To investigate the source of these errors, I tested the method of Victor (2002) on purely continuous data. I used the same method as described in section A.3, except instead of simulating Poisson processes I drew samples from a variety of standard continuous probability distributions where I set one parameter to $s \in 1..8$ while holding any other parameters fixed (at a value of 1 for all parameters except location parameters, which were set to zero). Figure A.7 shows the absolute percentage error between the analytically computed mutual information values and those estimated using the method of Victor (2002). There is considerable variability in the magnitude of the error depending on the distribution and which parameter varies with the stimulus. The best performance is achieved for normal, log-normal and extreme value distributions where the location parameter (i.e. the mean for a normal distribution) varies with the stimulus, as well as the gamma distribution where the shape parameter varies the stimulus. The worst performance is achieved for the beta distribution, the gamma distribution where the scale varies with the stimulus, and the exponential distribution. The latter may explain the poor performance of this method on spike trains simulated as Poisson processes, as the exponential distribution governs the inter-arrival time of events (here, spikes) in a Poisson processes. Victor (2002) did not perform any such tests of their method. Instead, they show that they can estimate entropies (not mutual information) for Gaussian-distributed data (which is one of the distributions their method perfoms best for according to my simulations) and simulated Poisson data, which they only test with five stimulus classes evoking large changes in firing rate. Thus, it may be that their method performs worse as the number of stimuli increases or when the variation in evoked firing rates are more subtle, although as the data in this appendix show, the relationship between estimated spike train information values and stimulus-dependent firing rates is complicated.

What does this all mean for the spike train PID results in chapter 3? On first inspection, the large absolute errors should render the results meaningless. However, consider the results from the two retinas recorded on the APS (figures 3.13 and 3.14), which are likely more representative than the MCS recordings due to the larger numbers of recorded cells. According to the data, the information contained in the spike trains is only marginally greater than that in the spike counts, for which information estimates are reasonably accurate. Moreover, inspection of the distributions of the spike count and spike train information in these retinas reveals that there is a considerable fraction of pairs for which there is apparently more information in the spike counts than the spike trains (for the MCS data, this fraction was about 35%). This is impossible, however, as one can derive the spike count from the spike train, so the latter must contain at least as much information as the former (this is the data processing inequality (Cover and Thomas 2006)). The results in figure A.4 show that both the single neuron information and the pair information usually tend to be underestimated by the spike train PID estimator developed here, which may explain why some RGC pairs appear to violate the data processing inequality.

The results in this appendix also show that the spike train PID estimator also tends to overestimate synergy (although often not by a large amount) and underestimate redundancy considerably. This has the potential to reverse the pattern of results seen for spike trains in chapter 3, where synergy tended to be large and redundancy small. This would also bring these results more in line with those Schneidman et al. (2011), who found that there was a small amount of synergy in RGC pair spike trains, but it is difficult to compare their results to mine as they only consider information carried by particular symbols and do not report information values for spike trains considered as a whole. In any case, it is clear that a more precise and less biased PID estimator for spike trains is necessary before any definitive conclusions can be made about the amount of synergy in RGC pair spike trains.

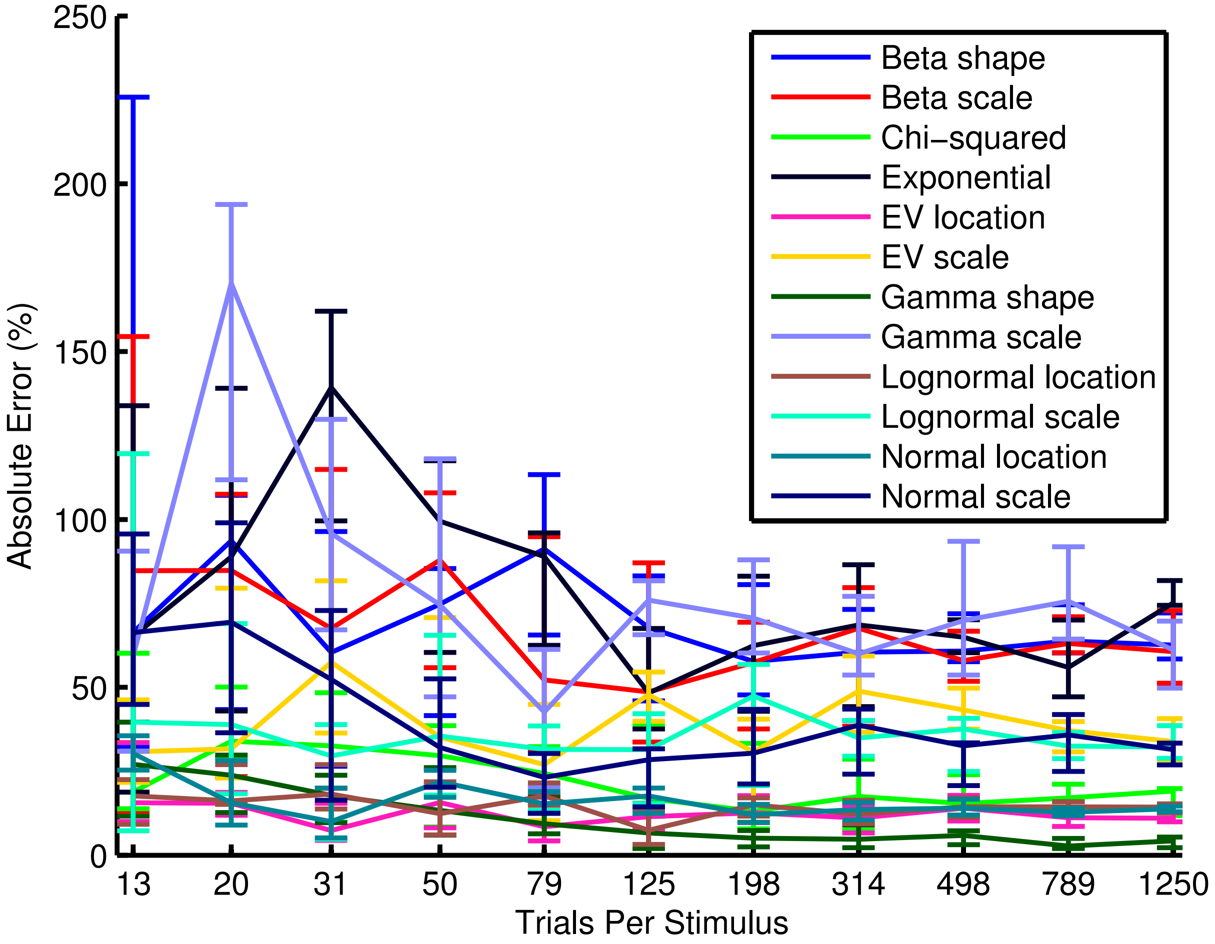

Figure A.7: Median absolute percentage error in estimated mutual information between a stimulus and samples from standard continuous probability distributions where the indicated parameter varies with the stimulus. Error bars are IQR across samples. Any parameters that were not varied were set to one, with the exception of location parameters, which were set to zero. EV = extreme value distribution.

Appendix B. Worked PID Examples

B.1 Different RGC Types Give Rise to Synergy Without Correlations

B.1.1 *The Model System and Task*

Imagine a simple retinal circuit (figure 3.23) with two cones, four bipolar cells (two ON and two OFF) and two ganglion cells (one ON and one OFF). The synapse between an ON bipolar cell and its postsynaptic RGC contains a rectifying nonlinearity such that the RGC receives an excitatory input if and only if the bipolar cell sees a light increment in its receptive field and vice-versa for an OFF bipolar cell.

Suppose that one presents this system with a uniform grey field, followed by one of three stimuli with equal probability: a black field, a split black and white field, or a white field. The split in the split field is such that one ON and one OFF bipolar cell each see the white half and the other two bipolar cells see the black half. An ON RGC (labelled A) will fire in response to the white and split fields but not the black field, whereas an OFF RGC (B) will fire in response to the black and split fields but not the white field. The variable representing the stimulus is denoted S. Table B.1 gives the marginal probability distributions of the stimulus and each cell's response. Table B.2 gives the joint probability distribution of A and B.

B.1.2 *Calculating the Partial Information Decomposition*

Recall from section 2.3.2 that the mutual information between two variables X and Y is the entropy of X less the entropy of X conditioned on Y:

$$I(X;Y) = H(X) - H(X|Y)$$

x	$P(S=x)$	$P(A=x)$	$P(B=x)$
0	$1/3$	$1/3$	$1/3$
1	$1/3$	$2/3$	$2/3$
2	$1/3$	-	-

Table B.1: Marginal probability distributions of S, A and B.

a	b	$P(A=a,B=b)$
0	0	0
0	1	$1/3$
1	0	$1/3$
1	1	$1/3$

Table B.2: Joint probability distribution of A and B.

However, each of A and B is completely determined by S (table B.3), so their conditional entropies are zero:

$$H(A|S) = H(B|S) = H(A,B|S) = 0$$

Thus:

$$I(R;S) = H(R) = -\tfrac{1}{3}\log_2\tfrac{1}{3} - \tfrac{2}{3}\log_2\tfrac{2}{3} = 0.9183 \quad \text{where } R = A \text{ or } B$$
$$I(A,B;S) = H(A,B) = -3 \times \tfrac{1}{3} = 1.585 = H(S)$$

That is, a single ON or OFF neuron provides about 58% of the maximum possible information about the stimulus, whereas one can completely determine which stimulus was presented from the responses of an ON and an OFF neuron taken together. Having multiple ON cells or multiple OFF cells gives the same information as having only one ON cell or one OFF cell and thus all of the information is necessarily redundant in this case.

To compute the PID for the system with one ON and one OFF neuron, first one must calculate the redundancy. As described in section 3.2.2, this is the expectation over the stimulus distribution of the minimum specific information provided by either RGC about each stimulus:

$$Red(A,B;S) = \sum_{s=0}^{2} P(S=s) \min_{R=A,B} I(R;S=s)$$

where

$$I(R;S=s) = \sum_{r=0}^{1} P(R=r|S=s)\log_2 \frac{P(R=r|S=s)}{P(R=r)}$$

Table B.3 gives the conditional probability distributions for A and B and table B.4 the specific information each RGC provides about each stimulus value. From these, it is easy

s	r	$P(A=r\|S=s)$	$P(B=r\|S=s)$
0	0	1	0
0	1	0	1
1	0	0	0
1	1	1	1
2	0	0	1
2	1	1	0

Table B.3: Probability distributions for A and B conditioned on S.

s	$I(A;S=s)$	$I(B;S=s)$
0	$\log_2 3$	$\log_2 3/2$
1	$\log_2 3/2$	$\log_2 3/2$
2	$\log_2 3/2$	$\log_2 3$

Table B.4: Specific information about S provided by A and B.

to see that

$$Red(A,B;S) = 3 \times \tfrac{1}{3}\log_2 \tfrac{3}{2} = 0.585$$

$$Unq(R;S) = I(R;S) - Red(A,B;S) = 0.333 \quad \text{where } R = A \text{ or } B$$

$$Syn(R;S) = I(A,B;S) - Unq(A;S) - Unq(B;S) - Red(A,B;S) = 0.333$$

That is, an ON and an OFF RGC provide 0.585 bits of redundant information about the stimulus, 0.333 bits each of unique information and 0.333 bits of synergistic information.

B.1.3 *Computing* ΔI

A and B are conditionally independent, that is $P(A,B|S) = P(A|S)P(B|S)$. Thus $P_{IND}(A,B|S) = P(A,B|S)$ and $P_{IND}(A,B) = P(A,B)$, therefore $\Delta I = 0$ trivially. In other words, pairwise correlations provide literally no information about the stimulus in this system.

B.2 Direction Selective RGCs with Perpendicular Preferred Directions

B.2.1 *The Model System and Task*

This example concerns very simple direction selective cells. Each cell has a preferred direction. If it is presented with a bar moving in this direction, it fires two spikes. A bar moving in the opposite direction evokes no response and a bar moving perpendicularly evokes a single spike.

Suppose there are two such cells, A and B, with perpendicular preferred directions and

x	$P(S=x)$	$P(A=x)$	$P(B=x)$
0	$1/4$	$1/4$	$1/4$
1	$1/4$	$1/2$	$1/2$
2	$1/4$	$1/4$	$1/4$
3	$1/4$	-	-

Table B.5: Marginal probability distributions of S, A and B. A's preferred direction is 0, B's preferred direction is 1, and 2 & 3 are the opposite directions to 0 & 1, respectively.

s	a	b	$P(A=a,B=b)$
0	2	1	$1/4$
1	1	2	$1/4$
2	0	1	$1/4$
3	1	0	$1/4$

Table B.6: Joint probability distribution of S, A, and B. Combinations that occur with zero probability are omitted for brevity.

that they are presented with bars moving either in or against one of the cells' preferred direction. Thus there are four possible stimulus directions. Further assume each stimulus is equiprobable. Once again, the stimulus variable is denoted S.

B.2.2 *Computing the Partial Information Decomposition*

The marginal and joint distributions of A, B and S are given in tables B.5 and B.6.

As in the previous example, the conditional entropies of A and B are zero, so the mutual informations are given by:

$I(R;S) = H(R) = -2 \times \frac{1}{4}\log_2\frac{1}{4} - \frac{1}{2}\log_2\frac{1}{2} = 1.5 \quad$ where $R = A$ or B

$I(A,B;S) = H(A,B) = -4 \times \frac{1}{4}\log_2\frac{1}{4} = 2 = H(S)$

Tables B.7 and B.8 give the probabilities of A and B conditioned on S and the resulting specific information provided by A or B about each state of S.

Note that the minimum specific information provided by either A or B about any state of S is always $\log_2 2 = 1$ (table B.8), so the redundancy is given by:

$Red(A,B;S) = 4 \times \frac{1}{4} \times 1 = 1$

Therefore

$Unq(R;S) = I(R;S) - Red(A,B;S) = 0.5 \quad$ where $R = A$ or B

$Syn(A,B;S) = I(A,B;S) - Unq(A;S) - Unq(B;S) - Red(A,B;S) = 0$

s	r	$P(A=r\|S=s)$	$P(B=r\|S=s)$
0	0	0	0
0	1	0	1
0	2	1	0
1	0	0	0
1	1	1	0
1	2	0	1
2	0	1	0
2	1	0	1
2	2	0	0
3	0	0	1
3	1	1	0
3	2	0	0

Table B.7: Probability distributions for A and B conditioned on S.

s	$I(A;S=s)$	$I(B;S=s)$
0	$\log_2 4$	$\log_2 2$
1	$\log_2 2$	$\log_2 4$
2	$\log_2 4$	$\log_2 2$
3	$\log_2 2$	$\log_2 4$

Table B.8: Specific information about S provided by A and B.

That is, there is one bit of redundant information, each of A and B provides half a bit of unique information, and there is no synergistic information.

Appendix C. Calculating Equivalent Photon Flux for the APS Projector

As noted in chapter 5, the APS projector has a maximum irradiance on the MEA of around 0.13 W/cm^2. This is far brighter than is necessary for most retinal physiology experiments, even those involving the relatively light insensitive ChR2, but neutral density filters can be used to bring the irradiance into more physiologically relevant ranges. However, the projector is a standard RGB projector, projecting broadband white light designed to be efficiently absorbed by the red, green, and blue light sensitive cones of the human retina. ChR2, by contrast, is most sensitive to blue light and hence much of the light from the projector in the longer wavelengths will not effectively stimulate ChR2. As such, a certain irradiance of light from the APS projector is effectively less ‘bright’ from the perspective of a ChR2-expressing retina than the same irradiance coming from, say, the µLEDs used in chapter 4. This section details the conversion from APS projector irradiance to equivalent photon flux at the peak of the ChR2 absorption spectrum.

First I measured the background-corrected (60s integration time, all room lights and monitors off) relative emission spectrum of the APS projector displaying a plain white background with no neutral density filters in place using a Thorlabs CCS100 spectrometer with a 20s integration time. To convert this to spectral flux density incident on the MEA, $F(\lambda)$, I divided the relative intensity at each wavelength, $f(\lambda)$, by the area under the relative intensity curve, then multiplied by the irradiance, I, as measured with a photodiode attached to a power meter:

$$F(\lambda) = If(\lambda) / \int_0^\infty f(\lambda) d\lambda$$

Note that this assumes the transmission spectra of air and any neutral density filters that were in place when the irradiance was measured are reasonably flat in the visible spectrum. This is justified as air is transparent to visible light and neutral density filters, as their name implies, are designed to transmit all wavelengths equally. Figure C.1 gives

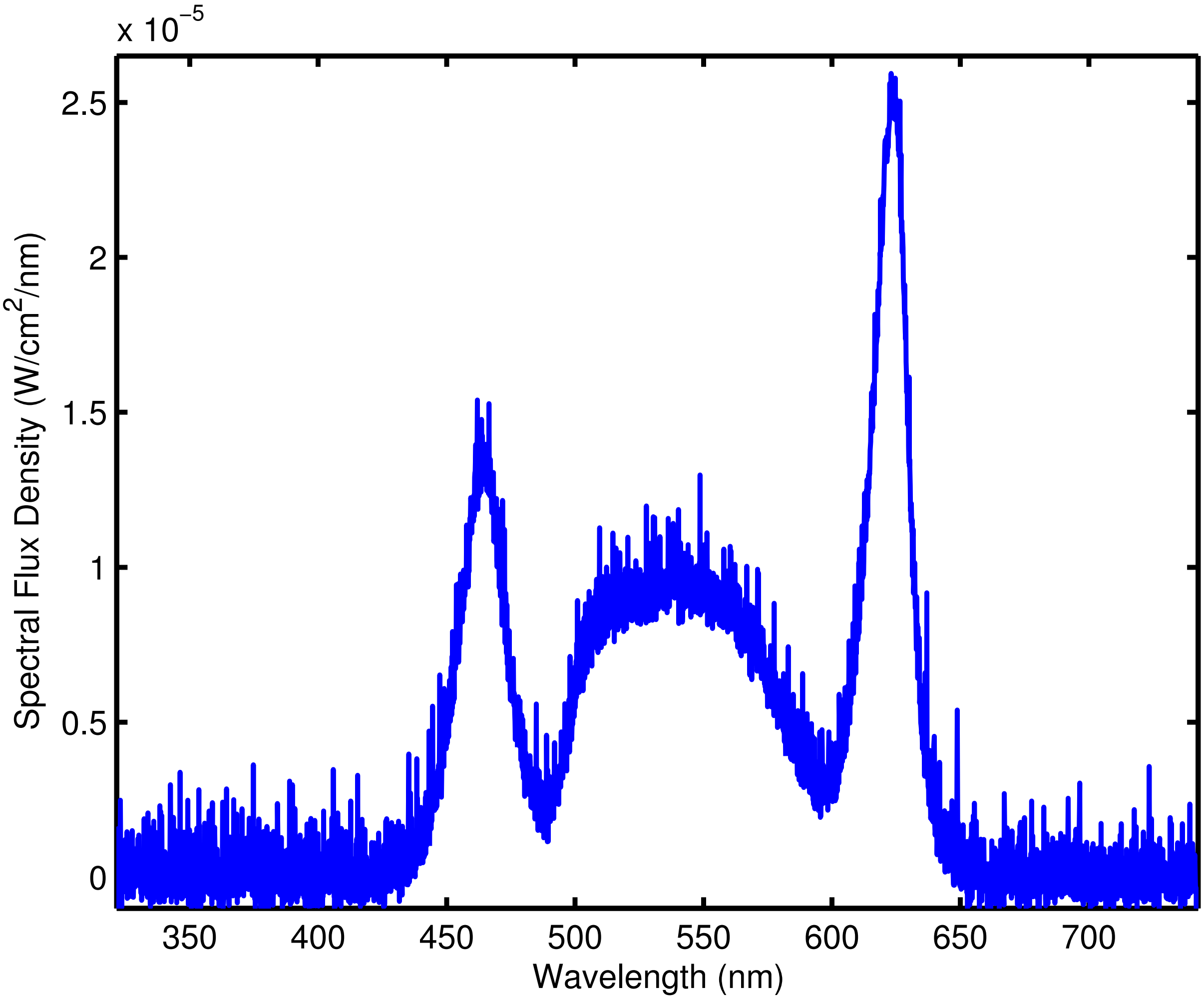

Figure C.1: Spectral flux density for the light from the APS projector incident on the retina after attenuation with an ND1.9 neutral density filter.

the spectral flux density of light incident on the MEA with an ND1.9 neutral density filter in place ($I = 1.650\text{mW/cm}^2$).

Per the Planck-Einstein relation, the energy of a photon, E, is given by

$$E(\lambda) = \frac{hc}{\lambda}$$

where $h = 6.626 \times 10^{-34}$J·s is Planck's constant, $c = 2.998 \times 10^8\text{ms}^{-1}$ is the speed of light, and λ is the wavelength. Thus, to get the number of photons of each wavelength incident on the MEA per unit area, I divided the spectral flux density by the photon energy at each wavelength:

$$N(\lambda) = F(\lambda)/E(\lambda) = F(\lambda)\frac{\lambda}{hc}$$

The result is shown in figure C.2 (blue curve). Integrating $N(\lambda)$ with respect to wavelength gives the total number of photons incident on the MEA per unit area. However, as noted, ChR2 does not absorb photons of all wavelengths equally. To correct for this, I took the absorption spectrum for ChR2 given in Scholz et al. (2012) and normalised it to have a peak value of unity (figure C.2, green curve). The peak wavelength was 450nm. To calculate the equivalent photon flux, P, from the perspective of ChR2 had all photons emitted by the projector been of this wavelength, I convolved $N(\lambda)$ with the ChR2 absorption spectrum, $R(\lambda)$:

$$P = \int_0^\infty N(\lambda)R(\lambda)d\lambda$$

Table C.1 gives the values of P with different neutral density filters. All integrals noted in this appendix were calculated numerically using trapezoidal integration with the `trapz` function in Matlab.

ND ($\log_{10}$ units)	I (mW/cm^2)	P (ph$\cdot$cm^{-2}s^{-1})
2.2	0.874	5.5×10^{14}
1.9	1.650	1.0×10^{15}

Table C.1: Equivalent photon flux at the wavelength that maximally excites ChR2 (i.e. 450nm) of the light incident on the retina from the MEA after attenuation with different neutral density filters.

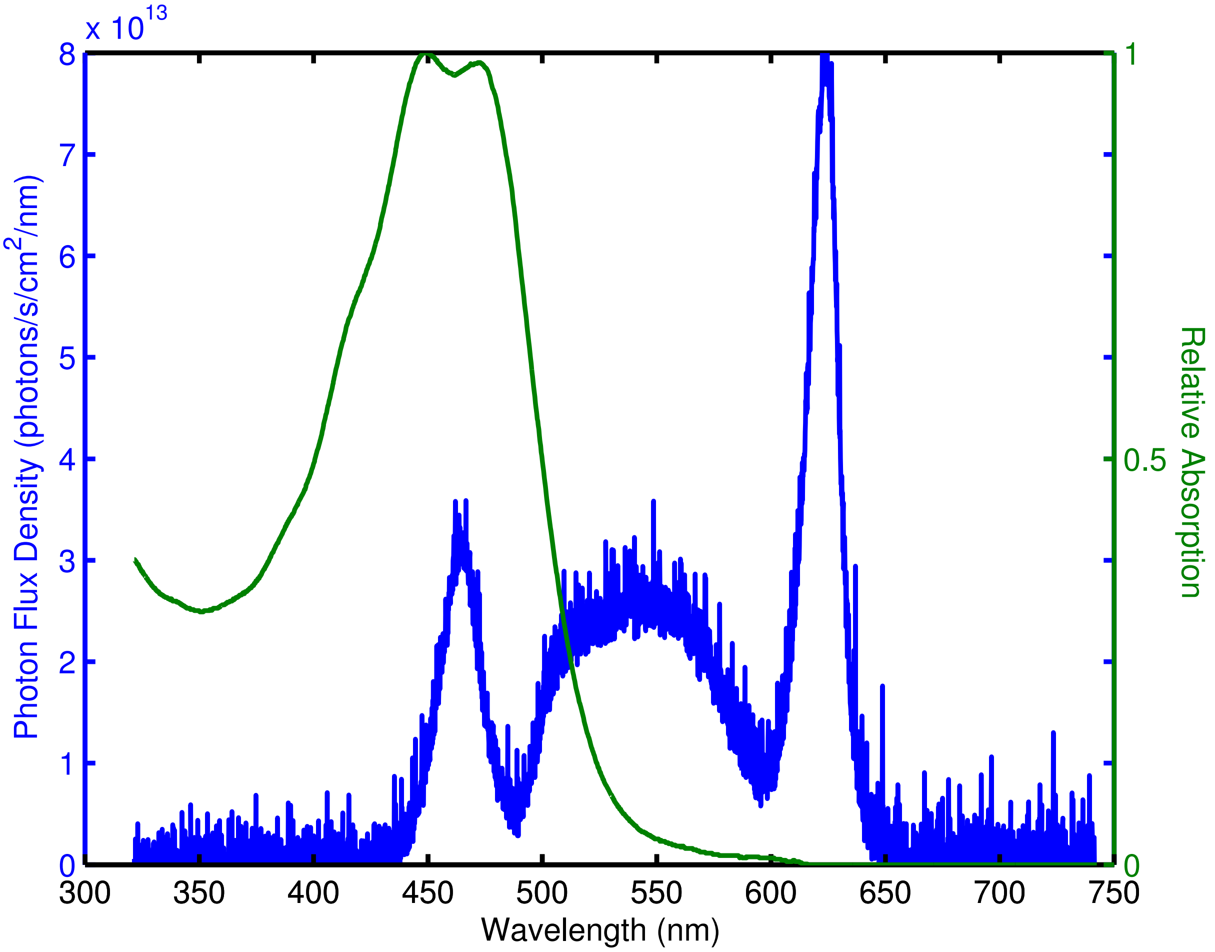

Figure C.2: Blue: photon flux density for the light from by APS projector incident on the MEA after attenuation with an ND1.9 neutral density filter. Green: relative absorption spectrum of ChR2.

Bibliography

Acland, G. M. and Aguirre, G. D. (1987). “Retinal degenerations in the dog: IV. Early retinal degeneration (erd) in Norwegian elkhounds”. *Experimental Eye Research* 44 (4), pp. 491–521.

Aguirre, G., Alligood, J., O’Brien, P., and Buyukmihci, N. (1982a). “Pathogenesis of progressive rod-cone degeneration in miniature poodles”. *Investigative Ophthalmology & Visual Science* 23 (5), pp. 610–30.

Aguirre, G., Farber, D., Lolley, R., Fletcher, R. T., and Chader, G. J. (1978). “Rod-cone dysplasia in Irish setters: a defect in cyclic GMP metabolism in visual cells”. *Science* 201 (4361), pp. 1133–4.

Aguirre, G., Farber, D., Lolley, R., O’Brien, P., Alligood, J., Fletcher, R. T., and Chader, G. (1982b). “Retinal degenerations in the dog III abnormal cyclic nucleotide metabolism in rod-cone dysplasia”. *Experimental Eye Research* 35 (6), pp. 625–642.

Ahnelt, P. and Kolb, H. (1994a). “Horizontal cells and cone photoreceptors in human retina: A Golgi-electron microscopic study of spectral connectivity”. *Journal of Comparative Neurology* 343 (3), pp. 406–427.

Ahnelt, P. and Kolb, H. (1994b). “Horizontal cells and cone photoreceptors in primate retina: A Golgi-light microscopic study of spectral connectivity”. *Journal of Comparative Neurology* 343 (3), pp. 387–405.

Alamusi, Matsuo, T., Hosoya, O., Tsutsui, K. M., and Uchida, T. (2015). “Vision maintenance and retinal apoptosis reduction in RCS rats with Okayama University-type retinal prosthesis (OUReP™) implantation.” *Journal of Artificial Organs.*

Allikmets, R., Singh, N., Sun, H., Shroyer, N. F., Hutchinson, A., Chidambaram, A., Gerrard, B., Baird, L., Stauffer, D., Peiffer, A., Rattner, A., Smallwood, P., Li, Y., Anderson, K. L., Lewis, R. A., Nathans, J., Leppert, M., Dean, M., and Lupski, J. R. (1997). “A photoreceptor cell-specific ATP-binding transporter gene (ABCR) is mutated in recessive Stargardt macular dystrophy." *Nature Genetics* 15 (3), pp. 236–46.

Applebury, M., Antoch, M., Baxter, L., Chun, L., Falk, J., Farhangfar, F., Kage, K., Krzystolik, M., Lyass, L., and Robbins, J. (2000). "The Murine Cone Photoreceptor". *Neuron* 27 (3), pp. 513–523.

Aramant, R. B. and Seiler, M. J. (2002). "Retinal transplantation—advantages of intact fetal sheets". *Progress in Retinal and Eye Research* 21 (1), pp. 57–73.

Arden, G. B. and Jacobson, J. J. (1978). "A simple grating test for contrast sensitivity: preliminary results indicate value in screening for glaucoma." *Investigative Ophthalmology & Visual Science* 17 (1), pp. 23–32.

Arenkiel, B. R., Peca, J., Davison, I. G., Feliciano, C., Deisseroth, K., Augustine, G. J., Ehlers, M. D., and Feng, G. (2007). "In Vivo Light-Induced Activation of Neural Circuitry in Transgenic Mice Expressing Channelrhodopsin-2". *Neuron* 54 (2), pp. 205–218.

Arshavsky, V. Y., Lamb, T. D., and Pugh, E. N. (2002). "G Proteins and Phototransduction". *Annual Review of Physiology* 64 (1), pp. 153–187.

Asl, M. N. and Hosseinzadeh, H. (2008). "Review of pharmacological effects of Glycyrrhiza sp. and its bioactive compounds." *Phytotherapy Research* 22 (6), pp. 709–24.

Al-Atabany, W., McGovern, B., Mehran, K., Berlinguer-Palmini, R., and Degenaar, P. (2013). "A processing platform for optoelectronic/optogenetic retinal prosthesis". *IEEE Transactions on Biomedical Engineering* 60 (3), pp. 781–791.

Azeredo da Silveira, R. and Roska, B. (2011). "Cell Types, Circuits, Computation". *Current Opinion in Neurobiology* 21 (5), pp. 664–671.

Bailey, C. H. and Gouras, P. (1985). "The retina and phototransduction". *Principles of Neural Science*. Ed. by E. R. Kandel and J. H. Schwartz. 2nd Ed. New York: Elsevier. Chap. 27, pp. 344–345.

Bailey, I. L. and Lovie, J. E. (1976). "New design principles for visual acuity letter charts." *American Journal of Optometry and Physiological Optics* 53 (11), pp. 740–5.

Bainbridge, J. W. B., Mehat, M. S., Sundaram, V., Robbie, S. J., Barker, S. E., Ripamonti, C., Georgiadis, A., Mowat, F. M., Beattie, S. G., Gardner, P. J., Feathers, K. L., Luong,

V. A., Yzer, S., Balaggan, K., Viswanathan, A., Ravel, T. J. L. de, Casteels, I., Holder, G. E., Tyler, N., Fitzke, F. W., Weleber, R. G., Nardini, M., Moore, A. T., Thompson, D. A., Petersen-Jones, S. M., Michaelides, M., Born, L. I. van den, Stockman, A., Smith, A. J., Rubin, G., and Ali, R. R. (2015). “Long-term effect of gene therapy on Leber’s congenital amaurosis.” *New England Journal of Medicine* 372 (20), pp. 1887–97.

Barlow, H. B., Hill, R. M., and Levick, W. R. (1964). “Retinal ganglion cells responding selectively to direction and speed of image motion in the rabbit”. *The Journal of Physiology* 173 (3), pp. 377–407.

Barlow, H. B. and Hill, R. M. (1963). “Selective Sensitivity to Direction of Movement in Ganglion Cells of the Rabbit Retina”. *Science* 139 (3553), p. 412.

Barrett, J. M., Berlinguer-Palmini, R., and Degenaar, P. (2014). “Optogenetic approaches to retinal prosthesis.” *Visual Neuroscience* 31 (4-5), pp. 345–54.

Beales, P. L., Elcioglu, N., Woolf, A. S., Parker, D., and Flinter, F. A. (1999). “New criteria for improved diagnosis of Bardet-Biedl syndrome: results of a population survey”. *Journal of Medical Genetics* 36 (6), pp. 437–446.

Benardete, E. A. and Kaplan, E. (1997a). “The receptive field of the primate P retinal ganglion cell, I: Linear dynamics”. *Visual Neuroscience* 14 (1), pp. 169–185.

Benardete, E. A. and Kaplan, E. (1997b). “The receptive field of the primate P retinal ganglion cell, II: Nonlinear dynamics”. *Visual Neuroscience* 14 (1), pp. 187–205.

Bernstein, J. G. and Boyden, E. S. (2011). “Optogenetic tools for analyzing the neural circuits of behavior”. *Trends in Cognitive Sciences* 15 (12), pp. 592–600.

Berson, E. L. (1993). “Retinitis pigmentosa: The Friedenwald lecture”. *Investigative Ophthalmology & Visual Science* 34 (5), pp. 1659–1676.

Bi, A., Cui, J., Ma, Y. P., Olshevskaya, E., Pu, M., Dizhoor, A. M., and Pan, Z. H. (2006). “Ectopic Expression of a Microbial-Type Rhodopsin Restores Visual Responses in Mice with Photoreceptor Degeneration”. *Neuron* 50 (1), pp. 23–33.

Biel, M., Seeliger, M., Pfeifer, A., Kohler, K., Gerstner, A., Ludwig, A., Jaissle, G., Fauser, S., Zrenner, E., and Hofmann, F. (1999). “Selective loss of cone function in mice lacking the cyclic nucleotide-gated channel CNG3." *Proceedings of the National Academy of Sciences of the United States of America* 96 (13), pp. 7553–7.

Bionic Vision Australia (2015). *The Bionic Eye*. URL: `http://bionicvision.org.au/eye` (visited on 09/02/2015).

Bisti, S., Maccarone, R., and Falsini, B. (2014). "Saffron and retina: neuroprotection and pharmacokinetics." *Visual Neuroscience* 31 (4-5), pp. 355–61.

Biswas, S., Haselier, C., Mataruga, A., Thumann, G., Walter, P., and Müller, F. (2014). "Pharmacological Analysis of Intrinsic Neuronal Oscillations in rd10 Retina." *PLoS ONE* 9 (6), e99075.

Bloomfield, S. A. and Völgyi, B. (2009). "The diverse functional roles and regulation of neuronal gap junctions in the retina". *Nature Reviews Neuroscience* 10 (7), pp. 495–506.

Boinagrov, D., Pangratz-Fuehrer, S., Goetz, G., and Palanker, D. (2014). "Selectivity of direct and network-mediated stimulation of the retinal ganglion cells with epi-, sub- and intraretinal electrodes." *Journal of Neural Engineering* 11 (2), p. 026008.

Borg-Graham, L. J. (2001). "The computation of directional selectivity in the retina occurs presynaptic to the ganglion cell". *Nature Neuroscience* 4 (2), pp. 176–183.

Borowska, J., Trenholm, S., and Awatramani, G. B. (2011). "An Intrinsic Neural Oscillator in the Degenerating Mouse Retina". *The Journal of Neuroscience* 31 (13), pp. 5000–5012.

Bourne, M. C., Campbell, D. A., and Tansley, K. (1938). "Hereditary Degeneration of the Rat Retina". *The British Journal of Ophthalmology* 22 (10), pp. 613–23.

Boycott, B. B. and Wässle, H. (1991). "Morphological Classification of Bipolar Cells of the Primate Retina". *European Journal of Neuroscience* 3 (11), pp. 1069–1088.

Boyden, E. S., Zhang, F., Bamberg, E., Nagel, G., and Deisseroth, K. (2005). "Millisecond-timescale, genetically targeted optical control of neural activity". *Nature Neuroscience* 8, pp. 1263–1268.

Boye, S. E., Boye, S. L., Lewin, A. S., and Hauswirth, W. W. (2013). "A Comprehensive Review of Retinal Gene Therapy". *Molecular Therapy* 21 (3), pp. 509–519.

Brainard, D. H. (1997). "The psychophysics toolbox". *Spatial Vision* 10, pp. 433–436.

Brindley, G. S. (1970). “Sensations produced by electrical stimulation of the occipital poles of the cerebral hemispheres, and their use in constructing visual prostheses.” *Annals of the Royal College of Surgeons of England* 47 (2), pp. 106–8.

Brindley, G. S., Donaldson, P. E., Falconer, M. A., and Rushton, D. N. (1972). “The extent of the region of occipital cortex that when stimulated gives phosphenes fixed in the visual field.” *The Journal of Physiology* 225 (2), 57P–58P.

Brindley, G. S. and Lewin, W. S. (1968). “The sensations produced by electrical stimulation of the visual cortex”. *The Journal of Physiology* 196 (2), pp. 479–493.

Brown, D. M., Michels, M., Kaiser, P. K., Heier, J. S., Sy, J. P., and Ianchulev, T. (2009). “Ranibizumab versus verteporfin photodynamic therapy for neovascular age-related macular degeneration: Two-year results of the ANCHOR study.” *Ophthalmology* 116 (1), 57–65.e5.

Busskamp, V., Duebel, J., Balya, D., Fradot, M., Viney, T. J., Siegert, S., Groner, A. C., Cabuy, E., Forster, V., Seeliger, M., Biel, M., Humphries, P., Paques, M., Mohand-Said, S., Trono, D., Deisseroth, K., Sahel, J. A., Picaud, S., and Roska, B. (2010). “Genetic reactivation of cone photoreceptors restores visual responses in retinitis pigmentosa”. *Science* 329 (5990), pp. 413–417.

Busskamp, V., Picaud, S., Sahel, J. A., and Roska, B. (2012). “Optogenetic therapy for retinitis pigmentosa”. *Gene Therapy* 19 (2), pp. 169–175.

Busskamp, V. and Roska, B. (2011). “Optogenetic approaches to restoring visual function in retinitis pigmentosa”. *Current Opinion in Neurobiology* 21 (6), pp. 942–946.

Carandini, M., Demb, J. B., Mante, V., Tolhurst, D. J., Dan, Y., Olshausen, B. A., Gallant, J. L., and Rust, N. C. (2005). “Do We Know What the Early Visual System Does?” *The Journal of Neuroscience* 25 (46), pp. 10577–10597.

Carcieri, S. M., Jacobs, A. L., and Nirenberg, S. (2003). “Classification of retinal ganglion cells: a statistical approach.” *Journal of Neurophysiology* 90 (3), pp. 1704–13.

Carlson, N. and Kurtz, D. (2012). *Clinical Procedures for Ocular Examination, Third Edition.* McGraw Hill Professional.

Carter-Dawson, L., LaVail, M., and Sidman, R. (1978). "Differential effect of the rd mutation on rods and cones in the mouse retina". *Investigative Ophthalmology & Visual Science* 17 (6), pp. 489–498.

Cehajic-Kapetanovic, J., Eleftheriou, C., Allen, A. E., Milosavljevic, N., Pienaar, A., Bedford, R., Davis, K. E., Bishop, P. N., and Lucas, R. J. (2015). "Restoration of Vision with Ectopic Expression of Human Rod Opsin". *Current Biology* (in press).

Cepko, C. L. (2012). "Emerging Gene Therapies for Retinal Degenerations". *The Journal of Neuroscience* 32 (19), pp. 6415–6420.

Chakravarthy, U., Adamis, A. P., Cunningham, E. T., Goldbaum, M., Guyer, D. R., Katz, B., and Patel, M. (2006). "Year 2 efficacy results of 2 randomized controlled clinical trials of pegaptanib for neovascular age-related macular degeneration." *Ophthalmology* 113 (9), 1508.e1–25.

Chang, B., Hawes, N. L., Pardue, M. T., German, A. M., Hurd, R. E., Davisson, M. T., Nusinowitz, S., Rengarajan, K., Boyd, A. P., Sidney, S. S., Phillips, M. J., Stewart, R. E., Chaudhury, R., Nickerson, J. M., Heckenlively, J. R., and Boatright, J. H. (2007). "Two mouse retinal degenerations caused by missense mutations in the beta-subunit of rod cGMP phosphodiesterase gene." *Vision Research* 47 (5), pp. 624–33.

Chang, B., Hawes, N., Hurd, R., Davisson, M., Nusinowitz, S., and Heckenlively, J. (2002). "Retinal degeneration mutants in the mouse". *Vision Research* 42 (4), pp. 517–525.

Chichilnisky, E. J. (2001). "A simple white noise analysis of neuronal light responses". *Network: Computation in Neural Systems* 12 (2), pp. 199–213.

Chichilnisky, E. J. and Baylor, D. A. (1999). "Receptive-field microstructure of blue-yellow ganglion cells in primate retina". *Nature Neuroscience* 2 (10), pp. 889–893.

Chichilnisky, E. J. and Kalmar, R. S. (2002). "Functional Asymmetries in ON and OFF Ganglion Cells of Primate Retina". *The Journal of Neuroscience* 22 (7), pp. 2737–2747.

Choi, H., Zhang, L., Cembrowski, M. S., Sabottke, C. F., Markowitz, A. L., Butts, D. A., Kath, W. L., Singer, J. H., and Riecke, H. (2014). "Intrinsic bursting of AII amacrine cells underlies oscillations in the rd1 mouse retina". *Journal of Neurophysiology* 112 (6), pp. 1491–1504.

Chow, A. Y. (2014). *Optobionics - The Eye.* URL: `http://optobionics.com/index.shtml` (visited on 09/02/2015).

Chow, A. Y., Bittner, A. K., and Pardue, M. T. (2010). “The artificial silicon retina in retinitis pigmentosa patients (an American Ophthalmological Association thesis)”. *Transactions of the American Ophthalmological Society* 108, pp. 120–54.

Chow, A. Y., Chow, V. Y., Packo, K. H., Pollack, J. S., Peyman, G. A., and Schuchard, R. (2004). “The artificial silicon retina microchip for the treatment of vision loss from retinitis pigmentosa.” *Archives of Ophthalmology* 122 (4), pp. 460–9.

Chu, Y., Humphrey, M. F., and Constable, I. J. (1993). “Horizontal cells of the normal and dystrophic rat retina: a wholemount study using immunolabelling for the 28-kDa calcium-binding protein.” *Experimental Eye Research* 57 (2), pp. 141–8.

Chuang, A. T., Margo, C. E., and Greenberg, P. B. (2014). “Retinal implants: a systematic review”. *The British Journal of Ophthalmology* 98 (7), pp. 852–6.

Claes, E., Seeliger, M., Michalakis, S., Biel, M., Humphries, P., and Haverkamp, S. (2004). “Morphological Characterization of the Retina of the CNGA3 -/- Rho -/- Mutant Mouse Lacking Functional Cones and Rods”. *Investigative Ophthalmology & Visual Science* 45 (6), p. 2039.

Clay Reid, R. (1999). “Vision”. *Fundamental Neuroscience.* Ed. by M. J. Zigmond, F. E. Bloom, S. C. Landis, J. L. Roberts, and L. R. Squire. San Diego, CA, USA: Academic Press. Chap. 28, pp. 821–855.

Cogan, S. F. (2008). “Neural Stimulation and Recording Electrodes”. *Annual Review of Biomedical Engineering* 10, pp. 275–309.

Cohen, A. I. (1961). “The fine structure of the extrafoveal receptors of the rhesus monkey”. *Experimental Eye Research* 1 (2), 128–IN16.

Cohen, A. I. (1965). “New details of the ultrastructure of the outer segments and ciliary connectives of the rods of human and macaque retinas”. *The Anatomical Record* 152 (1), pp. 63–79.

Cohen, E. D. and Miller, R. F. (1999). “The network-selective actions of quinoxalines on the neurocircuitry operations of the rabbit retina”. *Brain Research* 831 (1-2), pp. 206–228.

Cover, T. M. and Thomas, J. A. (2006). *Elements of information theory.* 2nd. Hoboken, NJ, USA: John Wiley & Sons, Inc.

Cuenca, N., Fernández-Sánchez, L., Campello, L., Maneu, V., De la Villa, P., Lax, P., and Pinilla, I. (2014). "Cellular responses following retinal injuries and therapeutic approaches for neurodegenerative diseases." *Progress in Retinal and Eye Research* 43, pp. 17–75.

Curcio, C. A., Medeiros, N. E., and Millican, C. L. (1996). "Photoreceptor loss in age-related macular degeneration." *Investigative Ophthalmology & Visual Science* 37 (7), pp. 1236–1249.

Curtis, R., Barnett, K. C., and Leon, A. (1987). "An early-onset retinal dystrophy with dominant inheritance in the Abyssinian cat. Clinical and pathological findings." *Investigative Ophthalmology & Visual Science* 28 (1), pp. 131–9.

Daiger, S. P., Sullivan, L. S., and Bowne, S. J. (2013). *RetNet.* URL: `https://sph.uth.edu/Retnet/home.htm`.

Davidson, J. S., Baumgarten, I. M., and Harley, E. H. (1986). "Reversible inhibition of intercellular junctional communication by glycyrrhetinic acid". *Biochemical and Biophysical Research Communications* 134 (1), pp. 29–36.

D'Cruz, P. M. (2000). "Mutation of the receptor tyrosine kinase gene Mertk in the retinal dystrophic RCS rat". *Human Molecular Genetics* 9 (4), pp. 645–651.

Degenaar, P., Grossman, N., Memon, M. A., Burrone, J., Dawson, M., Drakakis, E., Neil, M., and Nikolic, K. (2009). "Optobionic vision—a new genetically enhanced light on retinal prosthesis". *Journal of Neural Engineering* 6 (3), p. 35007.

Deisseroth, K. (2011). "Optogenetics". *Nature Methods* 8 (1), pp. 26–29.

Delbeke, J., Pins, D., Michaux, G., Wanet-Defalque, M.-C., Parrini, S., and Veraart, C. (2001). "Electrical Stimulation of Anterior Visual Pathways in Retinitis Pigmentosa". *Investigative Ophthalmology & Visual Science* 42 (1), pp. 291–297.

Dobelle, W. H. and Mladejovsky, M. G. (1974). "Phosphenes produced by electrical stimulation of human occipital cortex, and their application to the development of a prosthesis for the blind". *The Journal of Physiology* 243 (2), pp. 553–576.

Dobelle, W. H., Mladejovsky, M. G., and Girvin, J. P. (1974). "Artificial Vision for the Blind: Electrical Stimulation of Visual Cortex Offers Hope for a Functional Prosthesis". *Science* 183 (4123), pp. 440–444.

Dobelle, W. H. (2000). "Artificial Vision for the Blind by Connecting a Television Camera to the Visual Cortex". *ASAIO Journal* 46 (1), pp. 3–9.

Dorn, J. D., Ahuja, A. K., Caspi, A., Cruz, L. da, Dagnelie, G., Sahel, J. A., Greenberg, R. J., and McMahon, M. J. (2013). "The detection of motion by blind subjects with the epiretinal 60-electrode (Argus II) retinal prosthesis". *JAMA Ophthalmology* 131 (2), pp. 183–189.

Doroudchi, M. M., Greenberg, K. P., Liu, J., Silka, K. A., Boyden, E. S., Lockridge, J. A., Arman, A. C., Janani, R., Boye, S. E., Boye, S. L., Gordon, G. M., Matteo, B. C., Sampath, A. P., Hauswirth, W. W., and Horsager, A. (2011). "Virally delivered channelrhodopsin-2 safely and effectively restores visual function in multiple mouse models of blindness". *Molecular Therapy* 19 (7), pp. 1220–1229.

Drager, U. C. and Hubel, D. H. (1978). "Studies of visual function and its decay in mice with hereditary retinal degeneration". *Journal of Comparative Neurology* 180 (1), pp. 85–114.

Eiraku, M., Takata, N., Ishibashi, H., Kawada, M., Sakakura, E., Okuda, S., Sekiguchi, K., Adachi, T., and Sasai, Y. (2011). "Self-organizing optic-cup morphogenesis in three-dimensional culture." *Nature* 472 (7341), pp. 51–6.

Eisenfeld, A. J., Bunt-Milam, A. H., and Sarthy, P. V. (1984). "Müller cell expression of glial fibrillary acidic protein after genetic and experimental photoreceptor degeneration in the rat retina." *Investigative Ophthalmology & Visual Science* 25 (11), pp. 1321–8.

Ekström, P., Sanyal, S., Narfström, K., Chader, G. J., and Veen, T. van (1988). "Accumulation of glial fibrillary acidic protein in Müller radial glia during retinal degeneration." *Investigative Ophthalmology & Visual Science* 29 (9), pp. 1363–71.

Eleftheriou, C. G., Zimmermann, J. B., Kjeldsen, H. D., David-Pur, M., Hanein, Y., and Sernagor, E. (2012). "Towards the Development of Carbon Nanotube-Based Retinal Implant Technology: Electrophysiological and Ultrastructural Evidence of Coupling at the Biohybrid interface". *Proceedings of the 8th International Meeting on Substrate-Integrated Microelectrodes.* Reutlingen: NMI.

Enroth-Cugell, C. and Freeman, A. W. (1987). "The receptive-field spatial structure of cat retinal Y cells". *The Journal of Physiology* 384 (1), pp. 49–79.

Enroth-Cugell, C. and Robson, J. G. (1966). "The contrast sensitivity of retinal ganglion cells of the cat". *The Journal of Physiology* 187 (3), pp. 517–552.

Euler, T. and Wässle, H. (1995). "Immunocytochemical identification of cone bipolar cells in the rat retina". *Journal of Comparative Neurology* 361 (3), pp. 461–478.

Falsini, B., Piccardi, M., Minnella, A., Savastano, C., Capoluongo, E., Fadda, A., Balestrazzi, E., Maccarone, R., and Bisti, S. (2010). "Influence of saffron supplementation on retinal flicker sensitivity in early age-related macular degeneration." *Investigative Ophthalmology & Visual Science* 51 (12), pp. 6118–24.

Famiglietti, E. V. and Kolb, H. (1976). "Structural basis for ON-and OFF-center responses in retinal ganglion cells". *Science* 194 (4261), pp. 193–195.

Famiglietti, E. V. and Kolb, H. (1975). "A bistratified amacrine cell and synaptic circuitry in the inner plexiform layer of the retina". *Brain Research* 84 (2), pp. 293–300.

Fenno, L., Yizhar, O., and Deisseroth, K. (2011). "The Development and Application of Optogenetics". *Annual Review of Neuroscience* 34 (1), pp. 389–412.

Fine, I. and Boynton, G. M. (2015). "Pulse trains to percepts: the challenge of creating a perceptually intelligible world with sight recovery technologies." *Philosophical Transactions of the Royal Society B: Biological Sciences* 370 (1677), pp. 20140208–.

Förster, O. (1929). "Beiträge zur Pathophysiologie der Sehbahn und der Sehsphare". *Journal für Psychologie und Neurologie* 39, pp. 463–485.

Freeman, D. K., Rizzo III, J. F., and Fried, S. I. (2011). "Encoding visual information in retinal ganglion cells with prosthetic stimulation". *Journal of Neural Engineering* 8 (3), p. 35005.

Friedel, H. A. and Fitton, A. (1993). "Flupirtine". *Drugs* 45 (4), pp. 548–569.

Furukawa, T., Morrow, E. M., Li, T., Davis, F. C., and Cepko, C. L. (1999). "Retinopathy and attenuated circadian entrainment in Crx-deficient mice". *Nature Genetics* 23 (4), pp. 466–70.

Gaudiano, P. (1994). “Simulations of X and Y retinal ganglion cell behavior with a nonlinear push-pull model of spatiotemporal retinal processing”. *Vision Research* 34 (13), pp. 1767–1784.

Gauvain, G. and Murphy, G. J. (2015). “Projection-specific characteristics of retinal input to the brain.” *The Journal of Neuroscience* 35 (16), pp. 6575–83.

Gazères, N., Borg-Graham, L. J., and Frégnac, Y. (1998). “A phenomenological model of visually evoked spike trains in cat geniculate nonlagged X-cells”. *Visual Neuroscience* 15 (6), pp. 1157–1174.

Gerits, A., Farivar, R., Rosen, B., Wald, L., Boyden, E., and Vanduffel, W. (2012). “Optogenetically Induced Behavioral and Functional Network Changes in Primates”. *Current Biology* 22 (18), pp. 1722–1726.

Goldberg, D. H., Victor, J. D., Gardner, E. P., and Gardner, D. (2009). “Spike train analysis toolkit: enabling wider application of information-theoretic techniques to neurophysiology.” *Neuroinformatics* 7 (3), pp. 165–78.

Gollisch, T. and Meister, M. (2008). “Rapid neural coding in the retina with relative spike latencies”. *Science* 319 (5866), pp. 1108–1111.

Gollisch, T. and Meister, M. (2010). “Eye smarter than scientists believed: neural computations in circuits of the retina”. *Neuron* 65 (2), pp. 150–164.

Gonzalez-Cordero, A., West, E. L., Pearson, R. A., Duran, Y., Carvalho, L. S., Chu, C. J., Naeem, A., Blackford, S. J. I., Georgiadis, A., Lakowski, J., Hubank, M., Smith, A. J., Bainbridge, J. W. B., Sowden, J. C., and Ali, R. R. (2013). “Photoreceptor precursors derived from three-dimensional embryonic stem cell cultures integrate and mature within adult degenerate retina.” *Nature Biotechnology* 31 (8), pp. 741–7.

Goo, Y. S., Ahn, K. N., Song, Y. J., Ahn, S. H., Han, S. K., Ryu, S. B., and Kim, K. H. (2011). “Spontaneous Oscillatory Rhythm in Retinal Activities of Two Retinal Degeneration (rd1 and rd10) Mice.” *Korean Journal of Physiology & Pharmacology* 15 (6), pp. 415–22.

Green, W. R. and Enger, C. (1993). “Age-related macular degeneration histopathologic studies. The 1992 Lorenz E. Zimmerman Lecture.” *Ophthalmology* 100 (10), pp. 1519–35.

Greenberg, K., Pham, A., and Werblin, F. (2011). “Differential Targeting of Optical Neuromodulators to Ganglion Cell Soma and Dendrites Allows Dynamic Control of Center-Surround Antagonism”. *Neuron* 69 (4), pp. 713–720.

Grossman, N., Poher, V., Grubb, M. S., Kennedy, G. T., Nikolic, K., McGovern, B., Berlinguer-Palmini, R., Gong, Z., Drakakis, E. M., Neil, M. A. A., Dawson, M. D., Burrone, J., and Degenaar, P. (2010). “Multi-site optical excitation using ChR2 and micro-LED array”. *Journal of Neural Engineering* 7 (1), p. 16004.

Gunaydin, L. A., Yizhar, O., Berndt, A., Sohal, V. S., Deisseroth, K., and Hegemann, P. (2010). “Ultrafast optogenetic control”. *Nature Neuroscience* 13 (3), pp. 387–392.

Gust, J. and Reh, T. A. (2011). “Adult donor rod photoreceptors integrate into the mature mouse retina.” *Investigative Ophthalmology & Visual Science* 52 (8), pp. 5266–72.

Gütig, R., Gollisch, T., Sompolinsky, H., and Meister, M. (2013). “Computing complex visual features with retinal spike times.” *PLoS ONE* 8 (1), e53063.

Han, X. and Boyden, E. S. (2007). “Multiple-color optical activation, silencing and desynchronization of neural activity with single-spike temporal resolution”. *PLoS ONE* 2, e299.

Hartline, H. K. (1938). “The response of single optic nerve fibers of the vertebrate eye to illumination of the retina”. *American Journal of Physiology* 121 (2), pp. 400–415.

Hartong, D. T., Berson, E. L., and Dryja, T. P. (2006). “Retinitis pigmentosa”. *The Lancet* 368 (9549), pp. 1795–1809.

Heckenlively, J. R., Boughman, J., and Friedman, L. (1988). “Diagnosis and classification of retinitis pigmentosa”. *Retinitis Pigmentosa.* Ed. by J. R. Heckenlively. Philadelphia, PA: Lippincott, p. 21.

Heier, J. S., Brown, D. M., Chong, V., Korobelnik, J.-F., Kaiser, P. K., Nguyen, Q. D., Kirchhof, B., Ho, A., Ogura, Y., Yancopoulos, G. D., Stahl, N., Vitti, R., Berliner, A. J., Soo, Y., Anderesi, M., Groetzbach, G., Sommerauer, B., Sandbrink, R., Simader, C., and Schmidt-Erfurth, U. (2012). “Intravitreal aflibercept (VEGF trap-eye) in wet age-related macular degeneration.” *Ophthalmology* 119 (12), pp. 2537–48.

Hennig, M. H. and Funke, K. (2001). “A biophysically realistic simulation of the vertebrate retina”. *Neurocomputing* 38-40, pp. 659–665.

Ho, A. C., Humayun, M. S., Dorn, J. D., Cruz, L. da, Dagnelie, G., Handa, J., Barale, P.-O., Sahel, J.-A., Stanga, P. E., Hafezi, F., Safran, A. B., Salzmann, J., Santos, A., Birch, D., Spencer, R., Cideciyan, A. V., Juan, E. de, Duncan, J. L., Eliott, D., Fawzi, A., Olmos de Koo, L. C., Brown, G. C., Haller, J. A., Regillo, C. D., Del Priore, L. V., Arditi, A., Geruschat, D. R., and Greenberg, R. J. (2015). "Long-Term Results from an Epiretinal Prosthesis to Restore Sight to the Blind." *Ophthalmology* 122 (8), pp. 1547–1554.

Hornig, R., Zehnder, T., Velikay-Parel, M., Laube, T., Feucht, M., and Richard, G. (2007). "The IMI Retinal Implant System". *Artificial Sight.* Ed. by M. S. Humayun, J. D. Weiland, G. Chader, and E. Greenbaum. Biological and Medical Physics, Biomedical Engineering. New York, NY: Springer New York. Chap. 6, pp. 111–128.

Humayun, M. S., Prince, M., Juan, E. de, Barron, Y., Moskowitz, M., Klock, I. B., Milam, A. H., de Juan Jr, E., Barron, Y., Moskowitz, M., Klock, I. B., and al, E. (1999). "Morphometric analysis of the extramacular retina from postmortem eyes with retinitis pigmentosa". *Investigative Ophthalmology & Visual Science* 40 (1), pp. 143–148.

Humphries, M. M., Rancourt, D., Farrar, G. J., Kenna, P., Hazel, M., Bush, R. A., Sieving, P. A., Sheils, D. M., McNally, N., Creighton, P., Erven, A., Boros, A., Gulya, K., Capecchi, M. R., and Humphries, P. (1997). "Retinopathy induced in mice by targeted disruption of the rhodopsin gene". *Nature Genetics* 15 (2), pp. 216–9.

Hunter, I. W. and Korenberg, M. J. (1986). "The identification of nonlinear biological systems: Wiener and Hammerstein cascade models". *Biological Cybernetics* 55 (2-3), pp. 135–144.

Imai, H., Kefalov, V., Sakurai, K., Chisaka, O., Ueda, Y., Onishi, A., Morizumi, T., Fu, Y., Ichikawa, K., Nakatani, K., Honda, Y., Chen, J., Yau, K.-W., and Shichida, Y. (2007). "Molecular Properties of Rhodopsin and Rod Function". *Journal of Biological Chemistry* 282 (9), pp. 6677–6684.

International Council of Ophthalmology (1988). "Visual Acuity Measurement Standard". *Italian Journal of Ophthalmology* 2 (1), pp. 1–15.

Ivanova, E., Hwang, G. S., Pan, Z. H., and Troilo, D. (2010). “Evaluation of AAV-mediated expression of chop2-GFP in the marmoset retina”. *Investigative Ophthalmology & Visual Science* 51 (10), pp. 5288–5296.

Ivanova, E. and Pan, Z.-H. (2009). “Evaluation of the adeno-associated virus mediated long-term expression of channelrhodopsin-2 in the mouse retina”. *Molecular Vision* 15, pp. 1680–1689.

Ivanova, E., Yee, C. W., Baldoni, R., and Sagdullaev, B. T. (2015). “Aberrant activity in retinal degeneration impairs central visual processing and relies on Cx36-containing gap junctions.” *Experimental Eye Research.*

Jacobs, A. L., Fridman, G., Douglas, R. M., Alam, N. M., Latham, P. E., Prusky, G. T., and Nirenberg, S. (2009). “Ruling out and ruling in neural codes”. *Proceedings of the National Academy of Sciences of the United States of America* 106 (14), pp. 5936–5941.

Jacobs, G. H., Neitz, J., and Deegan, J. F. (1991). “Retinal receptors in rodents maximally sensitive to ultraviolet light”. *Nature* 353 (6345), pp. 655–656.

Jager, R. D., Mieler, W. F., and Miller, J. W. (2008). “Age-Related Macular Degeneration”. *New England Journal of Medicine* 358 (24), pp. 2606–2617.

Jaissle, G. B., May, C. A., Reinhard, J., Kohler, K., Fauser, S., Lütjen-Drecoll, E., Zrenner, E., and Seeliger, M. W. (2001). “Evaluation of the rhodopsin knockout mouse as a model of pure cone function”. *Investigative Ophthalmology & Visual Science* 42 (2), pp. 506–13.

Jarsky, T., Cembrowski, M., Logan, S. M., Kath, W. L., Riecke, H., Demb, J. B., and Singer, J. H. (2011). “A Synaptic Mechanism for Retinal Adaptation to Luminance and Contrast”. *The Journal of Neuroscience* 31 (30), pp. 11003–11015.

Jayakody, S. A., Gonzalez-Cordero, A., Ali, R. R., and Pearson, R. A. (2015). “Cellular strategies for retinal repair by photoreceptor replacement”. *Progress in Retinal and Eye Research* 46, pp. 31–66.

Jeon, C. J., Strettoi, E., and Masland, R. H. (1998). “The major cell populations of the mouse retina”. *The Journal of Neuroscience* 18 (21), pp. 8936–8946.

Jepson, L. H., Hottowy, P., Weiner, G. A., Dabrowski, W., Litke, A. M., and Chichilnisky, E. J. (2014). "High-fidelity reproduction of spatiotemporal visual signals for retinal prosthesis." *Neuron* 83 (1), pp. 87–92.

John, G. H. and Langley, P. (1995). "Estimating continuous distributions in Bayesian classifiers". *UAI'95 Proceedings of the Eleventh Conference on Uncertainty in Artificial Intelligence.* Morgan Kaufmann Publishers Inc., pp. 338–345.

Jones, B. W., Watt, C. B., Frederick, J. M., Baehr, W., Chen, C. K., Levine, E. M., Milam, A. H., Lavail, M. M., and Marc, R. E. (2003). "Retinal remodeling triggered by photoreceptor degenerations". *Journal of Comparative Neurology* 464, pp. 1–16.

Jones, B. W. and Marc, R. E. (2005). "Retinal remodeling during retinal degeneration". *Experimental Eye Research* 81, pp. 123–137.

Juszczak, G. R. and Swiergiel, A. H. (2009). "Properties of gap junction blockers and their behavioural, cognitive and electrophysiological effects: animal and human studies." *Progress in Neuro-Psychopharmacology & Biological Psychiatry* 33 (2), pp. 181–98.

Kandel, E. C., Schwartz, J. H., and Jessell, T. M. (2000). "Central Visual Pathways". *Principles of Neural Science.* 4th Editio. New York, NY: McGraw-Hill. Chap. 27, pp. 523–547.

Keat, J., Reinagel, P., Reid, R. C., and Meister, M. (2001). "Predicting every spike: a model for the responses of visual neurons". *Neuron* 30 (3), pp. 803–817.

Keeler, C. (1966). "Retinal degeneration in the mouse is rodless retina." *Journal of Heredity* 57 (2), pp. 47–50.

Kelly, D. H. (1975). "Spatial frequency selectivity in the retina". *Vision Research* 15 (6), pp. 665–672.

Kelly, S. K., Shire, D. B., Chen, J., Doyle, P., Gingerich, M. D., Cogan, S. F., Drohan, W. A., Behan, S., Theogarajan, L., Wyatt, J. L., and Rizzo, J. F. (2011). "A hermetic wireless subretinal neurostimulator for vision prostheses." *IEEE Transactions on Biomedical Engineering* 58 (11), pp. 3197–205.

Kelly, S. K., Shire, D. B., Chen, J., Gingerich, M. D., Cogan, S. F., Drohan, W. A., Ellersick, W., Krishnan, A., Behan, S., Wyatt, J. L., and Rizzo, J. F. (2013). "Developments on the Boston 256-channel retinal implant". *2013 IEEE International Conference on Multimedia and Expo Workshops (ICMEW).* IEEE, pp. 1–6.

Keserü, M., Feucht, M., Bornfeld, N., Laube, T., Walter, P., Rössler, G., Velikay-Parel, M., Hornig, R., and Richard, G. (2012). "Acute electrical stimulation of the human retina with an epiretinal electrode array." *Acta Ophthalmologica* 90 (1), e1–8.

Kim, C. S. and Oh, S. M. (2002). "Morphometric analysis of the macula in eyes with disciform age-related macular degeneration". *Retina* 22, pp. 471–477.

Kim, S. Y., Sadda, S., Humayun, M. S., Juan, E. de, Melia, B. M., and Green, W. R. (2002). "Morphometric analysis of the macula in eyes with geographic atrophy due to age-related macular degeneration." *Retina* 22 (4), pp. 464–70.

Klapoetke, N. C., Murata, Y., Kim, S. S., Pulver, S. R., Birdsey-Benson, A., Cho, Y. K., Morimoto, T. K., Chuong, A. S., Carpenter, E. J., Tian, Z., Wang, J., Xie, Y., Yan, Z., Zhang, Y., Chow, B. Y., Surek, B., Melkonian, M., Jayaraman, V., Constantine-Paton, M., Wong, G. K.-S., and Boyden, E. S. (2014). "Independent optical excitation of distinct neural populations". *Nature Methods* 11, pp. 338–346.

Klauke, S., Goertz, M., Rein, S., Hoehl, D., Thomas, U., Eckhorn, R., Bremmer, F., and Wachtler, T. (2011). "Stimulation with a wireless intraocular epiretinal implant elicits visual percepts in blind humans." *Investigative Ophthalmology & Visual Science* 52 (1), pp. 449–55.

Klawe, C. and Maschke, M. (2009). "Flupirtine: pharmacology and clinical applications of a nonopioid analgesic and potentially neuroprotective compound". *Expert Opinion on Pharmacotherapy* 10 (9), pp. 1495–500.

Kleiner, M., Brainard, D., Pelli, D., Ingling, A., Murray, R., and Broussard, C. (2007). "What's new in Psychtoolbox-3". *Perception* 36 (ECVP Abstract Supplement), p. 14.

Kolb, H. (1974). "The connections between horizontal cells and photoreceptors in the retina of the cat: Electron microscopy of Golgi preparations". *Journal of Comparative Neurology* 155 (1), pp. 1–14.

Kolb, H. (1979). "The inner plexiform layer in the retina of the cat: electron microscopic observations". *Journal of Neurocytology* 8 (3), pp. 295–329.

Kolb, H. and Famiglietti, E. V. (1974). “Rod and Cone Pathways in the Inner Plexiform Layer of Cat Retina”. *Science* 186 (4158), pp. 47–49.

Kolb, H., Fernandez, E., Schouten, J., Ahnelt, P., Linberg, K. A., and Fisher, S. K. (1994). “Are there three types of horizontal cell in the human retina?” *Journal of Comparative Neurology* 343 (3), pp. 370–386.

Kolb, H., Mariani, A., and Gallego, A. (1980). “A second type of horizontal cell in the monkey retina”. *Journal of Comparative Neurology* 189 (1), pp. 31–44.

Kolb, H., Nelson, R., and Mariani, A. (1981). “Amacrine cells, bipolar cells and ganglion cells of the cat retina: A Golgi study”. *Vision Research* 21 (7), pp. 1081–1114.

Kozachenko, L. F. and Leonenko, N. N. (1987). “Sample estimate of the entropy of a random vector”. *Problemy Peredachi Informatsii* 23 (2), pp. 9–16.

Krause, F. and Schum, H. (1931). *Neue deutsche Chirurgie.* Ed. by H. Küttner. Stuttgart.

Kriegeskorte, N., Simmons, W. K., Bellgowan, P. S. F., and Baker, C. I. (2009). “Circular analysis in systems neuroscience: the dangers of double dipping.” *Nature Neuroscience* 12 (5), pp. 535–40.

Kuffler, S. W. (1953). “Discharge patterns and functional organization of mammalian retina”. *Journal of Neurophysiology* 16 (1), pp. 37–68.

Lagali, P. S., Balya, D., Awatramani, G. B., Münch, T. A., Kim, D. S., Busskamp, V., Cepko, C. L., and Roska, B. (2008). “Light-activated channels targeted to ON bipolar cells restore visual function in retinal degeneration”. *Nature Neuroscience* 11 (6), pp. 667–675.

Lakowski, J., Baron, M., Bainbridge, J., Barber, A. C., Pearson, R. A., Ali, R. R., and Sowden, J. C. (2010). “Cone and rod photoreceptor transplantation in models of the childhood retinopathy Leber congenital amaurosis using flow-sorted Crx-positive donor cells.” *Human Molecular Genetics* 19 (23), pp. 4545–59.

Lakowski, J., Gonzalez-Cordero, A., West, E. L., Han, Y.-T., Welby, E., Naeem, A., Blackford, S. J. I., Bainbridge, J. W. B., Pearson, R. A., Ali, R. R., and Sowden, J. C. (2015). “Transplantation of Photoreceptor Precursors Isolated via a Cell Surface Biomarker Panel From Embryonic Stem Cell-Derived Self-Forming Retina.” *Stem Cells* 33 (8), pp. 2469–82.

Latham, P. E. and Nirenberg, S. (2005). “Synergy, redundancy, and independence in population codes, revisited.” *The Journal of Neuroscience* 25 (21), pp. 5195–206.

Leon, A. and Curtis, R. (1990). “Autosomal dominant rod-cone dysplasia in the Rdy cat 1. Light and electron microscopic findings”. *Experimental Eye Research* 51 (4), pp. 361–381.

Leon, A., Hussain, A., and Curtis, R. (1991). “Autosomal dominant rod-cone dysplasia in the Rdy cat”. *Experimental Eye Research* 53 (4), pp. 489–502.

Leskov, I. B., Klenchin, V. A., Handy, J. W., Whitlock, G. G., Govardovskii, V. I., Bownds, M., Lamb, T. D., Pugh, E. N., and Arshavsky, V. Y. (2000). “The Gain of Rod Phototransduction”. *Neuron* 27 (3), pp. 525–537.

Lewis, G. P., Erickson, P. A., Kaska, D. D., and Fisher, S. K. (1988). “An immunocytochemical comparison of Müller cells and astrocytes in the cat retina”. *Experimental Eye Research* 47 (6), pp. 839–53.

Li, P. H., Gauthier, J. L., Schiff, M., Sher, A., Ahn, D., Field, G. D., Greschner, M., Callaway, E. M., Litke, A. M., and Chichilnisky, E. J. (2015). “Anatomical identification of extracellularly recorded cells in large-scale multielectrode recordings.” *The Journal of Neuroscience* 35 (11), pp. 4663–75.

Lin, B., Koizumi, A., Tanaka, N., Panda, S., and Masland, R. H. (2008). “Restoration of visual function in retinal degeneration mice by ectopic expression of melanopsin”. *Proceedings of the National Academy of Sciences of the United States of America* 105 (41), pp. 16009–16014.

Lin, J. Y., Lin, M., Steinbach, P., and Tsien, R. (2009). “Characterization of engineered channelrhodopsin variants with improved properties and kinetics”. *Biophysical Journal* 96, pp. 1803–1814.

Lin, J. Y., Knutsen, P. M., Muller, A., Kleinfeld, D., and Tsien, R. Y. (2013). “ReaChR: a red-shifted variant of channelrhodopsin enables deep transcranial optogenetic excitation”. *Nature Neuroscience* 16 (10), pp. 1499–1508.

Lipinski, D. M., Barnard, A. R., Singh, M. S., Martin, C., Lee, E. J., Davies, W. I. L., and MacLaren, R. E. (2015). “CNTF Gene Therapy Confers Lifelong Neuroprotection in a Mouse Model of Human Retinitis Pigmentosa.” *Molecular Therapy.*

Lorach, H., Goetz, G., Smith, R., Lei, X., Mandel, Y., Kamins, T., Mathieson, K., Huie, P., Harris, J., Sher, A., and Palanker, D. (2015). "Photovoltaic restoration of sight with high visual acuity." *Nature Medicine* 21 (5), pp. 476–82.

Ma, J., Norton, J. C., Allen, A. C., Burns, J. B., Hasel, K. W., Burns, J. L., Sutcliffe, J. G., and Travis, G. H. (1995). "Retinal degeneration slow (rds) in mouse results from simple insertion of a t haplotype-specific element into protein-coding exon II." *Genomics* 28 (2), pp. 212–9.

Maccarone, R., Di Marco, S., and Bisti, S. (2008). "Saffron supplement maintains morphology and function after exposure to damaging light in mammalian retina." *Investigative Ophthalmology & Visual Science* 49 (3), pp. 1254–61.

Maccione, A., Hennig, M. H., Gandolfo, M., Muthmann, O., Coppenhagen, J. van, Eglen, S. J., Berdondini, L., and Sernagor, E. (2014). "Following the ontogeny of retinal waves: pan-retinal recordings of population dynamics in the neonatal mouse." *The Journal of Physiology* 592 (Pt 7), pp. 1545–63.

Macé, E., Caplette, R., Marre, O., Sengupta, A., Chaffiol, A., Barbe, P., Desrosiers, M., Bamberg, E., Sahel, J.-A., Picaud, S., Duebel, J., and Dalkara, D. (2015). "Targeting channelrhodopsin-2 to ON-bipolar cells with vitreally administered AAV Restores ON and OFF visual responses in blind mice." *Molecular Therapy* 23 (1), pp. 7–16.

Machida, S., Kondo, M., Jamison, J. A., Khan, N. W., Kononen, L. T., Sugawara, T., Bush, R. A., and Sieving, P. A. (2000). "P23H rhodopsin transgenic rat: correlation of retinal function with histopathology." *Investigative Ophthalmology & Visual Science* 41 (10), pp. 3200–9.

MacLaren, R. E., Pearson, R. A., MacNeil, A., Douglas, R. H., Salt, T. E., Akimoto, M., Swaroop, A., Sowden, J. C., and Ali, R. R. (2006). "Retinal repair by transplantation of photoreceptor precursors." *Nature* 444 (7116), pp. 203–7.

Macneil, M. A., Heussy, J. K., Dacheux, R. F., Raviola, E., and Masland, R. H. (1999). "The shapes and numbers of amacrine cells: Matching of photofilled with Golgi-stained cells in the rabbit retina and comparison with other mammalian species". *Journal of Comparative Neurology* 413 (2), pp. 305–326.

Maguire, A. M., Simonelli, F., Pierce, E. A., Pugh Jr, E. N., Mingozzi, F., Bennicelli, J., Banfi, S., Marshall, K. A., Testa, F., Surace, E. M., Rossi, S., Lyubarsky, A., Arruda, V. R., Konkle, B., Stone, E., Sun, J., Jacobs, J., Dell'Osso, L., Hertle, R., Ma, J. X., Redmond, T. M., Zhu, X., Hauck, B., Zelenaia, O., Shindler, K. S., Maguire, M. G., Wright, J. F., Volpe, N. J., McDonnell, J. W., Auricchio, A., High, K. A., and Bennett, J. (2008). "Safety and efficacy of gene transfer for Leber's congenital amaurosis". *New England Journal of Medicine* 358 (21), pp. 2240–2248.

Man, P. Y. W., Turnbull, D. M., and Chinnery, P. F. (2002). "Leber hereditary optic neuropathy". *Journal of Medical Genetics* 39 (3), pp. 162–169.

Marc, R. E., Jones, B. W., Anderson, J. R., Kinard, K., Marshak, D. W., Wilson, J. H., Wensel, T., and Lucas, R. J. (2007). "Neural reprogramming in retinal degeneration". *Investigative Ophthalmology & Visual Science* 48 (7), pp. 3364–3371.

Marc, R. E., Murry, R. F., and Basinger, S. F. (1995). "Pattern recognition of amino acid signatures in retinal neurons." *The Journal of Neuroscience* 15 (7 Pt 2), pp. 5106–29.

Marc, R. E. (2006a). "Functional Anatomy of the Neural Retina". *Principles and Practice of Ophthalmology.* Ed. by D. M. Albert and F. A. Jakobiec. 3rd. Philedelphia: Saunders. Chap. 122.

Marc, R. E. (2006b). *Schematic mouse, rat and human eyes.* Salt Lake City, UT, USA. URL: `http://prometheus.med.utah.edu/%7B~%7Dmarclab/eyes.pdf` (visited on 08/27/2015).

Marc, R. E., Jones, B. W., Watt, C. B., Vazquez-Chona, F., Vaughan, D. K., and Organisciak, D. T. (2008). "Extreme retinal remodeling triggered by light damage: implications for age related macular degeneration." *Molecular Vision* 14, pp. 782–806.

Marc, R. E., Jones, B. W., Watt, C. B., and Strettoi, E. (2003). "Neural remodeling in retinal degeneration". *Progress in Retinal and Eye Research* 22 (5), pp. 607–655.

Margalit, E., Maia, M., Weiland, J. D., Greenberg, R. J., Fujii, G. Y., Torres, G., Piyathaisere, D. V., O'Hearn, T. M., Liu, W., Lazzi, G., Dagnelie, G., Scribner, D. A., de Juan Jr., E., and Humayan, M. S. (2002). "Retinal Prosthesis for the Blind". *Survey of Ophthalmology* 47 (4), pp. 335–356.

Margolis, D. J., Gartland, A. J., Singer, J. H., and Detwiler, P. B. (2014). “Network oscillations drive correlated spiking of ON and OFF ganglion cells in the rd1 mouse model of retinal degeneration.” *PLoS ONE* 9 (1), e86253.

Margolis, D. J., Newkirk, G., Euler, T., and Detwiler, P. B. (2008). “Functional Stability of Retinal Ganglion Cells after Degeneration-Induced Changes in Synaptic Input”. *The Journal of Neuroscience* 28 (25), pp. 6526–6536.

Mariani, A. P. (1983). “Giant bistratified bipolar cells in monkey retina”. *The Anatomical Record* 206 (2), pp. 215–220.

Marmarelis, P. Z. and Naka, K.-I. (1972). “White-Noise Analysis of a Neuron Chain: An Application of the Wiener Theory”. *Science* 175 (4027), pp. 1276–1278.

Martin, D. F., Maguire, M. G., Fine, S. L., Ying, G.-s., Jaffe, G. J., Grunwald, J. E., Toth, C., Redford, M., and Ferris, F. L. (2012). “Ranibizumab and bevacizumab for treatment of neovascular age-related macular degeneration: two-year results.” *Ophthalmology* 119 (7), pp. 1388–98.

Martinez, J. J., Toledo, F. J., Fernandez, E., and Ferrandez, J. M. (2009). “Study of the contrast processing in the early visual system using a neuromorphic retinal architecture”. *Neurocomputing* 72 (4–6), pp. 928–935.

Martinez-Navarrete, G., Seiler, M., Aramant, R., Fernandez-Sanchez, L., Pinilla, I., and Cuenca, N. (2011). “Retinal degeneration in two lines of transgenic S334ter rats”. *Experimental Eye Research* 92 (3), pp. 227–237.

Martire, M., Castaldo, P., D’Amico, M., Preziosi, P., Annunziato, L., and Taglialatela, M. (2004). “M channels containing KCNQ2 subunits modulate norepinephrine, aspartate, and GABA release from hippocampal nerve terminals.” *The Journal of Neuroscience* 24 (3), pp. 592–7.

Masland, R. H. (2012). “The tasks of amacrine cells”. *Visual Neuroscience* 29 (1), pp. 3–9.

Masland, R. H. (2001a). “Neuronal diversity in the retina”. *Current Opinion in Neurobiology* 11 (4), pp. 431–436.

Masland, R. H. (2001b). “The fundamental plan of the retina”. *Nature Neuroscience* 4 (9), pp. 877–886.

Mathieson, K., Loudin, J., Goetz, G., Huie, P., Wang, L., Kamins, T. I., Galambos, L., Smith, R., Harris, J. S., Sher, A., and Palanker, D. (2012). “Photovoltaic retinal prosthesis with high pixel density”. *Nature Photonics* 6 (6), pp. 379–391.

Matsuo, T., Uchida, T., and Takarabe, K. (2009). “Safety, efficacy, and quality control of a photoelectric dye-based retinal prosthesis (Okayama University-type retinal prosthesis) as a medical device.” *Journal of Artificial Organs* 12 (4), pp. 213–25.

McFadden, J. (1965). “The entropy of a poisson process”. *Journal of the Society for Industrial and Applied Mathematics* 13 (4), pp. 988–994.

Medeiros, N. E. and Curcio, C. A. (2001). “Preservation of Ganglion Cell Layer Neurons in Age-Related Macular Degeneration”. *Investigative Ophthalmology & Visual Science* 42 (3), pp. 795–803.

Mei, Y. and Zhang, F. (2012). “Molecular Tools and Approaches for Optogenetics”. *Biological Psychiatry* 71 (12), pp. 1033–1038.

Meister, M. and Berry, M. J. (1999). “The neural code of the retina”. *Neuron* 22 (3), pp. 435–450.

Mellough, C. B., Collin, J., Sernagor, E., Wride, N. K., Steel, D. H. W., and Lako, M. (2014). “Lab generated retina: realizing the dream.” *Visual Neuroscience* 31 (4-5), pp. 317–32.

Menger, N., Pow, D. V., and Wässle, H. (1998). “Glycinergic amacrine cells of the rat retina”. *Journal of Comparative Neurology* 401 (1), pp. 34–46.

Menzel-Severing, J., Laube, T., Brockmann, C., Bornfeld, N., Mokwa, W., Mazinani, B., Walter, P., and Roessler, G. (2012). “Implantation and explantation of an active epiretinal visual prosthesis: 2-year follow-up data from the EPIRET3 prospective clinical trial”. *Eye* 26 (4), pp. 501–9.

Menzler, J. and Zeck, G. (2011). “Network Oscillations in Rod-Degenerated Mouse Retinas”. *The Journal of Neuroscience* 31 (6), pp. 2280–2291.

Mills, S. L. and Massey, S. C. (1994). “Distribution and coverage of A- and B-type horizontal cells stained with Neurobiotin in the rabbit retina”. *Visual Neuroscience* 11 (3), pp. 549–560.

Momiji, H., Hankins, M. W., Bharath, A. A., and Kennard, C. (2007). “A numerical study of red–green colour opponent properties in the primate retina”. *European Journal of Neuroscience* 25 (4), pp. 1155–1165.

Morigiwa, K. and Vardi, N. (1999). “Differential expression of ionotropic glutamate receptor subunits in the outer retina”. *Journal of Comparative Neurology* 405 (2), pp. 173–184.

Morillas, C., Romero, S., Martinez, A., Pelayo, F., Reyneri, L., Bongard, M., and Fernández, E. (2007). “A neuroengineering suite of computational tools for visual prostheses”. *Neurocomputing* 70 (16–18), pp. 2817–2827.

Muller, F., Wassle, H., and Voigt, T. (1988). “Pharmacological modulation of the rod pathway in the cat retina”. *Journal of Neurophysiology* 59 (6), pp. 1657–1672.

Munch, T. A., Silveira, R. A. da, Siegert, S., Viney, T. J., Awatramani, G. B., and Roska, B. (2009). “Approach sensitivity in the retina processed by a multifunctional neural circuit”. *Nature Neuroscience* 12 (10), pp. 1308–1316.

Mutter, M. and Münch, T. A. (2013). “Strategies for Expanding the Operational Range of Channelrhodopsin in Optogenetic Vision”. *PLoS ONE* 8 (11), e81278.

Nagel, G., Szellas, T., Huhn, W., Kateriya, S., Adeishvili, N., Berthold, P., Ollig, D., Hegemann, P., and Bamberg, E. (2003). “Channelrhodopsin-2, a directly light-gated cation-selective membrane channel”. *Proceedings of the National Academy of Sciences of the United States of America* 100 (24), pp. 13940–13945.

Nair, C., Prabhakar, B., and Shah, D. (2006). “On entropy for mixtures of discrete and continuous variables”, p. 10. arXiv: `0607075 [cs]`.

Nakano, T., Ando, S., Takata, N., Kawada, M., Muguruma, K., Sekiguchi, K., Saito, K., Yonemura, S., Eiraku, M., and Sasai, Y. (2012). “Self-formation of optic cups and storable stratified neural retina from human ESCs.” *Cell Stem Cell* 10 (6), pp. 771–85.

Narfstrom, K., Arden, G. B., and Nilsson, S. E. (1989). “Retinal sensitivity in hereditary retinal degeneration in Abyssinian cats: electrophysiological similarities between man and cat.” *British Journal of Ophthalmology* 73 (7), pp. 516–521.

Narfström, K. and Nilsson, S. E. (1986). "Progressive retinal atrophy in the Abyssinian cat. Electron microscopy." *Investigative Ophthalmology & Visual Science* 27 (11), pp. 1569–76.

Narfström, K. and Nilsson, S. E. (1989). "Morphological findings during retinal development and maturation in hereditary rod-cone degeneration in Abyssinian cats." *Experimental Eye Research* 49 (4), pp. 611–28.

Narfstrom, K. (1983). "Hereditary progressive retinal atrophy in the Abyssinian cat". *Journal of Heredity* 74 (4), pp. 273–276.

Nie, R. van, Iványi, D., and Démant, P. (1978). "A new H-2-linked mutation, rds, causing retinal degeneration in the mouse." *Tissue Antigens* 12 (2), pp. 106–8.

Nirenberg, S., Carcieri, S. M., Jacobs, A. L., and Latham, P. E. (2001). "Retinal ganglion cells act largely as independent encoders". *Nature* 411 (6838), pp. 698–701.

Nirenberg, S. and Pandarinath, C. (2012). "Retinal prosthetic strategy with the capacity to restore normal vision". *Proceedings of the National Academy of Sciences of the United States of America* 109 (37), pp. 15012–15017.

Nirenberg, S. and Latham, P. E. (2003). "Decoding neuronal spike trains: how important are correlations?" *Proceedings of the National Academy of Sciences of the United States of America* 100 (12), pp. 7348–53.

Nomura, A., Shigemoto, R., Nakamura, Y., Okamoto, N., Mizuno, N., and Nakanishi, S. (1994). "Developmentally regulated postsynaptic localization of a metabotropic glutamate receptor in rat rod bipolar cells". *Cell* 77 (3), pp. 361–369.

Olsson, J. E., Gordon, J. W., Pawlyk, B. S., Roof, D., Hayes, A., Molday, R. S., Mukai, S., Cowley, G. S., Berson, E. L., and Dryja, T. P. (1992). "Transgenic mice with a rhodopsin mutation (Pro23His): a mouse model of autosomal dominant retinitis pigmentosa." *Neuron* 9 (5), pp. 815–30.

Ong, J. M. and Cruz, L. da (2011). "The bionic eye: a review." *Clinical & Experimental Ophthalmology* 40 (1), pp. 6–17.

Osterberg, G. (1935). "Topography of the layer of rods and cones in the human retina". *Acta Ophthalmologica* 13 (S6), pp. 1–103.

Packer, A. M., Roska, B., and Häusser, M. (2013). "Targeting neurons and photons for optogenetics". *Nature Neuroscience* 16 (7), pp. 805–815.

Pan, F., Mills, S. L., and Massey, S. C. (2007). "Screening of gap junction antagonists on dye coupling in the rabbit retina." *Visual Neuroscience* 24 (4), pp. 609–18.

Paninski, L. (2004). "Maximum likelihood estimation of cascade point-process neural encoding models". *Network: Computation in Neural Systems* 15 (4), pp. 243–262.

Paninski, L., Pillow, J. W., and Lewi, J. (2007). "Statistical models for neural encoding, decoding, and optimal stimulus design". *Progress in Brain Research* 165, pp. 493–507.

Paninski, L., Pillow, J. W., and Simoncelli, E. P. (2004). "Maximum likelihood estimation of a stochastic integrate-and-fire neural encoding model". *Neural Computation* 16 (12), pp. 2533–2561.

Panzeri, S., Senatore, R., Montemurro, M. A., and Petersen, R. S. (2007). "Correcting for the sampling bias problem in spike train information measures." *Journal of Neurophysiology* 98 (3), pp. 1064–72.

Panzeri, S. and Treves, A. (1996). "Analytical estimates of limited sampling biases in different information measures". *Network: Computation in Neural Systems* 7, pp. 87–107.

Park, J. H., Moon, H.-J., Kang, D.-H., Hyung, S., Shin, H. J., and Suh, J.-K. F. (2014). "Off-linke responses to the blue-light in rd1/ChR2 mouse retina". *9th International Meeting on Substrate-Integrated Microelectrode Arrays.* Reutlingen, Germany: NMI, pp. 95–97.

Parzen, E. (1962). "On estimation of a probability density function and mode". *The Annals of Mathematical Statistics* 33 (3), pp. 1065–1076.

Pearson, R. A., Barber, A. C., Rizzi, M., Hippert, C., Xue, T., West, E. L., Duran, Y., Smith, A. J., Chuang, J. Z., Azam, S. A., Luhmann, U. F. O., Benucci, A., Sung, C. H., Bainbridge, J. W., Carandini, M., Yau, K.-W., Sowden, J. C., and Ali, R. R. (2012). "Restoration of vision after transplantation of photoreceptors." *Nature* 485 (7396), pp. 99–103.

Pelli, D. G. (1997). "The VideoToolbox software for visual psychophysics: Transforming numbers into movies". *Spatial Vision* 10, pp. 437–442.

Peng, Y. W., Hao, Y., Petters, R. M., and Wong, F. (2000). “Ectopic synaptogenesis in the mammalian retina caused by rod photoreceptor-specific mutations.” *Nature Neuroscience* 3 (11), pp. 1121–7.

Peng, Y., Zhang, Y., Huang, B., Luo, Y., Zhang, M., Li, K., Li, W., Wen, W., and Tang, S. (2014). “Survival and migration of pre-induced adult human peripheral blood mononuclear cells in retinal degeneration slow (rds) mice three months after subretinal transplantation.” *Current Stem Cell Research & Therapy* 9 (2), pp. 124–33.

Pennartz, C. M. A. and Grind, W. A. van de (1990). “Simulation of movement detection by direction-selective ganglion cells in the rabbit and squirrel retina”. *Vision Research* 30 (8), pp. 1223–1234.

Peretz, A., Degani, N., Nachman, R., Uziyel, Y., Gibor, G., Shabat, D., and Attali, B. (2005). “Meclofenamic acid and diclofenac, novel templates of KCNQ2/Q3 potassium channel openers, depress cortical neuron activity and exhibit anticonvulsant properties.” *Molecular Pharmacology* 67 (4), pp. 1053–66.

Perrault, I., Rozet, J. M., Gerber, S., Ghazi, I., Leowski, C., Ducroq, D., Souied, E., Dufier, J. L., Munnich, A., and Kaplan, J. (1999). “Leber congenital amaurosis.” *Molecular Genetics and Metabolism* 68 (2), pp. 200–8.

Petit, C. (2001). “USHER SYNDROME: From Genetics to Pathogenesis”. *Annual Review of Genomics and Human Genetics* 2 (1), pp. 271–297.

Petters, R. M., Alexander, C. A., Wells, K. D., Collins, E. B., Sommer, J. R., Blanton, M. R., Rojas, G., Hao, Y., Flowers, W. L., Banin, E., Cideciyan, A. V., Jacobson, S. G., and Wong, F. (1997). “Genetically engineered large animal model for studying cone photoreceptor survival and degeneration in retinitis pigmentosa.” *Nature Biotechnology* 15 (10), pp. 965–70.

Pillow, J. W., Paninski, L., Uzzell, V. J., Simoncelli, E. P., and Chichilnisky, E. J. (2005). “Prediction and Decoding of Retinal Ganglion Cell Responses with a Probabilistic Spiking Model”. *The Journal of Neuroscience* 25 (47), pp. 11003–11013.

Pillow, J. W., Shlens, J., Paninski, L., Sher, A., Litke, A. M., Chichilnisky, E. J., and Simoncelli, E. P. (2008). “Spatio-temporal correlations and visual signalling in a complete neuronal population”. *Nature* 454 (7207), pp. 995–999.

Pitkow, X. and Meister, M. (2012). "Decorrelation and efficient coding by retinal ganglion cells". *Nature Neuroscience* 15 (4), pp. 628–635.

Pittler, S. J. and Baehr, W. (1991). "Identification of a nonsense mutation in the rod photoreceptor cGMP phosphodiesterase beta-subunit gene of the rd mouse." *Proceedings of the National Academy of Sciences of the United States of America* 88 (19), pp. 8322–8326.

Press, W., Teukolsky, S., Vetterling, W., and Flannery, D. (2007). "Minimization or Maximization of Functions". *Numerical Recipes: The Art of Scientific Computing.* 3rd. New York, NY: Cambridge University Press. Chap. 10, pp. 487–562.

Publio, R., Oliveira, R. F., and Roque, A. C. (2009). "A Computational Study on the Role of Gap Junctions and Rod Ih Conductance in the Enhancement of the Dynamic Range of the Retina". *PLoS ONE* 4 (9), e6970.

Quian Quiroga, R. and Panzeri, S. (2009). "Extracting information from neuronal populations: information theory and decoding approaches." *Nature Reviews Neuroscience* 10 (3), pp. 173–85.

Quigley, H. A., Nickells, R. W., Kerrigan, L. A., Pease, M. E., Thibault, D. J., and Zack, D. J. (1995). "Retinal ganglion cell death in experimental glaucoma and after axotomy occurs by apoptosis". *Investigative Ophthalmology & Visual Science* 36 (5), pp. 774–786.

Ramon y Cajal, S. (1900). *Structure of the Mammalian Retina.*

RetroSense (2015). *RetroSense's optogenetic approach cleared by FDA to begin clinical trials in RP. #retinitis #blindnesss #genetherapy http://tinyurl.com/oear9aj.* URL: `https://twitter.com/RetroSense1/status/636173368434290688` (visited on 09/21/2015).

Reutsky-Gefen, I., Golan, L., Farah, N., Schejter, A., Tsur, L., Brosh, I., and Shoham, S. (2013). "Holographic optogenetic stimulation of patterned neuronal activity for vision restoration". *Nature Communications* 4, p. 1509.

Richardson, T. M. (1969). "Cytoplasmic and ciliary connections between the inner and outer segments of mammalian visual receptors". *Vision Research* 9 (7), pp. 727–731.

Rieke, F., Warland, D. K., de Ruyter van Steveninck, R., and Bialek, W. (1999). *Spikes: Exploring the Neural Code*. Cambridge, MA, USA: MIT Press.

Rivolta, C. (2002). “Retinitis pigmentosa and allied diseases: numerous diseases, genes, and inheritance patterns”. *Human Molecular Genetics* 11 (10), pp. 1219–1227.

Rockhill, R. L., Daly, F. J., MacNeil, M. A., Brown, S. P., and Masland, R. H. (2002). “The diversity of ganglion cells in a mammalian retina”. *The Journal of Neuroscience* 22 (9), pp. 3831–3843.

Rodieck, R. W. (1965). “Quantitative analysis of cat retinal ganglion cell response to visual stimuli”. *Vision Research* 5 (12), pp. 583–601.

Rodriguez, A. R., de Sevilla Müller, L. P., and Brecha, N. C. (2014). “The RNA binding protein RBPMS is a selective marker of ganglion cells in the mammalian retina”. *Journal of Comparative Neurology* 522 (6), pp. 1411–1443.

Rofagha, S., Bhisitkul, R. B., Boyer, D. S., Sadda, S. R., and Zhang, K. (2013). “Seven-year outcomes in ranibizumab-treated patients in ANCHOR, MARINA, and HORIZON: a multicenter cohort study (SEVEN-UP).” *Ophthalmology* 120 (11), pp. 2292–9.

Rosenblatt, M. (1956). “Remarks on some nonparametric estimates of a density function”. *The Annals of Mathematical Statistics* 27 (3), pp. 832–837.

Roska, B. (2014). “The First Steps in Vision: Computation and Repair”. *Society for Neuroscience Annual Meeting*. Washington, DC.

Rozental, R., Srinivas, M., and Spray, D. C. (2001). “How to Close a Gap Junction Channel”. *Connexin Methods and Protocols*. Ed. by R. Bruzzone and C. Giaume. Vol. 154. Methods in Molecular Biology. New York, NY: Humana Press. Chap. 25, pp. 447–476.

Saglam, M., Hayashida, Y., and Murayama, N. (2008). “A Retinal Circuit Model Accounting for Functions of Amacrine Cells”. *Neural Information Processing*. Ed. by M. Ishikawa, K. Doya, H. Miyamoto, and T. Yamakawa. Vol. 4984. Heidelberg, Germany: Springer Berlin. Chap. 1, pp. 1–6.

Sahel, J.-A. and Roska, B. (2013). “Gene Therapy for Blindness”. *Annual Review of Neuroscience* 36 (1), pp. 467–488.

Sakai, H. M. and Naka, K. (1995). “Response dynamics and receptive-field organization of catfish ganglion cells”. *Journal of General Physiology* 105 (6), pp. 795–814.

Samba, R., Herrmann, T., and Zeck, G. (2015). “PEDOT-CNT coated electrodes stimulate retinal neurons at low voltage amplitudes and low charge densities.” *Journal of Neural Engineering* 12 (1), p. 016014.

Santarelli, M., Diplotti, L., Samassa, F., Veritti, D., Kuppermann, B. D., and Lanzetta, P. (2015). “Advances in pharmacotherapy for wet age-related macular degeneration”. *Expert Opinion on Pharmacotherapy* 16 (12), pp. 1769–1781.

Santos, A., Humayan, M. S., de Juan Jr., E., Greenberg, R. J., Marsh, M. J., Klock, I. B., and Milam, A. H. (1997). “Preservation of the inner retina in retinitis pigmentosa. A morphometric analysis.” *Archives of Ophthalmology* 115 (4), pp. 511–515.

Sanyal, S., De Ruiter, A., and Hawkins, R. K. (1980). “Development and degeneration of retina in rds mutant mice: light microscopy.” *Journal of Comparative Neurology* 194 (1), pp. 193–207.

Sasaki, T. and Kaneko, A. (1996). “l-Glutamate-induced responses in OFF-type bipolar cells of the cat retina”. *Vision Research* 36 (6), pp. 787–795.

Saunders, A. L., Williams, C. E., Heriot, W., Briggs, R., Yeoh, J., Nayagam, D. A. X., McCombe, M., Villalobos, J., Burns, O., Luu, C. D., Ayton, L. N., McPhedran, M., Opie, N. L., McGowan, C., Shepherd, R. K., Guymer, R., and Allen, P. J. (2014). “Development of a surgical procedure for implantation of a prototype suprachoroidal retinal prosthesis”. *Clinical & Experimental Ophthalmology* 42 (7), pp. 665–74.

Schachter, M. J., Oesch, N., Smith, R. G., and Taylor, W. R. (2010). “Dendritic Spikes Amplify the Synaptic Signal to Enhance Detection of Motion in a Simulation of the Direction-Selective Ganglion Cell”. *PLoS Computational Biology* 6 (8), e1000899.

Schneidman, E., Bialek, W., and Berry, Michael J., I. (2003). “Synergy, Redundancy, and Independence in Population Codes”. *The Journal of Neuroscience* 23 (37), pp. 11539–11553.

Schneidman, E., Puchalla, J. L., Segev, R., Harris, R. A., Bialek, W., and Berry, M. J. (2011). “Synergy from silence in a combinatorial neural code”. *The Journal of Neuroscience* 31 (44), pp. 15732–41.

Scholz, F., Bamberg, E., Bamann, C., and Wachtveitl, J. (2012). “Tuning the primary reaction of channelrhodopsin-2 by imidazole, pH, and site-specific mutations.” *Biophysical journal* 102 (11), pp. 2649–57.

Schwartz, G., Macke, J., Amodei, D., Tang, H., and Berry, M. J. (2012a). “Low error discrimination using a correlated population code.” *Journal of Neurophysiology* 108 (4), pp. 1069–88.

Schwartz, G. W., Okawa, H., Dunn, F. A., Morgan, J. L., Kerschensteiner, D., Wong, R. O., and Rieke, F. (2012b). “The spatial structure of a nonlinear receptive field”. *Nature Neuroscience* 15 (11), pp. 1572–1580.

Seiler, M. J. and Aramant, R. B. (2012). “Cell replacement and visual restoration by retinal sheet transplants.” *Progress in Retinal and Eye Research* 31 (6), pp. 661–87.

Sekirnjak, C., Hulse, C., Jepson, L. H., Hottowy, P., Sher, A., Dabrowski, W., Litke, A. M., and Chichilnisky, E. J. (2009). “Loss of Responses to Visual But Not Electrical Stimulation in Ganglion Cells of Rats With Severe Photoreceptor Degeneration”. *Journal of Neurophysiology* 102, pp. 3260–3269.

Shoham, S., Fellows, M. R., and Normann, R. A. (2003). “Robust, automatic spike sorting using mixtures of multivariate t-Distributions”. *Journal of Neuroscience Methods* 127 (2), pp. 111–112.

Shoval, A., Adams, C., David-Pur, M., Shein, M., Hanein, Y., and Sernagor, E. (2009). “Carbon nanotube electrodes for effective interfacing with retinal tissue”. *Frontiers in Neuroengineering* 2, p. 4.

Simonelli, F., Maguire, A. M., Testa, F., Pierce, E. A., Mingozzi, F., Bennicelli, J. L., and al, E. (2010). “Gene therapy for Leber’s congenital amaurosis is safe and effective through 1.5 years after vector administration”. *Molecular Therapy* 18, pp. 643–650.

Singh, M. S., Charbel Issa, P., Butler, R., Martin, C., Lipinski, D. M., Sekaran, S., Barnard, A. R., and MacLaren, R. E. (2013). “Reversal of end-stage retinal degeneration and restoration of visual function by photoreceptor transplantation”. *Proceedings of the National Academy of Sciences of the United States of America* 110 (3), pp. 1101–1106.

Sloan, L. L. (1959). “New test Charts for the Measurement of Visual Acuity at far and Near Distances*”. *American Journal of Ophthalmology* 48 (6), pp. 807–813.

Soliman, G. S. H. and Truper, H. G. (1982). “Halobacterium pharaonis: a new, extremely haloalkaliphilic archaebacterium with low magnesium requirement”. *Zentralblatt für Bakteriologie Mikrobiologie und Hygiene erste Abteilung Originale C, Allgemeine, angewandte und ökologische Mikrobiologie* 3, pp. 318–329.

Soto, F., Ma, X., Cecil, J. L., Vo, B. Q., Culican, S. M., and Kerschensteiner, D. (2012). “Spontaneous activity promotes synapse formation in a cell-type-dependent manner in the developing retina.” *The Journal of Neuroscience* 32 (16), pp. 5426–39.

Stargardt, K. (1909). “Über familiäre, progressive Degeneration in der Maculagegend des Auges”. *Albrecht von Græfe’s Archiv für Ophthalmologie* 71 (3), pp. 534–550.

Stasheff, S. F. (2008). “Emergence of Sustained Spontaneous Hyperactivity and Temporary Preservation of off Responses in Ganglion Cells of the Retinal Degeneration (rd1) Mouse”. *Journal of Neurophysiology* 99 (3), pp. 1408–1421.

Stasheff, S. F., Shankar, M., and Andrews, M. P. (2011). “Developmental time course distinguishes changes in spontaneous and light-evoked retinal ganglion cell activity in rd1 and rd10 mice”. *Journal of Neurophysiology* 105 (6), pp. 3002–3009.

Steinberg, R. H., Flannery, J. G., Naash, M., Oh, P., Matthes, M. T., Yasumura, D., Lau-Villacorta, C., Chen, J., and Lavail, M. M. (1996). “Transgenic rat models of inherited retinal degeneration caused by mutant opsin genes”. *Investigative Ophthalmology & Visual Science* 37 (3), S698.

Stingl, K. K. T., Bartz-Schmidt, K. U., Besch, D., Braun, A., Bruckmann, A., Gekeler, F., Greppmaier, U., Hipp, S., Hörtdörfer, G., Kernstock, C., Koitschev, A., Kusnyerik, A., Sachs, H., Schatz, A., Stingl, K. K. T., Peters, T., Wilhelm, B., and Zrenner, E. (2013). “Artificial vision with wirelessly powered subretinal electronic implant alpha-IMS”. *Proceedings of the Royal Society B: Biological Sciences* 280 (1757), p. 20130077.

Stingl, K., Bartz-Schmidt, K. U., Besch, D., Chee, C. K., Cottriall, C. L., Gekeler, F., Groppe, M., Jackson, T. L., MacLaren, R. E., Koitschev, A., Kusnyerik, A., Neffendorf, J., Nemeth, J., Naeem, M. A. N., Peters, T., Ramsden, J. D., Sachs, H., Simpson, A., Singh, M. S., Wilhelm, B., Wong, D., and Zrenner, E. (2015). “Subretinal Visual Implant Alpha IMS - Clinical trial interim report." *Vision Research* 111 (Pt B), pp. 149–60.

Stone, J. L., Barlow, W. E., Humayan, M. S., de Juan Jr., E., and Milam, A. H. (1992). "Morphometric analysis of macular photoreceptors and ganglion cells in retinas with retinitis pigmentosa". *Archives of Ophthalmology* 110 (11), pp. 1634–1639.

Strauss, O., Stumpff, F., Mergler, S., Wienrich, M., and Wiederholt, M. (1998). "The Royal College of Surgeons rat: an animal model for inherited retinal degeneration with a still unknown genetic defect". *Acta Anatomica* 162 (2-3), pp. 101–11.

Strettoi, E. and Pignatelli, V. (2000). "Modifications of retinal neurons in a mouse model of retinitis pigmentosa". *Proceedings of the National Academy of Sciences of the United States of America* 97 (20), pp. 11020–11025.

Strettoi, E., Pignatelli, V., Rossi, C., Porciatti, V., and Falsini, B. (2003). "Remodeling of second-order neurons in the retina of rd/rd mutant mice". *Vision Research* 43 (8), pp. 867–877.

Strettoi, E., Porciatti, V., Falsini, B., Pignatelli, V., and Rossi, C. (2002). "Morphological and functional abnormalities in the inner retina of the rd/rd mouse". *The Journal of Neuroscience* 22 (13), pp. 5492–5504.

Strettoi, E., Raviola, E., and Dacheux, R. F. (1992). "Synaptic connections of the narrow-field, bistratified rod amacrine cell (AII) in the rabbit retina". *Journal of Comparative Neurology* 325 (2), pp. 152–168.

Strong, S. P., Koberle, R., de Ruyter van Steveninck, R. R., and Bialek, W. (1998). "Entropy and Information in Neural Spike Trains". *Physical Review Letters* 80 (1), pp. 197–200.

Sugano, E., Isago, H., Wang, Z., Murayama, N., Tamai, M., and Tomita, H. (2011). "Immune responses to adeno-associated virus type 2 encoding channelrhodopsin-2 in a genetically blind rat model for gene therapy". *Gene Therapy* 18 (3), pp. 266–274.

Sullivan, R., Penfold, P., and Pow, D. V. (2003). "Neuronal migration and glial remodeling in degenerating retinas of aged rats and in nonneovascular AMD". *Investigative Ophthalmology & Visual Science* 44 (2), pp. 856–65.

Sun, C., Warland, D. K., Ballesteros, J. M., List, D. van der, and Chalupa, L. M. (2008). "Retinal waves in mice lacking the beta2 subunit of the nicotinic acetylcholine receptor." *Proceedings of the National Academy of Sciences of the United States of America* 105 (36), pp. 13638–43.

Sun, H., Wen, Y., Ning, N., An, J., and Li, J. (2013). "Retinal toxicity associated with high dose of meclofenamic acid." *Drug and Chemical Toxicology* 36 (4), pp. 461–5.

Sun, W., Li, N., and He, S. (2002). "Large-scale morphological survey of mouse retinal ganglion cells." *Journal of Comparative Neurology* 451 (2), pp. 115–26.

Syed, M. M., Lee, S., Zheng, J., and Zhou, Z. J. (2004). "Stage-dependent dynamics and modulation of spontaneous waves in the developing rabbit retina." *The Journal of Physiology* 560 (Pt 2), pp. 533–49.

Szél, A., Röhlich, P., Caffé, A. R., Juliusson, B., Aguirre, G., and Van Veen, T. (1992). "Unique topographic separation of two spectral classes of cones in the mouse retina." *Journal of Comparative Neurology* 325 (3), pp. 327–42.

Szelenyi, I. (2013). "Flupirtine, a re-discovered drug, revisited." *Inflammation Research* 62 (3), pp. 251–8.

Testa, F., Maguire, A. M., Rossi, S., Pierce, E. A., Melillo, P., Marshall, K., Banfi, S., Surace, E. M., Sun, J., Acerra, C., Wright, J. F., Wellman, J., High, K. A., Auricchio, A., Bennett, J., and Simonelli, F. (2013). "Three-year follow-up after unilateral subretinal delivery of adeno-associated virus in patients with Leber congenital Amaurosis type 2." *Ophthalmology* 120 (6), pp. 1283–91.

Thorpe, S., Delorme, A., and Van Rullen, R. (2001). "Spike-based strategies for rapid processing". *Neural Networks* 14 (6–7), pp. 715–725.

Thyagarajan, S., Van Wyk, M., Lehmann, K., Löwel, S., Feng, G., and Wässle, H. (2010). "Visual function in mice with photoreceptor degeneration and transgenic expression of channelrhodopsin 2 in ganglion cells". *The Journal of Neuroscience* 30 (26), pp. 8745–8758.

Timme, N., Alford, W., Flecker, B., and Beggs, J. M. (2014). "Synergy, redundancy, and multivariate information measures: an experimentalist's perspective." *Journal of Computational Neuroscience* 36 (2), pp. 119–40.

To, K. W., Adamian, M., Jakobiec, F. A., and Berson, E. L. (1998a). “Histopathologic and immunohistochemical study of an autopsy eye with X-linked cone degeneration.” *Archives of Ophthalmology* 116 (1), pp. 100–3.

To, K. W., Adamian, M., Jakobiec, F. A., and Berson, E. L. (1998b). “Histopathologic and immunohistochemical study of dominant cone degeneration”. *American Journal of Ophthalmology* 126 (1), pp. 140–142.

Tochitsky, I., Polosukhina, A., Degtyar, V. E., Gallerani, N., Smith, C. M., Friedman, A., Van Gelder, R. N., Trauner, D., Kaufer, D., and Kramer, R. H. (2014). “Restoring visual function to blind mice with a photoswitch that exploits electrophysiological remodeling of retinal ganglion cells.” *Neuron* 81 (4), pp. 800–13.

Tomita, H., Sugano, E., Fukazawa, Y., Isago, H., Sugiyama, Y., Hiroi, T., and al, E. (2009). “Visual properties of transgenic rats harboring the channelrhodopsin-2 gene regulated by the thy-1.2 promoter”. *PLoS ONE* 4, e7679.

Tomita, H., Sugano, E., Isago, H., Hiroi, T., Wang, Z., Ohta, E., and Tamai, M. (2010). “Channelrhodopsin-2 gene transduced into retinal ganglion cells restores functional vision in genetically blind rats”. *Experimental Eye Research* 90 (3), pp. 429–436.

Tomita, H., Sugano, E., Yawo, H., Ishizuka, T., Isago, H., Narikawa, S., Kügler, S., and Tamai, M. (2007). “Restoration of visual response in aged dystrophic RCS rats using AAV-mediated channelopsin-2 gene transfer”. *Investigative Ophthalmology & Visual Science* 48 (8), pp. 3821–3826.

Toychiev, A. H., Ivanova, E., Yee, C. W.-M., and Sagdullaev, B. T. (2013). “Block of Gap Junctions Eliminates Aberrant Activity and Restores Light Responses during Retinal Degeneration”. *The Journal of Neuroscience* 33 (35), pp. 13972–13977.

Trenholm, S., Borowska, J., Zhang, J., Hoggarth, A., Johnson, K., Barnes, S., Lewis, T. J., and Awatramani, G. B. (2012). “Intrinsic oscillatory activity arising within the electrically coupled AII amacrine–ON cone bipolar cell network is driven by voltage-gated Na+ channels”. *The Journal of Physiology* 590 (10), pp. 2501–2517.

Troilo, D., Howland, H. C., and Judge, S. J. (1993). “Visual optics and retinal cone topography in the common marmoset (Callithrix jacchus).” *Vision Research* 33 (10), pp. 1301–10.

Ulshafer, R. J. and Allen, C. B. (1985). “Hereditary retinal degeneration in the Rhode Island Red chicken: Ultrastructural analysis”. *Experimental Eye Research* 40 (6), pp. 865–877.

Ulshafer, R. J., Allen, C., Dawson, W., and Wolf, E. (1984). “Hereditary retinal degeneration in the Rhode Island Red chicken. I. Histology and ERG”. *Experimental Eye Research* 39 (2), pp. 125–135.

Uzzell, V. J. and Chichilnisky, E. J. (2004). “Precision of Spike Trains in Primate Retinal Ganglion Cells”. *Journal of Neurophysiology* 92 (2), pp. 780–789.

Van Rullen, R. and Thorpe, S. J. (2001). “Rate coding versus temporal order coding: What the retinal ganglion cells tell the visual cortex”. *Neural Computation* 13 (6), pp. 1255–1283.

Vaney, D. I. (1990). “The mosaic of amacrine cells in the mammalian retina”. *Progress in Retinal Research* 9, pp. 49–100.

Vaney, D. I. (1991). “Many diverse types of retinal neurons show tracer coupling when injected with biocytin or Neurobiotin”. *Neuroscience Letters* 125 (2), pp. 187–190.

Vardi, N., Duvoisin, R., Wu, G., and Sterling, P. (2000). “Localization of mGluR6 to dendrites of ON bipolar cells in primate retina”. *Journal of Comparative Neurology* 423 (3), pp. 402–412.

Varela, C., Igartua, I., Rosa, E. J. de la, and Villa, P. de la (2003). “Functional modifications in rod bipolar cells in a mouse model of retinitis pigmentosa”. *Vision Research* 43 (8), pp. 879–885.

Veruki, M. L. and Hartveit, E. (2009). “Meclofenamic acid blocks electrical synapses of retinal AII amacrine and on-cone bipolar cells.” *Journal of Neurophysiology* 101 (5), pp. 2339–47.

Victor, J. D. (2002). “Binless strategies for estimation of information from neural data.” *Physical Review E: Statistical, Nonlinear, and Soft Matter Physics* 66 (5 Pt 1), p. 051903.

Völgyi, B., Chheda, S., and Bloomfield, S. A. (2009). “Tracer coupling patterns of the ganglion cell subtypes in the mouse retina”. *Journal of Comparative Neurology* 512 (5), pp. 664–687.

Vollrath, D., Feng, W., Duncan, J. L., Yasumura, D., D'Cruz, P. M., Chappelow, A., Matthes, M. T., Kay, M. A., and LaVail, M. M. (2001). "Correction of the retinal dystrophy phenotype of the RCS rat by viral gene transfer of Mertk." *Proceedings of the National Academy of Sciences of the United States of America* 98 (22), pp. 12584–9.

Wald, G. (1945). "Human vision and the spectrum". *Science* 101 (2635), pp. 653–658.

Wald, G. (1964). "The Receptors of Human Color Vision: Action spectra of three visual pigments in human cones account for normal color vision and color-blindness". *Science* 145 (3636), pp. 1007–1016.

Wallace, D. C., Singh, G., Lott, M. T., Hodge, J. A., Schurr, T. G., Lezza, A. M., Elsas II, L. J., and Nikoskelainen, E. K. (1988). "Mitochondrial DNA mutation associated with Leber's hereditary optic neuropathy". *Science* 242 (4884), p. 1427.

Wang, Q., Kulkarni, S. R., and Verdu, S. (2009). "Divergence Estimation for Multidimensional Densities Via k-Nearest-Neighbor Distances". *IEEE Transactions on Information Theory* 55 (5), pp. 2392–2405.

Waschkowski, F., Hesse, S., Rieck, A. C., Lohmann, T., Brockmann, C., Laube, T., Bornfeld, N., Thumann, G., Walter, P., Mokwa, W., Johnen, S., and Roessler, G. (2014). "Development of very large electrode arrays for epiretinal stimulation (VLARS)". *BioMedical engineering online* 13 (1), p. 11.

Wässle, H., Yamashita, M., Greferath, U., Grünert, U., and Müller, F. (1991). "The rod bipolar cell of the mammalian retina". *Visual Neuroscience* 7 (1-2), pp. 99–112.

Werblin, F. S. and Dowling, J. E. (1969). "Organization of the retina of the mudpuppy, Necturus maculosus. II. Intracellular recording". *Journal of Neurophysiology* 32 (3), pp. 339–355.

Werblin, F. S. (2011). "The retinal hypercircuit: a repeating synaptic interactive motif underlying visual function". *The Journal of Physiology* 589 (15), pp. 3691–3702.

Wichmann, F. A. and Hill, N. J. (2001a). "The psychometric function: I. Fitting, sampling, and goodness of fit." *Perception & Psychophysics* 63 (8), pp. 1293–313.

Wichmann, F. A. and Hill, N. J. (2001b). "The psychometric function: II. Bootstrap-based confidence intervals and sampling." *Perception & Psychophysics* 63 (8), pp. 1314–29.

Wiesel, T. N. (1959). “Recording Inhibition and Excitation in the Cat’s Retinal Ganglion Cells with Intracellular Electrodes”. *Nature* 183 (4656), pp. 264–265.

Williams, P. L. and Beer, R. D. (2010). “Nonnegative Decomposition of Multivariate Information”. *arXiv*, p. 1004.2515. arXiv: `1004.2515`.

Wladyka, C. L. and Kunze, D. L. (2006). “KCNQ/M-currents contribute to the resting membrane potential in rat visceral sensory neurons.” *The Journal of Physiology* 575 (Pt 1), pp. 175–89.

Wohrer, A. and Kornprobst, P. (2009). “Virtual Retina: A biological retina model and simulator, with contrast gain control”. *Journal of Computational Neuroscience* 26 (2), pp. 219–249.

Wolf, E. D., Vainisi, S. J., and Santos-Anderson, R. (1978). “Rod-cone dysplasia in the collie”. *Journal of the American Veterinary Medical Association* 173 (10), pp. 1331–3.

Wong, Y. T., Chen, S. C., Seo, J. M., Morley, J. W., Lovell, N. H., and Suaning, G. J. (2009). “Focal activation of the feline retina via a suprachoroidal electrode array.” *Vision Research* 49 (8), pp. 825–33.

Woodford, B., Liu, Y., Fletcher, R., Chader, G., Farber, D., Santos-Anderson, R., and Tso, M. O. (1982). “Cyclic nucleotide metabolism in inherited retinopathy in collies: A biochemical and histochemical study”. *Experimental Eye Research* 34 (5), pp. 703–714.

Worgotter, F. and Koch, C. (1991). “A detailed model of the primary visual pathway in the cat: comparison of afferent excitatory and intracortical inhibitory connection schemes for orientation selectivity”. *The Journal of Neuroscience* 11 (7), pp. 1959–1979.

Wu, C., Ivanova, E., Zhang, Y., and Pan, Z.-H. (2013). “rAAV-Mediated Subcellular Targeting of Optogenetic Tools in Retinal Ganglion Cells ¡italic¿In Vivo¡/italic¿”. *PLoS ONE* 8 (6), e66332.

Wyk, M. van, Pielecka-Fortuna, J., Löwel, S., and Kleinlogel, S. (2015). “Restoring the ON Switch in Blind Retinas: Opto-mGluR6, a Next-Generation, Cell-Tailored Optogenetic Tool.” *PLoS Biology* 13 (5), e1002143.

Yau, K. W. (1994). “Phototransduction mechanism in retinal rods and cones. The Friedenwald Lecture”. *Investigative Ophthalmology & Visual Science* 35 (1), pp. 9–32.

Yee, C. W.-M., Toychiev, A., and Sagdullaev, B. T. (2012). “Network deficiency exacerbates impairment in a mouse model of retinal degeneration”. *Frontiers in Systems Neuroscience* 6, p. 8.

Yeung, S. Y. M., Pucovský, V., Moffatt, J. D., Saldanha, L., Schwake, M., Ohya, S., and Greenwood, I. A. (2007). “Molecular expression and pharmacological identification of a role for K(v)7 channels in murine vascular reactivity.” *British Journal of Pharmacology* 151 (6), pp. 758–70.

Yoav, B. and Hochberg, Y. (1995). “Controlling the false discovery rate: a practical and powerful approach to multiple testing”. *Journal of the Royal Statistical Society: Series B (Methodological)* 57 (1), pp. 289–300.

Young, M. J., Ray, J., Whiteley, S. J. O., Klassen, H., and Gage, F. H. (2000). “Neuronal Differentiation and Morphological Integration of Hippocampal Progenitor Cells Transplanted to the Retina of Immature and Mature Dystrophic Rats”. *Molecular and Cellular Neuroscience* 16 (3), pp. 197–205.

Zampaglione, E., Ng, A., Litke, A. M., Feldheim, D., and Sher, A. (2014). “A multi-stimuli paradigm for functional characterization of mouse retinal ganglion cells”. *Retinal Neurobiology and Visual Processing.* Saxton’s River, VT, USA: FASEB.

Zemon, V. and Gordon, J. (2006). “Luminance-contrast mechanisms in humans: Visual evoked potentials and a nonlinear model”. *Vision Research* 46 (24), pp. 4163–4180.

Zhang, F., Vierock, J., Yizhar, O., Fenno, L. E., Tsunoda, S., Kianianmomeni, A., Prigge, M., Berndt, A., Cushman, J., Polle, J., Magnuson, J., Hegemann, P., and Deisseroth, K. (2011). “The microbial opsin family of optogenetic tools”. *Cell* 147 (7), pp. 1446–1457.

Zhang, F., Wang, L. P., Brauner, M., Liewald, J. F., Kay, K., Watzke, N., Wood, P. G., Bamberg, E., Nagel, G., Gottschalk, A., and Deisseroth, K. (2007). “Multimodal fast optical interrogation of neural circuitry”. *Nature* 446 (7136), pp. 633–639.

Zhang, Y., Ivanova, E., Bi, A., and Pan, Z. H. (2009). “Ectopic expression of multiple microbial rhodopsins restores ON and OFF light responses in retinas with photoreceptor degeneration”. *The Journal of Neuroscience* 29 (29), pp. 9186–9196.

Zhang, Y., Kim, I.-J., Sanes, J. R., and Meister, M. (2012). “The most numerous ganglion cell type of the mouse retina is a selective feature detector”. *Proceedings of the National Academy of Sciences of the United States of America* 109 (36), pp. 14297–14298.

Zhong, X., Gutierrez, C., Xue, T., Hampton, C., Vergara, M. N., Cao, L.-H., Peters, A., Park, T. S., Zambidis, E. T., Meyer, J. S., Gamm, D. M., Yau, K.-W., and Canto-Soler, M. V. (2014). “Generation of three-dimensional retinal tissue with functional photoreceptors from human iPSCs.” *Nature Communications* 5, p. 4047.